Hydraulic fracture growth in quasi-brittle materials

Nature is full of infinite causes
that have never occurred in experience.
— Leonardo da Vinci

To my parents - Guiqin Zhang and Bao'e Liu…

Acknowledgements

I would like to first express my sincere and deep gratitude to my thesis supervisor Prof. Brice Lecampion for bringing me to the world of hydraulic fracturing and computational mechanics. I feel lucky to spend several years in my life fully exploring a subject that interests me a lot. Many thanks for allowing me to test the new ideas that I came up with and for providing continuous help and guidance during my Ph.D.

I want to thank Prof. Dmitry Garagash, who contributes a lot to Chapter 3 in this thesis. Thank you for the insightful discussions. Your previous work on the tip of cohesive hydraulic fractures has inspired me a lot, which has finally led to the work presented in Chapter 4. I also want to thank Dr. Thomas Blum for guiding me on acoustic measurement and analysis. I appreciated a lot the help you gave me during the early stage of my experimental investigation.

I gratefully acknowledge my dissertation committee members, Professors Andrew Bunger, Marie Violay, John Kolinski, and Dr. Xi Zhang, for their efforts in reading the manuscript and the discussions during the defense. A special thanks goes to Professors Petro Reis, Marie Violay, and Lyesse Laloui who have kindly shared their experimental capabilities and allowed me to obtain important measurements on my samples. I also want to express my gratitude to Gary Perrenoud, Michael Monnet, Jeremie Bettex, and Swan Brede. I really appreciate the help you gave me during the experimental preparation. The experiments would not be successfully conducted without you. A big thanks goes to Laurent Gastaldo for your instructions on various experimental equipment and Antonio Salazar for your kind help in testing the elastic properties of rocks. I give a final thanks to my amazing colleagues, notably to my office mates Fatima and Federico. Thank you for those delightful conversations during the lunches on campus. Many thanks to Dmitry Nikolskiy, Haseeb, Carlo, Dmitry Loginov, Alexis, Andreas, Maalek, Mohsen, Guanyi, and Dominique for bringing lightness to the lab.

During these four years in Switzerland, I have met many new friends, and I would like to sincerely thank you for your accompany and support. Those memories of hikes, skis, and discussions would be a treasure of my life.

I want to also express my sincere gratitude to my professors of Master. Many thanks to Prof. Matthieu Vandamme for sharing this Ph.D. opportunity with me, which has finally led to this journey full of adventures and surprises, and Prof. Limin Sun for our discussions on the professional career.

Acknowledgements

A special thanks goes to François and Geneviève who have helped me learn better about the French culture. I am very grateful for your kind help upon my first arrival in Europe.

In the end, I would like to thank my parents for their unconditional love and support as always. I love you.

Acknowledgement of Support

Lausanne, April 17, 2021   Dong Liu

Abstract

Hydraulic fracturing is a technique used to increase the productivity of deep wells in low-permeability porous formations. It is extensively used in the oil and gas industry, but also in several mining, civil and environmental applications. It consists of the injection of a fluid from a wellbore at a sufficiently large rate to create and propagate a tensile fracture inside the rock formation. The growth of a hydraulic fracture is a highly non-linear moving boundary hydro-mechanical problem. Many physical processes are tightly coupled and influence the fracture growth, notably the elastic deformation of the material, the creation of new fracture surfaces, viscous fluid flow inside the propagating fracture, and fluid leak-off into the surrounding medium. The theory of linear hydraulic fracture mechanics (LHFM) is able to describe well the growth process, with adequate comparisons between predictions and experimental observations in linear brittle elastic materials. However, deviations from LHFM predictions have been reported at the laboratory and field scales in some cases, notably a larger fluid pressure and a shorter fracture length. These deviations are often associated with the non-linear nature of rock fracture deformation (notably its quasi-brittle behavior). However, the impact of these material non-linearities on the coupled problem of hydraulic fracture propagation is not yet fully understood.

In this context, this thesis investigates numerically and experimentally the effect of the quasi-brittle nature of rocks on hydraulic fracture growth. We first solve the propagation of a hydraulic fracture using a power-law fracture length-dependent fracture energy to model macroscopically the effect of an enlarging fracture process zone. Numerically, the use of Gauss-Chebyshev quadrature and barycentric Lagrange interpolation techniques reduces the hydraulic fracture moving boundary problem to a set of non-linear ordinary differential equations. We find that this increasing apparent toughness leads to a slower fracture growth, larger net pressure, and larger fracture opening compared with constant toughness LHFM solutions and a faster transition to the toughness dominated regime. We also show that the solution can be approximated by the self-similar constant toughness solutions with the instantaneous toughness value.

We then explore the impact of the quasi-brittle nature of rocks by using a cohesive zone model coupled to elastohydrodynamic lubrication fluid flow to simulate HF growth. We notably account for fluid cavitation at the fracture tip and the effect of fracture roughness on flow. By dimensional analysis, we obtain a time-scale that characterizes the nucleation of the cohesive zone and quantify three stages of fracture growth: a) a cohesive zone nucleation stage and b) an intermediate stage where predictions can deviate significantly from LHFM solutions,

Abstract

and c) a late stage where the fracture growth finally converges toward the LHFM predictions. The deviations in the first two stages include shorter fracture length, larger net pressure, and larger fracture opening and indicate an increase of fracture resistance/energy dissipation. The additional energy dissipation compared with LHFM comes mostly from the impact of the rough fracture process zone on viscous fluid flow. This additional viscous dissipation increases for a larger value of the ratio between the in-situ confining stress and the material peak cohesive stress.

We finally discuss hydraulic fracture experiments performed on two impermeable rocks (exhibiting different grain sizes) under different confinement and injection conditions. We notably develop an inversion technique to reconstruct the fracture front geometry using diffracted waves recorded via an array of 32 sources and 32 receivers piezo-electric transducers. We find that transmitted waves attenuate before the arrival of the fracture front estimated from diffracted waves, indicating the existence of a fracture process zone of centimeters extent in these laboratory experiments. This fracture process zone is found to be comparable with the fracture extent at the scale of decimeter sample sizes, thus implying an important limitation of laboratory HF experiments performed in quasi-brittle rocks on finite-size samples.

Keywords: Fluid-driven fractures, Quasi-brittle materials, Fracture process zone, Cohesive zone models, Fluid lag, Fracture roughness, Apparent toughness, Numerical modeling, Laboratory experiments, Active acoustic monitoring, True tri-axial tests.

Résumé

La fracturation hydraulique est une technique utilisée pour améliorer la productivité des puits situés dans des formations poreuses faiblement perméables. Cette technique est utilisée d'une manière routinière dans l'industrie pétrolière mais également dans le domaine minier, génie civil et environnemental. Le processus consiste à injecter depuis le puits un fluide à un débit suffisant pour créer et propager des fractures à l'intérieur de la formation rocheuse. La propagation d'une fracture hydraulique est un problème hydromécanique hautement non linéaire. De nombreux processus physiques sont étroitement couplés et influencent la propagation de la fracture, tels que la déformation élastique du matériau, la création de nouvelle surface de fracture, l'écoulement du fluide visqueux à l'intérieur de la fracture et la fuite du fluide injecté dans la roche poreuse environnante. La théorie de la mécanique de la fracture hydraulique linéaire (LHFM) décrit bien ce processus couplé, avec des comparaisons satisfaisantes entre les prévisions et les observations expérimentales pour le cas de milieu élastique fragile linéaire. Cependant, des écarts par rapport aux prévisions ont été signalés à l'échelle du laboratoire et sur le terrain dans certains cas, notamment une pression de fluide plus importante et une longueur de fracture plus courte. Ces différences sont souvent associées au caractère non linéaire de la déformation des roches (notamment leur comportement quasi-fragile). Cependant, l'impact des non-linéarités des matériaux sur la propagation des fractures hydrauliques n'est pas encore entièrement compris.

Dans ce contexte, cette thèse étudie numériquement et expérimentalement l'effet de la nature quasi fragile des roches sur la propagation des fractures hydrauliques. Nous résolvons d'abord la propagation d'une fracture hydraulique en utilisant une énergie de fracture dépendante de la longueur de fracture pour modéliser macroscopiquement l'effet d'agrandissement de la zone de transition en bout de fissure. Numériquement, l'utilisation d'une quadrature de Gauss-Chebyshev et des techniques d'interpolation barycentriques réduit le problème à un système d'équations différentielles ordinaires non linéaires. Nous constatons que cette augmentation de la ténacité apparente avec la longueur conduit à une croissance de fracture plus lente, une pression de fluide et une ouverture de fracture plus élevés par rapport aux solutions LHFM à ténacité constante. Une transition plus rapide vers le régime dominé par la ténacité est également constatée. Nous montrons également que la solution peut être approximée par les solutions à ténacité constante avec la valeur de ténacité instantanée correspondante.

Nous étudions ensuite l'impact de la nature quasi fragile des roches en utilisant un modèle de zone cohésive en combinaison avec l'écoulement élastohydrodynamique pour simuler la propagation d'une fracture hydraulique. Nous prenons compte l'évolution de la zone de

cavitation du fluide en pointe de fracture et de l'effet de la rugosité des surfaces de la fracture sur l'écoulement. Par analyse dimensionnelle, nous obtenons un temps caractéristique gouvernant la nucléation de la zone cohésive et délimitons trois étapes de propagation de la fracture : a) une étape de nucléation de la zone cohésive et b) une étape intermédiaire où les prédictions peuvent s'écarter significativement des solutions LHFM, et c) une étape finale où la propagation tend vers les prédictions de la théorie linéaire (LHFM). Les écarts dans les deux premières étapes comprennent une longueur de fracture plus courte, une pression de fluide et une ouverture de fracture plus élevées. Ils indiquent une augmentation de la résistance globale à la fracturation. La dissipation d'énergie supplémentaire par rapport à la théorie linéaire LHFM provient principalement de l'impact de la rugosité de la fracture sur l'écoulement visqueux du fluide. Cette dissipation augmente pour un rapport plus élevé entre la contrainte in situ et la cohésion maximale du matériau.

Nous présentons ensuite des expériences de fracturation hydraulique réalisées sur deux roches imperméables (présentant des granulométries différentes) dans des conditions de confinement et d'injection variées. Nous développons notamment une technique d'inversion pour reconstruire la géométrie du front de fracture à l'aide d'ondes acoustiques diffractées enregistrées via un réseau de 32 sources et 32 récepteurs piézoélectriques. Nous constatons que les ondes transmises s'atténuent avant l'arrivée du front de fracture, qui est estimé à partir des ondes diffractées. Cela indique l'existence d'une zone de transition de quelques centimètres en bout de fissure. Cette zone non-linéaire est comparable à la longueur de la fracture. Cela implique un artefact important des expériences en laboratoire effectuées dans des roches quasi-fragiles sur des échantillons de taille décimétrique.

Mots clés : Fracturation hydraulique, Matériaux quasi-fragiles, Zone de transition, Modèle de zone cohésive, Cavitation en bout de fissure, Rugosité de fracture, Ténacité apparente, Monitoring acoustique active, Essais triaxiaux.

Contents

Contents

Contents

1 Introduction

Hydraulic fracturing is the most commonly used technique to stimulate the production of wells in all types of reservoir. It has notably allowed a dramatic increase in the hydrocarbon production from tight reservoirs in the past two decades. Its process involves the injection of a fluid at a given flow rate into a wellbore in order to propagate fractures in rocks and thus ultimately increase the overall reservoir/wellbore hydraulic conductivity. Although predictions of hydraulic fracture growth based on coupling linear elastic fracture mechanics and lubrication flow are able to reproduce well some experiments performed in model/fine-grain materials, deviations have been observed both at the laboratory and field scales for different rock types. The non-linearities associated with the solid fracture behavior in quasi-brittle rocks have been put forward to explain these deviations. The aim of this thesis is to perform numerical simulations and laboratory experiments to investigate in details the effect of solid non-linearity on hydraulic fracture (HF) growth and notably to decipher the interplay between the process zone development and the fluid flow in the process zone.

1.1 Hydraulic fracturing

HFs are tensile fractures that propagate in a solid under initially compressive stresses. Their growth is driven by internal pressurization due to fluid injection. They manifest naturally at the geological scale as kilometer-long vertical dikes bringing magma from deep underground chambers to the Earth's surface (Spence et al., 1987; Lister and Kerr, 1991; Rubin, 1995; Roper and Lister, 2005, 2007); subhorizontal fractures, known as sills, that divert magma from dikes (Pollard and Holzhausen, 1979; Spence and Sharp, 1985; Bunger and Cruden, 2011); and cracks propagating at glacier beds (Tsai and Rice, 2010). They are also engineered in industrial applications, such as remediation projects of contaminated soils (Murdoch, 2002), preconditioning of block cave mining (Van As and Jeffrey, 2002; Jeffrey et al., 2013), waste disposals at depths, and in-situ stress measurement at depths. Among multiple applications, HFs are most commonly adopted in the stimulation of hydrocarbon-bearing rock strata to increase the production of oil and gas wells (Economides et al., 1989), known as hydraulic fracturing, fracking, or hydrofracturing.

In the industry, for production, we delineate reservoirs with respect to their permeability. There are "unconventional reservoirs" such as shale rock or coal beds, where no sufficient permeability or reservoir pressure allows the flow of natural gas and oil from the rock into the wellbore at high economic return. In order to facilitate extraction from these unconventional reservoirs, hydraulic fracturing is applied to create conductive fractures in the rock formations. The process involves first the high-pressure injection of "fracturing fluid" (primarily water, containing sand or high strength ceramic or others suspended with the aid of additives) into a wellbore to create fractures. Then, the hydraulic pressure is removed from the well. Small grains of hydraulic fracturing proppants (either sand or aluminum oxide) are adopted to hold the fractures open. These open fractures increase the permeability of the formation and ensure the flow of petroleum and natural gas.

As of 2012, 2.5 million "frac jobs" had been performed worldwide on oil and gas wells (King et al., 2012) since its first commercially successful application in 1949. The decade-long boom has increased a lot the oil and gas production and lowered prices for consumers, with near-record lows of the share of household income going to energy expenditures (Elliot and Santiago, 2019). The trend of global primary energy consumption (Fig. 1.1) indicates that oil and gas still take a very important part of the current energy supply. Compared with coal, they are characterized with cleaner burn and less CO2 emission, which will probably lead to an increasing consumption demand of oil and gas in the following tens of years. This calls for more efficient oil and gas extraction and of course a deeper understanding of the hydraulic fracturing technique. However, the full investigation of hydraulic fracturing remains difficult due to the interplay between multiple physical processes, the complex nature of rocks and the fluid flow, the complicated fracture geometries, and in-situ conditions. In this thesis, we mainly focus on the influence of the quasi-brittle nature of rocks on HF growth.

1.2 Motivations

Linear hydraulic fracture mechanics (LHFM) (Detournay, 2016) combine the linear elastic fracture mechanics (LEFM) and lubrication flow (Poiseuille's law) and have successfully predicted the HF growth in transparent materials, such as PMMA and glass (Bunger and Detournay, 2008; Lecampion et al., 2017; Xing et al., 2017). However, deviations from LHFM have been reported in rocks with inconsistent observations between the laboratory (Thallak et al., 1993; Van Dam and de Pater, 1999) and field scales (Shlyapobersky, 1985; Shlyapobersky et al., 1988), some of which indicate an underestimation of the fluid pressure and an overestimation of the fracture length by LHFM. Papanastasiou (1999) argues that LHFM's prediction on net pressures (the difference between fracturing fluid pressure and far-field normal stress) were found 33 to 50 percent lower than the net-pressures encountered in the field (according to a worldwide survey on net-pressures by the Delft Fracturing Consortium). Chudnovsky et al. (2008) reports a plateau of the net pressure during the HF growth rather than the monotonic decrease predicted by LHFM. Makhnenko et al. (2010) points out that the fracture path deviates from the LHFM predictions in near-surface HF laboratory injections and that these
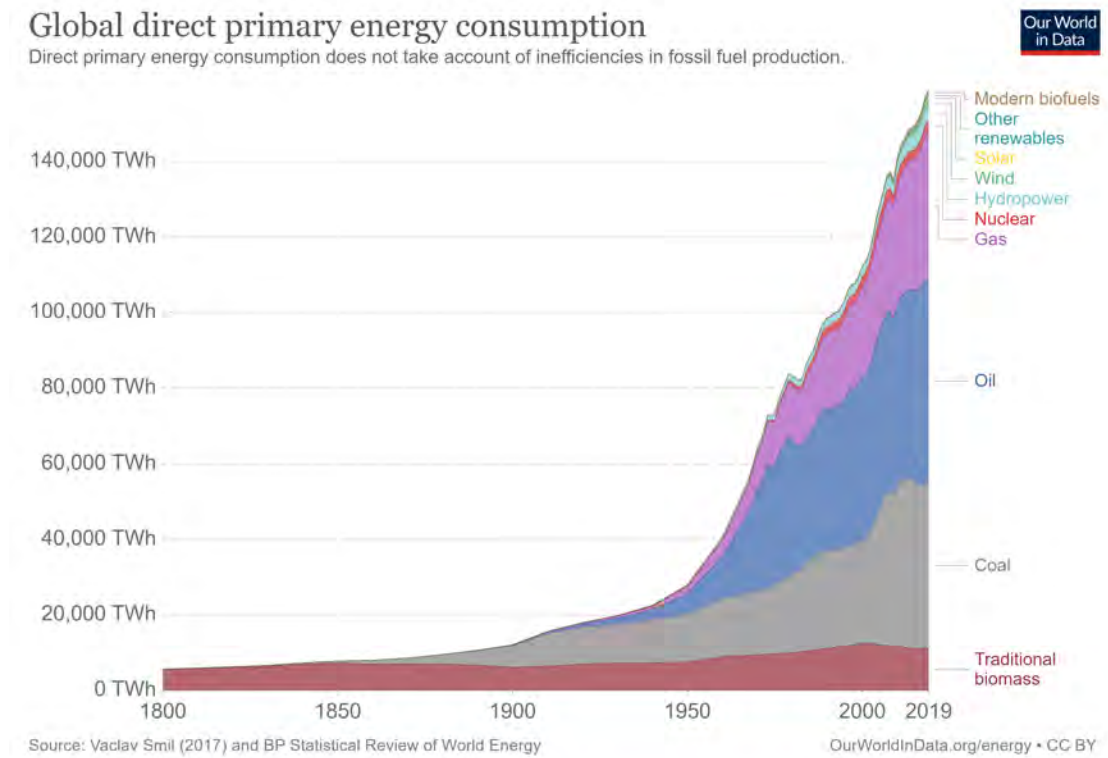
a)
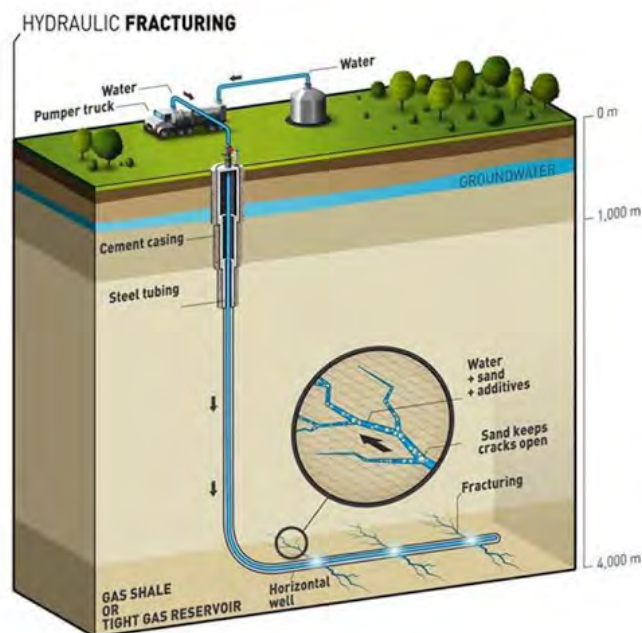
b)

Figure 1.1 – Illustration of a) the trend of global primary energy consumption (2019) and b) the hydraulic fracturing process (http://www.oil-gasportal.com/technologies/unconventional-oilgas/technologyapplications/?print=print, figure taken originally from Total). In this thesis, we focus more on the mode I planar hydraulic fractures with simple geometries, which are different from the fractures illustrated in b).

3

deviations depend on the size of rock specimens.

These deviations have been owed to the solid non-linearity of rocks: a nonlinear zone (process zone) exists around the fracture tip and removes the stress singularity predicted by LEFM. This zone consists of a plastic hardening / perfect yielding part and a progressive softening part (Bazant and Planas, 1997). Different approaches have been put forward in numerical investigations depending on whether plastic deformations or material softening dominate this non-linear zone. For ductile materials like some soft or unconsolidated rocks, plastic deformations have been accounted for in previous investigations (van Dam, 1999; Papanastasiou and Thiercelin, 1993; Papanastasiou, 1997, 1999; Papanastasiou and Atkinson, 2006; Sarris and Papanastasiou, 2013), where they have shown that the presence of the plastic zone results in an increase of the fracture growth resistance and a larger energy dissipation than LHFM. For quasi-brittle materials like most crystalline rocks, cohesive zone models (CZM) Barenblatt (1959); Dugdale (1960); Needleman (2014); Park and Paulino (2011) have been adopted to characterize the progressive damage and material softening in the nonlinear zone. Most numerical investigations (Chen et al., 2009; Chen, 2012; Lecampion, 2012; Yao et al., 2015) neglect the possible existence and evolution of a fluidless cavity due to suction close to the fracture tip (often referred to as a fluid lag). These CZM simulations are also limited to the cases where the cohesive zone only takes a small fraction of the fracture. They show that the HF growth can be well approximated with LEFM/LHFM solutions. However, when accounting for a fluid lag and a cohesive zone model at the same time, the growing fluid lag during the HF growth may perturb the stress field around the tip and leads to off-plane inelastic deformation (Rubin, 1993). Recently, Garagash (2019) investigates the complete solution of a steadily moving semi-infinite cohesive fracture with a fluid lag. He demonstrates that the interplay between the fluid lag and the cohesive zone results in significant deviations from LHFM predictions when the confining stress is larger than the peak cohesive strength (which is the case in most practical configurations at depth). Moreover, Garagash (2015a) reports that viscous fluid flow in rough apertures leads to extra viscous dissipation for a semi-infinite HF. Laboratory and filed observations and theoretical predictions tend to indicate that the solid non-linearity results in an increase in fracture resistance. No quantitative investigation is yet available to decipher the effect of this increasing fracture resistance on the HF growth. Moreover, the possible toughening mechanism due to solid non-linearity remains unclear. The nucleation process of the process zone during HF growth needs further investigation. So does the interplay between the fluid front evolution, fracture roughness and process zone, in particular for a finite HF.

The existence of micro-cracking and crack bridging around the tip of a HF propagating have been confirmed by post-mortem observations (see Lhomme (2005); Chen et al. (2015) for example). Efforts have also been made experimentally to capture this process zone growth. Indirect descriptions on the growth of process zone, such as the measurement of the crack resistance (Hashida et al., 1993) and the HF tip bluntness (van Dam, 1999) have been conducted. Ultrasonic waves act as another approach to directly detect the damage in rocks. Recording the start of the attenuation of transmitted waves (Labuz et al., 1987), or detecting the arrivals of

reflected waves from cracks (Glaser and Hand, 1998), gives a rough estimation of the process zone size around the fracture tip. Passive acoustic emissions provide a clearer region of the zone by showing a map of seismic events (Zietlow and Labuz, 1998; Zang et al., 2000; Stanchits et al., 2014). To better locate the process zone with respect to the fracture tip, an accurate description of the fracture geometry is necessary.

van Dam (1999) points out the strong correlation between the process zone size (estimated from the near-tip stress field) and fracture roughness. Relations between the process zone size and roughness have been reported for dry fractured surfaces (Morel et al., 2002; Nasseri et al., 2010; Barak et al., 2019): the off-plane height variation may present different roughness exponents above and below a "process zone" length scale (Mourot et al., 2005; Bonamy et al., 2006; Ponson et al., 2007; Morel et al., 2008). Moreover, a cut-off length scale can be extracted from the spatial correlations of the slopes of a rough fracture surface, which characterizes the process zone size (Vernède et al., 2015). However, these fractal analysis have not been performed for hydraulic fracture surfaces.

1.3 Key questions

The main question we want to address in this thesis is the effect of the solid non-linearity on the hydraulic fracture growth. We will investigate both numerically and experimentally the hydraulic fracture growth in quasi-brittle materials. More specifically, we will address the following questions.

- Is the LHFM theory still valid to describe the fracture growth in quasi-brittle materials? Does the solid non-linearity effect necessarily augment the apparent fracture toughness? What if we approximate the effect of solid non-linearity with an increasing toughness with fracture length using LHFM? What would be the corresponding time evolution of fracture widths, fracture lengths and fluid pressures? Does the ratio between the maximum width and the fracture length still remain the same as the constant toughness case?

- How does the solid non-linearity influence the HF growth? How does the fluid flow in small rough fractures change the hydraulic conductivity in the process zone? What is the interplay between process zone development and fluid flow? Is the in-situ confining stress involved in this interplay?

- Why different deviations from LHFM are reported at the lab and field scales? Does the process zone exist in quasi-brittle rocks? What is its dimension and evolution? Is it negligible compared to the fracture length? What are the relations between the process zone size and grain size? What is the shape and location of the process zone? How does the process zone evolve during the HF growth?

To answer these questions, we have developed hydro-mechanical models accounting for

either a fracture length dependent apparent toughness or accounting for a cohesive zone model and a fluid lag. We have performed both scaling analysis and numerical simulations to understand their impact on the HF growth. We have also conducted HF experiments under different stresses at the decimeter scale using low porosity/low permeability rocks exhibiting different grain sizes. We have reconstructed the fracture geometry using acoustic diffracted waves. We hope to understand the evolution of apparent fracture toughness and its associated process zone during the HF propagation.

1.4　Outline of this thesis

This thesis is organized as follows.

Chapter 2 summarizes the current theoretical understanding of HF based on linear elastic hydraulic fracture mechanics. We present time and length scales related to transitions between the different physical process at play (elasticity, fracture creation, viscous flow). We report the scaling of the fracture length, width, and net pressures for a finite fracture and different tip asymptotics for a semi-infinite fracture. Informed readers may skip this chapter.

Chapter 3 macroscopically embeds the development of micro-cracking via an increase of toughness with length. We discuss the time evolution of the fracture length, width, and net pressure under the frame of LHFM. We point out that the HF growth can be well grasped by an instant dimensionless toughness. We also discuss the emplacement scaling of magma dikes.

Chapter 4 investigates the growth of a finite plane-strain HF accounting for a rough cohesive zone. We relax the assumptions of LHFM: we adopt a CZM to simulate the process zone effect and account for the deviated fluid flow in small rough apertures. We quantify the impact of the fluid lag, cohesive zone length evolution on the growth of a rough fracture from nucleation to the late stage of growth. We notably show that the co-evolution of the fluid lag and cohesive zone length is governed by a nucleation time-scale that can be significantly large. Moreover, we also clarify the convergence of CZM models toward LHFM predictions at large times.

Chapter 5 demonstrates how we reconstruct the fracture geometry in nontransparent rocks using active acoustic monitoring. We perform a Bayesian analysis to select different possible geometrical models and estimate the errors of geometrical predictions. We test this reconstruction method in this chapter on two experiments performed in two different rocks (marble and gabbro) under experimental conditions characteristic respectively of the fluid lag-viscosity (marble) and toughness (gabbro) dominated HF propagation regimes.

Chapter 6 presents HF experiments conducted under different compressive stresses in rocks exhibiting different grain sizes (a possible proxy for the size of the process zone). We show that the attenuation of the transmitted waves occurs prior to the arrival of the fracture front which indicates that a zone exists ahead of the measured front where the material properties are modified (likely due to micro-cracking). Besides, we try to understand the evolution of the

process zone during the HF growth via the apparent toughness and fracture surface roughness.

Conclusions and perspectives are reported in Chapter 7.

Different appendices cover respectively the material characterization of the two rocks (marble and gabbro), lag-dominated experiments performed in marble and gabbro, and other information regarding the HF experiments.

2 Linear hydraulic fracture mechanics (LHFM)

The propagation of a hydraulic fracture is a highly non-linear hydro-mechanical problem. It includes several physical processes: the creation of new fracture surfaces, the flow of viscous fluid strongly coupled with the elastic deformation of the material, the leak-off of the fluid out of the fracture and the possible existence of a fluid lag near the fracture tip to name a few (Detournay, 2016). In this chapter, we review a number of important results of the theory of linear hydraulic fracture mechanics (LHFM). This theory is developed based on a series of simplified assumptions:

- linear elastic fracture mechanics (LEFM) models the creation and deformation of fracture surfaces.

- the theory of thin-film lubrication models the flow of viscous fluid in the created fracture.

- the leak-off of the fracturing fluid in the surrounding media is approximated by a 1D diffusion process under the assumption that the fluid pressure is roughly constant for such a process - resulting in pressure independent model initially developed by Carter (Howard and Fast, 1957).

- the fluid can not sustain any tensile stress and that its cavitation pressure is sufficiently small that it can be neglected.

Predictions from LHFM have well described the HF propagation with simple geometries (radial, plane-strain), in particular the competition between physical processes in terms of dissipation (toughness / viscosity) and volume conservation (storage / leak-off). They have also pointed out multiple length and time scales characterizing the transition between different energy dissipation mechanisms where depending on conditions, some mechanisms dominate over the others, and as a result, the fracture behavior is widely different. These competing processes also result in a multi-scale structure of the solution near the moving fracture tip: the tip region presents asymptotes associated with different physical processes: the fracture creation closer to the tip, the formation of the cavity in the fluid lag, leak-off of the fluid into the solid, and the viscous fluid flow.

In this chapter, we first recall tip asymptotes associated with different energy dissipation mechanisms. We then discuss the case of a finite fracture and notably the transition between different limiting solutions for simple geometries.

These tip asymptotes, length scales and time scales are functions of different material parameters. For the sake of clarity and to keep in line with the previous contribution, we will use the following material parameters

$$E' = \frac{E}{1-v^2}, \quad K' = 4\left(\frac{2}{\pi}\right)^{1/2} K_{Ic}, \quad \mu' = 12\mu, \quad C' = 2C_L \tag{2.1}$$

where E' is the plane strain modulus, and K', μ' and C' are respectively effective parameters characterizing the fracture toughness K_{Ic}, fluid viscosity μ and Carter's leak-off. Note that the mode I fracture toughness K_{Ic} can be also expressed as function of the fracture energy $G_c = K_{Ic}^2/E'$.

2.1 Tip asymptotes of a semi-infinite hydraulic fracture

If we zoom into the tip region of an arbitrary finite hydraulic fracture, the elasticity and lubrication equation reduce to the ones governing a semi-infinite hydraulic fracture propagating at a constant velocity V. The elasticity reduces to the singular integral equation for a semi-infinite crack under plane-strain conditions by considering distances from the front that are small compared to its local radius of curvature and by noting that any variation of the crack opening near the tip takes place in the direction normal to the front (see Detournay (2016) and the references therein). The asymptotic behavior presents a traveling wave solution and these results imply that the dependence of the opening w and the net fluid pressure $p = p_f - \sigma_o$ on the position and time reduces to a dependence on the distance from the crack front $\hat{x}$, with the current local-front velocity acting as a time-dependent parameter.

Notably, under the LHFM assumptions, the following asymptotic solutions for the fracture opening an fluid net pressure $p = p_f - \sigma_o$ do appear (Garagash, 2019):

- k-asymptote: $w = \beta_k \ell_k^{1/2} \hat{x}^{1/2}$, $p = \dfrac{E'}{\beta_k^2} \dfrac{\ell_m}{\ell_k} \ln(\hat{x}) + \text{const}$

- o-asymptote: $w = \beta_o \dfrac{\sigma_o}{E'} \dfrac{\hat{x}^{3/2}}{\ell_o^{1/2}}$, $p = -\sigma_o$

- $\tilde{m}$-asymptote: $w = \tilde{\beta}_o \ell_{\tilde{m}}^{3/8} \hat{x}^{5/8}$, $p = \tilde{\beta}_o \dfrac{5\cot(5\pi/8)}{32} E' \dfrac{\ell_{\tilde{m}}^{3/8}}{\hat{x}^{3/8}}$

- m-asymptote: $w = \beta_m \ell_m^{1/3} \hat{x}^{2/3}$, $p = E'\beta_m \dfrac{\cot(-\pi/3)}{4} \dfrac{\ell_m^{1/3}}{\hat{x}^{1/3}}$

where different prefactors are respectively: $\beta_k = 4\sqrt{2/\pi}$ (Rice, 1968), $\beta_m = 2^{1/3}3^{5/6}$ (Desroches

et al., 1994), $\beta_o \approx 1.796$ (Garagash and Detournay, 2000), $\tilde{\beta}_o = 4/(15^{1/4}(\sqrt{2}-1)^{1/4})$ (Lenoach, 1995). The different lengthscales appearing in the asymptote above are functions of the material parameters (Eq. (2.1)) and fracture velocity:

$$\ell_m = \frac{\mu' V}{E'}, \quad \ell_k = \frac{\pi}{32}\frac{K'^2}{E'^2}, \quad \ell_o = \left(\frac{E'}{\sigma_o}\right)^3 \ell_m, \quad \ell_{\tilde{m}} = \left(C'V^{1/2}\frac{\mu'}{E'}\right)^{2/3} \tag{2.2}$$

These length scales are associated with distinct processes (viscosity, toughness, leak-off). The k and m asymptotes represent respectively the fracture propagation dominated by the dissipation in creation of fracture surfaces and that in the lubricated fluid flow. The $\tilde{m}$ asymptote indicates an important effect of the leak-off and fluid viscosity, while the o asymptote an important effect of the fluid lag. Among these four asymptotes, the m asymptote is the only dissipation process that is not localized to the fracture tip but realized at large enough distances from the tip. Thus, the near tip hydraulic fracture solution can be framed as a sequence of nested asymptotes listed in the above realized over their corresponding length scales (as long as those separate), transitions between them, and eventual transition to the far field m asymptote. We obtain the transitional length scales

$$\ell_{km} = \frac{\ell_k^3}{\ell_m^2}, \quad \ell_{ko} = \frac{E'}{\sigma_o}\ell_k^{1/2}\ell_o^{1/2}, \quad \ell_{om} = \ell_o, \quad \ell_{m\tilde{m}} = \frac{\ell_{\tilde{m}}^9}{\ell_m^8} \tag{2.3}$$

for the toughness-viscosity (k $\rightarrow$ m), toughness-lag (k $\rightarrow$ o), viscosity-leak-off to viscosity ($\tilde{m}$ $\rightarrow$m) transitions. Two dimensionless parameters are defined related to these length scales

$$\tilde{\chi} = \sqrt{\frac{32}{\pi}}\frac{C'E'}{K'V^{1/2}} = \frac{\ell_{\tilde{m}}^{3/2}}{\ell_m \ell_k^{1/2}}, \quad \kappa = \frac{K'}{E'}\left(\frac{\sigma_o}{\mu'V}\right)^{1/2} = \sqrt{\frac{32}{\pi}}\frac{E'}{\sigma_o}\left(\frac{\ell_k}{\ell_o}\right)^{1/2} \tag{2.4}$$

where $\tilde{\chi}$ permits discrimination (Garagash et al., 2011) between the two limits ($C' = 0$ and $C' \rightarrow \infty$) by setting $\tilde{\chi} = 0$ and $\tilde{\chi} \rightarrow \infty$ (Garagash et al., 2011). κ represents the dimensionless toughness which characterizes the energy dissipation between the creation of fracture surfaces and viscous fluid flow, and determines the disappearance of the fluid lag ($\kappa \rightarrow \infty$). As shown in Fig. 2.1, the classical linear elastic fracture mechanics asymptotic k-asymptote is valid at the tip, and the effect of leak-off ($\tilde{m}$) and fluid lag (o) appears as an intermediate asymptotic between the LEFM k-asymptote and m-asymptote as a function of the dimensionless numbers $\tilde{\chi}$ and κ.

2.2 Propagation of a finite hydraulic fracture

We discuss in this section the propagation of a finite hydraulic fracture driven by a constant injection rate Q_o provided that the material properties and initial stress are uniform over a length scale large enough compared to the ultimate fracture dimension. We focus here on the growth of hydraulic fractures in simple geometries (results of homogeneity) : a plane-strain (KGD) and radial hydraulic fracture. Solving the fracture growth is to determine the
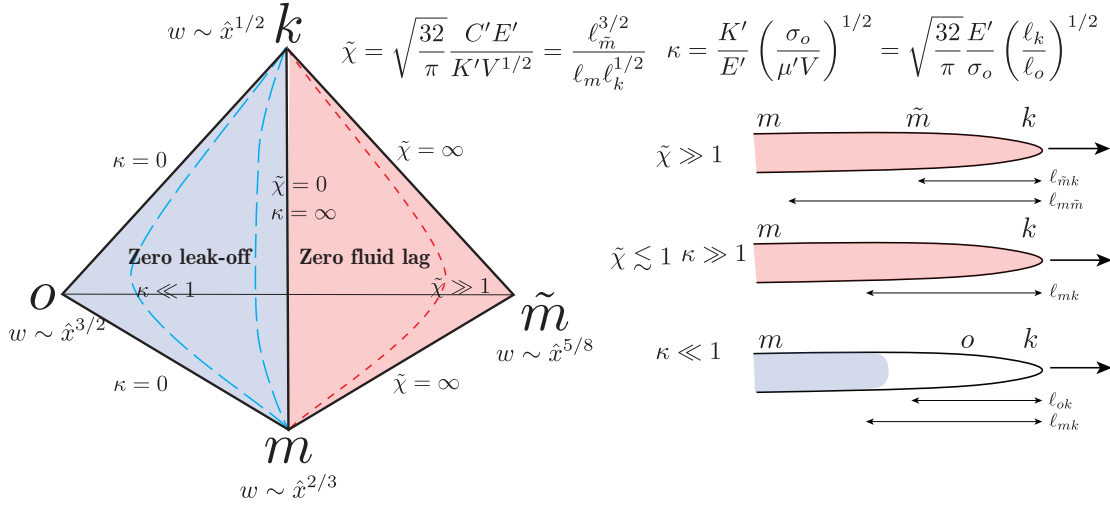
Figure 2.1 – Schematic illustration of asymptotes, adapted from figure 2 in Garagash et al. (2011).

evolution of the fracture extent, fluid extent, fracture opening and net pressure in function of the time and fracture coordinate. We will not go into the details of the solutions but put corresponding references of known solutions in Table. 2.1. In this section, we summarize the evolution between the different limiting regimes and the corresponding time evolution relation of fracture behaviors.

2.2.1 The plane-strain hydraulic fracture

For a fracture propagating in an impermeable medium, the fracture initiates with the fluid front lagging behind the fracture front. The fluid front evolves with time and coalesces with the fracture front over a time scale t_{om}.

$$t_{om} = \frac{E'^2 \mu'}{\sigma_o^3} \tag{2.5}$$

When the fluid lag vanishes, the fracture growth is then only characterized by a dimensionless toughness $\mathcal{K}_m$.

$$\mathcal{K}_m = \frac{K'}{E'} \left(\frac{E'}{\mu' Q_o} \right)^{1/4}, \quad \text{plane-strain} \tag{2.6}$$

This number characterizes the energy dissipation between the creation of fracture surfaces and the viscous fluid flow. $\mathcal{K}_m \ll 1$ and $\mathcal{K}_m \gg 1$ correspond respectively to the toughness K and viscosity M dominated regimes.

When the medium is permeable, the fracture growth also depends on another $t_{m\tilde{m}}$ related to the leak-off of fluid into the solid.

$$t_{m\tilde{m}} = \frac{\mu' Q_o^3}{E' C'^6} \tag{2.7}$$

Plane-strain hydraulic fracture (KGD)
Storage/ K and near K (Garagash, 2006a)
Storage/ M (Adachi and Detournay, 2002; Spence and Sharp, 1985)
Storage/ near M (Garagash and Detournay, 2005)
Storage/ O, O-K edge, lag to zero-lag transition (Garagash, 2006b)
Leak-off/ $\tilde{K}$ (Bunger et al., 2005a)
Leak-off/ $\tilde{M}$ and near $\tilde{M}$ (Adachi and Detournay, 2008)
Complete numerical solutions (Hu and Garagash, 2010)
Radial hydraulic fracture
Storage-compressibility/ $\hat{K}$ (Lhomme et al., 2005)
Storage/ near K (Abe et al., 1976)
Storage/ M and near M, K and near K (Savitski and Detournay, 2002)
Storage/ O (Bunger and Detournay, 2007)
Leak-off/ $\tilde{K}$ (Bunger et al., 2005a)
Leak-off/ M-$\tilde{M}$ (Madyarova, 2004)
Complete numerical solutions (Madyarova, 2004)

Table 2.1 – Known solutions for hydraulic fracture propagation with a simple geometry, adapted from Lecampion et al. (2018).

Regime	L	W	P
M, K	$\sim t^{2/3}$	$\sim t^{1/3}$	$\sim t^{-1/3}$
$\tilde{M}, \tilde{K}$	$\sim t^{1/2}$	$\sim t^{1/4}$	$\sim t^{-1/4}$

Table 2.2 – Power-law evolution of the fracture length L, width W and net pressure P with time for a plane-strain hydraulic fracture corresponding to M, K, $\tilde{M}$ and $\tilde{K}$ vertexes.

In this case, the fracture growth will slowly transition to leak-off dominated regimes. As shown in Fig. 2.2, the growth of a plane-strain hydraulic fracture in an infinite permeable medium depends on two other time-dependent dimensionless numbers in addition to the dimensionless toughness $\mathcal{K}_m$.

$$\mathcal{T}_m = \left(\frac{t}{t_{om}} \right)^{1/3}, \quad \mathcal{C}_m = \left(\frac{t}{t_{m\tilde{m}}} \right)^{1/6} \tag{2.8}$$

where $\mathcal{T}_m$ is related to the disappearance of the fluid lag, $\mathcal{C}_m$ is related to the fluid leak-off, and t is the hydraulic fracture propagation time. We present the corresponding power-law of the time evolution of the fracture length, net pressure and opening in different regimes in Table. 2.2. It is interesting to notice that the power law of the time evolution is the same in viscosity and toughness dominated regimes for a plane-strain HF, however their coefficient depends on different material parameters. We show references of available analytic solutions in Table. 2.1.
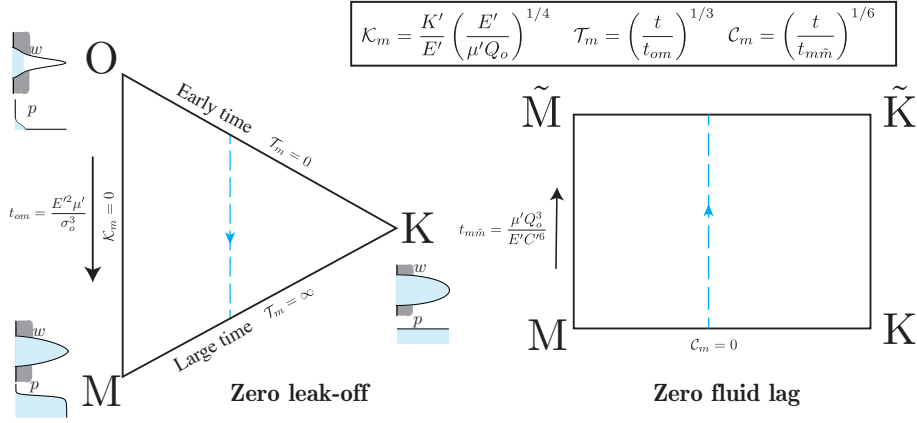
Figure 2.2 – Schematic illustration of the propagation of a plane-strain hydraulic fracture in dimensionless space, adapted from figure 2 in Garagash (2006b) and figure 2 in Hu and Garagash (2010)

2.2.2   The radial hydraulic fracture

A radial HF initiates with an important fluid lag (Bunger and Detournay, 2007). The fluid front catches up with the fracture front over a time scale t_{om}, which is the same as the case of a plane-strain hydraulic fracture as shown in Eq. (2.5). As the fracture continues to grow, the perimeter of the fracture front increases with the fracture extent, and more and more energy is dissipated in the creation of fracture surfaces. The fracture growth transitions from a viscosity dominated M regime to a toughness dominated K regime. The start of this transition from energy dissipation in viscous fluid flow to fracture surface creation is characterized by a time scale t_{mk}:

$$t_{mk} = \left(\frac{E'^{13} \mu'^{5} Q_o^3}{K'^{18}} \right)^{1/2} \tag{2.9}$$

The fracture growth can be therefore characterized by a dimensionless toughness $\mathcal{K}_m$ related to t_{mk}.

$$\mathcal{K}_m = \left(\frac{t}{t_{mk}} \right)^{1/9}, \quad \text{radial} \tag{2.10}$$

For $\mathcal{K}_m \leq 1$, the fracture growth is dominated by the fluid viscosity and for $\mathcal{K}_m > 3.5$, the fracture growth is dominated by fracture toughness (Savitski and Detournay, 2002).

When the medium is permeable, in addition to the two competing dissipative processes associated with the fluid viscosity and fracture toughness, the fracture growth is also governed by the competition between fluid storage in the fracture and leak-off in the surrounding rock. Another time scale $t_{m\tilde{m}}$ characterizes this transition between the storage- and the

Figure 2.3 – Schematic illustration of the propagation of a radial hydraulic fracture in dimensionless space, adapted from figure 3 in Lecampion et al. (2017) and figure 7 in Detournay (2016).

Regime	L	W	P
M	$\sim t^{4/9}$	$\sim t^{1/3}$	$\sim t^{-1/3}$
K	$\sim t^{2/5}$	$\sim t^{1/5}$	$\sim t^{-1/5}$
$\tilde{M}$	$\sim t^{1/4}$	$\sim t^{1/16}$	$\sim t^{-3/16}$
$\tilde{K}$	$\sim t^{1/4}$	$\sim t^{1/8}$	$\sim t^{-1/8}$

Table 2.3 – Power-law evolution of the fracture length L, width W and net pressure P with time for a radial hydraulic fracture, corresponding to M, K, $\tilde{M}$ and $\tilde{K}$ vertices.

leak-off-dominated regime for zero toughness (Madyarova, 2004).

$$t_{m\tilde{m}} = \left(\frac{\mu'^4 Q_o^6}{E'^4 C'^{18}} \right)^{1/7} \tag{2.11}$$

We summarize the corresponding power-law of the time evolution of the fracture length, net pressure and opening in Table. 2.3 with references of available analytic solutions presented in Table. 2.1.

The fracture growth can be strongly influenced by the compressibility when accounting for the injection system compliance U. This compressibility effect cannot be ignored in lab experiments - it plays a role at early time and results in an instability if the injection system is not stiff enough. In this case, the injection rate is no longer constant and does not equal Q_o. We depict this early time evolution in a triangular diagram (as shown in Fig. 2.3) with each vertex corresponding respectively to a $\hat{O}$ lag-compressibility dominated, a $\hat{M}$ viscosity-compressibility dominated, and a $\hat{K}$ toughness-compressibility dominated regime. The transition from the early-time compressibility/viscosity to the early-time compressibility/toughness regime is

governed by a different time scale:

$$t_{\hat{m}\hat{k}} = \left(\frac{E'^5 U \mu'^2}{K'^6} \right)^{1/2}$$
(2.12)

, which depends notably on the injection system compliance U. The wellbore radius a and initial notch length ℓ_o also play a role at early time, especially on the value of the fracture initiation pressure. Their influence is captured by their ratio with a length scale $(E'U)^{1/3}$ associated with the release of the fluid stored during the wellbore pressurization prior to initiation: $\mathscr{L} = \ell_o/(E'U)^{1/3}$ and $\mathscr{A} = a/(E'U)^{1/3}$. It is important to note that such a compressibility length scale $(E'U)^{1/3}$ is typically larger than both the initial defect length ℓ_o and the wellbore radius a ($\mathscr{L} < 1$ and $\mathscr{A} < 1$) in most practical situations as $E'U \approx E'c_f V_{inj} \approx O(10^{10}\text{Pa}) \times O(10^{-10}\text{Pa}^{-1}) \times V_{inj} \approx V_{inj}$ (where V_{inj} denotes the volume of the injection line). This indicates that the compressibility effect and the associated release of fluid after breakdown typically dominate the early stage of growth of a radial HF (Lecampion et al., 2017).

We show the complete transition in Fig. 2.3. For a radial hydraulic fracture propagating in an infinite medium with a system compliance and wellbore, the fracture growth starts from the $\hat{O}$ vertex and ends at the $\tilde{K}$ vertex. The trajectory between different vertexes is described by three dimensionless parameters.

$$\phi = \left(\frac{t_{mk}}{t_{m\tilde{m}}} \right)^{14/9}, \quad \psi = \frac{t_{mk}}{t_{om}}, \quad \chi = \frac{t_{mk}}{t_{\hat{m}\hat{k}}}$$
(2.13)

where ϕ describes the trajectory in $M - K - \tilde{M} - \tilde{K}$, ψ the trajectory in $O - M - K$, and χ the trajectory in $\hat{O} - \hat{M} - \hat{K} - O - M - K$.

2.3 Laboratory HF injection design

In this thesis, we have performed HF injections in rocks that are isotropic and homogeneous with very low permeability. We favor a planar fracture by setting the minimum confining stress parallel to the wellbore. The hydraulic fracture propagates approximately in a radial shape, and we use the LHFM theory for a radial HF driven by a constant injection rate to design the laboratory HF tests.

Our experimental set-up is characterized with an important compressibility effect with $\mathscr{L} \sim 10^{-2}$ and $\mathscr{A} \sim 10^{-2}$. We control the sudden release of the fluid due to the compressibility by putting a needle value in the injection line. The needle value is slightly open and dumps the increase of the flux after the fracture initiation. As a result, the inlet flux does not necessarily equal the injection rate of the pump. For a given rock sample, we can design the HF experiment with the fracture propagating under a certain regime by varying the fluid type, the confining stresses, and the flux entering the fracture. The flux is controlled through the injection pump together with the needle valve.

Regime	Requirements		
M	$\psi \gg 1$,	$t_{om} < t_{prop} < t_{mk}$	$L/L_{mk} < 0.06$, $\quad L/L_{om} > 5.7$
K	$\psi \gg 1$,	$t_{om} < t_{mk} < t_{prop}$	$L/L_{mk} > 2.4$, $\quad L/L_{om} > 5.7$

Table 2.4 – Parameter requirements for viscosity-dominated regime and toughness-dominated regime (Bunger et al., 2005b; Bunger and Detournay, 2008).

We consider the case of an impermeable rock and neglect the compressibility effect due to the restraint of the valve. As a result, The propagation regime depends on the relation between the propagation duration t_{prop} and the time scales t_{om}, t_{mk} or that between the characteristic specimen size L (for example, the distance between the injection point to the nearest side of a cubic sample) and the length scales L_{om}, L_{mk}, as shown in Table. 2.4. L_{om} and L_{mk} are length scales associated with the large lag to zero lag transition and the large viscous dissipation to zero viscous dissipation.

$$L_{om} = \frac{E'\mu'^{1/3}Q_o^{1/3}}{\sigma_o^{4/3}}, \quad L_{mk} = \frac{E'^3\mu'Q_o}{K'^4} \tag{2.14}$$

Requirements of the typical HF propagation growth are presented in Table. 2.4. The idea is to meet these requirements while ensuring a sufficiently long propagation duration ($t_{prop} \sim O(1)$-$O(10)$ minutes). However, we can not apply directly these requirements in our case. Due to the maximum confining stress limits $\sigma_o \leq 20$ MPa, we have always $t_{mk} < t_{om}$ (see more details in Chapter 6). As a result, it is difficult to design a viscosity-dominated experiment without a fluid lag, which requires $t_{mk} > t_{prop} > t_{om}$. However, it is easier to perform a toughness-dominated experiment, which requires only $t_{prop} \gg t_{mk}$. This ensures that no fluid lag appears even if $t_{prop} \ll t_{om}$. The requirement $t_{prop} \gg t_{mk}$ calls for a very good control of the inlet flux through the injection pump and the needle valve. We summarize here different types of HF experiments we have performed using the experimental set-up in the lab (see more details in Chapter 5 and Chapter 6).

- O-regime and O-M regime experiments. They call for the use of a very viscous fluid, and the propagation duration much smaller than the fluid lag disappearance time scale $t_{prop} \ll t_{om}$.

- K-regime experiments. They call for the use of a less viscous fluid and the good control of the inlet flux. The latter can be done through a small injection rate and a strong restraint of the valve which damps the flux increase after the fracture initiation due to the system compliance.

2.4 Conclusions

In this chapter, we have reviewed important results of LHFM. These theoretical results will offer a basis for the design of HF experiments as well as its comparison with numerical results when

investigating effects not accounted for by the theory of linear hydraulic fracture mechanics: namely, the effect of solid non-linearity and fracture roughness on flow.

Theories and Simulations Part I

3 HF growth with fracture length dependent apparent toughness

This chapter investigates the growth of a hydraulic fracture assuming a power-law dependence of material toughness with fracture length. Such a toughness fracture length dependence models a toughening mechanism for rocks in a simple manner. We develop an efficient numerical method for the hydraulic fracture growth problem combining Gauss-Chebyshev quadrature and barycentric Lagrange interpolation techniques. Scaling and numerical results demonstrate that the transition from the viscosity to the toughness dominated regime occurs earlier. The toughness dominated regime always governs growth at large time for both plane strain and radial fracture geometries. In all cases, larger net pressure and shorter length are obtained. The solution is very well approximated by the existing constant toughness solutions using the instantaneous value of toughness. If the apparent fracture toughness saturates beyond a given length scale, the solution transitions back to the constant toughness solutions.

This chapter is a modified version of the following scientific article:

Liu, D., Lecampion, B., & Garagash, D. I. (2019). Propagation of a fluid-driven fracture with fracture length dependent apparent toughness. *Engineering Fracture Mechanics*, 220, 106616.

Authors contributions

D. Liu comes up with the idea of adopting the fracture-length dependent apparent toughness to investigate the effect of solid non-linearity under the frame of LHFM. He has formulated the problem and performed the dimensional analysis under the guidance of B. Lecampion. D. Liu has applied the Gauss-Chebyshev and Lagrange barycentric interpolation methods developed by D. Garagash to the specific case of a finite HF growth with fracture length-dependent apparent toughness. D. Garagash and D. Liu have written the numerical solver, more specifically, D. Garagash has performed the numerical discretization, while D. Liu's contribution to the numerical solver lies mainly in the idea of adopting a simple Mathematica built-in ordinary differential equation solver and approximating the initial solution of these ordinary differential equations with the analytical solution of a viscosity-dominated radial HF and that of a plane-strain HF. D. Liu has performed the validation and visualization. D. Liu, B.

Lecampion, and D. Garagash have written the manuscript.

3.1 Introduction

The propagation of a hydraulic fracture (HF) in an impermeable elastic solid is relatively well understood, with theoretical predictions matching laboratory scale experiments in model material (e.g. PMMA, glass, cement) at least for simple planar fracture geometries (Lecampion et al., 2017; Xing et al., 2016; Bunger and Detournay, 2008). In particular, the ratio between the energy dissipated in the creation of fracture surfaces (fracture energy) versus the energy dissipated in fluid flow (Garagash, 2009; Detournay, 2016) governs HF growth, leading to either toughness dominated or viscosity dominated propagation.

Despite the relatively good agreement of hydraulic fracture mechanics predictions with laboratory experiments performed in brittle/fine-grained materials, deviations from theoretical predictions have been reported in field observations and micro-HF treatments in vertical wells (Shlyapobersky et al., 1998; Shlyapobersky, 1985; Shlyapobersky et al., 1988; Thallak et al., 1993). Apart from a possible increase of fracture energy[1] in the field compared to the laboratory scale, such deviations, in particular a larger propagation net pressure (the difference between the fluid pressure and the confining stress) might also be explained by other factors such as the additional frictional losses associated with near well-bore fracture tortuosity (Palmer and Veatch Jr, 1990; Bunger and Lecampion, 2017). In any case, these field observations indicate a higher energy demand for larger scale fractures, and hint to further study of the HF growth in quasi-brittle materials.

A process zone develops around the fracture tip in quasi-brittle materials, where non-elastic processes such as micro-cracking and plastic deformations are present. The size of the process zone acts as a good indicator of the apparent fracture energy. Rubin (1993) has investigated theoretically a propagating HF under high confining stress adopting a cohesive zone model. He argues that the tip cavity (fluid lag) generated by viscous fluid flow grows with the fracture and results in an increase of the process zone size and energy consumption via the perturbation of the near-tip stress field. Numerical studies (Papanastasiou, 1999; Papanastasiou and Thiercelin, 1993; Papanastasiou, 1997; Papanastasiou and Atkinson, 2006; Sarris and Papanastasiou, 2013) accounting for plastic dissipation of a propagating hydraulic fracture have shown a higher net pressure and wider inlet opening, implying an increase of the apparent fracture toughness[2] up to more than one order of magnitude (Papanastasiou, 1999, 1997). Hashida et al. (1993) have reported hydraulic fracturing experiments on Iidate granite spanning fracture radius between a few millimeters up to 20 centimeters (on specimen size up to metric scale). These tests clearly show an increase of the toughness with fracture radius following approximately a power law (see Fig. 3.1-right). In plaster blocks, van Dam

---

[1]We define the fracture energy G_R as the energy spent in the creation of unit (nominal) fracture surface.

[2]The fracture toughness K_{Ic} is calculated from Irwin's equation using the fracture energy $K_{Ic} = \sqrt{G_R E'}$, where E' is the plane-strain elastic modulus defined.
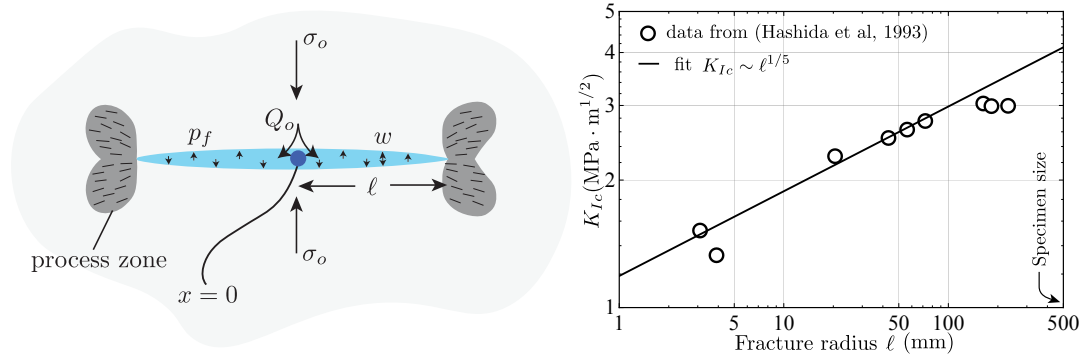
Figure 3.1 – Sketch of a hydraulic fracture with fracture length dependent apparent toughness (left) and the evolution of apparent toughness with fracture radius in hydraulic fracturing tests in Iidate granite from Hashida et al. (1993) (right). The evolution of the apparent toughness can be fitted by a power-law $K_{Ic} \propto \ell^{1/5}$ for $\ell < 100$ mm. The deviation for $\ell > 150$ mm might be possibly due to multiple reasons, such as the full development of the non-linear zone around the fracture tip and the restriction of the limited specimen size on the continuous growth of the apparent toughness.

(1999) have reported a development of the fracture tip bluntness, indicating an increase of the process zone size.

Another line of observations comes from the analysis of magmatic dikes. Dikes are natural hydraulic fractures driven by magma, spanning a range of scale up to tens of kilometers. A recent review on dike propagation (Rivalta et al., 2015) reports that apparent fracture toughness values in the range 100-4000 MPa.m$^{1/2}$ are often needed to reconcile field observations (Olson, 2003; Delaney and Pollard, 1981; Jin and Johnson, 2008; Rivalta and Dahm, 2006; Bunger and Cruden, 2011). These ranges of toughness are larger by 2-3 orders of magnitude than values O(1) MPa.m$^{1/2}$ measured in the laboratory rock fracture (Atkinson, 1984; Atkinson and Meredith, 1987). Moreover, field observations indicate that the process zone of dikes can be much larger than those produced at the tips of tensile fractures at the laboratory scale and exhibit a direct proportionality with fracture dimension (Rivalta et al., 2015; Delaney et al., 1986; Pollard, 1987; Engvik et al., 2005). Such observations imply further a scale-dependent or fracture length dependent characteristic of the apparent fracture energy. Scholz (2010) analyses the emplacement of dikes (Schultz et al., 2008a) and finds that a linear displacement-length scaling provides a better fit to the data rather than a square-root scaling (Delaney and Pollard, 1981; Olson, 2003; Schultz et al., 2008a,b), from which he infers that the fracture toughness scales with the square-root of fracture length instead of being a constant rock property. The proposed linear scaling of mode I natural fractures happens to be consistent with the well known linear relation between fault length and accumulated slip (and damage zone) for shear type fractures (mode II/III) in the earth crust (Cowie and Scholz, 1992).

There is not yet a clear consensus among researchers regarding the evolution of fracture toughness at large scales in quasi-brittle rocks in the upper earth crust (Scholz, 2010; Olson

23

and Schultz, 2011). The complexity of various physical mechanisms contributes to multiple possible explanations (Rivalta et al., 2015; Olson and Schultz, 2011): in-situ stress (Rubin, 1993; Bunger, 2008; Funatsu et al., 2004), rock tensile strength (Rubin, 1993), rock mass scale (Pollard, 1987), temperature (Schultz et al., 2008a; Funatsu et al., 2004) and the enhanced viscous losses due to roughness (Garagash, 2015b) are all reported more or less responsible for higher apparent toughness in hydraulic fractures at a larger scale. The goal of this chapter is to quantify the impact of an increase of fracture energy with fracture length on HF propagation without presuming the exact toughening mechanism. We restrict ourselves to the case of an impermeable material and the injection at a constant rate Q_o of a Newtonian fluid of viscosity μ.

3.2 A power-law-like fracture length dependent toughness with a possible saturation

3.2.1 R-curve behaviour and its size effect

Numerous toughness measurements of quasi-brittle materials in the lab present a power-law like evolution of the fracture growth resistance as the fracture advances. Such increase then approaches a critical value – an evolution referred to as the "R-curve" (Anderson, 2017). This critical fracture growth resistance is commonly considered as a material property, which is presumed measurable when the specimen is large compared to the intrinsic material length scale (e.g. process zone size, which may possibly be much larger than typical laboratory samples). A size effect of the R-curve, though rarely mentioned in literature, has been reported in some experiments with specimen dimensions much larger than the ones typically used in the laboratory. Dempsey et al. (1999) report a series of toughness measurements on sea ice plates, spanning from the common laboratory cm-m scale up to 80 m × 80 m, with the same plate width of 1.8 m for all specimens. The authors report an increase of the apparent fracture toughness with specimen dimensions up to 3 m × 3 m × 1.8 m with a value nearly twice the one measured on smaller specimens (0.5 m × 0.5 m × 1.8 m). Findings on wood (Morel et al., 2002) also report a size effect of the R-curve behaviour. They show that the critical fracture resistance scales with the width of the cracked-through plate specimen and follows a power-law-like evolution with specimen width. Different from the observations on sea ice (Dempsey et al., 1999), no plateau value is reported in the evolution of the critical fracture resistance with specimen width, with a maximum thickness of 60 mm for all the geometrically self-similar specimens in their experiments. These findings, combined with observations from lab HF tests (Hashida et al., 1993) and dikes (Scholz, 2010), imply a possible power-law evolution of the apparent fracture toughness and an existence of a finite toughness value beyond a certain length scale.

3.2.2   A power-law dependence of apparent fracture toughness

In this chapter, we investigate the case where the apparent fracture energy follows a power-law-like fracture length dependence. We assume that the underlying increase of the process zone that results in the macroscopic increase of the apparent fracture toughness remains small compared to the fracture length. This hypothesis of small scale yielding (Rice, 1968) allows to approximate the fracture growth within the principles of linear elastic fracture mechanics (i.e. a single fracture characterised by the apparent fracture toughness). In terms of material toughness, we write

$$K_{Ic} = A\ell^{\alpha}, \quad A = \frac{K_*}{\ell_*^{\alpha}} \tag{3.1}$$

where K_* is the apparent fracture toughness measured at a given fracture length scale of ℓ_* and α the power-law scaling exponent. Such a power-law dependence does not introduce any new length scale as the pair of ℓ_* and K_* is selected so as to characterise the fracture length dependence of the toughness. Noticeably, such fracture length dependence of the apparent toughness is different from the one observed in a R-curve. In the R-curve, the evolution of the fracture growth resistance does not depend on the initial fracture length ℓ_o but is a function of the fracture extension length $\Delta\ell = \ell - \ell_o$ (the difference of the fracture length ℓ with respect to its initial value ℓ_o).

Different toughening mechanisms are embedded into such a power-law dependence model. The scaling exponent α is most likely function of material properties and in-situ conditions. According to Papanastasiou (1999); Papanastasiou et al. (2015), the increase of the apparent toughness during the growth of a planar and smooth HF in weak formations is related to the size of plastic zone and depends on the level of in-situ stress, the rock strength and elastic modulus as well as the pumping parameters. It is therefore very likely that the power-law scaling exponent is function of these parameters as there are practical implications that the apparent fracture toughness will be higher when the fracture front propagates in the vertical than the horizontal directions (Papanastasiou and Atkinson, 2006; Papanastasiou et al., 2015; Papanastasiou and Atkinson, 2000; Papanastasiou et al., 2016). Such argument is consistent with the findings of Funatsu et al. (2004) who report a dependence of the rock toughness on confining stresses. Morel et al. (2002) also argue that the scaling exponent is material-dependent and is closely related to self-affine fracture surfaces and their anomalous roughening characteristic. The through-the-plate fracture in their experiments initiates at a small length scale such that the initial fracture length in the propagation direction is much smaller than the length (perimeter) $\ell_{\parallel}$ of the fracture front (given by the plate thickness). In this case, the magnitude of the roughness increases as a function of the fracture length ℓ (case a). This results in an increasing discrepancy between the real fracture surface area at the micro scale and the nominal fracture surface at the macro scale. As a result, the fracture energy increases with the fracture length and presents a relation similar to Eq. (3.1), where α is function of self-affine scaling exponents of fracture surfaces. When the fracture length becomes comparable to the specimen width $\ell_{\parallel}$ in Morel et al. (2002), the magnitude of the roughness saturates at a value dependent on $\ell_{\parallel}$ (case b). The toughness scaling changes

Table 3.1 – Power-law scaling exponents for the evolution of apparent fracture toughness for different materials and geometries. The power-law exponents for plane-strain and axisymmetric fractures are estimated by using Eq. (4.6) and Eq. (4.7) in Morel et al. (2002) respectively and using the roughness self-affine scaling exponents in Morel et al. (2002) for pine and spruce, López and Schmittbuhl (1998) for granite and Mourot et al. (2006) for mortar.

Material	Plane-strain (α)	Axisymmetric (α_c)
Pine	0.062-0.183	0.365
Spruce	0.055-0.131	0.235
Granite	0.171	0.205
Mortar	0.039	0.275

to $K_{Ic} \propto \ell_\parallel{}^{\alpha_c}$, where α_c, also material-dependent and function of the self-affine scaling exponents, characterises the fracture roughness growth within the length of the fracture front $\ell_\parallel$. These observations (a and b) suggest different power-law scaling exponents for different fracture geometries. For a plane-strain hydraulic fracture in an infinite medium, the fracture front is infinite ($\ell_\parallel = \infty$), which suggests the apparent toughness scaling with the fracture length $K_{Ic} \propto \ell^\alpha$ as in case (a). For a radial fracture, the fracture length (radius) is comparable to the front length ($\ell_\parallel = 2\pi\ell$), suggesting the apparent toughness scaling with fracture radius, $K_{Ic} \propto \ell_\parallel{}^{\alpha_c}$, as in case (b). We compile different power-law scaling exponents of different materials from the literature in Table 3.1. The exponents for granite and mortar are obtained based on the argument of Morel et al. (2002) and roughness self-affine scaling exponents in López and Schmittbuhl (1998); Mourot et al. (2006). Moreover, a power-law scaling exponent of $\alpha \approx 1/2$ is suggested (Schultz et al., 2008b) based on the field observations of emplacement scaling on dikes and a value of $\alpha \approx 0.1$ for Nevada Tuff is also reported (Olson and Schultz, 2011) from laboratory measurements (Weisinger et al., 1980).

3.2.3   Possible appearance of a finite apparent toughness beyond a length scale

The exact evolution of apparent fracture toughness with fracture length remains an open question. As reported in the previously mentioned experiments (Hashida et al., 1993; Dempsey et al., 1999), the toughening effect is likely curtailed beyond a certain length scale ℓ_s (fracture length beyond which the apparent toughness reaches an asymptotic value). Such an upper limit of the increase of apparent toughness may result from different mechanisms. Papanastasiou (1999, 1997) examines the apparent fracture toughness of a smooth plane-strain HF in an infinite domain using a coupled elasto-plastic finite element model with cohesive interface elements for propagation criterion. The author shows that the apparent toughness increases initially with fracture length following approximately a power law, and then reaches an asymptotic value. The author owes the observed plateau of the apparent toughness to the full development of plastic(or process) zones that shield the tip. However, the appearance of the finite toughness is also possibly due to the restraints of the specimen(or crust) dimensions. If we account for the fracture roughness and extend the findings in Morel et al. (2002) to large scale fractures, a potentially unabated fracture toughening with fracture growth is expected

for an unbounded domain. However, when the fracture grows close to the specimen (or earth crust) dimensions in the lab (or at depth), a finite apparent toughness may also appear due to such dimension limit on the continuous growth of apparent toughness. It may be likely that the saturation length scale ℓ_s can be potentially large given that the large toughness values reported in dikes (Olson, 2003; Delaney and Pollard, 1981; Jin and Johnson, 2008; Rivalta and Dahm, 2006; Bunger and Cruden, 2011) correspond to a fracture length of the order of kilometers.

In the following, we investigate the growth of a fluid-driven fracture assuming a power-law dependence of toughness with fracture length as described by Eq. (3.1) and also account for a possible saturation of the fracture toughness above a given scale. We focus on both plane-strain and axisymmetric (radial) fracture geometries. We first perform a dimensional analysis to describe the solution structure as well as the governing dimensionless parameters. We then solve the complete evolution problem numerically. We notably develop a scheme combining a Gauss-Chebyshev quadrature with Barycentric Lagrange interpolation and differentiation techniques (Viesca and Garagash, 2017). In Section 3.3, 3.4, 3.6, 3.7.1 and 3.7.2, we assume that the saturation length scale ℓ_s is very large ($\ell_s \rightarrow \infty$) so that the toughness follows a power-law-like evolution without reaching the asymptotic value ($\ell < \ell_s$). We then discuss the effect of the plateau of apparent fracture toughness beyond a saturation length scale ℓ_s in Section 3.7.3.

3.3   Mathematical model

We introduce a parameter d in order to represent the governing equations for a plane-strain ($d = 1$) and an axisymmetric hydraulic fracture ($d = 2$) simultaneously. In view of the problem symmetry, we write the governing equations for the fracture half-length $\ell(t)$ in plane-strain, and also denote the fracture radius as $\ell(t)$ for the axisymmetric / radial geometry. Following Savitski and Detournay (2002); Detournay (2004), we use the following set of effective material parameters for clarity:

$$K'_* = \sqrt{\frac{32}{\pi}} K_*, \quad E' = \frac{E}{1 - v^2}, \quad \mu' = 12\mu \tag{3.2}$$

where E is the solid elastic modulus, v Poisson's ratio, μ the fluid viscosity, and K_* the reference apparent fracture toughness measured at $\ell = \ell_*$.

3.3.1   Elasticity

For a strictly Mode I fracture, the elasticity equations reduce to a single boundary integral equation relating the fracture opening w and the net pressure p defined as $p = p_f - \sigma_o$ where σ_o is the in-situ compressive stress normal to the fracture plane (the minimum stress) (Hills

et al., 2013):

$$\frac{1}{4\pi} \frac{1}{\ell} \int_{-1}^{1} G_d(\xi, \xi') \frac{\partial w}{\partial \xi'} \mathrm{d}\xi' = \frac{1}{E'} p, \quad \xi \in [-1, 1] \tag{3.3}$$

where $\xi = x/\ell$ is the dimensionless spatial coordinate in the fracture. G_d is the elastic kernel, representing the stress component normal to the fracture plane induced by a unit dislocation. It is function of the fracture geometry:

- In plane-strain ($d = 1$)

$$G_1(\xi, \xi') = \frac{1}{\xi - \xi'} \tag{3.4}$$

- and in axisymmetry ($d = 2$)

$$G_2(\xi, \xi') = \begin{cases} \mathrm{sign}(\xi\xi') \left[\dfrac{1}{\xi - \xi'} \mathbf{E}(k) - \dfrac{1}{\xi} \mathbf{K}(k) \right], & |\xi'| < |\xi| \\[2ex] \dfrac{1}{\xi - \xi'} \mathbf{E}(1/k), & |\xi'| > |\xi| \end{cases} \tag{3.5}$$

where $k = \xi'/\xi$ and $\mathbf{E}(k)$ and $\mathbf{K}(k)$ denote the complete elliptic integrals. The axisymmetric kernel is obtained from the solution for a ring dislocation at $\xi' \in [0, 1]$ (Cleary and Wong, 1985; Gordeliy and Detournay, 2011a), and the symmetric continuation onto $\xi' \in [-1, 0]$.

3.3.2 Lubrication flow

The elastic compliance of an open fracture is much larger than the fluid compressibility (Lecampion et al., 2018). As a result, under the assumption of an impermeable medium (zero leak-off) and zero fluid lag, the width-averaged fluid mass conservation reduces to volume conservation:

$$\frac{\partial w}{\partial t} + \frac{1}{x^{d-1}} \frac{\partial}{\partial x} \left(x^{d-1} q \right) = 0 \tag{3.6}$$

Similarly, for laminar flow conditions, the width averaged fluid balance of momentum reduces to Poiseuille law relating the local fluid flux q to the local pressure gradient (Batchelor, 2000):

$$q = -\frac{w^3}{\mu'} \frac{\partial p}{\partial x} \tag{3.7}$$

where we have implicitly assumed that the in-situ compressive stress σ_o is uniform.

3.3.3 Boundary conditions

The fluid is injected at the fracture center $x = 0$ either as a line ($d = 1$) or a point ($d = 2$) source. We assume a constant injection rate Q_o in the following. A zero fluid flux and zero fracture opening conditions apply at the fracture tip $x = \ell$ (Detournay and Peirce, 2014):

$$2 \lim_{x/\ell \to 0} (\pi x)^{d-1} q = Q_o, \quad q(\ell) = 0, \quad w(\ell) = 0 \tag{3.8}$$

3.3.4 Global continuity equation

The integration of the lubrication equation (3.6) combined with the previous boundary conditions (3.8) yield a global fluid continuity equation:

$$2 \int_0^\ell (\pi x)^{d-1} w \, \mathrm{d}x = Q_o t \tag{3.9}$$

3.3.5 Propagation criterion

Under the assumption of small scale yielding, the process zone size is much smaller than the fracture length and linear elastic fracture mechanics is valid to describe the fracture propagation. The propagation criterion of a quasi-static hydraulic fracture translates into the classical square-root asymptote near the fracture tip (Rice, 1968), with the mode I stress intensity factor K_I equal to the fracture toughness K_{Ic} at all time: $K_I = K_{Ic}$. In view of the fracture length dependent evolution of the toughness described by the power law in Eq. (3.1), the linear elastic fracture mechanics asymptote for fracture width near the tip becomes:

$$w \sim \frac{K'_*}{E'} \left(\frac{\ell}{\ell_*} \right)^\alpha (\ell - x)^{1/2}, \quad \ell - x \ll \ell \tag{3.10}$$

3.4 Scalings and Structure of the solution for a fracture-length-dependent toughness

3.4.1 Viscosity and toughness scaling

The propagation of plane-strain and radial hydraulic fractures are well understood for the case of fracture length independent fracture toughness. Solutions (Garagash and Detournay, 2005; Garagash, 2006a; Savitski and Detournay, 2002) have been obtained in limiting propagation regimes where either the dissipation associated with fluid viscous flow (viscosity dominated - M−regime) or with the creation of new fracture surfaces (toughness dominated - K−regime). For the case of a plane-strain hydraulic fracture in an impermeable medium, the propagation is actually always self-similar and is defined by a single dimensionless parameter characterising the relative importance of toughness versus viscous forces: e.g. a dimensionless toughness $\mathcal{K}$. The radial fracture geometry yields a different solution structure. Indeed, as the perimeter of the fracture increases with time, the energy associated with the creation of new surfaces increases and eventually dominates over viscous forces at large time. As a result, for a radial fracture, the dimensionless toughness $\mathcal{K}$ increases with time: the propagation transitions from the M−regime to the K−regime. In what follows, using similar procedures, we investigate the scaling of the solution for both geometries in the case of a fracture length dependent fracture toughness and discuss the corresponding modifications of the structure of the propagation of a hydraulic fracture in an impermeable medium.

We introduce a dimensionless fracture opening Ω, net pressure Π, and fracture half-length or fracture radius γ as follows:

$$\ell(t) = L(t)\gamma(\xi,\mathcal{G}), \quad w(x,t) = \epsilon(t)L(t)\Omega(\xi,\mathcal{G}), \quad p(x,t) - \sigma_o = \epsilon(t)E'\Pi(\xi,\mathcal{G}) \tag{3.11}$$

In these definitions, $\epsilon(t)$ is a small dimensionless number capturing the fact that the fracture characteristic scale $W(t)$ is much smaller than the characteristic length $L(t)$. Similarly the characteristic net pressure $P(t) = \epsilon(t)E'$ is much smaller than the rock elastic modulus. $\mathcal{G}(t)$ denotes additional dimensionless parameters of which the solution depends on. All yet to be defined and possibly dependent on time to reflect the moving boundary nature of the hydraulic fracture problem.

With such a scaling, we thus obtain the following dimensionless form of the governing equations.

- Elasticity

$$\frac{1}{4\pi}\frac{1}{\gamma}\int_{-1}^{1} G_d(\xi,\xi')\frac{\partial\Omega}{\partial\xi'}\mathrm{d}\xi' = \Pi(\xi) \tag{3.12}$$

- Lubrication flow (Reynold's equation obtained combining fluid continuity and Poiseuille law) written in the moving coordinates system ($\xi = x/\ell(t)$):

$$\left(\frac{\dot{\epsilon}t}{\epsilon} + \frac{\dot{L}t}{L}\right)\Omega - \frac{\dot{L}t}{L}\xi\frac{\partial\Omega}{\partial\xi} + \dot{\mathcal{G}}t\left(\frac{\partial\Omega}{\partial\mathcal{G}} - \frac{\xi}{\gamma}\frac{\mathrm{d}\gamma}{\mathrm{d}\mathcal{G}}\frac{\partial\Omega}{\partial\xi}\right) = \frac{1}{\mathcal{G}_m}\frac{1}{\gamma^2\xi^{d-1}}\frac{\partial}{\partial\xi}\left(\xi^{d-1}\Omega^3\frac{\partial\Pi}{\partial\xi}\right) \tag{3.13}$$

- Global continuity equation

$$2\pi^{d-1}\gamma^d\int_0^1 \xi^{d-1}\Omega\mathrm{d}\xi = \mathcal{G}_v \tag{3.14}$$

- Propagation condition (in terms of the fracture width near-tip asymptote) for the case of a power-law dependence of the fracture toughness on the fracture length (Eq. (3.1)):

$$\Omega \sim \mathcal{G}_k\gamma^{\alpha+1/2}(1-\xi)^{1/2}, \quad 1-\xi \ll 1 \tag{3.15}$$

In these dimensionless equations, $\mathcal{G}_m$, $\mathcal{G}_v$ and $\mathcal{G}_k$ are three independent dimensionless groups emerging from lubrication flow, global continuity and propagation criterion respectively, whose expressions are given by:

$$\mathcal{G}_m = \frac{\mu'}{\epsilon^3 E' t}, \quad \mathcal{G}_v = \frac{Q_o t}{\epsilon L^{d+1}}, \quad \mathcal{G}_k = \frac{K'_*}{\epsilon E' L^{1/2}}\left(\frac{L}{\ell_*}\right)^{\alpha} \tag{3.16}$$

In order to define a particular scaling, we set two of these dimensionless groups to unity and solve for the corresponding $\epsilon(t)$ and $L(t)$. For an impermeable medium, the fracture volume always equals the injected volume, i.e. $\mathcal{G}_v = 1$. Two scalings are therefore obtained by

3.4. Scalings and Structure of the solution for a fracture-length-dependent toughness

Table 3.2 – Viscosity and toughness scaling for plane-strain ($d = 1$) and radial ($d = 2$) hydraulic fractures in the case of a power-law dependence of fracture toughness with fracture length.

Scaling	Viscosity	Toughness
$\epsilon(t)$	$\epsilon_m = \left(\dfrac{\mu'}{E' t}\right)^{1/3}$	$\epsilon_k = \left(\dfrac{K_*'^{\,d+1}}{E'^{d+1} Q_o^{1/2-\alpha} \ell_*^{\,\alpha(d+1)} t^{1/2-\alpha}}\right)^{1/(\alpha+d+1/2)}$
$L(t)$	$L_m = \left(\dfrac{E' Q_o^3 t^4}{\mu'}\right)^{1/(3(d+1))}$	$L_k = \left(\dfrac{Q_o E' \ell_*^{\,\alpha} t}{K_*'}\right)^{1/(\alpha+d+1/2)}$
$W(t)$	$W_m = \left(\dfrac{\mu'^d Q_o^3 t^{3-d}}{E'^d}\right)^{1/(3(d+1))}$	$W_k = \left(\dfrac{K_*'^{\,d} Q_o^{\alpha+1/2} t^{\alpha+1/2}}{E'^d \ell_*^{\,\alpha d}}\right)^{1/(\alpha+d+1/2)}$
$P(t)$	$P_m = \left(\dfrac{E'^2 \mu'}{t}\right)^{1/3}$	$P_k = \left(\dfrac{K_*'^{\,d+1}}{E'^{1/2-\alpha} Q_o^{1/2-\alpha} \ell_*^{\,\alpha(d+1)} t^{1/2-\alpha}}\right)^{1/(\alpha+d+1/2)}$
$\mathcal{G}(t)$	$\mathcal{G}_m = 1$ $\mathcal{G}_k = \mathcal{K} = (t/t_{mk})^{(d-1+4\alpha)/(3(d+1))}$	$\mathcal{G}_m = \mathcal{M} = (t/t_{mk})^{-(d-1+4\alpha)/(\alpha+d+1/2)}$ $\mathcal{G}_k = 1$

assuming that either viscous forces ($\mathcal{G}_m = 1$) or toughness ($\mathcal{G}_k = 1$) dominate. It results in a viscosity and a toughness scaling respectively. Table 3.2 lists the different characteristic scales and dimensionless parameters in these two scalings as functions of the material parameters, injection rate, time and fracture geometry.

In the viscosity scaling, $\mathcal{G} = \mathcal{G}_k$ is the only remaining dimensionless parameter appearing in the set of governing equations which we rename as dimensionless toughness $\mathcal{K}$. It characterises the relative importance of the solid apparent toughness compared to viscosity on the propagation of a hydraulic fracture. In the toughness scaling, we define similarly the dimensionless viscosity $\mathcal{M}$ from $\mathcal{G} = \mathcal{G}_m$. The scalings are of course related to one another - via the following relations:

$$\mathcal{K} = \left(\frac{t}{t_{mk}}\right)^{(d-1+4\alpha)/(3(1+d))} , \quad \mathcal{M} = \mathcal{K}^{-3(1+d)/(\alpha+d+1/2)}, \quad \frac{\epsilon_m}{\epsilon_k} = \mathcal{K}^{-(d+1)/(\alpha+d+1/2)}, \quad \frac{L_m}{L_k} = \mathcal{K}^{1/(\alpha+d+1/2)}$$
$$(3.17)$$

In the previous relation, we have introduced a timescale t_{mk}, which corresponds to the time when the characteristic fracture scales in the two scalings are equal, i.e. $L_m = L_k$ at $t = t_{mk}$. Such a timescale quantifies the time of transition from the $M-$regime to the $K-$regime. We can define the corresponding transitional characteristic scales $L_{mk} = L(t_{mk})$, $W_{mk} = W(t_{mk})$, and $P_{mk} = P(t_{mk})$:

$$t_{mk} = \left(\frac{\mu'^{d+\alpha+1/2} Q_o^{3/2-3\alpha} E'^{2d-\alpha+5/2} \ell_*^{3\alpha(d+1)}}{K_*'^{\,3(1+d)}}\right)^{1/(4\alpha+d-1)} , \quad L_{mk} = \left(\frac{\mu' Q_o E'^3 \ell_*^{4\alpha}}{K_*'^{\,4}}\right)^{1/(4\alpha+d-1)} ,$$

$$W_{mk} = \left(\frac{\mu'^{\alpha+1/2} Q_o^{\alpha+1/2} E'^{5/2-d-\alpha} \ell_*^{\alpha(3-d)}}{K_*'^{\,(3-d)}}\right)^{1/(4\alpha+d-1)} , \quad P_{mk} = \left(\frac{K_*'^{\,d+1}}{\mu'^{1/2-\alpha} Q_o^{1/2-\alpha} E'^{3/2-3\alpha} \ell_*^{\alpha(d+1)}}\right)^{1/(4\alpha+d-1)}$$
$$(3.18)$$

It is worthwhile to note that the viscosity scaling does not depend on fracture toughness.

The expressions obtained are similar to the ones derived in Garagash and Detournay (2005); Savitski and Detournay (2002). Only the toughness dominated scaling is modified compared to the case of the fracture length independent toughness. By setting $\alpha = 0$, we obviously recover the well-known scalings for the case of the fracture length independent fracture toughness (Garagash and Detournay, 2005; Garagash, 2006a; Savitski and Detournay, 2002). For example, in a plane-strain fracture ($d = 1$), when the fracture toughness is fracture length independent $\alpha = 0$, the dimensionless toughness $\mathcal{K}$ becomes time-independent

$$d = 1 : \mathcal{K}(\alpha = 0) = \frac{K'_*}{E'}\left(\frac{E'}{\mu' Q_o}\right)^{1/4} \tag{3.19}$$

coincident with the expression obtained in Garagash and Detournay (2005); Garagash (2006a).

3.4.2 Zero-viscosity / toughness dominated solutions

The fracture propagation problem reduces to a self-similar problem at small ($\mathcal{K} \ll 1$) and large time ($\mathcal{K} \gg 1$). The early-time viscosity dominated solutions already available in the literature are of course also valid for the case of fracture length dependent toughness (fracture toughness does not play a role in the viscosity dominated regime). We derive here large-toughness solutions in a similar manner as in the case of fracture length independent toughness (Garagash, 2000; Savitski and Detournay, 2002; Garagash and Detournay, 2005). These zero viscosity solutions are expressed in the toughness scalings, and the corresponding dimensionless opening, length and net pressure are referred with a subscript ko in reference to the zero-viscosity solutions. As the viscosity is negligible, the net pressure is uniform in the fracture. The governing equations reduce to the elastic solution for a uniformly pressurized fracture, global volume balance and fracture propagation condition, i.e.:

$$\Omega_{ko} = 4\left(\frac{2}{\pi}\right)^{d-1}\gamma_{ko}\Pi_{ko}\sqrt{1 - \xi^2} \tag{3.20}$$

$$2\gamma_{ko}^d \int_0^1 (\pi\xi)^{d-1}\Omega_{ko}\,\mathrm{d}\xi = 1 \tag{3.21}$$

$$\Omega_{ko} \sim \gamma_{ko}^{\alpha+1/2}(1 - \xi)^{1/2}, \quad 1 - \xi \ll 1 \tag{3.22}$$

where Ω_{ko}, γ_{ko} and Π_{ko} are the dimensionless fracture opening, fracture half-length ($d = 1$) or fracture radius ($d = 2$), and net pressure. The solutions for a plane-strain fracture are thus

$$\gamma_{ko} = \left(\frac{2\sqrt{2}}{\pi}\right)^{1/(\alpha+3/2)}, \Pi_{ko} = \frac{1}{2\pi}\left(\frac{\pi}{2\sqrt{2}}\right)^{2/(\alpha+3/2)}, \Omega_{ko} = \frac{2}{\pi}\left(\frac{\pi}{2\sqrt{2}}\right)^{1/(\alpha+3/2)}\sqrt{1 - \xi^2} \tag{3.23}$$

and for an axisymmetric fracture:

$$\gamma_{ko} = \left(\frac{3}{\pi\sqrt{2}}\right)^{1/(\alpha+5/2)}, \Pi_{ko} = \frac{3}{16}\left(\frac{\pi\sqrt{2}}{3}\right)^{3/(\alpha+5/2)}, \Omega_{ko} = \frac{3}{2\pi}\left(\frac{\pi\sqrt{2}}{3}\right)^{2/(\alpha+5/2)}\sqrt{1 - \xi^2} \tag{3.24}$$

We recover the zero-viscosity solutions for fracture length independent fracture toughness (Garagash, 2006a; Savitski and Detournay, 2002) when setting $\alpha = 0$ in (3.23) and (3.24).

3.4.3 Effect of fracture length dependent toughness

One important difference brought by the fracture length dependent toughness ($\alpha > 0$) is that the dimensionless toughness increases with time in both geometries. This notably changes the partition between the viscous and the fracture energy dissipation during the growth of a hydraulic fracture even for a plane-strain fracture. In both geometries, as the fracture toughness increases with length, the energy spent in the creation of new fracture surface necessarily increases with time and ultimately dominates. This constitutes a qualitative change in the evolution of plane-strain HF from the case with fracture length independent toughness, when the dissipation partition is time-invariant. A plane-strain hydraulic fracture will eventually transition to the toughness dominated regime for the case of unabated increase of the apparent fracture toughness, even if it is initially dominated by viscosity.

For a radial fracture, the transition from the viscosity to the toughness dominated regime is accelerated due to the increase of the fracture toughness with fracture length. Larger α implies a faster increase of the energy dissipated in the solid and leads to a smaller value of the transition timescale t_{mk}. The increase of the fracture energy results in a higher net pressure required to drive the fracture propagation. Smaller fracture length and wider fracture opening are obtained for the same volume of the injected fluid.

It is interesting to note that when $\alpha = 1/2$, $\mathcal{K} \propto (t/t_{mk})^{1/3}$, for both geometries (Table 3.2). Notably for that particular value of α, the characteristic pressure scale $P_k(t)$ becomes independent of time, i.e. the propagation is driven by a constant pressure at large time: this pressure exactly balance the toughness increase with length. For values of the power-law scaling exponent α larger than $1/2$, we observe that the characteristic toughness dominated pressure $P_k(t)$ increases with time for both geometries. This is a significant difference compared to the fracture length independent toughness case. In other words, for $\alpha > 1/2$, the increase of the stress intensity with fracture length (in $\propto P_k \ell^{1/2}$) is not sufficient to compensate the increase of the toughness with length (in $\propto \ell^{\alpha}$ from Eq. (3.1)). Classically in hydraulic fracturing, a net pressure increase with time is related to the propagation of a height contained / blade-like fracture (also referred to as the PKN geometry) under the assumption of a fracture length independent toughness (Economides et al., 1989). Existing field observations of net pressure increases are usually relatable to contained-height hydraulic fracture growth (PKN fracture) as monitored by micro-seismicity (Gulrajani et al., 1997). It is thus interesting to contrast such a behaviour for very different fracture geometry (radial or plane-strain) for a power-law dependent toughness with $\alpha > 1/2$. We therefore see that in the field in order to decipher between these two possible causes, independent measurements of fracture geometry and pressure are required.

3.5 Numerical algorithm

We now describe a numerical method for the solution of the complete evolution problem from a given initial state - e.g. the viscosity dominated solution which is valid for time smaller than $t_{mk}(\alpha)$. Our method is based on a non-uniform moving mesh discretized using a Gauss-Chebyshev quadrature and a collocation method (Erdogan et al., 1973; Viesca and Garagash, 2017).

Extrapolation, integration, and differentiation operations are simplified as matrix multiplications using Barycentric techniques (Berrut and Trefethen, 2004; Viesca and Garagash, 2017). We turn the fully coupled hydraulic fracture propagation problem into a system of ordinary differential equations in time that can be integrated with classical methods for ordinary differential equations.

We first present the Gauss-Chebyshev quadratures associated with the discretization of the elastic equation. We then select the corresponding Barycentric operators listed in Viesca and Garagash (2017) and show how they can be applied to the discretization of a radial and plane-strain fracture. The corresponding vector and matrix are denoted respectively by bold type and blackboard bold type.

3.5.1 Gauss-Chebyshev quadrature

Gauss-Chebyshev quadrature methods for the solution of boundary integral equation arising in fracture mechanics is a classical technique (Erdogan et al., 1973). The method makes use of a primary $\mathbf{s} = \{s_j\}$, $j = 1, ..., n$, and a complimentary $\mathbf{z} = \{z_i\}$, $i = 1, ..., m$, sets of nodes, discretizing the fracture interval $(-1, 1)$, which corresponds to the roots of the respective Chebyshev polynomials denoted as $\phi_n(s)$ and $\psi_m(z)$ respectively (Erdogan et al., 1973). The choice of $\phi_n(s), \psi_m(z)$ and corresponding sets of nodes $\mathbf{s}$ and $\mathbf{z}$ stems from the type of the dislocation density singularity at the fracture tips. Specifically, the square-root singularity of linear elastic fracture mechanics can be directly embedded in the discretization. The dislocation density is expressed as:

$$\frac{\mathrm{d}w}{\mathrm{d}s} = \omega(s)F(s), \quad \omega(s) = \frac{1}{\sqrt{1 - s^2}} \tag{3.25}$$

where $\omega(s)$ is a weight function with the required tip singularity and $F(s)$ an unknown non-singular function.

For the type of singularity embedded in Eq. (3.25), the primary and complimentary polynomials are the Chebyshev's of the first $\phi_n(s) = T_n(s)$, and second $\psi_m(z) = U_m(z)$ (with $m = n - 1$) kinds respectively; and the two sets of spatial nodes are given by:

$$s_j = \cos\left(\frac{\pi(j - 1/2)}{n}\right), j = 1, ..., n; \quad x_i = \cos\left(\frac{\pi i}{n}\right), i = 1, ..., n - 1, \tag{3.26}$$

3.5.2 Hilbert transform operator for the dislocation density

The Hilbert transform

$$\mathscr{H}[w](z) = \frac{1}{\pi} \int_{-1}^{1} \frac{1}{z-s} \frac{\partial w}{\partial s} \mathrm{d}s \tag{3.27}$$

is evaluated on the complimentary $\mathbf{z}-$set of nodes using representation (3.25) of the dislocation density on the $\mathbf{s}-$set, $\{F(s_j)\}$. This results in the following:

$$\mathscr{H}[w](z_i) = \sum_{j=1}^{n} H_{ij} F(s_j), \quad H_{ij} = \frac{1}{n} \frac{1}{z_i - s_j} \tag{3.28}$$

3.5.3 Operators for extrapolation, differentiation and integration

The unknown function F representing the unknown dislocation density as Eq. (3.25) can be extrapolated from the Gauss-Chebyshev nodes to the fracture tip:

$$F(-1) = \sum_{j=1}^{n} P_j F(s_j), \quad F(1) = \sum_{j=1}^{n} Q_j F(s_j) \tag{3.29}$$

where, according to Table 3 of Viesca and Garagash (2017).

$$P_j = (-1)^j \frac{\tan(\arccos(s_j)/2)}{n}, \quad Q_j = -(-1)^j \frac{\cot(\arccos(s_j)/2)}{n} \tag{3.30}$$

Integration operators can be defined on either grid with the result of integration on the same or the other grid. For example, consider the integration of a regular function $g(s)$ defined on the $\mathbf{z}-$grid, $\{g(z_i)\}$, with the result evaluated on the same grid:

$$\int_{0}^{z_i} g(z) \mathrm{d}z = \sum_{i'=1}^{m} T_{ii'} g(z_{i'}), \quad T_{ii'} = \sum_{k=0}^{m-1} [\Psi_k(z_i) - \Psi_k(0)] B_{ki'} \tag{3.31}$$

where, from Table 2 in Viesca and Garagash (2017), $\Psi_k(z)$ is the indefinite integral of the complimentary set of Chebyshev's polynomials (i.e. $\psi_k = U_k(z)$),

$$\Psi_k(z) = \int^{z} \psi_k(z) \mathrm{d}z = \frac{\cos(k+1)\theta}{k+1}, \quad \theta = \arccos(z) \tag{3.32}$$

and

$$B_{ki'} = \frac{2}{m+1} \sin\left(\frac{\pi i'}{m+1}\right) \sin\left(\frac{\pi(k+1)i'}{m+1}\right) \tag{3.33}$$

For another example, consider integration of the dislocation density $\mathrm{d}w/\mathrm{d}s = \omega(s)F(s)$, with $F(s)$ defined on the $\mathbf{s}-$grid, $\{F(s_j)\}$, and results evaluated on the $\mathbf{z}-$grid (Viesca and Garagash, 2017):

$$\int_{z_i}^{+1} \frac{\partial w}{\partial s} \mathrm{d}s = -\sum_{j=1}^{n} S_{ij} F(s_j), \quad S_{ij} = \sum_{k=0}^{n-1} [\Phi_k(z_i) - \Phi_k(1)] B_{kj} \tag{3.34}$$

where, from Table 2 in Viesca and Garagash (2017),

$$\Phi_k(z) = \int^z \phi_k(s)\mathrm{d}s = -\frac{\sin k\theta}{k} \tag{3.35}$$

and

$$B_{kj} = \begin{cases} \dfrac{1}{n}, & k = 0 \\ \dfrac{2}{n}\cos\left(\dfrac{\pi k(j - 1/2)}{n}\right), & k > 0 \end{cases} \tag{3.36}$$

Specifically, the integration matrix $\{S_{ij}\}$ simplifies to a vector $\{S_{Aj}\}$ on the integration interval $[-1, 1]$ and simplifies to $\{S_{Hj}\}$ on $[0, 1]$.

$$\int_{-1}^{+1} \frac{\partial w}{\partial s}\mathrm{d}s = \sum_{j=1}^{n} S_{Aj} F(s_j), \quad S_{Aj} = \sum_{k=0}^{n-1} [\Phi_k(1) - \Phi_k(-1)]B_{kj} \tag{3.37}$$

$$\int_{0}^{+1} \frac{\partial w}{\partial s}\mathrm{d}s = \sum_{j=1}^{n} S_{Hj} F(s_j), \quad S_{Hj} = \sum_{k=0}^{n-1} [\Phi_k(1) - \Phi_k(0)]B_{kj} \tag{3.38}$$

A differentiation operator can be defined on either grid. In the following, we utilize differentiation on the $\mathbf{z}$−grid. For a regular function $g(z)$, we obtain

$$g'(z_i) \approx \sum_{i'=1}^{m} D_{ii'}g(z_i); \quad D_{ii'} = \frac{\omega_{i'}/\omega_i}{z_i - z_{i'}}, \quad i \neq i'; \quad D_{ii} = -\sum_{i'=1, i'\neq i}^{m} D_{ii'} \tag{3.39}$$

where $\omega_i = (-1)^i \sin^2(\pi i/n)$ (see Table 3 in Viesca and Garagash (2017)).

3.5.4 Discretized governing equations

Using the previously defined operators, we discretize the governing equations of the problem as follows.

Elasticity

The elasticity equation (3.3) after discretization reads:

$$\frac{4\ell}{E'}p(z_i) = \sum_{j=1}^{n} \frac{1}{n}G_d(z_i, s_j)F(s_j) \tag{3.40}$$

written in the matrix form as:

$$\frac{4\ell}{E'}\mathbf{p} = \mathbb{G}_d \cdot \mathbf{F} \tag{3.41}$$

where $\mathbf{p} = \{p(z_i)\}$, $\mathbf{F} = \{F(s_j)\}$ are unknown vectors and $\mathbb{G}_d = \{\frac{1}{n}G_d(z_i, s_j)\}$ is the elasticity quadrature matrix.

The quadrature (3.40) has spectral accuracy for the plane-strain fracture (Viesca and Garagash, 2017; Erdogan et al., 1973), when kernel $G_1(z, s) = \dfrac{1}{z - s}$ is the Cauchy one, and the corresponding quadrature matrix $\mathbb{G}_1 = \mathbb{H} = \{\dfrac{1}{n} \dfrac{1}{z_i - s_j}\}$.

For an axisymmetric fracture, the kernel is to the leading order of the Cauchy type, but it also contains a weaker logarithm singularity. We therefore write it as:

$$G_2(z, s) = \frac{1}{z - s} + \frac{\ln|z - s|}{2z} + \Delta G(z, s) \tag{3.42}$$

where $\Delta G(z, s)$ corresponds to the non-singular part of $G_2(z, s)$. In order to maintain the accuracy of the quadrature in this case, we represent the logarithm-term as an integral of the Cauchy-like term, $\ln|z - s| = \int_0^z \dfrac{\mathrm{d}z}{z - s} + \ln s$, where the latter term is inconsequential (i.e. it gives zero contribution to the elasticity integral). Using integration on the $\mathbf{z}$–grid for the logarithm-term, the final elasticity matrix for the axisymmetric fracture case becomes:

$$\mathbb{G}_2 = \mathbb{H} + \frac{1}{2\mathbf{z}} \mathbb{T} \cdot \mathbb{H} + \Delta\mathbb{G} \tag{3.43}$$

where $\mathbb{T} = \{T_{ii'}\}$ is the $\mathbf{z}$–grid integration matrix and $\Delta\mathbb{G} = \{\dfrac{1}{n} \Delta G(z_i, s_j)\}$.

Lubrication flow

We integrate the lubrication equation (3.6) from the $\mathbf{z}$–grid nodes to the fracture tip accounting for the tip boundary condition $w(\xi = 1) = 0$ (Eq. (3.8)):

$$-\left(\frac{\partial w_i}{\partial t} \frac{1}{d} z_i^d + \frac{\partial}{\partial t} \frac{1}{d} \int_{z_i}^1 \xi^d \frac{\partial w}{\partial \xi} \mathrm{d}\xi \right) - \frac{\dot{\ell}}{\ell} \int_{z_i}^1 \xi^d \frac{\partial w}{\partial \xi} \mathrm{d}\xi = -\frac{1}{\mu' \ell^2} z_i^{d-1} w_i^3 \left. \frac{\partial p}{\partial \xi} \right|_{\xi = z_i} \tag{3.44}$$

where w_i is the fracture opening evaluated at z_i. The discretization of these terms is obtained in the following by using the integration operator $\mathbb{S} = \{S_{ij}\}$ and differentiation operator $\mathbb{D} = \{D_{ii'}\}$ and by back-substituting the discretized elasticity equation (3.40).

$$\left\{ \frac{\partial w_i}{\partial t} \frac{1}{d} z_i^d \right\} = \frac{1}{d} \mathbf{z}^d \frac{\partial}{\partial t} (\mathbb{S} \cdot \mathbf{F}) \tag{3.45}$$

$$\left\{ \frac{1}{d} \int_{z_i}^1 \xi^d \frac{\partial w}{\partial \xi} \mathrm{d}\xi \right\} = \frac{1}{d} \left(-\mathbb{S} \cdot \left(\mathbf{s}^d \mathbf{F} \right) \right) \tag{3.46}$$

$$\left\{ \frac{1}{\mu' \ell^2} w_i^3 z_i^{d-1} \left. \frac{\partial p}{\partial \xi} \right|_{\xi = z_i} \right\} = \frac{E'}{4\mu' \ell^3} (\mathbb{S} \cdot \mathbf{F})^3 \mathbf{z}^{d-1} (\mathbb{D} \cdot \mathbb{G}_d \cdot \mathbf{F}) \tag{3.47}$$

We then obtain the final discretized $(n - 1)$ lubrication equations:

$$-\frac{1}{d} \mathbf{z}^d \frac{\partial}{\partial t} (\mathbb{S} \cdot \mathbf{F}) + \frac{1}{d} \frac{\partial}{\partial t} \left(\mathbb{S} \cdot \left(\mathbf{s}^d \mathbf{F} \right) \right) + \frac{\dot{\ell}}{\ell} \left(\mathbb{S} \cdot \left(\mathbf{s}^d \mathbf{F} \right) \right) = -\frac{E'}{4\mu' \ell^3} (\mathbb{S} \cdot \mathbf{F})^3 \mathbf{z}^{d-1} (\mathbb{D} \cdot \mathbb{G}_d \cdot \mathbf{F}) \tag{3.48}$$

3.5.5 Global continuity equation

The global continuity equation reduces to the following using the integration operators $\mathbf{S}_A = \{S_{Aj}\}$ or $\mathbf{S}_H = \{S_{Hj}\}$ defined above:

- Plane-strain

$$\int_{-1}^{1} \xi \frac{\partial w}{\partial \xi} \, d\xi + \frac{Q_o t}{\ell} = \mathbf{S}_A \cdot (\mathbf{s}\,\mathbf{F}) + \frac{Q_o t}{\ell} = 0 \tag{3.49}$$

- Axisymmetry

$$\int_{0}^{1} \xi^2 \frac{\partial w}{\partial \xi} \, d\xi + \frac{Q_o t}{\pi \ell^2} = \mathbf{S}_H \cdot (\mathbf{s}^2\,\mathbf{F}) + \frac{Q_o t}{\pi \ell^2} = 0 \tag{3.50}$$

3.5.6 Propagation criterion

The opening asymptote near the tip (3.10) indicates a square root singularity of the dislocation density at the tip as shown in Eq. (3.51), which is already embedded in the Gauss-Chebyshev quadrature (3.25):

$$\lim_{z \to 1} \frac{dw}{dz} = \lim_{z \to 1} \frac{dw}{d\xi} \frac{d\xi}{dz} = -\frac{K'_*}{E'} \frac{\ell^{1/2}}{2} \left(\frac{\ell}{\ell_*} \right)^\alpha \lim_{z \to 1} \frac{1}{\sqrt{1-z}} \tag{3.51}$$

$$\lim_{z \to 1} \frac{dw}{dz} = \lim_{s \to 1} \omega(s) F(s) = \frac{F(1)}{\sqrt{2}} \lim_{s \to 1} \frac{1}{\sqrt{1-s}} \tag{3.52}$$

By setting the coefficients before the singularity in Eq. (3.51) and Eq. (3.52) equal to each other and applying the extrapolation operator $\mathbf{Q} = \{Q_j\}$, the propagation condition for a fracture length dependent toughness simplifies to

$$F(1) \approx \mathbf{Q} \cdot \mathbf{F} = -\frac{1}{\sqrt{2}} \frac{K'_* \ell^{1/2}}{E'} \left(\frac{\ell}{\ell_*} \right)^\alpha \tag{3.53}$$

We therefore get a set of discretized equations (3.48), (3.49) or (3.50) depending on the geometry, and (3.53), all of which are function of ℓ and $\mathbf{F}$. By differentiating Eq. (3.49) or (3.50), and Eq. (3.53) with respect to t, we finally get a system of ODEs that can be schematically written as:

$$\mathbb{M}(\mathbf{Y}, t) \frac{d\mathbf{Y}}{dt} = \mathscr{F}(\mathbf{Y}, t) \tag{3.54}$$

where $\mathbf{Y} = \{\ell, \mathbf{F}\}$ is the unknown vector and $\mathbb{M}$ and $\mathscr{F}$ are the matrix and vector functions of $\mathbf{Y}$ and t which follow from the above differentiation.

On the account of the problem symmetry for a plane-strain fracture, choosing an even n, we set

$$\mathbf{F} = \{F_1, F_2, ..., F_{n/2}, -F_{n/2}, ..., -F_2, -F_1\} \tag{3.55}$$

The first $(n/2 - 1)$ equations of Eq. (3.48) are thus equivalent to the last $(n/2 - 1)$ equations. By taking advantage of the symmetry, we account for the first $(n/2 - 1)$ equations in Eq. (3.48)

when building the ODEs of Eq. (3.54).

For a radial fracture, we select an odd n since the choice of an even n would result in infinite values of the elasticity matrix (3.43). We therefore set:

$$\mathbf{F} = \{F_1, F_2, ..., F_{(n-1)/2}, 0, -F_{(n-1)/2}, ..., -F_2, -F_1\} \tag{3.56}$$

Similarly, we take the first $((n-1)/2 - 1)$ equations of Eq. (3.48) to build the ODE system.

The final non-linear system of ODEs (3.54) can be solved using appropriate numerical algorithms. We have used the built-in ODE solver of Mathematica 11.0 (Wolfram Research, Inc., 2016). In terms of initial conditions, assuming a fracture length dependent toughness of Eq. (3.1), the fracture propagation for both geometries starts from a viscosity dominated solution[3]. We therefore use the solutions of the self-similar problem with $\mathcal{K} \ll 1$ for a plane-strain fracture (see 3.9 for more details) and the zero-toughness solution for a radial fracture (Savitski and Detournay, 2002). In the latter, we initialize the fracture growth at time $t_o \ll t_{mk}(\alpha)$ with a fracture radius of $\ell_o \ll L_{mk}(\alpha)$ and a fracture toughness of $K_*(\ell_o/\ell_*)^\alpha$.

We use $n = 100$ for a plane-strain fracture and $n = 101$ for a radial fracture for all the simulations presented in this chapter. The computational cost using the default settings of the Mathematica ODE solver is of several seconds for a simulation spanning 6-15 decades of time (e.g. two seconds for the case of Fig. 3.2, around 30 seconds for the case of Fig. 3.12)[4] on a personal computer (MacBook Pro, 2015, 2.9 GHz Intel Core i5).

3.5.7   Numerical verification - fracture length independent fracture toughness case

We first benchmark our numerical solver for the case of a fracture length independent fracture toughness for which a number of (semi-) analytical solutions are known. The solver is able to reproduce all propagation regimes for both geometries in a very efficient manner.

We present here comparisons for a radial fracture for which the solution evolves from viscosity to toughness dominated regime with time for a fracture length independent toughness.

The fracture behaviour is characterised by different power laws in the $M-$ and $K-$regime, as illustrated in Fig. 3.2, where the departure from the viscosity dominated regime is observed to start at t_{mk}. The profiles of the fracture opening and net pressure for $\mathcal{K} = 0.32, 2.7, 5.0$ are displayed in Fig. 3.3, showing an excellent match with the zero-toughness ($\mathcal{K} = 0$) and large-toughness ($\mathcal{M} \ll 1$) solutions (Savitski and Detournay, 2002) respectively.

---

[3]If we account for a non-zero toughness at initiation, the approximation of zero-toughness solutions for a radial fracture is still valid at early time, since the energy dissipation in the solid is limited by the small geometry and viscosity dominates the fracture growth. However, this may differ for a plane-strain fracture: any state between the viscosity or toughness dominated regimes can serve as an initial condition, see Section 3.7.2 for more discussions.

[4]The computational cost is related to the complexity and non-linearity of the system. The system of Fig. 3.12 is more non-linear due to a smoothed toughness saturation function and is thus more time-consuming than the case of Fig. 3.2.
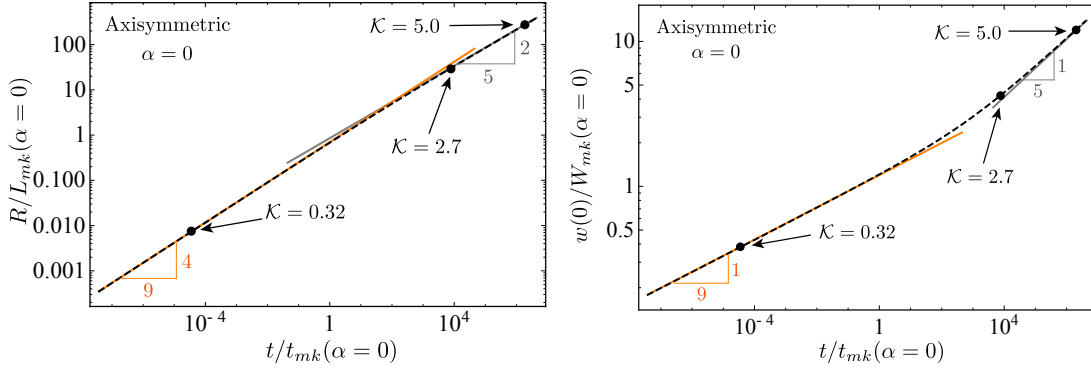
Figure 3.2 – Evolution of the dimensionless fracture radius and inlet opening with dimensionless time for the case of a fracture length independent toughness ($\alpha = 0$). Dashed curves indicate numerical solutions while the orange and gray lines correspond to zero-toughness ($\mathcal{K} = 0$) and zero-viscosity ($\mathcal{M} = 0$) solutions respectively.
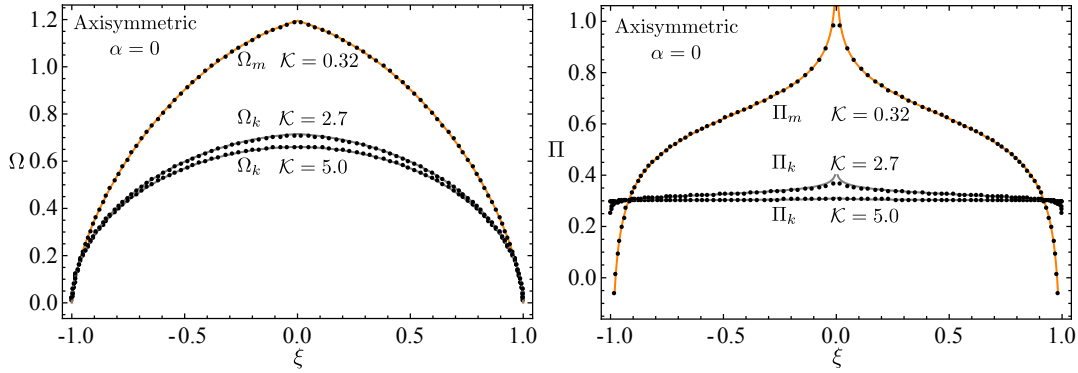

Figure 3.3 – Profile of fracture opening and net pressure in a radial fracture for the case of a fracture length independent toughness ($\alpha = 0$) with $\mathcal{K} = (t/t_{mk}(\alpha = 0))^{1/9} = 0.32, 2.7, 5.0$, scaled separately by viscosity scaling Ω_m, Π_m and toughness scaling Ω_k, Π_k. The near M−vertex solution ($\mathcal{K} = 0.32 \leq 1$ (Savitski and Detournay, 2002)) can be approximated the by zero-toughness solution which is indicated by the orange curve. The gray curves indicate the corresponding large-toughness solutions (Savitski and Detournay, 2002) with $\mathcal{K} = 2.7, 5.0$ respectively.
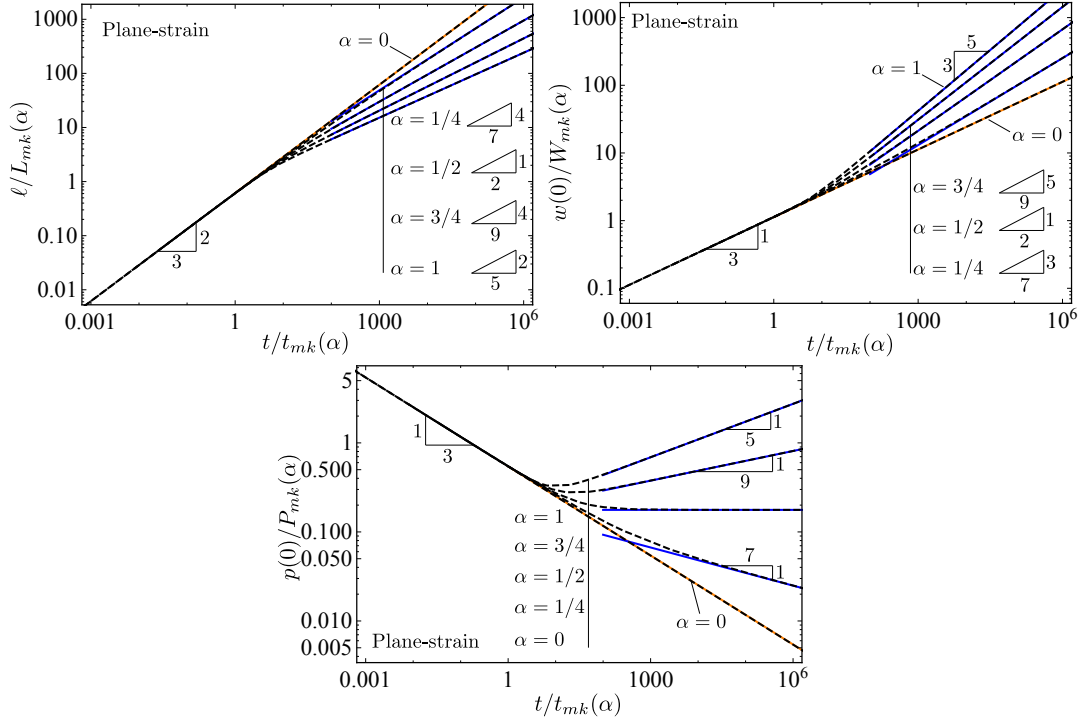
Figure 3.4 – Evolution of the dimensionless fracture half-length (up-left), inlet opening (up-right) and net pressure at the inlet (down) with dimensionless time in a plane-strain fracture, dashed curves indicate the numerical simulations while the blue solid lines indicate the fracture length dependent zero-viscosity solutions and orange solid lines the viscosity dominated solutions.

3.6 Results for fracture length dependent toughness

We now discuss the effect of a fracture length dependent toughness on the growth of hydraulic fractures for $\alpha \in [0, 1]$.

We first discuss the plane-strain geometry. Fig. 3.4 displays the evolution of fracture half-length, net pressure and width at the fracture inlet for different values of α. As observed from the scaling considerations discussed in Section 3.4, the hydraulic fracture propagation evolves from the viscosity to the toughness dominated regime. We observe from the simulation that the transition starts at time larger than $t_{mk}(\alpha)$ in line with the scaling arguments. At large time, the numerical solutions approximately coincide with the large toughness / zero viscosity asymptotes (blue lines on Fig. 3.4). A power-law dependence toughness leads to a shorter fracture length and larger net pressure in the toughness dominated regime. We observe a propagation under constant net pressure for $\alpha = 1/2$ and even an increase of net pressure with time for $\alpha > 1/2$ as expected.

Similar evolutions are observed for a radial hydraulic fracture. The time evolution of the fracture radius and inlet width are displayed in Fig. 3.5 for different α.
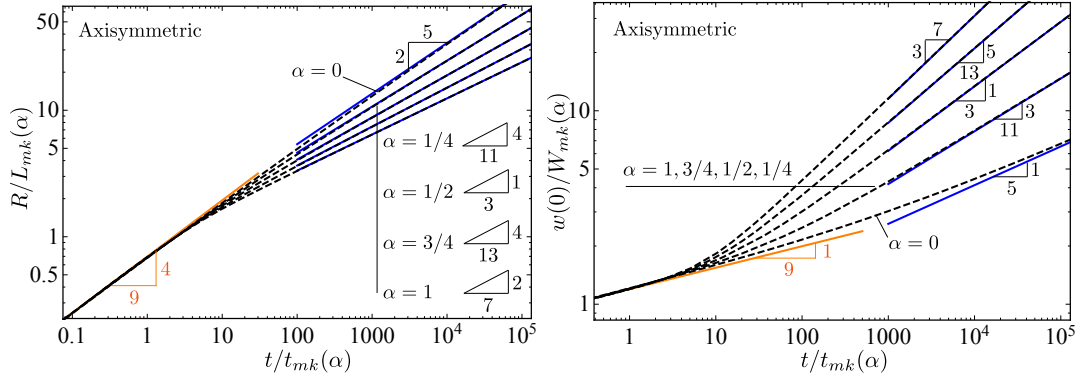
Figure 3.5 – Evolution of the dimensionless fracture radius (left) and inlet opening (right) with dimensionless time for a radial fracture. Dashed lines indicate the numerical simulations while the blue solid lines indicate the fracture length dependent zero-viscosity solutions and orange solid lines the zero-toughness solution.

It is interesting to re-scale these numerical results using the viscosity scaling and to redefine the dimensionless toughness by using the current value of toughness $K_*(\ell/\ell_*)^\alpha$ as function of the current fracture length i.e.:

- Plane-strain ($d = 1$)

$$\bar{\mathcal{K}}_1 = \frac{K'_*}{E'}\left(\frac{E'}{\mu' Q_o}\right)^{1/4}\left(\frac{\ell}{\ell_*}\right)^\alpha \tag{3.57}$$

- Axisymmetric ($d = 2$)

$$\bar{\mathcal{K}}_2 = \frac{K'_*}{E'}\left(\frac{E'^5 t^2}{\mu'^5 Q_o^3}\right)^{1/18}\left(\frac{\ell}{\ell_*}\right)^\alpha \tag{3.58}$$

Such a definition explicitly embeds the fracture length dependence of the fracture toughness in the same dimensionless parameter as the fracture length independent toughness case (Garagash, 2000). After doing so, the dimensionless solution for any value of α expressed as function of $\bar{\mathcal{K}}_d$ approximately collapses on the same curve as the solution for fracture length independent toughness - see Figs 3.6, 3.7 for the dimensionless length and inlet opening. Fig. 3.8 presents the relative difference of the dimensionless length between the fracture length dependent and fracture length independent cases. The difference is null in both viscosity ($\bar{\mathcal{K}}_d = 0$) and toughness dominated ($\bar{\mathcal{K}}_d \to \infty$) regimes. Both end-member regimes are described by the fracture length independent solution with instantaneous value of toughness exactly, e.g. at large time, from Eq. (3.23), Eq. (3.24) and Eq. (3.17), the evolution of dimensionless fracture length with $\bar{\mathcal{K}}_d$ becomes independent of α:

$$\text{Plane-strain, } \gamma_m \approx \left(\frac{2\sqrt{2}}{\pi \bar{\mathcal{K}}_1}\right)^{2/3}; \quad \text{Axisymmetric, } \gamma_m \approx \left(\frac{3}{\pi\sqrt{2}\bar{\mathcal{K}}_2}\right)^{2/5} \tag{3.59}$$

The relative difference in the transient regime is not zero but remains very small with a
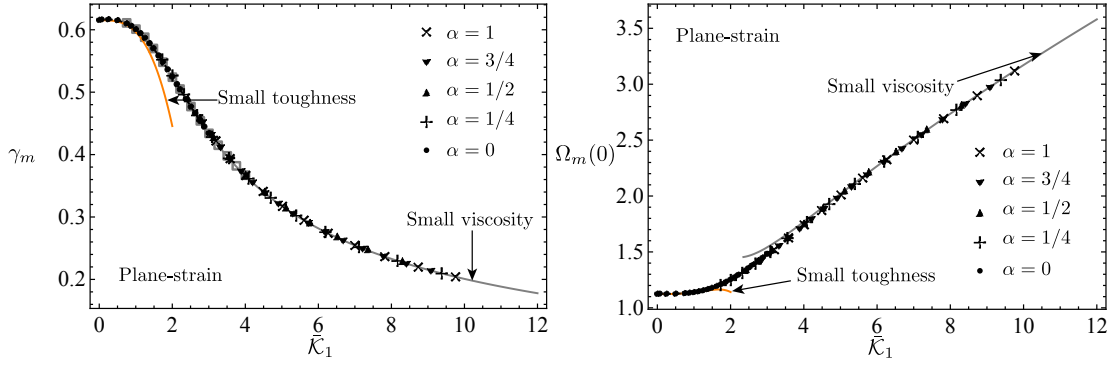
Figure 3.6 – Dependence of the dimensionless half-length γ_m (left) and inlet opening Ω_m (right) in the viscosity scaling on the scale-related dimensionless toughness $\bar{\mathcal{K}}_1$. Numerical solutions of $\alpha = 1/4, 1/2, 3/4, 1$ approximately coincide with the small-toughness (Garagash and Detournay, 2005) and small-viscosity (Garagash, 2006a) solutions ($\alpha = 0$) with first-order corrections, the previous numerical results (gray empty squares) (Garagash and Detournay, 2005) as well as the self-similar solutions (disks) calculated via the procedures in 3.9.
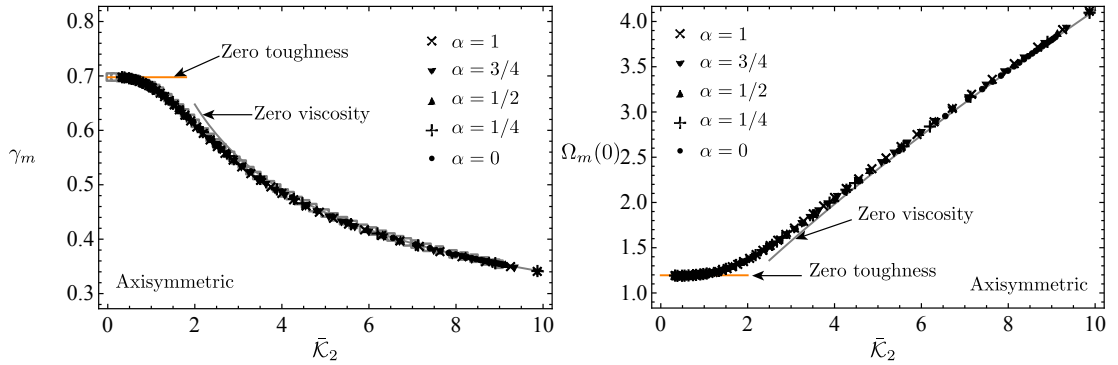

Figure 3.7 – Dependence of the dimensionless fracture radius γ_m (left) and inlet opening Ω_m (right) in the viscosity scaling on the scale-related dimensionless toughness $\bar{\mathcal{K}}_2$. Numerical solutions of $\alpha = 1/4, 1/2, 3/4, 1$ approximately coincide with the fracture length independent toughness solution ($\alpha = 0$) and the previous numerical solutions (gray empty squares) reported in (Madyarova, 2004) for the case of a fracture length independent toughness.
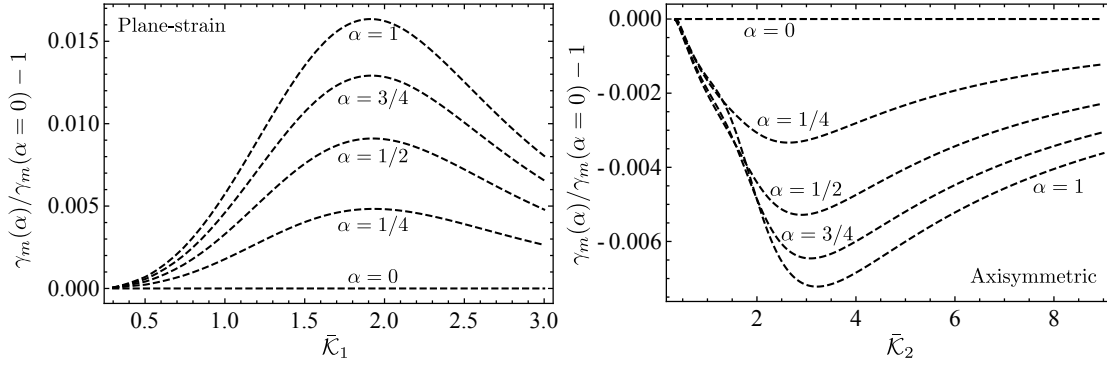
Figure 3.8 – Evolution of the relative difference of the dimensionless fracture length/radius γ_m (between the fracture length independent and fracture length dependent cases) with the instantaneous dimensionless toughness $\bar{\mathcal{K}}_d$. At the same value of $\bar{\mathcal{K}}_d$, a non-zero α results in a shorter fracture radius in the axisymmetric geometry, but a longer fracture length in the plane-strain geometry than the case of $\alpha = 0$ (fracture length independent). Such a discrepancy of a plane-strain fracture is due to the fact that $\bar{\mathcal{K}}_d(\alpha = 0)$ stays constant during the fracture growth instead of increasing as in the case of a radial fracture. For $\alpha > 0$, in order to reach the same value of $\bar{\mathcal{K}}_1(> \mathcal{K})$ for a plane-strain fracture in the fracture length dependent and -independent cases, the fracture toughness increases in the fracture length dependent cases before reaching such value of $\bar{\mathcal{K}}_1(> \mathcal{K})$. During this period of toughness increase, the instantaneous fracture toughness in the fracture length dependent case is smaller than that of the fracture length independent case, therefore indicates less energy dissipation in the creation of fracture surfaces and a longer fracture length.

maximum value of less than 2% as illustrated in Fig. 3.8.

For $\alpha \in [0, 1]$, the change of apparent toughness has therefore a nearly instantaneous impact on the propagation of a plane-strain or axisymmetric fracture. The propagation of a hydraulic fracture can be therefore approximately dominated by one master curve, no matter how the apparent fracture toughness evolves in different scales and all solutions can be obtained from the fracture length independent toughness solution. It indicates that the solution obtained here numerically could be obtained from the fracture length independent toughness solution and a non-linear root finding scheme to determine the current length embedded in the definition of $\bar{\mathcal{K}}_d$.

3.7 Discussions

3.7.1 Emplacement scaling

The displacement to length or emplacement scaling is often used in geology to discuss the physics of the fracture propagation of magmatic dikes and natural fractures. Field observations of displacement-length scaling have nourished discussions about the fracture length dependence of fracture toughness (Scholz, 2010; Olson and Schultz, 2011). In this section, we discuss
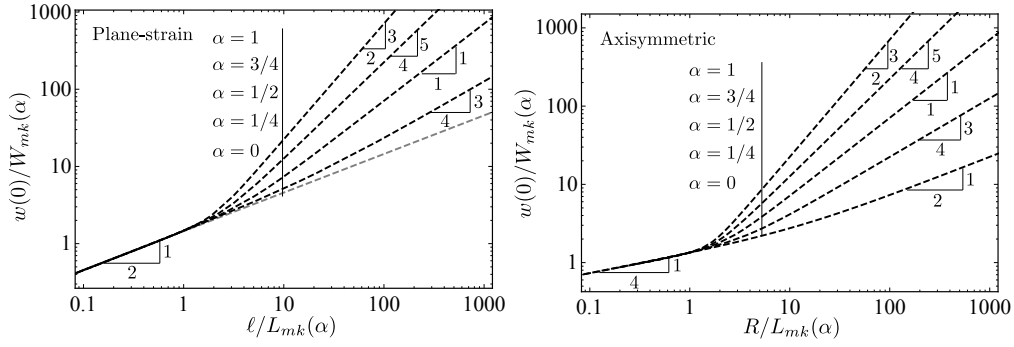
Figure 3.9 – Evolution of displacement-length scaling in two geometries: plane-strain (left) and axisymmetric (right) for different α values, scaled respectively by W_{mk} and L_{mk}.

the obtained displacement-length scaling for axisymmetric and plane-strain geometries for the power-law fracture length dependent toughness model.

The dimensional analysis reveals that both fracture opening and fracture length evolve with time and are related to the propagation regime associated with the principal source of energy dissipation. From Table 3.2, we obtain

$$M-\text{regime}, \quad W \propto L^{(3-d)/4}; \quad K-\text{regime}, \quad W \propto L^{\alpha+1/2} \tag{3.60}$$

At early time, when the fracture toughness has a negligible influence, the emplacement scaling is only geometry-dependent. At large time, for toughness dominated fractures, the emplacement scaling becomes independent of the geometry and is solely function of α: the larger α is, the larger the emplacement scaling W/L.

Fig. 3.9 illustrates the complete evolution of the emplacement scaling from the early time $M-$regime to the large time $K-$regime. For a plane-strain fracture with fracture length independent toughness, the scaling parameter happens to remain the same in all propagation regimes. For a fracture length dependent fracture toughness, the emplacement scaling increases from a lower value in the $M-$regime to a geometry-independent value in the $K-$regime at large time in both geometries. The displacement-length ratio reflects the evolution of the partitioning of energy between viscous flow and the creation of fracture surfaces during propagation.

A square-root emplacement scaling corresponds to the fracture length independent toughness as reported in the literature (Olson, 2003; Schultz et al., 2008b,a). The linear emplacement scaling $W \propto L$ reported from field studies (Scholz, 2010) corresponds to the case of a square-root fracture length dependent toughness ($\alpha = 1/2$). It is therefore interesting that, although debate exists in regards to the emplacement scaling observed in the field (either 1/2 or linear), emplacement scaling ratio larger than one have not been reported. This seems to indicate that a power-law exponent larger than $\alpha = 1/2$ for the fracture length dependent toughness is unlikely.

Table 3.3 – Time dependence of the difference ratio between the large toughness solutions for fracture length dependent toughness and fracture length independent toughness, respectively. Such difference ratios of inlet opening, net pressure and fracture length scale are power laws of the dimensionless time $(t/t_{mk}(\alpha = 0))^\beta$ for an axisymmetric fracture and $(t/t_*)^\beta$ for a plane-strain fracture, with the exponent β a function of the geometry index d and toughness power-law scaling exponent α.

Geometry	Time power-law exponent β	
	Plane-strain ($d = 1$)	Axisymmetric ($d = 2$)
$w(0,\alpha)/w(0,\alpha = 0)$	$2\alpha/(3\alpha + 9/2)$	$4\alpha/(5\alpha + 25/2)$
$p(0,\alpha)/p(0,\alpha = 0)$	$4\alpha/(3\alpha + 9/2)$	$6\alpha/(5\alpha + 25/2)$
$\ell(\alpha)/\ell(\alpha = 0)$	$-2\alpha/(3\alpha + 9/2)$	$-2\alpha/(5\alpha + 25/2)$

3.7.2 Difference brought by the fracture length dependent toughness

The apparent fracture toughness may exhibit a lower cut-off K_c within a cross-over length scale ℓ_c. For most quasi-brittle materials, ℓ_c is of the same order of magnitude as specimen dimensions in the lab. In order to grasp the difference brought by an increasing toughness, it is natural to choose a reference state corresponding to a fracture toughness $K_* \approx K_c$ measured at a laboratory length scale $\ell_* \approx \ell_c$. In this section, we analyse the difference brought by the power-law dependence compared with the fracture length independent case assuming $\ell_s \to \infty$.

When $\ell \leq \ell_*$, the fracture energy reduces to a constant and does not vary with the fracture length. The growth of hydraulic fractures is the same as the case of the fracture length independent toughness with $K_{Ic} = K_*$. We define t_* as the time for the fracture to propagate with a constant toughness K_* in order to reach a fracture length of ℓ_*. When $\ell > \ell_*$, the apparent toughness scales with the fracture length and the propagation transitions to large toughness solutions as discussed in Section 3.6. The ratio between the large toughness solutions of the fracture length dependent and independent cases are shown in Table 3.3, where the corresponding power laws can be recovered at large time by the numerical solutions as illustrated in Figs 3.10 and 3.11. The evolution of the difference ratio depends strongly on the reference state where the apparent toughness starts to scale with the fracture length. Such a reference state can be characterised by $\ell_*/L_{mk}(\alpha = 0)$ for a radial fracture and by $\mathcal{K}(\ell = \ell_*, \alpha = 0)$ for a plane-strain fracture. As shown in Fig. 3.10, a transition of principal energy dissipation from viscosity to toughness appears if the viscosity happens to dominate the fracture growth at the reference state. Both a smaller length scale for the initiation of the toughening effect and a larger value of the power-law exponent α result in a more pronounced difference as illustrated in Fig. 3.10 and Fig. 3.11.

Using values for material and injection parameters - representative of an industrial fracturing treatment, we quantify the departure of the solution from the fracture length independent toughness case for a radial fracture in Table 3.4. The characteristic net pressure increases with α while the characteristic length, as well as, the characteristic transition time from the
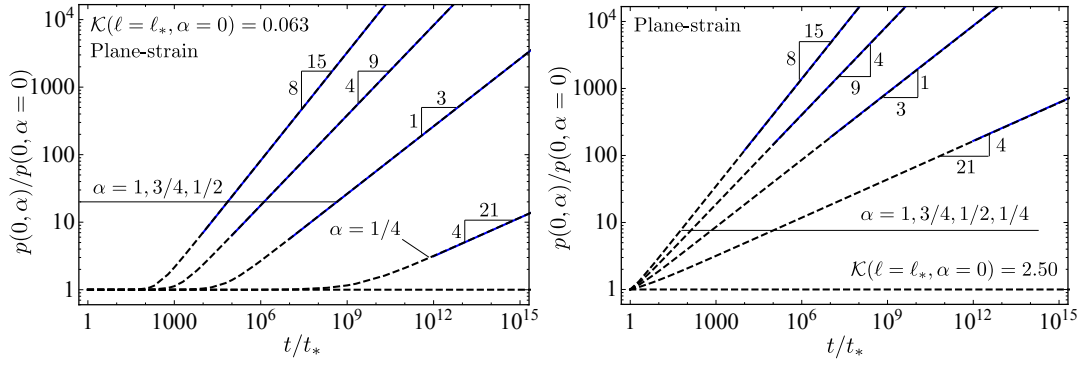
Figure 3.10 – Evolution of the difference ratio of net pressure at the inlet with dimensionless time in a plane-strain fracture for $\mathcal{K}(\ell = \ell_*, \alpha = 0) = 0.063$ (left), 2.50 (right), dashed lines indicate the numerical simulations while the blue solid lines indicate the fracture length dependent zero-viscosity solutions.
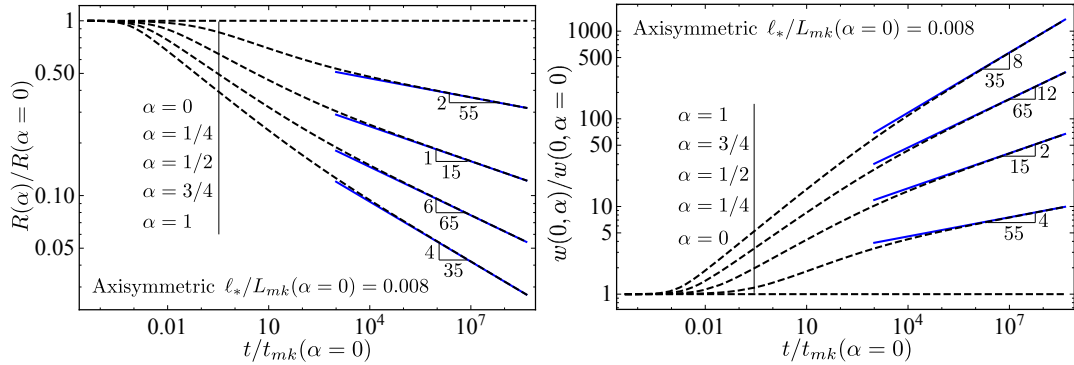

Figure 3.11 – Evolution of the difference ratio of fracture radius (left) and inlet opening (right) with dimensionless time in a radial fracture ($\ell_*/L_{mk}(\alpha = 0) = 0.008$), dashed lines indicate the numerical simulations while the blue solid lines indicate the fracture length dependent zero-viscosity solutions.

Table 3.4 – Characteristic scales and difference ratio values for different values of the toughness power-law scaling exponent α in the axisymmetric geometry ($E' = 20\,\text{GPa}$, $Q_o = 2 \times 10^{-2}\,\text{m}^3/\text{s}$, $\mu' = 3\,\text{Pa.s}$, $K_* = 1.5\,\text{MPa.m}^{1/2}$, $\ell_* = 0.1\,\text{m}$ and $\ell_*/L_{mk}(\alpha = 0) = 1.03 \times 10^{-8}$)

	$\alpha = 0$	$\alpha = 1/4$	$\alpha = 1/2$
$t_{mk}(\alpha)$ (s)	3.56×10^{14}	3.67×10^5	3.70×10^2
$L_{mk}(\alpha)$ (m)	9.84×10^6	9.97×10^2	46.5
$P_{mk}(\alpha)$ (kPa)	0.150	1.48×10^2	1.48×10^3
$R/R(\alpha = 0)$ ($t = 90$ min)	1	1.00	0.88
$w(0)/w(\alpha = 0)$ ($t = 90$ min)	1	1.00	1.14
$R/R(\alpha = 0)$ ($t = 3$ d)	1	0.98	0.60
$w(0)/w(\alpha = 0)$ ($t = 3$ d)	1	1.01	2.26

viscosity to the toughness dominated regime, decreases with α. The relative difference of the fracture radius can go up to 40% after long injection duration for $\alpha = 1/2$.

3.7.3 Effect of a finite apparent fracture toughness beyond a given length scale

The fracture toughness might reach an asymptotic value beyond a certain length scale ℓ_s, possibly due to the saturation of the process zone size or the limits of the constraints of the medium dimensions (earth crust). In this section, we model such possible saturation of the fracture toughness ($\ell_s < \infty$) as follows:

$$K_{Ic} = K_* (\ell/\ell_*)^\alpha (1 - f((\ell - \ell_s)/\ell_*)) + K_s f((\ell - \ell_s)/\ell_*), \quad K_s = K_* (\ell_s/\ell_*)^\alpha \tag{3.61}$$

Here f is a smoothed Heaviside step function $f(m) = 1/(1 + \exp(-2hm))$, where h is a positive dimensionless number controlling the smoothing of the approximation (a smaller value entails a "smoother step" - we have used $h = 130$ here). Under the same assumption that $\ell_* \approx \ell_c$ as in Section 3.7.2, the saturation length scale is comparable to or larger than the reference length scale: $\ell_s \geq \ell_*$. $(\ell_s/\ell_*)^\alpha$ therefore describes the difference of apparent toughness between the reference and final state whereas α characterises the slope of the power law branch. When $\ell_s \gg \ell_*$, the saturated apparent toughness K_s can be exceedingly large compared to K_*.

As illustrated in Fig. 3.12 (for $\alpha = 1/2$ and different values of $\ell_s/L_{mk}(\alpha)$), the hydraulic fracture evolves by first following the solution obtained previously for the power-law fracture length dependent toughness and then transitions back to the fracture length independent toughness solution ($\alpha = 0$ with $K_{Ic} = K_s$) when the fracture reaches the saturation length scale $\ell = \ell_s$. The impact of the toughness evolution on fracture growth is nearly instantaneous for $\alpha \in [0, 1]$ in both geometries as previously shown in Figs. 3.6 and 3.7, however, the transition towards the toughness dominated solution at large timescale with a fracture length independent toughness ($\alpha = 0$ with $K_{Ic} = K_s$) can be much more gradual for a radial fracture when $\ell_s/L_{mk}(\alpha) \ll 1$ in Fig. 3.12.

The effect of the toughness saturation on the propagation of a hydraulic fracture with fracture
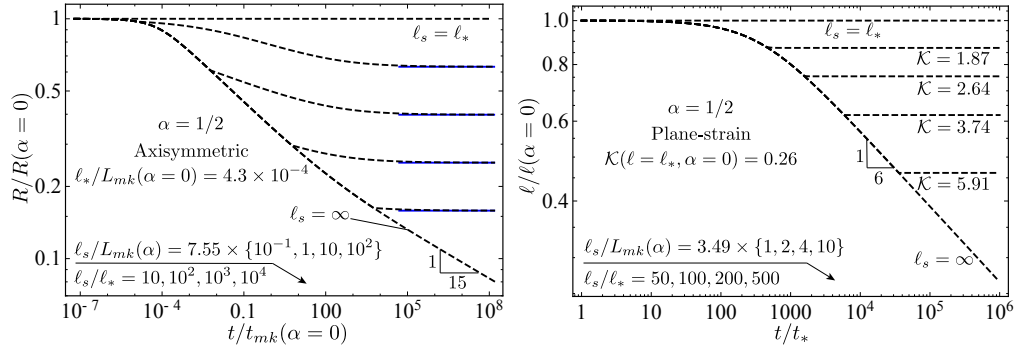
Figure 3.12 – Evolution of the difference ratio of dimensionless fracture radius (left) and fracture half-length (right) with dimensionless time where $\alpha = 1/2$. Dashed curves indicate the numerical transition and blue solid lines refer to zero-viscosity solutions.
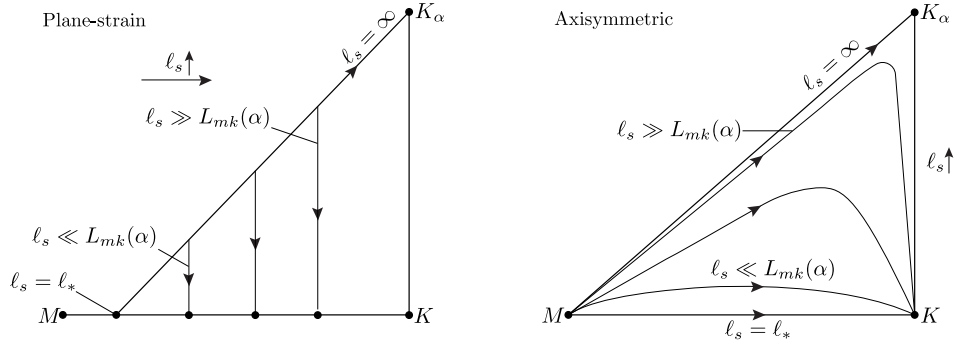

Figure 3.13 – Propagation diagram illustrating the propagation of a hydraulic fracture in a material exhibiting a fracture length dependent toughness with a saturated length scale ℓ_s for plane-strain and axisymmetric geometries. K_α signifies the fracture length dependent toughness dominated regime.

length dependent toughness up to ℓ_s can be summarized in the propagation diagram of Fig. 3.13. A plane-strain hydraulic fracture evolves initially from the reference state which can be either viscosity or toughness dominated towards the fracture length dependent toughness edge ($M - K_\alpha$) (see Fig. 3.13-left), and, as soon as the fracture half-length ℓ reaches ℓ_s, the propagation switches to the fracture length independent toughness, plane-strain self-similar solution characterised by a constant dimensionless toughness $\bar{\mathcal{K}}_1(\ell = \ell_s)$ from Eq. (3.57). Depending on the value of $\bar{\mathcal{K}}_1(\ell = \ell_s)$, any state between the $M-$ and $K-$regime is possible at large time for a plane-strain hydraulic fracture. The effect of toughness saturation for the radial hydraulic fracture is similar pending the fact that due to the geometry, the propagation always ends up being toughness dominated at large time - with the final toughness K_s governing the characteristic scales (see Fig. 3.13-right).

3.8 Conclusions

We have investigated theoretically the growth of a plane-strain and axisymmetric hydraulic fracture, assuming a power-law dependence of the fracture toughness with fracture length $K_{Ic} \propto \ell^\alpha$. We have posed the hydraulic fracture propagation problem based on the usual assumptions of linear elastic fracture mechanics, assuming that the small scale yielding approximation remains always valid and that the fracture is much larger than the process zone size.

In order to solve such a HF problem, we have developed a highly efficient and accurate numerical scheme based on the combination of Gauss-Chebyshev quadrature with barycentric differentiation and interpolation. Using such a spatial discretization allows to recast the non-linear, non-local hydraulic fracture evolution problem into a system of non-linear ordinary differential equations (ODEs) that can be solved by existing ODE integration schemes. The scheme performs extremely well against the published hydraulic fracture growth solutions for constant fracture toughness.

Our numerical results quantify precisely the impact of a power-law fracture length dependent toughness on HF growth. The increase of fracture energy with fracture length yields shorter and wider hydraulic fracture, and larger net fluid pressure. Our results demonstrate a shortening of the viscosity dominated to toughness dominated propagation for a radial fracture and show the existence of a viscosity to-toughness transition for a plane-strain fracture, a transition which does not exist in the case of a constant fracture toughness. The hydraulic fracture growth with a power-law toughness can be always very accurately approximated by the constant toughness solution when using the instantaneous value of toughness (function of the current fracture length), as per Eq. (3.57) and Eq. (3.58). If the fracture toughness saturates beyond a given scale ℓ_s, the hydraulic fracture propagation transitions back to the constant toughness solution as soon as $\ell > \ell_s$ - as depicted in Fig. 3.12.

Our results obviously depend on the value of the power-law scaling exponent α, with large changes between $\alpha \leq 1/2$ and $\alpha > 1/2$. The predicted emplacement scaling (ratio of displace-

ment to length) is geometry-dependent in the viscosity dominated regime: $W \propto L^{1/2}$ for plane-strain, $W \propto L^{1/4}$ for axisymmetric geometry. It is however solely dependent on α in the toughness dominated regime with $W \propto L^{1/2+\alpha}$. Compared to these theoretical predictions, emplacement W/L observations of dikes tend to indicate that the power-law scaling exponent α should at most be equal to 1/2 (Scholz, 2010). Such a limit appears consistent with available experimental evidences (Table 3.1) pointing to values of α lower than 1/2.

More field and experimental studies are needed in order to better quantify the importance of a possible fracture length dependence of fracture energy in relation to industrial as well as natural hydraulic fractures. The scalings and numerical results derived here could help decipher the validity of the power-law dependence hypothesis of apparent fracture toughness and guide further investigations.

3.9 Supporting information: discretization for the plane-strain self-similar problem

For a plane-strain hydraulic fracture, the dimensionless toughness $\mathcal{K}$ determines the solution of the self-similar problem. We rewrite the dimensionless governing equations in the viscosity scaling by introducing a new dimensionless opening (Garagash and Detournay, 2005).

$$\bar{\Omega} = \Omega/\gamma \tag{3.62}$$

The governing equations becomes:

- Elasticity

$$4\Pi = \frac{1}{\pi} \int_{-1}^{+1} \frac{\partial \bar{\Omega}}{\partial \xi'} G_1(\xi, \xi') \mathrm{d}\xi' \tag{3.63}$$

- Lubrication flow

$$\int_{\xi}^{1} \frac{\partial \bar{\Omega}}{\partial \xi} \mathrm{d}\xi + \frac{2}{3}\xi\bar{\Omega} + \bar{\Omega}^3 \frac{\mathrm{d}\Pi}{\mathrm{d}\xi} = 0 \tag{3.64}$$

- Global continuity equation

$$\int_{-1}^{1} \bar{\Omega} \mathrm{d}\xi = \frac{1}{\gamma^2} \tag{3.65}$$

- Propagation criterion

$$\bar{\Omega} \sim \frac{\mathcal{K}}{\sqrt{\gamma}} (1 - \xi)^{1/2} \tag{3.66}$$

We select the Gauss-Chebyshev polynomials of the first type T_n for discretization.

$$\frac{\partial \bar{\Omega}}{\partial s} = \omega(s)F(s), \quad \omega(s) = \frac{1}{\sqrt{1-s^2}} \tag{3.67}$$

The discretized equations reduce to

$$4\Pi = \mathbb{G}_1 \cdot \mathbf{F} \tag{3.68}$$

$$-\mathbf{z}(\mathbb{S} \cdot \mathbf{F}) + \mathbb{S} \cdot (\mathbf{s}\mathbf{F}) + \frac{2}{3}\mathbf{z}(\mathbb{S} \cdot \mathbf{F}) + (\mathbb{S} \cdot \mathbf{F})^3 (\mathbb{D} \cdot \Pi) = 0 \tag{3.69}$$

$$\mathbf{S}_A \cdot (\mathbf{s}\mathbf{F}) + \frac{1}{\gamma^2} = 0 \tag{3.70}$$

$$\mathbf{Q} \cdot \mathbf{F} + \frac{1}{\sqrt{2}} \frac{\mathcal{K}}{\sqrt{\gamma}} = 0 \tag{3.71}$$

By back-substituting the elasticity (3.68) into the lubrication equations (3.69), we get $(n+1)$ equations including the global continuity (3.70) and the propagation criterion (3.71). On the account of the problem symmetry as in Eq. (3.55), the first $(n/2 - 1)$ equations of Eq. (3.48) are

equivalent to the last $(n/2-1)$ equations. We hence account for the first $(n/2-1)$ equations of Eq. (3.69) together with Eq. (3.70) and (3.71) and solve the solutions of $\{\gamma, \mathbf{F}\}$ using the Mathematica built-in function $FindRoot$. As illustrated in Fig. 3.6, the numerical results fit well the small-toughness and small-viscosity solutions (Garagash and Detournay, 2005; Garagash, 2006a), and also the previous numerical solutions (Garagash and Detournay, 2005).

4 Propagation of a plane-strain HF accounting for a rough cohesive zone

This chapter aims to propose a mechanism for the extra energy demand of hydraulic fracture growth in quasi-brittle materials. The quasi-brittle nature of rocks challenges the basic assumptions of linear hydraulic fracture mechanics (LHFM): namely, linear elastic fracture mechanics and smooth parallel plates lubrication fluid flow inside the propagating fracture. We relax these hypotheses and investigate in details the growth of a plane-strain hydraulic fracture in an impermeable medium accounting for a rough cohesive zone and a fluid lag. In addition to a dimensionless toughness and the time-scale t_{om} of coalescence of the fluid and fracture fronts governing the fracture evolution in the LHFM case, the solution now also depends on the ratio between the in-situ stress and material peak cohesive stress σ_o/σ_c and the intensity of the flow deviation induced by aperture roughness (captured by a dimensionless power exponent). We show that the solution is appropriately described by a nucleation time-scale $t_{cm} = t_{om} \times (\sigma_o/\sigma_c)^3$, which delineates the fracture growth into three distinct stages: a nucleation phase ($t \ll t_{cm}$), an intermediate stage ($t \sim t_{cm}$) and late time ($t \gg t_{cm}$) stage where convergence toward LHFM predictions finally occurs. A highly non-linear hydro-mechanical coupling takes place as the fluid front enters the rough cohesive zone which itself evolves during the nucleation and intermediate stages of growth. This coupling leads to significant additional viscous flow dissipation. As a result, the fracture evolution deviates from LHFM predictions with shorter fracture lengths, larger widths and net pressures. These deviations from LHFM ultimately decrease at late times ($t \gg t_{cm}$) as the ratios of the lag and cohesive zone sizes with the fracture length both become smaller. The deviations increase with larger dimensionless toughness and larger σ_o/σ_c ratio, as both have the effect of further localizing viscous dissipation near the fluid front located in the small rough cohesive zone. The convergence toward LHFM can occur at very late time compared to the nucleation time-scale t_{cm} (by a factor of hundred to thousand times) for realistic values of σ_o/σ_c encountered at depth. The impact of a rough cohesive zone appears to be prominent for laboratory experiments and short in-situ injections in quasi-brittle rocks with ultimately a larger energy demand compared to LHFM predictions.

This chapter is a modified version of the following scientific article:

Liu, D., Lecampion, B. (2021), Propagation of a plane-strain hydraulic fracture accounting for a rough cohesive zone, *Journal of the Mechanics and Physics of Solids*,104322.

Authors contributions

D. Liu and B. Lecampion have formulated the problem and performed the dimensional analysis. D. Liu has developed the numerical scheme and validated the numerical solver with linear elastic solutions. Under the guidance of B. Lecampion, D. Liu has visualized and analyzed the numerical results. D. Liu and B. Lecampion have written the manuscript.

4.1 Introduction

The growth of a hydraulic fracture (HF) in an impermeable linear elastic solid is now relatively well understood, in particular the competition between the energy dissipated in the creation of new fracture surfaces and the one dissipated in viscous fluid flow. Such a competition leads to distinct propagation regimes depending on the main dissipative mechanism (Detournay, 2016). Linear elastic fracture mechanics (LEFM) combined with lubrication theory (linear hydraulic fracture mechanics - LHFM for short) have successfully predicted experimental observations for the growth of a simple planar fracture in model materials such as PMMA and glass (Bunger and Detournay, 2008; Lecampion et al., 2017; Xing et al., 2017). However, some observations on rocks at the laboratory (Thallak et al., 1993; Van Dam and de Pater, 1999) and field scales (Shlyapobersky, 1985; Shlyapobersky et al., 1988) are not consistent, and some indicate that linear hydraulic fracture mechanics (LHFM) underestimates the observed fluid pressure and overestimates the fracture length. These observations hint toward a possibly larger energy demand compared to LHFM predictions and challenge two of its basic assumptions: i) fracture process governed by LEFM and ii) lubrication flow between two smooth parallel surfaces resulting in Poiseuille's law. A non-linear process zone always exists in the vicinity of the fracture tip (Fig. 4.1). This is especially true for quasi-brittle materials like rocks. The stresses are capped by a finite peak strength in the fracture process zone while the aperture roughness is no longer negligible and decreases the fracture permeability. How such non-linearities affect the solid-fluid coupling inside the fracture and as a result its growth is the main goal of this chapter. We focus on the propagation of a plane-strain hydraulic fracture from nucleation to the late stages of growth where the process zone is inherently much smaller than the fracture length.

A number of previous investigations have dealt with the relaxation of the LEFM assumption on HF growth: either using theories accounting for bulk plastic dissipation around the tip (Papanastasiou, 1997, 1999; Papanastasiou and Atkinson, 2006; Sarris and Papanastasiou, 2013), or with an increasing apparent fracture toughness with length embedding different toughening mechanisms (Liu et al., 2019b), or/and adopting cohesive zone models (CZM) as
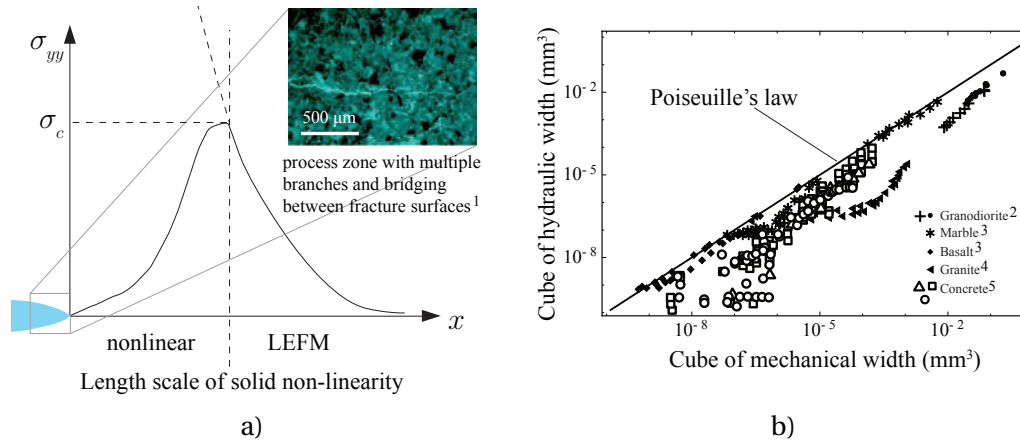
Figure 4.1 – Illustration of a) the length scale of solid non-linearity and b) deviated fluid flow from Poiseuille's law (cubic law). Figure b) is adapted from figure 5 in Renshaw (1995) with additional data. The superscripts indicate the source of the image in figure a) 1. Lhomme (2005), and the source of the data in figure b): 2. Schrauf and Evans (1986); 3. Witherspoon et al. (1980); 4. Raven and Gale (1985); 5. Garagash (2015a); Breysse and Gérard (1997).

a propagation criterion (see Lecampion et al. (2018) for review). Among these approaches, cohesive zone models are the most widely used due to their simplicity: the fracture growth is simply tracked via a cohesive traction-separation law. Studies of hydraulically driven fracture using CZM (Chen et al., 2009; Chen, 2012; Lecampion, 2012; Yao et al., 2015) all show that the numerical solutions can be well approximated with LEFM/LHFM solutions. However these conclusions just follow from the fact that these simulations fall in the small-scale-yielding limit where the cohesive zone only takes up a small fraction of the whole fracture. In addition, in all these contributions, the existence of a fluid lag is neglected as well as the effect of roughness on flow. The assumption of a negligible fluid lag is often claimed to be valid for sufficiently deep fractures (where the confining stress is large) on the basis of the LHFM results.

However, the existence of a fluid lag is to lubrication flow what the process zone is to fracture mechanics. It removes the negative fluid pressure singularities at the fracture tip associated with suction resulting from the elasto-hydrodynamics coupling (Desroches et al., 1994; Garagash and Detournay, 2000). In fact, the presence of a fluid lag is necessary if accounting for the presence of a cohesive zone in order to ensure that the stresses remain finite. Rubin (1993) has pioneered studies accounting for a cohesive zone and a fluid lag by investigating the stress field around a plane-strain HF. The obtained results are, however, restricted to the particular case where the fluid lag is always larger than the cohesive zone. Rubin (1993) argues that the fluid lag increases with the fracture length and thus possibly influences the off-plane inelastic deformation. Recently, Garagash (2019) has derived the complete solution of a steadily moving semi-infinite smooth cohesive fracture with a fluid lag. The results demonstrate the strong influence of the ratio between the minimum in-situ compressive stress and the material peak cohesive stress σ_o/σ_c on the near tip asymptotes. Such a semi-infinite fracture solution is

obviously valid only when the process zone has fully nucleated and is smaller than the fracture length. These investigations assume smooth fracture surfaces in the cohesive zone (and thus Poiseuille's law). The effect of roughness on the interplay between the fluid front and cohesive zone growth still calls for further investigation.

In this chapter, we investigate the growth of a finite plane-strain hydraulic fracture from nucleation to the late stage of growth accounting for the presence of both a cohesive zone and a fluid lag. We also investigate the impact of a decreased hydraulic conductivity in the rough cohesive zone using existing phenomenological approximations. After a description of the model, we discuss the overall structure of the solution thanks to a scaling analysis. We then explore the coupled effect of the fluid lag, cohesive zone and roughness numerically using a specifically developed numerical scheme. We then discuss implications for the HF growth both at the laboratory and field scales.

4.2 Problem Formulation

We consider a plane-strain hydraulic fracture of half-length ℓ propagating in an infinite homogeneous impermeable quasi-brittle isotropic medium (Fig. 4.2). We denote σ_o as the minimum in-situ compressive stress acting normal to the fracture plane. The fracture growth occurs in pure tensile mode and is driven by the injection of an incompressible Newtonian fluid at a constant rate Q_o in the fracture center. We account for both the existence of a cohesive zone (of length ℓ_{coh}) and a fluid-free cavity (of length $\ell - \ell_f$) near the tips of the propagating fracture as described in Fig. 4.2.
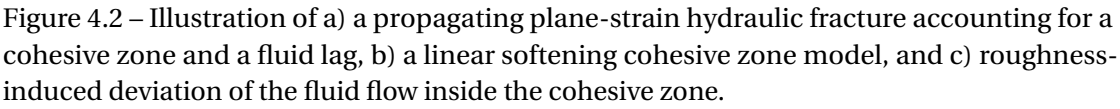
4.2.1 Solid mechanics

Cohesive zone model

We adopt for simplicity a linear-softening cohesive zone model to simulate the fracture process zone, where cohesive traction decreases linearly at the tip from the peak cohesive stress σ_c to zero at a critical aperture w_c, as illustrated in Fig. 4.2. Such a traction separation law can be simply written as:

$$\sigma_{coh}(w) = \begin{cases} \sigma_c(1 - w_c) & 0 \leq w < w_c \\ 0 & w > w_c \end{cases} \tag{4.1}$$

where σ_c is the material peak strength (the maximum cohesive traction). The length of the cohesive zone ℓ_{coh} is given by the distance from the fracture tip where the critical opening is reached: $w(\ell_{coh}) = w_c$. For such a linear weakening model, the fracture energy is given by:

$$G_c = \frac{1}{2}\sigma_c w_c \tag{4.2}$$

Figure 4.2 – Illustration of a) a propagating plane-strain hydraulic fracture accounting for a cohesive zone and a fluid lag, b) a linear softening cohesive zone model, and c) roughness-induced deviation of the fluid flow inside the cohesive zone.

Note that in linear elastic fracture mechanics in pure mode I, the fracture energy is related to the material fracture toughness K_{Ic} by Irwin's relation for co-planar growth $G_c^{LEFM} = K_{Ic}^2/E'$, where E' is the plane-strain elastic modulus. Equalizing the quasi-brittle fracture energy with the LEFM expression allows to define an equivalent fracture toughness $K_{Ic} = \sqrt{G_c E'}$ thus allowing comparison with known results for HF growth under the LEFM assumption.

Elastic deformation

For a purely tensile plane-strain fracture, in an infinite elastic medium, the quasi-static balance of momentum reduces to the following boundary integral equation (see for example Hills et al. (1996)):

$$\frac{E'}{4\pi} \int_{-\ell}^{\ell} \frac{\partial w(x', t)}{\partial x'} \frac{\mathrm{d}x'}{x - x'} = p_f(x, t) - \sigma_o - \sigma_{coh}(w(x, t)), \quad x, x' \in [-\ell, \ell] \tag{4.3}$$

where $E' = E/(1 - v^2)$ is the plane-strain modulus, v the Poisson's ratio of the material. In view of the problem symmetry, the previous integral equation can be conveniently written for on one-wing of the fracture:

$$\frac{E'}{4\pi} \int_0^{\ell} \left(\frac{1}{x - x'} - \frac{1}{x' + x} \right) \frac{\partial w(x', t)}{\partial x'} \mathrm{d}x' = p_f(x, t) - \sigma_o - \sigma_{coh}(w(x, t)), \quad x, x' \in [0, \ell] \tag{4.4}$$

Due to the presence of cohesive forces and the traction separation law, this boundary integral equation is non-linear.

Using a cohesive zone model, the fracture advance $\ell(t)$ is based on the stress component σ_{yy} perpendicular to the fracture plane ahead of the current fracture tip. In other words, the fracture propagates when

$$\sigma_{yy}(x = \ell) = \sigma_c \tag{4.5}$$

It is worth pointing out that at any given time, the cohesive forces cancel the stress singularity at the fracture tip that would be otherwise present. The stress intensity factor K_I must thus be zero at all times. For a pure mode I crack, the stress intensity factor is obtained via the weight function approach directly from the profile of the net loading (Bueckner, 1970; Rice, 1972):

$$K_I = \frac{2\sqrt{\ell}}{\sqrt{\pi}} \int_0^{\ell} \frac{p_f(x, t) - \sigma_o - \sigma_{coh}(w(x, t))}{(\ell^2 - x^2)^{1/2}} \, \mathrm{d}x = 0 \tag{4.6}$$

The requirement $K_I = 0$ can be altenatively used as a propagation condition, or checked a posteriori as an error estimate.

4.2.2 Laminar lubrication flow in a rough tensile fracture

Under the lubrication approximation, for an incompressible fluid and an impermeable medium (negligible leak-off), the fluid mass conservation in the deformable fracture reduces

to

$$\frac{\partial w}{\partial t} + \frac{\partial q}{\partial x} = 0 \text{ in the fluid filled part } x \in [0, \ell_f] \qquad (4.7)$$

where $q(x, t)$ is the local fluid flux inside the fracture and $\ell_f(t)$ denotes the current fluid front position.

As the aperture is small near the tip and especially in the cohesive zone, it can not be considered as much larger than its small scale spatial variation - i.e. its roughness. The rough surfaces in possibly partial contact in the cohesive zone results in a decrease of the hydraulic transmissivity of the fracture compared to the cubic law. This has been observed in a large number of flow experiments under laminar condition in rock joints under different normal stress (Fig. 4.1). A number of empirical approximations have been put forward in literature to describe such a deviation from the cubic Poiseuille's law observed in the laminar regime. A typical approach consists in introducing a friction/correction factor f in Poiseuille's law relating fluid flux to the pressure gradient:

$$q = -\frac{w^3}{\mu' f} \frac{\partial p_f}{\partial x}, \qquad 0 < x < \ell_f, \quad f = 1 + \alpha_c \times \left(\frac{w_R}{w}\right)^{\alpha_e} \qquad (4.8)$$

where $\mu' = 12\mu$ is the effective fluid viscosity. w_R quantifies the fracture roughness, and is for example, taken as the peak asperity height or the standard deviation of the aperture (see Table. 4.1). It grasps the width scale characterizing the deviation from the cubic law. α_c and α_e are experimentally determined parameters dependent on the fractal properties of the self-affine rough fracture surfaces (Talon et al., 2010; Jin et al., 2017). Interestingly, the fracture roughness properties are also related to the size of the process zone, above and below which the off-plane height variation may present different roughness exponents (Mourot et al., 2005; Bonamy et al., 2006; Ponson et al., 2007; Morel et al., 2008). Moreover, a process zone length scale can be extracted from the spatial correlations of the slopes of a rough fracture surface (Vernède et al., 2015). Fracture roughness therefore appears to correlate with both the process zone w_c and the fluid flow deviation w_R width scales, yet the exact relation between w_c and w_R has not been clearly deciphered to our knowledge. On the account that w_R and $w_c \sim 1 - 500\mu$m in most rocks (Renshaw, 1995; Garagash, 2015a, 2019), we assume $w_R \approx w_c$. One has to note, that α_c and α_e are fitted from experiments and α_c is not independent of the choice of w_R - $\alpha_c \times w_R^{\alpha_e}$ is the controlling constant when expanding Eq. (4.8). α_e governs the power-law dependence of the friction factor with the mechanical width w. The number of experiments dedicated to flow in rough fractures provide a guideline for α_c and α_e although a significant scatter can be observed (see Table. 4.1). In the following, we assume $\alpha_c = 1$ (and $w_R = w_c$) for simplicity in order to investigate the mechanism associated with fracture roughness although we recognize that it may not be the case. The friction factor therefore reduces to

$$f = 1 + \left(\frac{w_c}{w}\right)^{\alpha_e} \qquad (4.9)$$

where $\alpha_e = 0$ in the smooth fracture limit. For the case of a rough fracture, we will perform simulations for $\alpha_e = 2$ which corresponds to the largest power-law exponent reported exper-

w_R definition	Reference	α_e	α_c	w_R (μm)
Standard deviation of the aperture	Renshaw (1995) [*]	2	1.5	Basalt (1.6), marble (13) granite (0.63-320), granodiorite (500)
	Zimmerman and Bodvarsson (1996) [*]	2	1.5	Granite (34-295)
	Garagash (2015a)	1	1	Concrete (150)
Peak asperity height	Lomize (1951)	1.5	6.0	Sand-coated glass
	Zhang et al. (2015)	1.12	10^{-3}	Granite (2320-3140), limestone (4050)

Table 4.1 – Different empirical models suggested in literature for the friction factor (Eq. (4.8)). The superscript [*] indicates that the expression of the friction factor reported does not exactly correspond to the functional form of Eq. (4.8). As a result, for those cases, we obtain α_c, α_e from the two leading terms of a Taylor expansion of the reported expression.

imentally (and as such will lead to the largest impact of fracture roughness). The resulting deviation between mechanical and hydraulic aperture for such a simplified fluid flow deviation model (4.9) is illustrated in Fig. 4.2.

4.2.3   Boundary and initial conditions

The fluid is injected at the fracture center at a constant injection rate Q_o (in m^2/s under plane-strain conditions), such that the flow entering one-wing of the fracture is:

$$q(x = 0^+, t) = Q_o/2 \tag{4.10}$$

which can be alternatively be accounted by the global fluid volume balance, integrating the continuity equation (4.7) for the fluid:

$$2 \int_0^{\ell_f(t)} w(x,t)\mathrm{d}x = Q_o t \tag{4.11}$$

In the fluid lag near the fracture tip, the fluid is vaporized and its pressure is equal to the cavitation pressure p_{cav}, which is typically much smaller than the liquid pressure p_f in the fluid filled part and the in-situ confining stress σ_o. We thus have the following pressure boundary condition in the lag:

$$p_f(x, t) = p_{cav} \approx 0, \quad x \in [\ell_f(t), \ell(t)] \tag{4.12}$$

The fluid front velocity $\dot{\ell}_f$ is equal to the mean fluid velocity q/w at that fluid front location $x = \ell_f$ (Stefan condition):

$$\dot{\ell}_f = -\frac{w^2}{\mu' f(w)} \frac{\partial p_f}{\partial x}\bigg|_{x=\ell_f} \tag{4.13}$$

The fracture opening is zero at the fracture tip taken as the beginning of the cohesive zone:

$$w(x = \ell, t) = 0 \tag{4.14}$$

Initial conditions We model the nucleation process, and the coupled developments of the cohesive zone and the fluid lag. We start from a negligibly small fracture in which cohesive forces have not completely vanished: the fracture length equals the cohesive zone length initially. Upon the start of injection, this initially static flaw is fully filled with fluid at a pressure slightly larger than the in-situ stress σ_o.

4.2.4 Energy balance

The energy balance for a propagating hydraulic fracture can be constructed by combining two separate energy balance equations, one for the viscous fluid flow and the other one for the quasi-brittle medium deformation of an advancing crack (Lecampion and Detournay, 2007). The external power $P_e = Q_o p_{f0}$ (where $p_{f0} = p_f(x = 0, t)$ is the fluid pressure at the inlet) provided by the injecting fluid is balanced by five terms:

- the rate of work done to overcome the in-situ confining stress: $\dot{W}_o = Q_o \sigma_o$

- the rate of change of the elastic energy stored in the solid $\dot{W}_e$:

$$\dot{W}_e = \int_0^{\ell_f} p \frac{\partial w}{\partial t} dx + \int_0^{\ell_f} w \frac{\partial p}{\partial t} dx - \sigma_o \int_{\ell_f}^{\ell} \frac{\partial w}{\partial t} dx \tag{4.15}$$

- a power associated with the rate of the change of the fluid lag cavity volume times the in-situ far-field stress $\dot{W}_l$:

$$\dot{W}_l = 2\sigma_o \frac{d}{dt} \int_{\ell_f}^{\ell} w dx \tag{4.16}$$

- the viscous dissipation rate in the fluid filled region of the fracture D_v:

$$D_v = -2 \int_0^{\ell_f} q \frac{\partial p}{\partial x} dx \tag{4.17}$$

- the energy rate associated with the debonding of cohesive forces and the creation of new fracture surfaces D_k:

$$D_k = -\int_0^{\ell} w \frac{\partial \sigma_{coh}}{\partial t} dx + \int_0^{\ell} \sigma_{coh} \frac{\partial w}{\partial t} dx. \tag{4.18}$$

Accounting for the symmetry of the problem, we can define an apparent fracture energy

$$G_{c,app} = \frac{D_k}{2\dot{\ell}} \tag{4.19}$$

In the coordinate system of the moving tip, we can rewrite Eq. (4.19) for the linear weakening cohesive zone model as follows (see more details in Supplemental Materials):

$$G_{c,app} = \frac{1}{2}\sigma_c w(\hat{x} = \ell_{coh}) + \frac{1}{2\dot{\ell}}\sigma_c \int_0^{\ell_{coh}} \frac{\partial w}{\partial t}\bigg|_{\hat{x}} d\hat{x}, \quad \hat{x} = \ell - x \qquad (4.20)$$

When the fracture has already nucleated and the cohesive zone size is negligible compared to the fracture length ($\ell \gg \ell_{coh}$), the first term in Eq. (4.20) equals the real fracture energy G_c with $w(\hat{x} = \ell_{coh}) = w_c$. For a large fracture, where the cohesive zone is nearly constant, the second term tends to zero as the material time derivative of width is negligible for fracture with slow variation of velocity: more precisely, in the tip reference frame the convective derivative $\dot{\ell}\frac{\partial \cdot}{\partial \hat{x}}$ (which leads when integrated to the first term) dominates over the material time derivative $\frac{\partial \cdot}{\partial t}|_{\hat{x}}$. As a result, the apparent energy tends to equal to the real fracture energy $G_{c,app} \approx G_c$ at large time. However, it does not necessarily imply that the fracture width asymptote in the near tip region follows the LEFM limit. It only results from the fact that the convective derivative dominates - and as such the travelling semi-infinite fracture solution of Garagash (2019) applies (where different tip asymptotes emerge as function of the ratio σ_o/σ_c). However the equivalence $G_{c,app} = G_c$ does not hold when the fracture length is comparable to the cohesive zone $\ell \geq \ell_{coh}$. The first term increases with time until $w(\hat{x} = \ell_{coh})$ reaches the critical opening w_c at nucleation while the second term results from the competition between the fracture velocity and the material rate change of the volume embedded inside the cohesive zone. As a result of this second term, the evolution of the apparent fracture energy may not be necessarily monotonic in an intermediate phase as we shall see later from our numerical simulations.

4.3 Structure of the solution

Before investigating the problem numerically, we discuss the evolution of such a quasi-brittle HF in light of dimensional analysis. We notably highlight the difference brought upon the existence of a process zone compared to the linear elastic fracture mechanics case (Garagash and Detournay, 2005; Garagash, 2006b; Lecampion and Detournay, 2007). Following previous work on hydraulic fracturing (Garagash, 2000; Detournay, 2004), we scale the flux q with the injection rate Q_o, and scale the fracture width w, net pressure $p_f - \sigma_o$, fracture length ℓ, and the extent of the liquid filled part of the fracture ℓ_f introducing corresponding width W, pressure P, fracture length L and fluid extent L_f characteristic scales as:

$$w(x,t) = W(t)\Omega(\xi,\mathscr{P}), \quad p_f(x,t) - \sigma_o = P(t)\Pi(\xi,\mathscr{P}), \quad q(x,t) = Q_o\Psi(\xi,\mathscr{P}) \qquad (4.21)$$

$$\ell(t) = L(t)\gamma(\mathscr{P}), \quad \ell_f(t) = L_f(t)\gamma_f(\mathscr{P}) \qquad (4.22)$$

where $\xi = x/\ell$ is a dimensionless coordinate. The dimensionless variables also depend on one or more dimensionless number $\mathscr{P}$ (which may depend on time). Introducing such a scaling in the governing equations of the problem allows to isolate different dimensionless

groups associated with the different physical mechanisms at play (elasticity, injected volume, viscosity, fracture energy) and define relevant scalings.

Before going further, we briefly list the dimensionless form of the governing equations and the expression of the different dimensionless groups appearing in the governing equations (4.1)-(4.14).

- The elasticity equation can be re-written as:

$$\Pi - \Sigma_{coh}(\Omega(\xi)) = \mathcal{G}_e \frac{1}{4\pi} \frac{1}{\gamma} \int_0^1 \frac{\partial \Omega}{\partial \xi} \left(\frac{1}{\xi - \xi'} - \frac{1}{\xi + \xi'} \right) d\xi', \quad 0 < \xi, \xi' < 1 \tag{4.23}$$

  with $\mathcal{G}_e = \dfrac{WE'}{PL}$ and the dimensionless traction-separation law as

$$\Sigma_{coh} = \mathcal{G}_t \times \left(1 - \frac{\Omega}{\mathcal{G}_w} \right), \quad \Omega < \mathcal{G}_w \tag{4.24}$$

  with $\mathcal{G}_t = \sigma_c/P$ and $\mathcal{G}_w = w_c/W$.

- The dimensionless fluid continuity and roughness corrected Poiseuille's law are better expressed by scaling the spatial coordinate with the fluid front position - thus introducing the ratio of scales $\mathcal{G}_l = L_f/L$ - $\hat{\xi} = x/\ell_f = \xi \times (\gamma/\gamma_f)/\mathcal{G}_l$:

$$t \frac{\partial \Omega}{\partial t} + t \frac{\dot{W}}{W} \Omega + \mathcal{G}_v \frac{1}{\gamma_f} \frac{\partial \Psi}{\partial \hat{\xi}} = 0 \tag{4.25}$$

$$\Psi = -\frac{1}{\mathcal{G}_m} \frac{\Omega^3}{f \times \gamma_f} \frac{\partial \Pi}{\partial \hat{\xi}} \tag{4.26}$$

  with $\mathcal{G}_v = \dfrac{Q_o t}{WL_f}$ related to the fracture volume, and $\mathcal{G}_m = \dfrac{\mu' Q_o L_f}{PW^3}$ related to fluid viscosity, while the friction roughness correction f can be simply re-written as $f = 1 + (\mathcal{G}_w/\Omega)^{\alpha_e}$.

- the entering flux boundary condition becomes

$$\Psi(\xi = 0^+, t) = 1/2 \tag{4.27}$$

  while the dimensionless net pressure Π in the fluid lag is

$$\Pi(\xi \leq \xi_f = \ell_f/\ell) = -\mathcal{G}_o = -\frac{\sigma_o}{P} \tag{4.28}$$

It is worth noting that for the linear weakening law the dimensionless fracture energy is simply $\mathcal{G}_c = (w_c \sigma_c)/(2PW) = \frac{1}{2} \mathcal{G}_w \mathcal{G}_t$. In addition, in order to make the link with the LEFM scalings that use a reduced fracture toughness defined as $K' = \sqrt{32/\pi} K_{Ic}$, we use the equivalent dimensionless fracture toughness: $\mathcal{G}_k = \sqrt{32/\pi} \sqrt{\mathcal{G}_e \mathcal{G}_c} = \sqrt{16/\pi} \sqrt{\mathcal{G}_e \mathcal{G}_w \mathcal{G}_t}$ in the following.

The well-known scalings under the LHFM assumptions for the case of negligible lag ($\mathcal{G}_l = L_f/L = 1$) are obtained by recognizing that elasticity is always important ($\mathcal{G}_e = 1$), and the fact that without fluid leak-off the fracture volume equals the injected volume at all time ($\mathcal{G}_v = 1$). The viscosity and toughness scalings are then obtained by either setting $\mathcal{G}_m$ (M/viscous scaling) or $\mathcal{G}_k$ (K/toughness scaling) to unity. Alternatively, the fluid lag dominated scaling (O-vertex) is obtained by recognizing that viscous effects are necessary for cavitation to occur ($\mathcal{G}_m = 1$) and the lag covers a significant part of the fracture such that the pressure scale is given by the in-situ stress ($\mathcal{G}_o = 1$). Similarly elasticity ($\mathcal{G}_e = 1$) and fluid volume ($\mathcal{G}_v = 1$) are driving mechanisms. These well-known scalings for the different limiting propagation regimes are recalled in Table 4.2.

Under the assumption of linear elastic fracture mechanics, as discussed in Garagash (2006b); Lecampion and Detournay (2007), a plane-strain HF evolves from an early-time solution where the fluid lag is maximum to a late solution where the fluid and fracture front coalesces (zero lag case) over a time-scale

$$t_{om} = \frac{E'^2 \mu'}{\sigma_o^3} \qquad (4.29)$$

This time-scale directly emerges as the time it takes for the dimensionless in-situ stress $\mathcal{G}_o$ to reach unity in the zero lag scalings. In addition, the solution also depends on a dimensionless toughness $\mathcal{K}_m$ (or alternatively dimensionless viscosity) independent of time. The fluid lag is the largest for small dimensionless toughness and is negligible at all time for large dimensionless toughness. The propagation can thus be illustrated via a triangular phase diagram, whose three vertices (O-M-K) corresponds to three limiting regimes. The O-vertex corresponds to the limiting case of a large lag / negligible toughness, the M-vertex corresponds to viscosity dominated propagation with a negligible fluid lag while the K-vertex corresponds to a toughness dominated propagation where viscous effects are always negligible and as a result no fluid lag exists.

The introduction of a cohesive zone modifies partly this propagation diagram. One can define a cohesive zone scaling (which will be coined with the letter C) by setting the pressure scales P to the peak cohesive stress σ_c ($\mathcal{G}_t = 1$), the opening scale W to the critical opening w_c ($\mathcal{G}_w = 1$). We then readily obtain from elasticity ($\mathcal{G}_e = 1$) that the fracture characteristic length L equals the classical cohesive characteristic length scale (Rice, 1968; Hillerborg et al., 1976):

$$L_{coh} = \frac{E' w_c}{\sigma_c} \qquad (4.30)$$

Such a scaling is relevant at early time when the cohesive zone scale is of the order of the fracture length. We know from the LHFM limit that the fluid lag is also important at early time. From lubrication flow, combining fluid continuity and Poiseuille's law to obtain the Reynolds equation enables to define the corresponding fluid front scale L_f as $w_c\sqrt{\sigma_c t/\mu'}$ (by setting the resulting dimensionless group $\mathcal{G}_v/\mathcal{G}_m$ in the Reynolds equation to one). Another time-scale t_{cm} thus emerges as the characteristic time for which the fluid front in that cohesive scaling is

of the same order of magnitude than the characteristic fracture / cohesive length:

$$t_{cm} = \frac{E'^2 \mu'}{\sigma_c^3} = t_{om} \times \left(\frac{\sigma_o}{\sigma_c}\right)^3 . \tag{4.31}$$

This time-scale quantifies the time required for the cohesive zone to develop in relation to the penetration of the fluid. It is worth noting that the ratio of time-scales t_{cm}/t_{om} related to the fluid lag in the cohesive (C) and LHFM (O) scalings is directly related to the ratio between the in-situ confining stress and the peak cohesive stress.

Three stages of growth can thus be delineated as function of the evolution of the cohesive zone.

- Stage I for early time ($t \ll t_{cm}$): the whole fracture length is embedded inside the cohesive zone. The cohesive zone develops with time yet is not fully nucleated. We will refer to this stage as the nucleation stage in the following.

- Stage II for intermediate times (of the order of t_{cm}): the cohesive zone has now fully nucleated and part of the fracture surfaces are completely separated without cohesion ($w > w_c$ in the central part of the fracture). The cohesive zone remains important compared to the whole fracture length and may be not yet stabilized. We will refer to this stage as the intermediate propagation stage.

- Stage III ($t \gg t_{cm}$): the cohesive zone now only takes up a very small fraction of the whole fracture such that the small-scale-yielding assumption becomes valid. We will refer to this stage as the late time propagation stage/small-scale-yielding stage.

From the different scalings in Table 4.2, we see that using t_{cm} as a characteristic time-scale, the evolution of a HF in a quasi-brittle material depends only on i) a dimensionless toughness $\mathcal{K}_m$, ii) the ratio between the confining stress and material strength σ_o/σ_c and iii) the dimensionless roughness exponent α_e. Possibly, a value different than unity for the coefficient α_c in relation to the flow-roughness relationship (4.8) would also play a role.

For a quasi-brittle impermeable material, the propagation can be schematically grasped by the propagation diagram depicted on Fig. 4.3. The propagation starts in a cohesive / nucleation regime (vertex C) and ultimately ends up at large time on the M-K edge (LHFM / small-scale-yielding limit) at a point depending on the (time-independent) dimensionless toughness $\mathcal{K}_m$. How the fracture evolves from the nucleation (vertex C) stages to the large time LHFM limits is function of the ratio σ_o/σ_c as well as the roughness exponent. When $\sigma_o \ll \sigma_c$ ($t_{cm} \ll t_{om}$), the cohesive zone develops faster than the time required for the fluid front to coalesce with the fracture front. In that case, the small-scale-yielding assumption may become valid early in conjunction with the presence of a fluid lag (O-K edge) - the fluid front will lie outside of the cohesive zone for some time. On the other limit, for $\sigma_o > \sigma_c$, the fluid front tends to remain inside the cohesive zone which develops slower than the fluid front progress.

	C	O	M	K
L	$L_{coh} = \dfrac{E' w_c}{\sigma_c}$	$\dfrac{E' Q_o^{1/2} \mu'^{1/4} t^{1/4}}{\sigma_o^{5/4}}$	$\dfrac{E'^{1/6} Q_o^{1/2} t^{2/3}}{\mu'^{1/6}}$	$\dfrac{E'^{2/3} Q_o^{2/3} t^{2/3}}{K'^{2/3}}$
P	σ_c	σ_o	$\dfrac{E'^{2/3} \mu'^{1/3}}{t^{1/3}}$	$\dfrac{K'^{4/3}}{E'^{1/3} Q_o^{1/3} t^{1/3}}$
W	w_c	$\dfrac{Q_o^{1/2} \mu'^{1/4} t^{1/4}}{\sigma_o^{1/4}}$	$\dfrac{Q_o^{1/2} \mu'^{1/6} t^{1/3}}{E'^{1/6}}$	$\dfrac{K'^{2/3} Q_o^{1/3} t^{1/3}}{E'^{2/3}}$
L_f/L	$(t/t_{cm})^{1/2}$	$(t/t_{om})^{1/2}$	1	1
$\mathscr{G}_m$	$(16/\pi)^2 \mathscr{K}_m^{-4} (t/t_{cm})^{1/2}$	1	1	$\mathscr{K}_m^{-4}$
$\mathscr{G}_k$	$(16/\pi)^{1/2}$	$\mathscr{K}_m = \dfrac{K'}{E'^{3/4} Q_o^{1/4} \mu'^{1/4}}$	$\mathscr{K}_m$	1
$\mathscr{G}_o$	σ_o/σ_c	1	$(t/t_{om})^{1/3}$	$(t/t_{om})^{1/3} \mathscr{K}_m^{-4/3}$
$\mathscr{G}_w$	1	$\left(\dfrac{t_{cm}}{t}\dfrac{\sigma_o}{\sigma_c}\right)^{1/4} \dfrac{\pi}{16}\mathscr{K}_m^2$	$\left(\dfrac{t_{cm}}{t}\right)^{1/3}\dfrac{\pi}{16}\mathscr{K}_m^2$	$\left(\dfrac{t_{cm}}{t}\right)^{1/3}\dfrac{\pi}{16}\mathscr{K}_m^{4/3}$

Table 4.2 – Characteristic scales and dimensionless numbers governing the evolution of a plane-strain quasi-brittle HF in the different limiting regimes: C - lag/cohesive/nucleation, O - lag/viscous/ LHFM, M - fully filled/viscous/LHFM, K - fully filled/toughness/LHFM. The evolution of the HF is also function of the dimensionless roughness exponent α_e. The time-scales t_{om} and t_{cm} defined in Eqs (4.29), (4.31) are related as $t_{cm}/t_{om} = (\sigma_o/\sigma_c)^3$. The $16/\pi$ factors appearing in the dimensionless numbers are due to the use of $K' = \sqrt{32/\pi}K_{Ic}$ in the LHFM based scalings (Detournay, 2004; Garagash, 2006b) and the fact that for the linear weakening cohesive law $G_c = w_c\sigma_c/2$.

How exactly, the growth of the HF is influenced by the interplay between the cohesive zone and lag evolution for different values of σ_o/σ_c, dimensionless toughness and fracture roughness intensity will be now investigated numerically.

4.4   Numerical scheme

In order to decipher the interplay between the fluid front and cohesive zone, it is necessary to account for the nucleation of both the cohesive zone and the fluid lag. Previous numerical investigation using LHFM either tracks explicitly the fluid front in addition to the fracture front (Lecampion and Detournay, 2007; Zhang et al., 2005; Gordeliy and Detournay, 2011b) or uses a cavitation algorithm introducing a fluid state variable $\theta \in [0, 1]$ (1 for the liquid phase, 0 for the vapour phase) (Shen, 2014; Mollaali and Shen, 2018) in a similar way than thin-film lubrication cavitation models (see for example Szeri (2010)).

The cavitation approach enables the spontaneous nucleation of the fluid lag but adds another variables and additional inequalities conditions ($p_f \geq 0$, $0 \leq \theta \leq 1$, $p_f(1 - \theta) = 0$) in each element. The computational cost of such cavitation schemes increases significantly as quadratic programing problem needs to be solved at each time-step. We therefore propose here an algorithm taking advantage of both the cavitation scheme at early time (when the fluid lag nucleates from an initially fully liquid filled flaw) and a fluid-front-tracking scheme at later
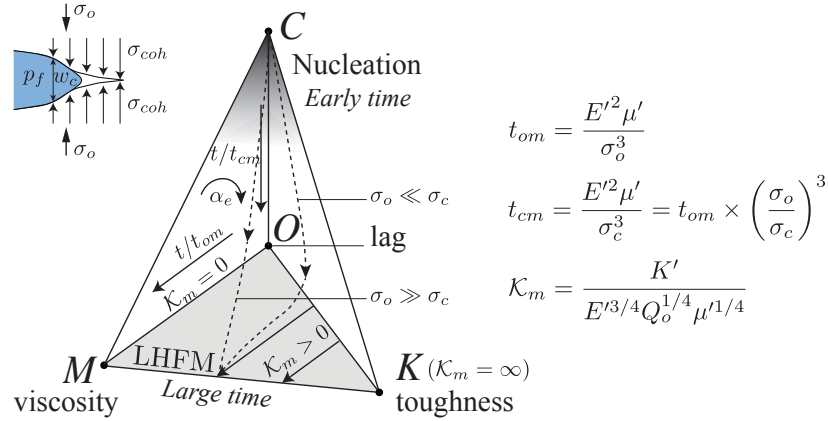
Figure 4.3 – Propagation diagram of a plane-strain hydraulic fracture with a rough cohesive fracture tip. The bottom $O - M - K$ triangle corresponds to the LHFM limit. Note that possibly, a value of α_c (see Eq. (4.8)) different than unity will impact the solution.

times.

Our algorithm consists of the use of two successive schemes, both based on a fixed regular grid with constant mesh size. At the beginning of the simulation, we adopt an Elrod-Adams type scheme similar to the one described in Mollaali and Shen (2018). This scheme automatically captures the appearance of the fluid lag in the most accurate manner (Liu and Lecampion, 2019). In a second stage of the simulation, we use the results of the previous algorithm to initialize a scheme similar to Gordeliy and Detournay (2011b) where the fluid front position is tracked explicitly via the introduction of a filling fraction variable in the partly filled element at the lag boundary. We discretize respectively the elasticity and fluid mass conservation using a displacement discontinuity method with piece-wise constant elements and finite difference. We use an implicit time-integration scheme to solve iteratively for the fluid pressure and the associated opening. An additional outer loop solves for the time-step increment corresponding to a fixed increment of fracture length. More details are given in 4.8.

Mesh requirements A sufficient number of cohesive elements is necessary to ensure the stress accuracy ahead of the fracture tip and the resolution of the fracture propagation condition. A minimum of three elements are suggested to mesh the cohesive zone to ensure sufficient accuracy of the near tip stress field (Falk et al., 2001; Moës and Belytschko, 2002; Turon et al., 2007). In dry fracture mechanics, the technique of artificially enlarging the cohesive zone length while keeping the fracture energy constant is often used (increasing w_c and decreasing σ_c accordingly) (Bazant and Planas, 1997; Turon et al., 2007) thus allowing the use of coarser meshes. Unfortunately, such a technique is not adequate for cohesive hydraulic fractures. It is only valid when the confining σ_o is adjusted together with σ_c in order to keep the ratio of time scales t_{cm}/t_{om} unchanged (see Eq. (4.31)). If not, this will change the physics of the fluid
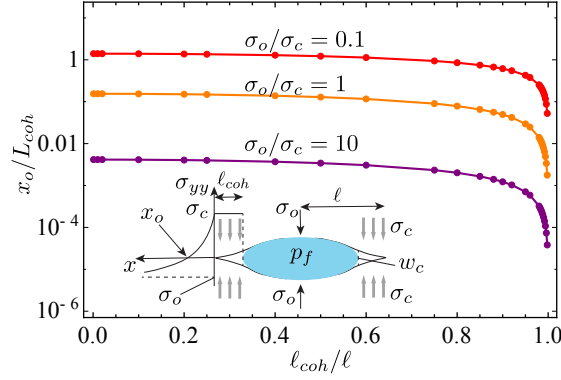
Figure 4.4 – Evolution of the size of the tensile zone ahead of the fracture tip with the cohesive fraction for different confining to peak cohesive stress ratios. The pressure is uniform everywhere inside the fracture but no fluid is allowed to enter the cohesive zone (Dugdale cohesive zone model).

front-cohesive zone coupling. Another important difference with dry fracture mechanics is the fact that the fracture propagates in a medium under initially compressive state of stresses, as such the tensile region ahead of the fracture shrinks as the confinement increases. Assuming a fluid lag the same size as the cohesive zone, Fig. 4.4 displays the evolution of the tensile zone ahead of the fracture tip as the uniformly pressurized HF grows under different confinements. The tensile zone significantly shrinks as the confining stress increases, and therefore requires for a finer mesh. Such a confinement-related mesh requirement has been seldomly discussed in previous studies (Chen et al., 2009; Chen, 2012; Sarris and Papanastasiou, 2011; Carrier and Granet, 2012; Salimzadeh and Khalili, 2015; Wang, 2015; Li et al., 2017) where the fluid front-cohesive zone coupling is often neglected (zero fluid lag, small cohesive zone) and the simulation performed under zero confinement. In this chapter, we release the confinement-related requirement by adapting the time-step for a given fixed fracture increment to fulfill the propagation stress propagation condition. We also check a posteriori that the stress intensity factor is indeed null using Eq. (4.6). We obtain an absolute error on Eq. (4.6) of about 5% (in a range between 0.1 and 8%) for all the reported simulations.

Apart from the tensile zone ahead of the fracture tip, one also needs to resolve the fluid lag which shrinks tremendously as the fracture grows but still influences the solution (Garagash, 2019). At least one partially-filled (lag) element is necessary to account for the influence of the fluid cavity on the tip stress field. At large time, the fluid lag becomes negligible compared to the cohesive zone. This is ultimately the bottle-neck governing the computational burden due to the mesh requirement of at minima one element in the fluid lag. For all the results presented in the following, we actually stop the simulations when the fluid fraction $\xi_f = \ell_f / \ell$ reached 0.99 or when the fracture length was already within five percent of the LHFM solutions.
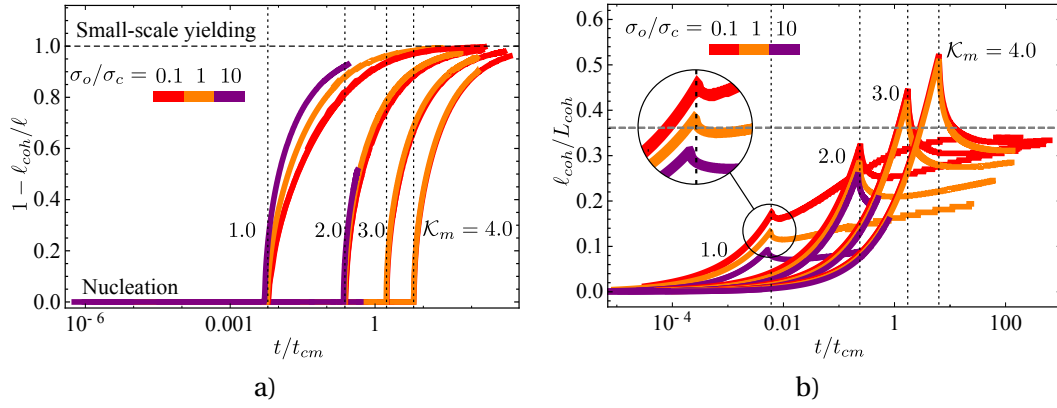
Figure 4.5 – Evolution of a) the non-cohesive fraction $1 - \ell_{coh}/\ell$ and b) dimensionless cohesive length ℓ_{coh}/L_{coh} with t/t_{cm} for $\mathcal{K}_m = 1 - 4$. The red, orange, and purple curves correspond to $\sigma_o/\sigma_c = 0.1, 1.0, 10$ respectively. The dotted vertical lines indicate the cohesive zone nucleation period for $\sigma_o/\sigma_c = 0.1$, $\mathcal{K}_m = 1 - 4$. The dashed horizontal line represents the small-scale yielding asymptote ($\approx 0.115\pi$) of the cohesive zone length for the linear-softening cohesive model (Dempsey et al., 2010).

4.5 Results

We now numerically explore the propagation diagram described in Fig. 4.3. We perform a series of simulations covering dimensionless toughness from 1 to 4 and different level of confining to peak cohesive stress ratio σ_o/σ_c from 0.1 to 10 for either a smooth ($\alpha_e = 0$) or rough ($\alpha_e = 2$) fracture. These conditions span the transition from viscosity to toughness dominated growth regimes, as well as laboratory ($\sigma_o/\sigma_c = 0.1 - 1$) and field conditions ($\sigma_o/\sigma_c = 10$).

4.5.1   A smooth cohesive fracture ($\alpha_e = 0$)

The three stages related to nucleation, intermediate and late time propagation are well visible on the time evolution of the dimensionless cohesive length (Fig. 4.5), apparent fracture energy (Fig. 4.6), fracture length (Fig. 4.9), as well as inlet width (Fig. 4.10) and net-pressure (Fig. 4.11).

Cohesive zone growth The scaled cohesive length ℓ_{coh}/L_{coh} evolves non-monotonically with time (Fig. 4.5). This evolution is dependent on both the dimensionless toughness $\mathcal{K}_m$ and σ_o/σ_c. At early time during the nucleation phase, when the fracture length is completely embedded inside the cohesive zone ($1 - \ell_{coh}/\ell = 0$), the cohesive zone increases monotonically (Fig. 4.5). We define the time t_c as the end of the nucleation phase, when here after $1 - \ell_{coh}/\ell > 0$. From our simulations, we found that t_c follows approximately an exponential relation $t_c/t_{cm} \sim \mathcal{K}_m^{5.17}$ for $\mathcal{K}_m \in [1 - 4]$. This exponent is consistent with the range of exponents in the viscosity ($t_c/t_{cm} \sim \mathcal{K}_m^6$) and toughness ($t_c/t_{cm} \sim \mathcal{K}_m^4$) dominated regimes which can be obtained by setting $\mathcal{G}_w = W/w_c = 1$ in respectively the M- and K-scaling in Table 4.2. In addition, t_c also slightly depends on the dimensionless confinement σ_o/σ_c, see the inset
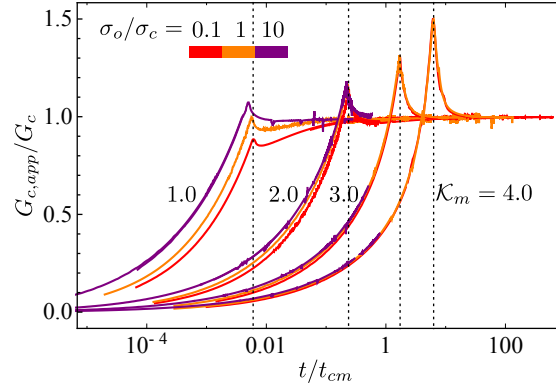
Figure 4.6 – Smooth cohesive fracture tip: evolution of the apparent fracture energy $G_{c,app}/G_c$ with t/t_{cm} for $\mathcal{K}_m = 1-4$. The red, orange, and purple curves correspond to $\sigma_o/\sigma_c = 0.1, 1.0, 10$ respectively. The dotted vertical lines indicate the cohesive zone nucleation period for $\sigma_o/\sigma_c = 0.1$, $\mathcal{K}_m = 1-4$.

on Fig. 4.5. Larger confinement slightly reduces this nucleation period for a given $\mathcal{K}_m$. The cohesive zone length at nucleation are larger for larger dimensionless toughness and then decreases with time after nucleation.

At large time, we observe that - at least for low dimensionless confinement - the cohesive zone length tends to a similar value for all dimensionless toughness. Unfortunately, this is less observable for larger dimensionless confinement which leads to prohibitive computational cost such that the simulations were stopped prior to stabilization of the cohesive zone length. However, the trend for $\sigma_o/\sigma_c = 1$ hints that a similar behavior holds for larger confinement albeit possibly much later in time.

Associated energy dissipation The energy spent in debonding cohesive forces (apparent fracture energy) increases similarly to the growth of the cohesive zone length (Fig. 4.6). This is due to the fact that $\dot{\ell} \approx \dot{\ell}_{coh}$ during the nucleation stage. Interestingly, the apparent fracture energy may even go above the fracture energy G_c at nucleation for large dimensionless toughness / large dimensionless confinement as illustrated in Fig. 4.6. At large time, the apparent fracture energy converges to the fracture energy G_c, confirming the fact that the material derivative of width (in the moving tip frame) becomes negligible in Eq. (4.20). This confirms that at large time (when $1 - \ell_{coh}/\ell \sim 1$) one can use the solution of a steadily moving semi-infinite hydraulic fracture solution accounting for cohesive forces (Garagash, 2019). However, care must be taken to use such a semi-infinite fracture solution when the cohesive zone length is of the same order than the overall fracture length. For example, the results obtained in Garagash (2019) based on the use of an equation of motion and the semi-infinite cohesive HF solution lead to cohesive zone length larger than the finite fracture length under the premises of the constant apparent fracture energy. This ultimately leads to an over-estimation of fracturing energy dissipation and larger deviation from LEFM solutions as it neglects the evolution of the

apparent fracture energy associated with the nucleation phase.

Comparisons with linear hydraulic fracture mechanics (LHFM) The time evolution of dimensionless fracture length (scaled by the viscosity dominated LHFM growth length scale $L_m(t)$ - see Table. 4.2) is displayed as dashed curves on Fig. 4.9. The corresponding inlet net-pressure and width evolution for the smooth cohesive zone are displayed as dashed curves on Fig. 4.10 and 4.11 respectively. Our results indicate that the CZM solutions converge toward the LHFM ones (for the corresponding dimensionless toughness) at large times $t \gg t_{cm}$. The exact dimensionless time for such a convergence toward the LHFM solution is larger for larger dimensionless toughness, and smaller for larger σ_o/σ_c.

Interestingly, the fracture length is larger at the early stage of growth compared to the LHFM estimate while the inlet opening and pressure are smaller. These differences directly result from the fact that the cohesive forces greatly increases the fluid lag size and impacts its evolution during the nucleation and intermediate stages of growth. Indeed, in the LHFM case, the fluid lag is negligible at all times for dimensionless toughness $\mathcal{K}_m$ larger than ~ 1.5 as reported in Garagash (2006b); Lecampion and Detournay (2007). For $\mathcal{K}_m = 1$, the fluid fraction in the LHFM case is already small at early time: it evolves from 0.9 (when $t \ll t_{om}$) to 1 (for $t \approx t_{om}$, see Fig. 4.18 in appendix). For the same dimensionless toughness, the fluid fraction is lower than 0.6 at early time when accounting for the cohesive zone (see Fig. 4.12). The large extent of the fluid lag is similarly found for larger dimensionless toughness - a striking difference with the LHFM case for which no fluid lag is observed for $\mathcal{K}_m > 1.5$. The cohesive forces significantly enhance the suction effect and thus lag size during nucleation. For the same value of $\mathcal{K}_m$, a larger confinement compared to peak strength (larger σ_o/σ_c) decreases the lag size. Larger σ_o/σ_c results in steeper fluid pressure gradient and accelerates the penetration of the fluid front into the cohesive zone during the nucleation and intermediate phase (see Fig. 4.13) .

As the dimensionless toughness increases, the effect of σ_o/σ_c becomes limited to the nucleation phase (see the length, inlet width and inlet net pressure evolution on Figs. 4.9, 4.10, 4.11). After nucleation, the solutions appear independent of σ_o/σ_c for $t > t_{cm}$ for the $\mathcal{K}_m = 3$ and 4 cases. The fact that σ_o/σ_c does not influence the growth after nucleation for large toughness can be traced back to the fact that the fluid lag cavity is very small in comparison to the cohesive zone length as can be seen on Fig. 4.13.

Fig. 4.7 displays the dimensionless fracture length, fluid fraction, inlet width and pressure for a small dimensionless toughness case ($\mathcal{K}_m = 0.495$). We have plotted these time evolution as function of t/t_{om} for better comparison with the LHFM solution accounting for a fluid lag (Lecampion and Detournay, 2007). For low dimensionless toughness $\mathcal{K}_m$, the response converges well to the LHFM lag solution (Lecampion and Detournay, 2007) relatively quickly after nucleation (contrary to the case of large $\mathcal{K}_m$). On Fig. 4.7, the convergence occurs earlier for smaller σ_o/σ_c in term of t/t_{om} - actually later for smaller σ_o/σ_c in term of $t/t_{cm} = t/t_{om} \times (\sigma_o/\sigma_c)^{-3}$ (in line with observations for larger $\mathcal{K}_m$).
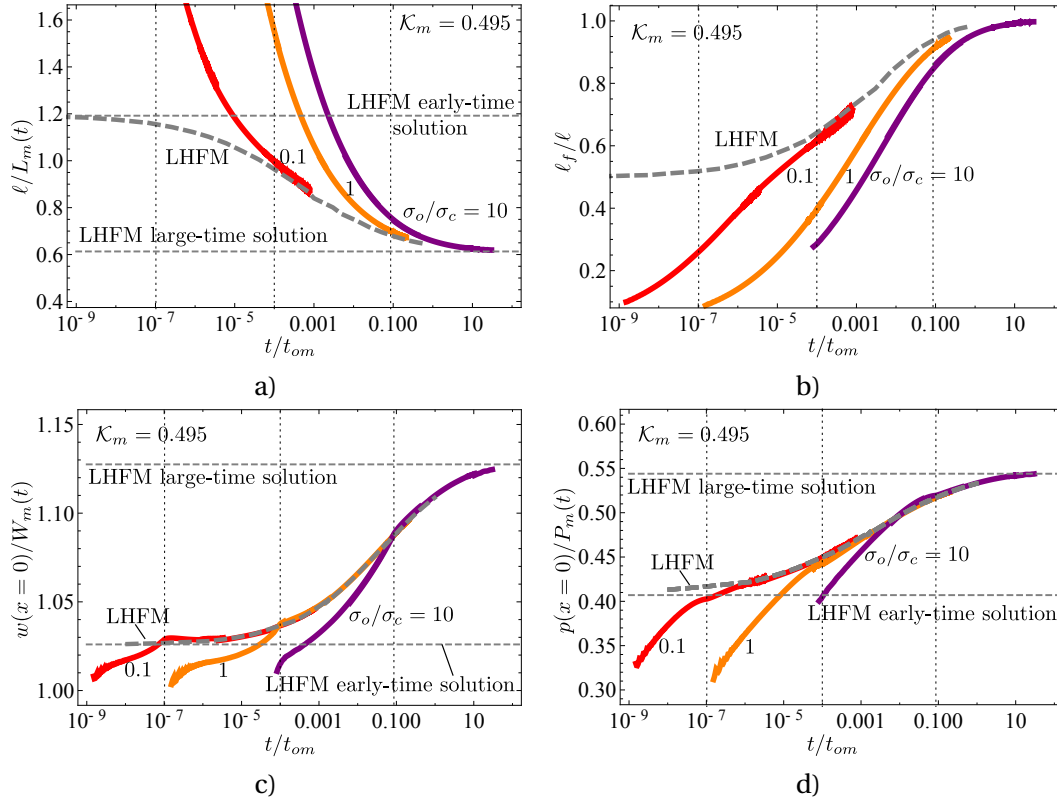
a)

b)

c)

d)

Figure 4.7 – $\mathscr{K}_m = 0.495$: evolution of a) the fracture half length, b) fluid fraction, c) inlet width, and d) inlet net pressure with t/t_{om}. The red, orange and purple curves correspond to different confining stress $\sigma_o/\sigma_c = 0.1, 1, 10$ in a smooth cohesive HF with the dotted vertical lines as their corresponding cohesive zone nucleation period. The gray dashed curves indicate LHFM numerical results with a lag. The two gray horizontal lines correspond respectively to the LHFM early-time solutions with a lag (Garagash, 2006b) and large-time solutions without a lag (Garagash and Detournay, 2005). The time evolution of the cohesive zone length and the ratio between the lag and cohesive zone sizes, fracture apparent energy and ratio of energy dissipation in viscous flow to that in fracture surface creation is shown in Supplemental Materials.
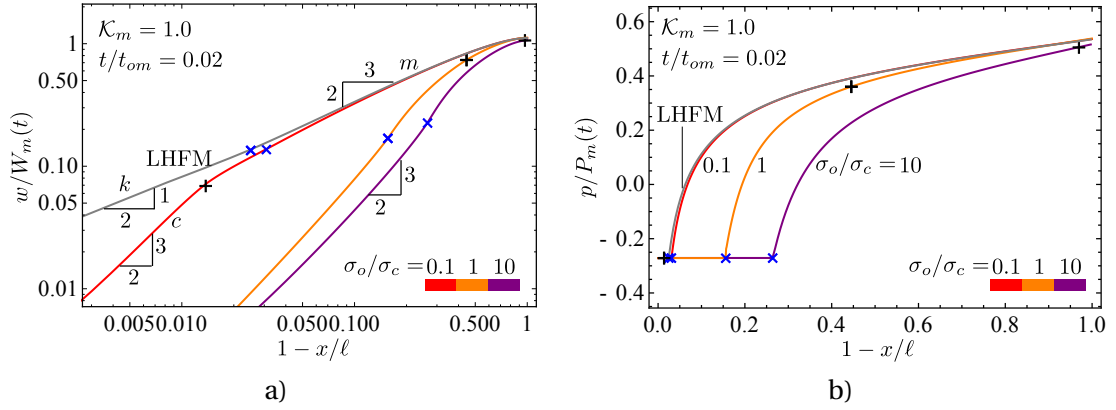
Figure 4.8 – a) Dimensionless opening, and b) net pressure profiles at $t/t_{om} = 0.02$ for $\mathcal{K}_m = 1.009$. "+" indicates the boundary of the cohesive zone and "×" indicates the fluid front location. The red, orange, and purple curves represent different confining stress level $\sigma_o/\sigma_c = 0.1, 1.0, 10$. The gray curves represent the LHFM solutions with a lag at the same time $t/t_{om} = 0.02$.

Tip asymptotes The width and net pressure profiles in the tip reference frame for $\mathcal{K}_m = 1$ is displayed on Fig. 4.8 at time $t/t_{om} = 0.02$ for different σ_o/σ_c (thus at different t/t_{cm} for the different σ_o/σ_c and different ratio ℓ_{coh}/ℓ). On can observe different asymptotic behavior as function of distance from the tip on Fig. 4.8. In the far-field, the 2/3 viscosity 'm' asymptote (Desroches et al., 1994) is visible in the low confinement case - for which at this time, the fluid front is actually outside the cohesive zone. Closer to the tip, the 3/2 cohesive zone 'c' asymptote is visible. These results are in line with the cohesive tip solution of Garagash (2019), although here the cohesive zone is not necessarily small compared to the overall fracture length. This induces a significant offset compared to the semi-infinite results reported in Garagash (2019) (see Supplemental Materials for details).

4.5.2   A rough cohesive fracture ($\alpha_e = 2$)

The additional resistance to fluid flow associated with fracture aperture roughness has a profound impact on growth both at the nucleation and intermediate stage. The effect is amplified for larger σ_o/σ_c and larger $\mathcal{K}_m$. This can be well observed from the evolution of length, inlet width and net pressures displayed on Figures 4.9, 4.10 and 4.11 respectively. In particular the net pressure and width are significantly larger compared to the smooth cohesive zone and LHFM cases, while the dimensionless length is shorter after nucleation.

The convergence toward the LHFM solutions with zero lag are in some cases not fully achieved even at very large time ($t \gg t_{cm}$ especially for the large σ_o/σ_c cases. As mentioned earlier, we actually stop these simulations when the fluid fraction $\xi_f = \ell_f/\ell$ reached 0.99 or the fracture length was within five percent of the LHFM solutions.

Faster nucleation of the cohesive zone As the fluid front is necessarily embedded in the cohesive zone during the nucleation stage, the effect of roughness is significant during nucleation. For the same stress ratio σ_o/σ_c and dimensionless toughness $\mathcal{K}_m$, roughness influences the fracture growth by decreasing the fluid front penetration into the cohesive zone as illustrated by the evolution of the ratio between the lag and cohesive zone sizes in Fig. 4.13.

The increase of the fluid flow resistance brought by roughness can also be observed on the net pressure and width profiles (see Fig. 4.14). The steeper pressure gradient near the fluid front results in a wider opening in the fluid-filled part of the fracture, ultimately making it easier to completely debond the cohesive tractions ($w > w_c$) near the tip. The nucleation process is therefore accelerated as shown in Figs. 4.15, 4.16. The cohesive length is shorter at nucleation compared to the smooth case, but tends to converge to the same value as the smooth case at late time at least for smaller dimensionless toughness. In spite of the lack of stabilized cohesive zone length for the large dimensionless toughness / large σ_o/σ_c cases, the trend for $\sigma_o/\sigma_c = 1$ hints a similar behavior for larger confinement albeit at a much later dimensionless time.

Additional energy dissipation These observations indicate an increase of the overall energy dissipated in the hydraulic fracturing process in the rough cohesive zone case. As shown in Figs. 4.16, 4.17, the extra energy dissipation comes from viscous fluid flow inside the rough cohesive zone and not from additional energy requirement to create new fracture surfaces. The evolution $G_{c,app}$ is not fundamentally different, with actually a smaller maximum at nucleation compared to the smooth cohesive zone case (Fig. 4.16). The ratio D_v/D_k of the energies dissipated in fluid viscous flow and in the creation of new fracture surfaces is significantly larger than the smooth and LHFM cases in the nucleation and intermediate stages (Fig. 4.17), especially for larger σ_o/σ_c. However, the D_v/D_k ratio converges toward the LHFM limit at very large time ($t \gg t_{cm}$).

Fracture aperture roughness has an impact on the fracture growth only when the fluid front is located within the cohesive zone ($\ell - \ell_f < \ell_{coh}$). For small dimensionless toughness and stress ratio, the fluid lag is larger or just slightly smaller than the cohesive zone length after nucleation (see for example the $\mathcal{K}_m = 1, \sigma_o/\sigma_c = 0.1$ case). As a result roughness has little effect and the growth is similar to the smooth case in the intermediate stage of growth. A larger dimensionless confining stress level or/and larger dimensionless toughness facilitates the penetration of the fluid front into the cohesive zone and results in additional fluid viscous dissipation due to the roughness.

At large time, the cohesive zone and fluid lag size becomes much smaller than the overall fracture length such that the effect of roughness on growth is significantly reduced. The large time trend for $\sigma_o/\sigma_c = 1$ (for all toughness) both in terms of length, width, pressure (see Figs. 4.9, 4.10, 4.11) as well as energy (Figs. 4.16) hints that the growth of a rough cohesive fracture tends to LHFM limits at sufficiently large time, similarly than for the smooth case. However, the time at which fracture growth finally follows the LHFM prediction appears much
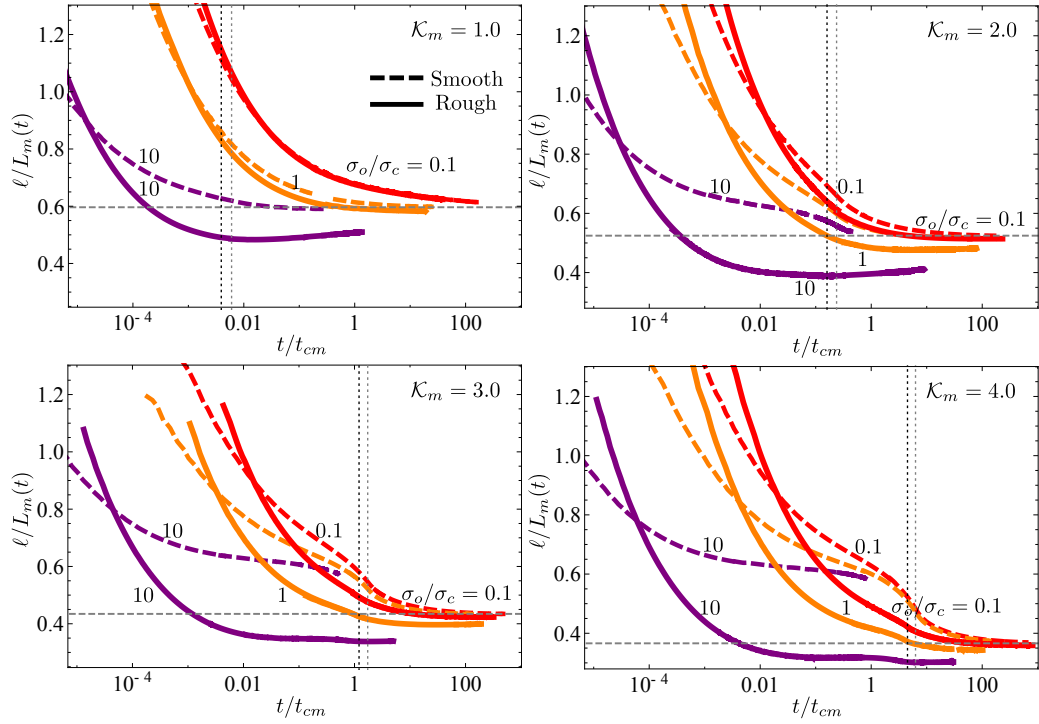
Figure 4.9 – Evolution of the dimensionless fracture half length $\ell/L_m(t)$ with t/t_{cm} for $\mathcal{K}_m = 1 - 4$. The red, orange, and purple curves correspond respectively to $\sigma_o/\sigma_c = 0.1, 1.0, 10$ and the solid and dashed curves correspond respectively to a rough ($\alpha_e = 2$) and smooth fracture ($\alpha_e = 0$). The dotted vertical lines indicate the cohesive zone nucleation period of $\sigma_o/\sigma_c = 0.1$ for a smooth (gray) and a rough (black) fracture. The gray horizontal lines indicate the LHFM solutions in the zero fluid lag limit.

larger than t_{cm} especially for larger $\mathcal{K}_m$ and σ_o/σ_c.

4.6 Discussions

4.6.1 Implications for HF at laboratory and field scales

To gauge the implications for real systems, we consider typical values relevant to laboratory and field scales hydraulic fractures in oil/gas bearing shale/mudstone formation. These rocks have a large range of reported tensile strength ($2 - 12$ MPa - Rybacki et al. (2015)), elastic modulus ($4 - 30$ GPa - Rybacki et al. (2015)) and fracture toughness (0.18-1.43 MPa.m$^{1/2}$ - Chandler et al. (2016)). We assume in what follows $\sigma_c = 3$ MPa, $G_c = 45$ N/m, $w_c = 30\mu$m and $E' = 30$ GPa. We report the corresponding characteristic scales and dimensionless numbers for different type of injection in Table. 4.3.

Laboratory HF tests are performed on finite size samples L_s (typically with L_s at most half a meter) with a minimum confining stresses either smaller or on par with the material cohesive
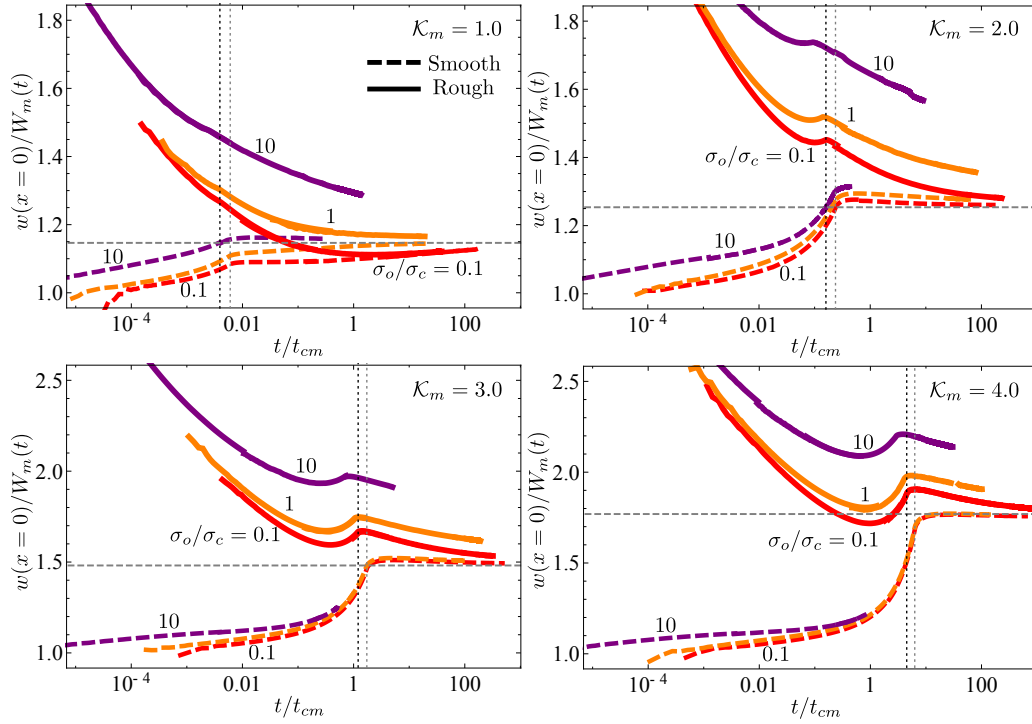
Figure 4.10 – Evolution of the inlet width $w(x = 0)/W_m(t)$ with dimensionless time t/t_{cm} for $\mathcal{K}_m = 1 - 4$. The red, orange, and purple curves correspond respectively to $\sigma_o/\sigma_c = 0.1, 1.0, 10$ and the solid and dashed curves correspond respectively to a rough ($\alpha_e = 2$) and smooth fracture ($\alpha_e = 0$). The dotted vertical lines indicate the cohesive zone nucleation period of $\sigma_o/\sigma_c = 0.1$ for a smooth (gray) and a rough (black) fracture. The gray horizontal lines indicate the LHFM solutions in the zero fluid lag limit.

	Fracturing fluid	μ' (Pa.s)	Q_o (m²/s)	σ_o	Injection duration (s)
Lab injection (1)	Silicone oil	12×1000	1.0×10^{-9}	3	600-1800
Lab injection (2)	Glycerol	12×0.6	1.0×10^{-9}	0.3	30-1800
Micro-HF test	Slick water	12×0.005	1.0×10^{-5}	30	60-240
Well stimulation	Slick water	12×0.005	1.0×10^{-3}	30	1800-7200
	$\mathcal{K}_m$	σ_o/σ_c	t_{cm} (s)	t_c (s)	L_{coh} (m)
Lab injection (1)	0.88	1.0	4.0×10^5	$\approx 1.6 \times 10^3$	0.3
Lab injection (2)	5.6	0.1	2.4×10^2	$> 1.1 \times 10^3$	0.3
Micro-HF test	1.8	10	2.0	≈ 0.19	0.3
Well stimulation	0.6	10	2.0	$< 4.9 \times 10^{-3}$	0.3

Table 4.3 – Examples of characteristic scales for laboratory and field scale HF injection. We report the corresponding time t_c and length scale L_{coh} for nucleation in the rough cohesive zone case ($\alpha_e = 2$).
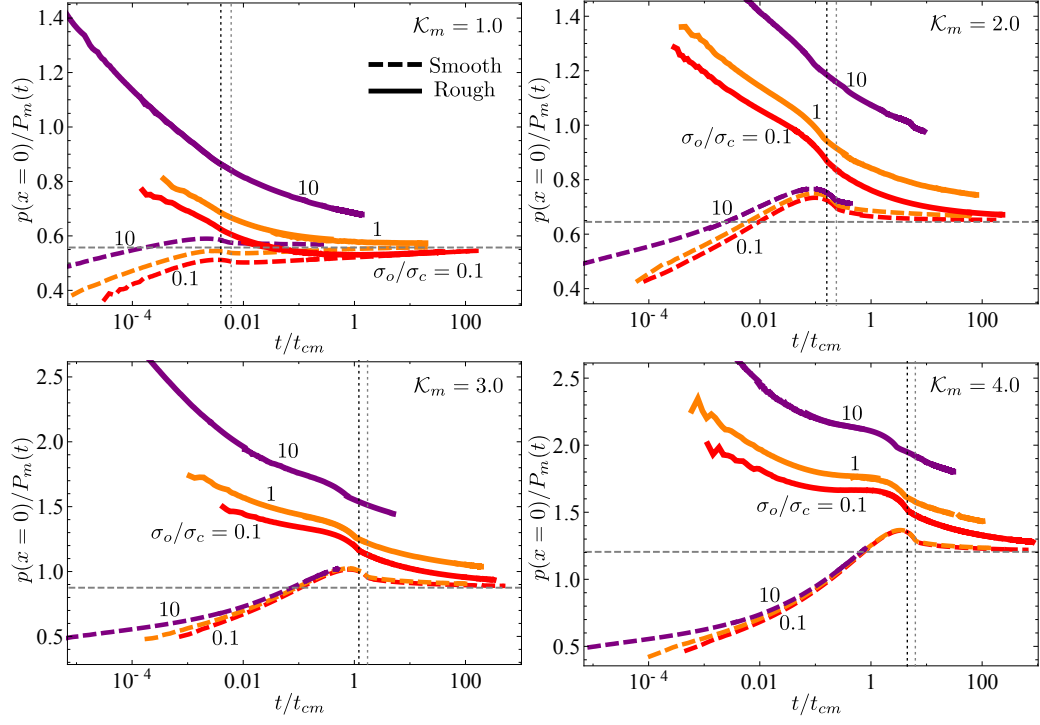
Figure 4.11 – Evolution of the inlet net pressure $p(x = 0)/P_m(t)$ with t/t_{cm} for $\mathcal{K}_m = 1 - 4$. The red, orange, and purple curves correspond respectively to $\sigma_o/\sigma_c = 0.1, 1.0, 10$ and the solid and dashed curves correspond respectively to a rough ($\alpha_e = 2$) and smooth fracture. The dotted vertical lines indicate the cohesive zone nucleation period of $\sigma_o/\sigma_c = 0.1$ for a smooth (gray) and a rough (black) fracture. The gray horizontal lines indicate the LHFM solutions in the zero fluid lag limit.
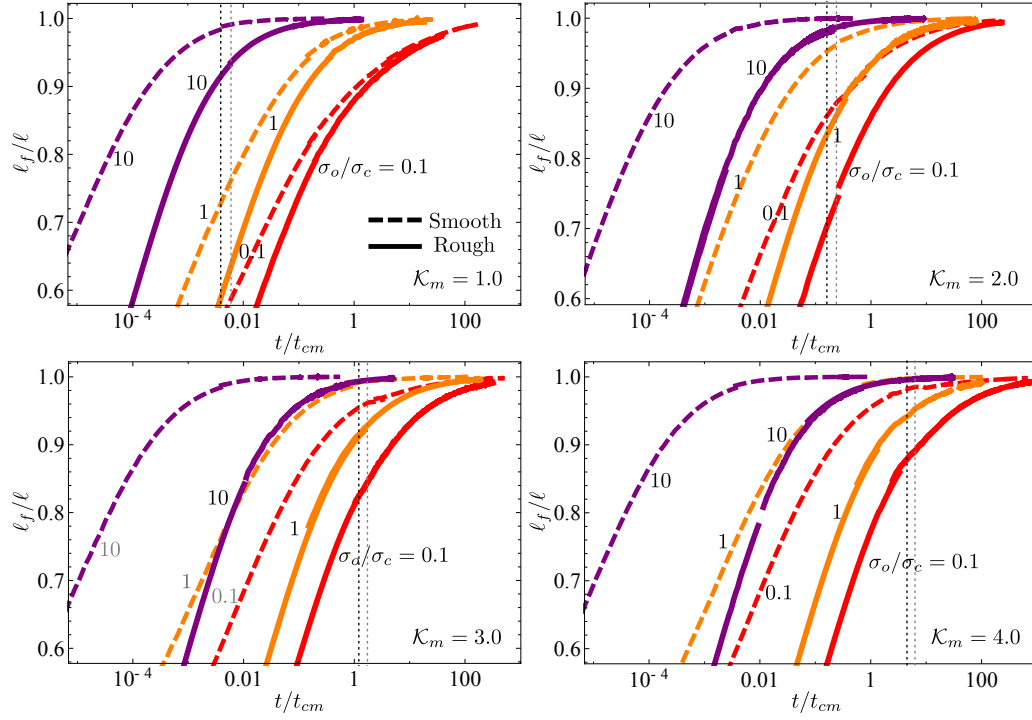
Figure 4.12 – Evolution of the fluid fraction $\xi_f = \ell_f/\ell$ with t/t_{cm} for $\mathcal{K}_m = 1 - 4$. The red, orange, purple curves correspond to $\sigma_o/\sigma_c = 0.1, 1.0, 10$ and the solid and dashed curves correspond respectively to a rough ($\alpha_e = 2$) and smooth fracture ($\alpha_e = 0$). The dotted vertical lines indicate the cohesive zone nucleation period of $\sigma_o/\sigma_c = 0.1$ for a smooth (gray) and a rough (black) fracture.
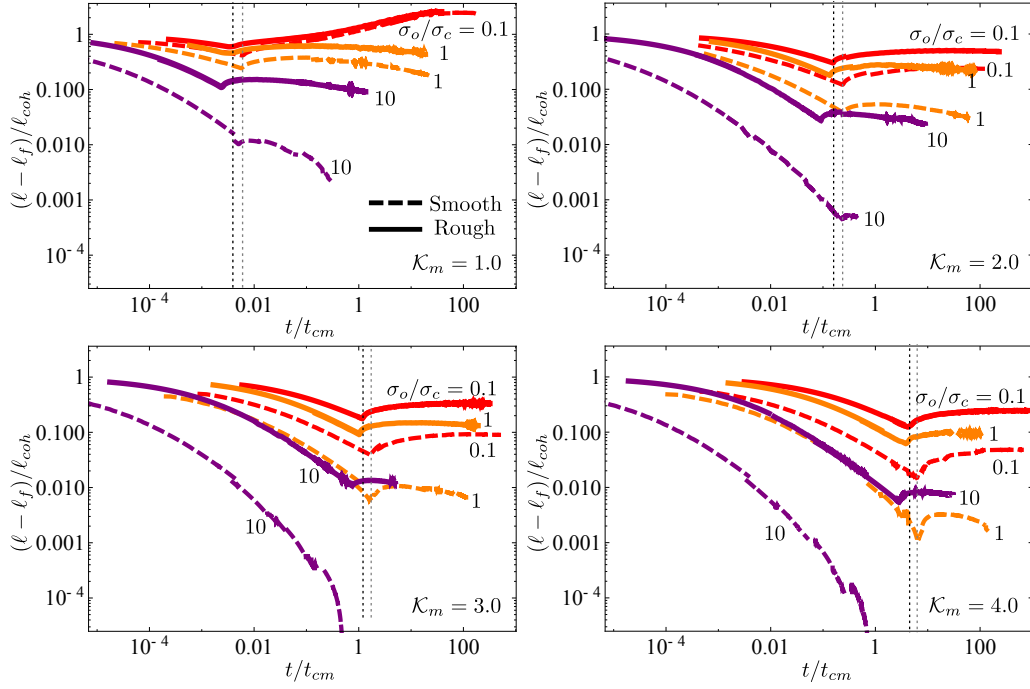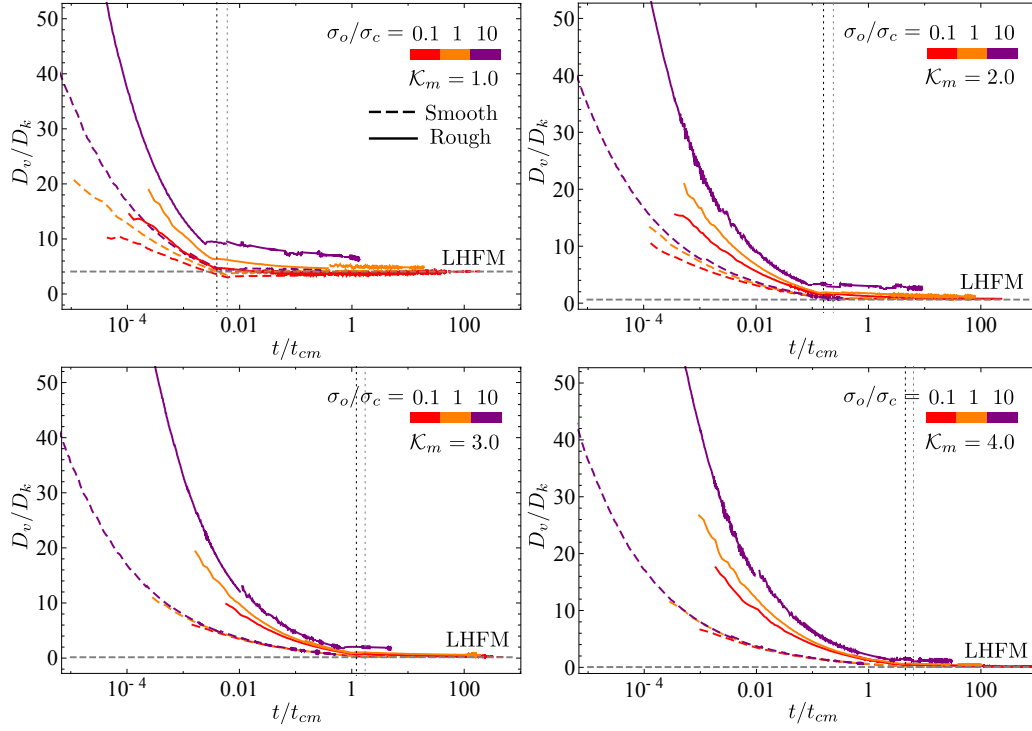
Figure 4.13 – Time evolution of the ratio between the lag and cohesive zone sizes $(\ell - \ell_f)/\ell_{coh}$ for $\mathcal{K}_m = 1 - 4$. The red, orange, and purple curves correspond to $\sigma_o/\sigma_c = 0.1, 1.0, 10$ respectively and the solid and dashed curves correspond respectively to a rough ($\alpha_e = 2$) and smooth fracture ($\alpha_e = 0$). The dotted vertical lines indicate the cohesive zone nucleation period of $\sigma_o/\sigma_c = 0.1$ for a smooth (gray) and a rough (black) fracture.
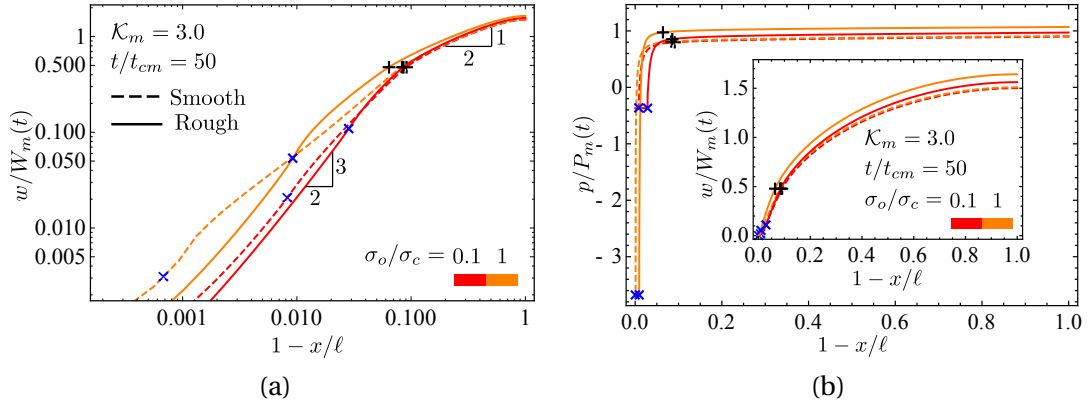
Figure 4.14 – a) Dimensionless opening and b) net pressure profiles at $t/t_{cm} = 50$ for $\mathcal{K}_m = 3.0$. "+" indicates the boundary of the cohesive zone and "×" indicates the fluid front location. The red and orange curves correspond to $\sigma_o/\sigma_c = 0.1, 1.0$ respectively. The solid and dashed curves indicate respectively a rough ($\alpha_e = 2$) and smooth fracture ($\alpha_e = 0$).

81
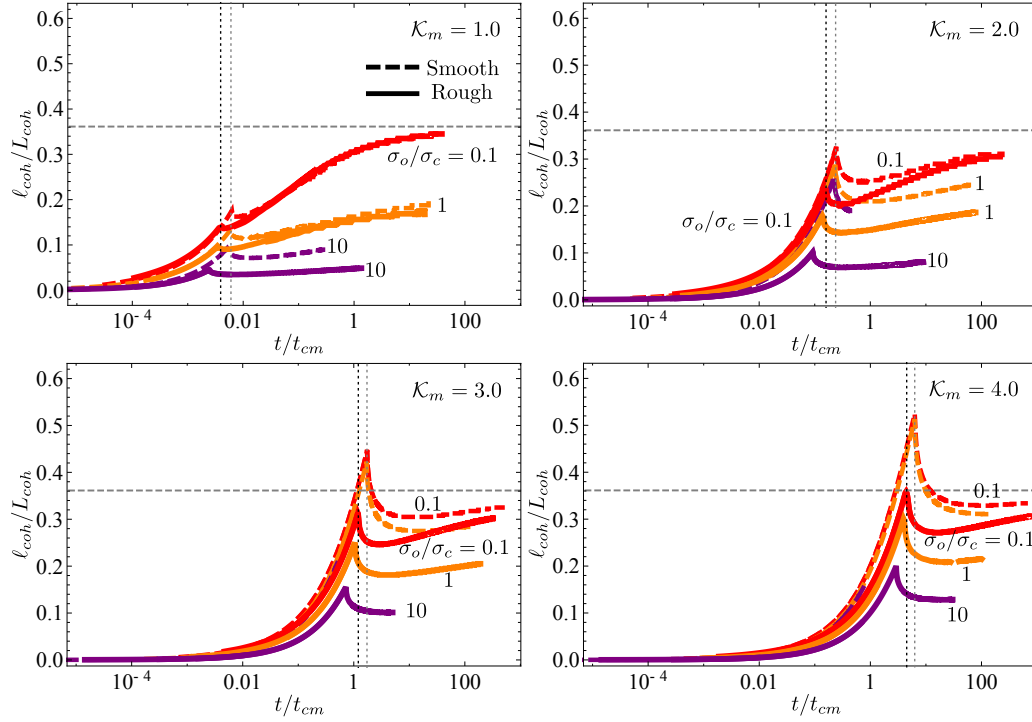
Figure 4.15 – Time evolution of the cohesive length ℓ_{coh}/L_{coh} for $\mathcal{K}_m = 1-4$. The red, orange, and purple curves correspond respectively to $\sigma_o/\sigma_c = 0.1, 1.0, 10$ and the solid and dashed curves correspond respectively to a rough ($\alpha_e = 2$) and smooth fracture ($\alpha_e = 0$). The dotted vertical lines indicate the cohesive zone nucleation period of $\sigma_o/\sigma_c = 0.1$ for a smooth (gray) and a rough (black) fracture. The dashed horizontal line represents the small-scale yielding asymptote ($\approx 0.115\pi$) of the cohesive zone length for the linear-softening cohesive model (Dempsey et al., 2010).
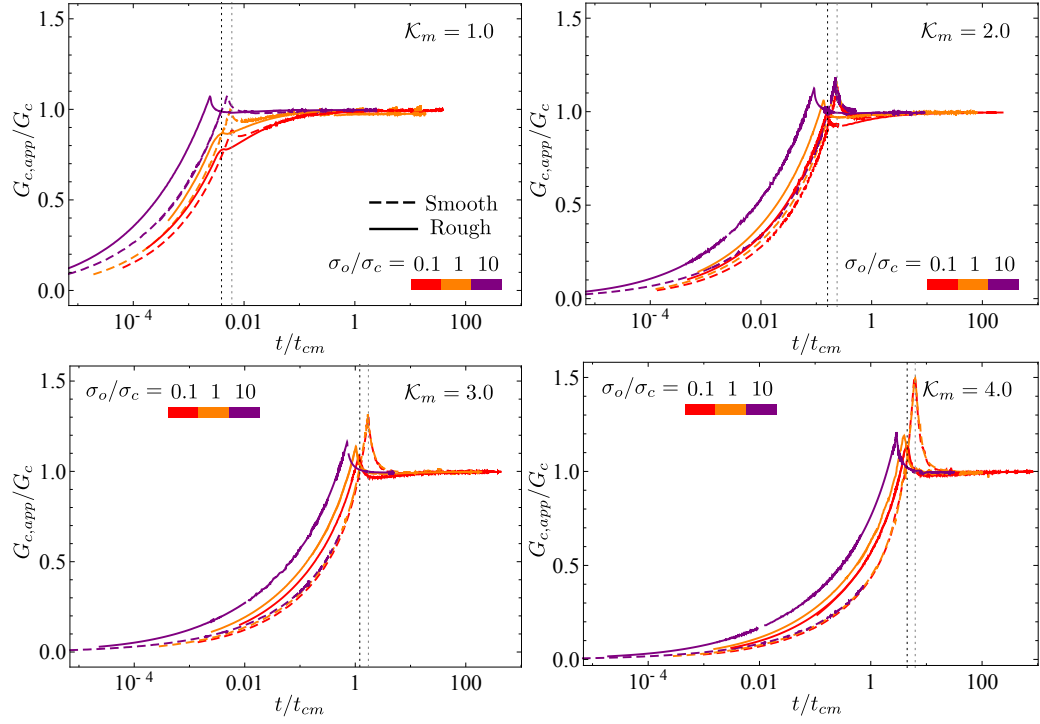
Figure 4.16 – Time evolution of the apparent fracture energy $G_{c,app}/G_c$ for $\mathcal{K}_m = 1 - 4$. The red, orange, and purple curves correspond respectively to $\sigma_o/\sigma_c = 0.1, 1.0, 10$ and the solid and dashed curves correspond respectively to a rough ($\alpha_e = 2$) and smooth fracture ($\alpha_e = 0$). The dotted vertical lines indicate the cohesive zone nucleation period of $\sigma_o/\sigma_c = 0.1$ for a smooth (gray) and a rough (black) fracture.

Figure 4.17 – Time evolution of the ratio of the energies dissipated in fluid viscous flow and in the creation of new fracture surfaces D_v/D_k for $\mathcal{K}_m = 1-4$. The red, orange, and purple curves correspond respectively to $\sigma_o/\sigma_c = 0.1, 1.0, 10$ and the solid and dashed curves correspond respectively to a rough ($\alpha_e = 2$) and smooth fracture ($\alpha_e = 0$). The dotted vertical lines indicate the cohesive zone nucleation period of $\sigma_o/\sigma_c = 0.1$ for a smooth (gray) and a rough (black) fracture. The gray horizontal lines are the corresponding LHFM limits with zero fluid lag.

stress ($\sigma_o/\sigma_c \approx 0.1 - 2$). In the case where the sample dimension L_s is smaller or of the order of the characteristic scale of the cohesive zone L_{coh}, laboratory HF tests will only span the nucleation and intermediate stages of growth, and as a result will strongly deviate from LHFM predictions. If L_s is sufficiently larger than L_{coh} ($L_s \gtrsim 10L_{coh}$), the fracture growth will possibly converge to LHFM solutions at late time for small $\mathcal{K}_m$ (Lab injection (1) case in Table. 4.3). Nevertheless, it will still present significant deviations from LHFM solutions in the inlet width and net pressure (see Figs. 4.10, 4.11) for larger $\mathcal{K}_m$ values (Lab injection (2) case in Table. 4.3).

In-situ HF operations are performed at depth (anything from 1.5 to 4 km), and as a result the ratio σ_o/σ_c is always much larger than unity ($\sigma_o/\sigma_c \sim 10$ or even larger). We evaluate the characteristic scales by assuming injection of slick water in micro-HF tests and well stimulation operations (see Table. 4.3). A micro-HF test (typically performed at a small injection rate) is characterized by a dimensionless toughness $\mathcal{K}_m$ around two. Based on the results presented previously, significant deviations from LHFM predictions are expected in that case with a fracture length shorter by about 15% (see Fig. 4.9), a fracture opening larger by about 20% (Fig. 4.10), and a net pressure larger by about 40% (Fig. 4.11) after less than a minute of propagation ($t \sim 100t_{cm}$). For well stimulation applications, the fracture growth will converge toward the LHFM predictions after few minutes thanks to the smaller dimensionless toughness resulting from the larger injection rate. This convergence will be delayed for deeper injections / larger σ_o/σ_c. One should bare in mind that very different responses can be encountered as function of rocks properties (notably of w_c, σ_c) and in-situ stress conditions.

4.6.2 Limitations and possible extensions of the current study

We have used a simple linear-weakening cohesive zone model to simulate the fracture process zone and a phenomenological correction to Poiseuille's law (assuming $w_R = w_c$) to account for the effect of aperture roughness on fracture hydraulic conductivity. These choices are actually the simplest possible ones, and may well be oversimplified. More advanced traction-separation relations with both a non-linear hardening and softening branch are often found to better reproduce experimental observations of fracture growth in quasi-brittle materials (Park and Paulino, 2011; Needleman, 2014). Similarly, the precise relation between the width scale of solid non-linearity w_c and that of the one related to the flow deviation w_R remains to be better constrained from experiments. A better description of the details of both the traction-separation law and the effect of roughness on fluid flow will likely modify quantitatively the hydraulic fracturing growth at the early and intermediate stages. However, the scaling and qualitative structure of HF growth presented here will remain similar. We also have to recall that a difference between w_c and w_R, or similarly a value of α_c different than unity is clearly possible in view of the scatter of the available experimental data (Table 4.1). This would add another dimensionless parameter (α_c) in addition to σ_o/σ_c, α_e and the dimensionless toughness $\mathcal{K}_m$.

Our results indicate a convergence of HF growth in quasi-brittle materials toward LHFM

predictions at large time, even though the investigation of the parametric space reported here is only partial due to the extremely significant numerical cost of the simulation in the vanishing lag size limits as time increases. The numerical difficulty results from the requirement of a sufficiently fine mesh to resolve the shrinking fluid lag at large time as well as the small tensile zone ahead of the tip which significantly decreases for large σ_o/σ_c. An algorithm with an adaptive mesh refinement must be developed to ensure a sufficiently fine resolution of the process zone and fluid lag in order to further investigate fracture growth for large σ_o/σ_c cases.

We have assumed the flow to be strictly laminar in the rough fracture. In some specific cases where very large injection rates are used, turbulence may appear in the fracture (Lecampion and Zia, 2019; Zia and Lecampion, 2017; Dontsov, 2016). Interestingly, the deviation from smooth laminar flow via the introduction of a friction correction bears similarity with the case where turbulent flow is accounted for (Tsai and Rice, 2010; Lecampion and Zia, 2019). The impact of turbulent flow in fractures is also captured via a friction correction albeit with a different functional form. The effect of turbulence has been shown to be restricted to the early time of fracture growth (Lecampion and Zia, 2019). As such it may possibly influence the nucleation and intermediate phases of growth previously discussed for large injection rate field conditions.

The discussions and results presented here pertain to a plane-strain geometry, but can be extended to a radial hydraulic fracture (Liu et al., 2019a; Garagash, 2019). For a radial cohesive HF, the energy dissipated in the creation of fracture surfaces increases with the fracture perimeter. In particular, the dimensionless toughness $\mathscr{K}_m$ increases with time as $\mathscr{K}_m = (t/t_{mk})^{1/9}$ (Savitski and Detournay, 2002), with

$$t_{mk} = \frac{E'^{13/2} Q_o^{3/2} \mu'^{5/2}}{K'^9} \tag{4.32}$$

This introduces another time-scale into the problem besides t_{om} and $t_{cm} = t_{om} \times (\sigma_o/\sigma_c)^3$. As a result, the exact growth of a radial cohesive HF will be impacted by the ratio t_{cm}/t_{mk}, or in other words by the competition between hydro-mechanical effects associated with nucleation and the overall transition toward the late-time toughness dominated regime. The results of Garagash (2019) obtained using an equation of motion based on the solution of a steadily moving HF provides an estimate of the propagation, but should be taken with caution as this approach does not necessarily ensure that the cohesive zone length is smaller than the fracture length. Additional quantitative investigation of the radial cohesive HF are left for further studies.

4.7   Conclusions

We have investigated the growth of a plane-strain HF in a quasi-brittle material using a cohesive zone model including the effect of aperture roughness on fluid flow in the simplest possible manner. In parallel to the cohesive zone, it is necessary to account for the presence

of a fluid lag to ensure that both the fluid pressure and stresses in the near tip region remain finite. Resolving with sufficient accuracy these potentially small regions near the fracture tip renders the problem extremely challenging numerically.

We have shown that a plane-strain cohesive HF presents three distinct stages of growth: a nucleation phase, an intermediate phase during which the results slowly converge toward linear hydraulic fracture mechanics (LHFM) predictions in a third stage. The overall solution is characterized by a cohesive zone nucleation time scale $t_{cm} = E'^2 \mu'/\sigma_c^3$, a dimensionless fracture toughness $\mathcal{K}_m$ (whose definition is similar to the LHFM case) and the ratio between in-situ and material cohesive stress σ_o/σ_c. In addition, the enhanced flow dissipation associated with fracture roughness significantly influences the solution as it re-inforces the hydro-mechanical coupling in the near tip region.

After the nucleation stage, for large $\mathcal{K}_m$, the effect of σ_o/σ_c for a smooth cohesive zone case is not significant when the solutions tend toward the LHFM predictions. This convergence toward LHFM occurs at later t/t_{cm} for larger $\mathcal{K}_m$. For small $\mathcal{K}_m$, the fluid lag diminishes faster for larger σ_o/σ_c and the convergence to LHFM occurs for smaller t/t_{cm} as a result.

Roughness significantly modifies the convergence toward LHFM notably for dimensionless toughness larger than 1. In addition, for these large toughness cases, larger σ_o/σ_c results in larger deviations and a much slower convergence toward the LHFM predictions (which now occur for orders of magnitude of the nucleation time scale t_{cm}). Fracture roughness leads to additional energy dissipation in the viscous fluid flow associated with the fluid penetration in the cohesive zone. This ultimately results in larger openings, larger net pressures, shorter fracture extension and thus larger input energy. This additional viscous dissipation is further amplified for larger σ_o/σ_c, which facilitates the penetration of the fluid in the rough cohesive zone. It is also worth noting that counter-intuitively the effect is stronger and remains in effect longer for larger dimensionless toughness: the viscous pressure drop localizes to an even smaller region near the tip for larger $\mathcal{K}_m$ such that viscous flow dissipation increases as a result.

Different models for the impact of roughness on flow (such as different values for α_c and the power-law flow roughness exponent α_e taken here equal to 1 and 2 respectively) will impact quantitatively the fracture evolution although the structure of the solution described here will remain. The same can be said with regards to the simple linear-weakening traction separation law used which may be replaced by a more elaborate one if required.

The theoretical predictions presented here need to be tested experimentally on well characterized quasi-brittle materials. This is particularly challenging as one must ensure that the sample size is at least ten times larger than the characteristic cohesive zone length $L_{coh} = E' w_c/\sigma_c$ in order to hope capturing the convergence toward LHFM predictions. It is actually worth noting that so far all the quantitative experimental validations of linear hydraulic fracture mechanics have been obtained on transparent and/or model materials - all with very small process zone sizes (see Lecampion et al. (2017) and references therein). HF experiments in

rocks need to be performed with a quantitative measurement of the time evolution of the fracture and fluid fronts, as well as fracture opening. This is achievable via active acoustic imaging (Liu et al., 2020). However, the accurate spatiotemporal imaging of the process zone of a growing hydraulic fracture under realistic stress and injection conditions remains truly challenging.

4.8 Appendix: Numerical scheme accounting for the nucleation of a cohesive zone and a fluid lag

As suggested in Liu and Lecampion (2019), the problem is solved numerically via a fully implicit scheme based on the boundary element method. We automatically nucleate the fluid lag using the Elrod-Adams lubrication cavitation model at the early stage of fracture growth (Mollaali and Shen, 2018). We then switch to a level-set algorithm for computational efficiency by precisely tracking the fluid front (Gordeliy and Detournay, 2011b).

4.8.1 Fluid-lag-nucleation algorithm

We initiate the fracture aperture from the solution of a static elastic fracture under a uniform fluid pressure slightly larger than σ_o. For a given fracture length increment, the solution is obtained using three nested iterative loops: we start from a trial time step and solve the fluid pressure for all elements inside the fracture using a quasi-Newton method. Such a procedure is repeated until each element in the fracture reaches a consistent state: either fluid or vapor. A converged estimate of the cohesive forces is then updated using fixed-point iterations with under-relaxation. The time step is finally adjusted in an outer loop using a bi-section and secant method to fulfill the propagation criterion.

Elasticity

$$\mathbb{A}\mathbf{w} = \mathbf{p}_f - \sigma_{coh}(\mathbf{w}) - \sigma_o \tag{4.33}$$

where $\mathbb{A}$ is the elastic matrix obtained via the discretization of the elastic operator using the displacement discontinuity method with piece-wise constant elements, and $\mathbf{p}_f, \sigma_o, \sigma_{coh}$ are respectively vectors of the fluid pressure, minimum compressive stress and cohesive forces.

Elrod-Adams lubrication A state variable θ is introduced in the mass conservation, characterizing the percentage of liquid occupying the fracture within one element. All the elements inside the fracture fulfil the condition $p_f(1 - \theta) = 0$ and can be classified into three domains according to the filling condition of the element: η_p (elements fully filled with fluid), η_θ

Repeat solving for pressure p_{fi}, θ_i for $i \in \eta_p \cup \eta_\theta$ using Newton's method;
    for $i \in \eta_\Gamma$ **do**
        if $p_{f,i} < 0$ **then** set $p_{f,i} = 0$, $\eta_p \leftarrow \eta_p \setminus \{i\}$, $\eta_\theta \leftarrow \eta_\theta \cup \{i\}$, $\eta_{ex} \leftarrow \eta_\Gamma \setminus (\eta_p \cup \eta_\theta)$
        if $\theta_i > 1$ **then** set $\theta_i = 1$, $\eta_\theta \leftarrow \eta_\theta \setminus \{i\}$, $\eta_p \leftarrow \eta_p \cup \{i\}$, $\eta_{ex} \leftarrow \eta_\Gamma \setminus (\eta_p \cup \eta_\theta)$
        if $\theta_i < 0$ **then** set $\theta_i = 0$, $\eta_\theta \leftarrow \eta_\theta \setminus \{i\}$, $\eta_{ex} \leftarrow \eta_\Gamma \setminus (\eta_p \cup \eta_\theta)$
    end
until all constraints $p_{f,i} \geq 0$, $0 \leq \theta_i \leq 1$ for $i \in \eta_\Gamma$ are satisfied, in other words, $p_{f,i}(1 - \theta_i) = 0$.

Table 4.4 – Algorithm using the Elrod-Adams model (adapted from Mollaali and Shen (2018)) within one iteration with a given cohesive force vector

(elements partially filled with fluid) and η_{ex} (empty or vapor elements).

$$
\begin{aligned}
\eta_p &= \{i \in \eta_\Gamma \mid \theta_i = 1, \quad p_{fi} > 0\} \\
\eta_\theta &= \{i \in \eta_\Gamma \mid 0 < \theta_i < 1, \quad p_{fi} = 0\} \\
\eta_{ex} &= \{i \in \eta_\Gamma \mid i \notin (\eta_p \cup \eta_\theta), \quad p_{fi} = 0, \quad \theta_i = 0\}
\end{aligned}
\tag{4.34}
$$

where $\eta_p \cap \eta_\theta = \emptyset$ and $\eta_\Gamma = \eta_p \cup \eta_\theta \cup \eta_{ex}$. We integrate the lubrication equation over element i:

$$
\underbrace{\int_i \frac{\partial(\theta w)}{\partial t} dx}_{1} + \underbrace{\int_i \frac{\partial}{\partial x}\left(-\frac{w^3}{\mu'}\frac{\partial p_f}{\partial x}\right) dx}_{2} - \underbrace{\frac{Q_o}{2}\delta_{(i,1)}}_{3} = 0
\tag{4.35}
$$

The first and the second terms are respectively discretized as follows,

$$
\int_i \frac{\partial \theta w}{\partial t} dx = \frac{1}{\Delta t} h(\theta_i w_i - \theta_i^o w_i^o)
\tag{4.36}
$$

$$
\begin{aligned}
\int_i \frac{\partial}{\partial x}\left(-\frac{w^3}{\mu' f}\frac{\partial p_f}{\partial x}\right) dx &= \left[-\frac{w^3}{\mu' f}\frac{\partial p_f}{\partial x}\right]_{i-1/2}^{i+1/2} \\
&= \frac{1}{\mu' f_{i-1/2}} w_{i-1/2}^3 \left(\frac{p_{f,i} - p_{f,i-1}}{h}\right) - \frac{1}{\mu' f_{i+1/2}} w_{i+1/2}^3 \left(\frac{p_{f,i+1} - p_{f,i}}{h}\right), \\
w_{i-1/2} &= \frac{w_i + w_{i-1}}{2}, \quad w_{i+1/2} = \frac{w_i + w_{i+1}}{2}
\end{aligned}
\tag{4.37}
$$

where h is the element size and the superscript o denotes the solution at the previous time step.

We back-substitute the elasticity into the lubrication equation and use the quasi-Newton method to solve the non-linear problem. We set the solution of the previous time step as an initial guess and solve iteratively for $p_{f,i}(i \in \eta_p)$ and $\theta_i(i \in \eta_\theta)$. The lag-nucleation algorithm then updates the sets of η_p and η_θ as demonstrated in Table 4.4.

Propagation condition In the context of a cohesive zone, we check the equality of the tensile stress component ahead of the fracture tip with the material peak strength:

$$\sigma_{yy,n+1} = A_{n+1,j} w_j - \sigma_o = \sigma_c, \quad j = 1...n \tag{4.38}$$

where n is the number of elements inside the fracture at the current time step.

4.8.2 Fluid-front-tracking algorithm

The fluid-front tracking algorithm (Gordeliy and Detournay, 2011b) assumes a clear boundary between the fluid and cavity. The n elements inside the fracture is divided into m fluid channel elements fully-filled with fluid ($p_f > 0$), ($n - m - 1$) fluid lag elements with a negligible cavitation pressure ($p_f = 0$) and one partially filled element ($p_f = 0$) where locates the fluid front. By introducing a filling fraction ϕ, we estimate the fluid front position using the solution of the lag-nucleation / Elrod-Adams based algorithm. We assume that fluid-front-tracking algorithm initializes with a solution ($w^O, p_f^O, V^O, m^O, \phi^O, \ell_f^O$) obtained from the lag-nucleation / Elrod-Adams based algorithm at a chosen time step k. m^O is the number of elements in the domain η_p. ϕ^O is the filling fraction obtained by gathering the fluid mass of all lag elements from the lag-nucleation algorithm in the partially-filled element (the $(m^O + 1)^{\text{th}}$ element) of the fluid-front-tracking algorithm.

$$\phi^O = \sum_i \theta_i^k w_i^k / w_{m^O+1}, \quad i \in \eta_\theta \tag{4.39}$$

We then obtain the fluid front position ℓ_f^O and the fluid front velocity V^O for a chosen time step k.

$$\begin{aligned} \ell_f^O &= (m^O + \phi^O)h, \\ V^O &= (\ell_{f,k+1} - \ell_{f,k-1})/(t_{k+1} - t_{k-1}) \end{aligned} \tag{4.40}$$

where t_{k-1} and t_{k+1} are respectively propagation time at the $(k-1)^{\text{th}}$ and $(k+1)^{\text{th}}$ time step in the lag-nucleation algorithm.

Based on this initial estimation of the fluid front, we solve iteratively the increment of the opening in the channel elements for a given fracture front through three nested loops in the fluid-front-tracking algorithm. One loop tracks the fluid front, one updates the time step to fulfill the propagation condition and another solves the non-linear system due to the cohesive forces and lubricated fluid flow through a fixed-point scheme. We present in the following the discretization of the non-linear system.

Elasticity

$$\mathbf{p}_c - \sigma_o - \sigma_{cohc} = \mathbb{A}_{cw} \mathbf{w} + \mathbb{A}_{ol}(-\sigma_o - \sigma_{cohl}) \tag{4.41}$$

where $\mathbf{p}_c$ is the vector net pressures in the channel part of the fracture; σ_{cohc} and σ_{cohl}

cohesive forces applied in the fluid channel and fluid lag.

$$\mathbb{A}_{cw} = \mathbb{A}_{cc} - \mathbb{A}_{cl}\mathbb{A}_{ll}^{-1}\mathbb{A}_{lc}$$
$$\mathbb{A}_{ol} = \mathbb{A}_{cl}\mathbb{A}_{ll}^{-1}$$
(4.42)

$\mathbb{A}_{cc}, \mathbb{A}_{cl}, \mathbb{A}_{lc}, \mathbb{A}_{ll}$ are sub-matrix of the elastic matrix $\mathbb{A}$ associated with elements inside the fluid channel and lag.

Lubrication flow For fluid channel elements ($1 \le i \le m$),

$$
\begin{aligned}
\Delta w_i = & \frac{\Delta t}{\mu' h^2}\left(\frac{1}{f_{i-1/2}}w_{i-1/2}^3 p_{c,i-1} + \frac{1}{f_{i+1/2}}w_{i+1/2}^3 p_{c,i+1}\right) \\
& - \frac{\Delta t}{\mu' h^2}(\frac{1}{f_{i-1/2}}w_{i-1/2}^3 + \frac{1}{f_{i+1/2}}w_{i+1/2}^3)p_{c,i} + \delta_{(i,1)}\frac{Q_o \Delta t}{2h} \\
& - \delta_{(i,m)}F_m - H(i-m^o)\sum_{k=m^o+1}^{m}\delta_{(i,k)}F_k
\end{aligned}
$$
(4.43)

The second term on the second line represents the contribution due to a constant injection rate and the two terms on the third line are mass corrections due to the partially-filled element where the fluid front locates. $H(\cdot)$ is the Heaviside step function.

$$
F_m = \begin{cases} \phi w_{m+1} - \phi^o w_{m+1}^o, & m = m^o \\ \phi w_{m+1} - \phi^o w_{m^o+1}^o - \sum_{i=m+1}^{m^o} w_i, & m < m^o \end{cases}
$$
(4.44)

$$
F_k = \begin{cases} (1-\phi^o)w_k^o, & k = m^o+1 \\ w_k^o, & k > m^o+1 \end{cases}
$$
(4.45)

where the superscript o refers to the solutions at the previous time step. The lubrication equation can be thus arranged as

$$\Delta\mathbf{w} = \mathbb{L}\cdot\mathbf{p}_c + \mathbf{S}_1 - \mathbf{S}_m - \mathbf{S}_{m^o}$$
(4.46)

Coupled system of equations We back-substitute the elasticity and write the coupled system as in Eq. (4.47). For a given fracture front and a trial time step, we solve for incremental apertures $\Delta\mathbf{w}$ using fixed-point iterations. The tangent linear system reads:

$$(\mathbb{I} - \mathbb{L}(\Delta\mathbf{w}^{(s-1)})\mathbb{A}_{cw})\Delta\mathbf{w}^s = \mathbb{L}(\Delta\mathbf{w}^{(s-1)})\mathbb{A}_{cw}\mathbf{w}^o + \mathbb{L}(\Delta\mathbf{w}^{(s-1)})\mathbb{A}_{ol}(-\sigma_o - \sigma_{cohl}(\Delta\mathbf{w}^{(s-1)}))$$
(4.47)

where s refers to the solution at the previous iteration.

Update of the fluid front position The fluid front position is estimated as

$$\ell_f^{(s)} = (m^o + \phi^o)h + V^{(s-1)}\Delta t, m^{(s)} = \text{floor}[\ell_f^{(s)}/h], \phi^{(s)} = \ell_f^{(s)}/h - m^{(s)} \tag{4.48}$$

where V is the fluid front velocity and it can be obtained through lubrication theories,

$$
\begin{aligned}
V &= \frac{1}{2}\left(V^o - \frac{1}{\mu' f_m}w_m^2\frac{\partial p}{\partial x}\right), \\
\frac{\partial p}{\partial x} &= \left(p_{c,m} - \frac{p_{c,m}+\sigma_o}{\phi+1/2} - p_{c,m-1}\right)/(2h), \quad m > 1
\end{aligned}
\tag{4.49}
$$

The iteration starts with $V^{(0)} = V^o$ and continues until $|(\ell_f^{(s)} - \ell_f^{(s-1)})/\ell_f^{(s-1)}|$ is within a set tolerance.

Control of overestimation of the fluid front position We may possibly overestimate the fluid front position using Eq. (4.48) especially when the fracture front advances too much compared to the previous time step. As a result, negative pressure may be detected in the channel elements near the fluid front.

In order to better locate the fluid front, we adopt a strategy similar to the one in Gordeliy et al. (2019). Once the scheme detects a negative fluid pressure in the channel elements (where the elements are fully-filled with fluid) during the sth iteration at the current time step, we utilizes the bi-section algorithm to estimate the fluid front position (Liu et al., 2019a). We set the fluid front position at the previous time step as the lower bound $\ell_{f-} = \ell_f^o$ and the current position obtained from the previous iteration as the upper bound $\ell_{f+} = \ell_f^{(s-1)}$. As long as the fluid front advances during the fracture growth, the trial fluid front position for the next iteration can be estimated from

$$\ell_f^{(s)} = (\ell_{f+} + \ell_{f-})/2 \tag{4.50}$$

We iterate on ℓ_f until that $|(\ell_f^{(s)} - \ell_f^{(s-1)})/\ell_f^{(s-1)}|$ is within a set tolerance and that all fluid pressure in the channel elements remain positive.

4.8.3 Benchmark of the growth of a linear elastic fracture

We simulate the growth of a plane-strain HF in a linear elastic medium by adapting the propagation condition as

$$w_n = \frac{2}{3}\frac{K'\sqrt{h}}{E'} \tag{4.51}$$

where w_n is the opening of the element closest to the fracture tip obtained by the integration of the tip asymptote. We benchmark our scheme using different $\mathcal{K}_m$ values and formulate the problem with the viscosity scaling in the time-domain t/t_{om} similar to Lecampion and Detournay (2007). We show in Fig. 4.18 that our results (CZMLAG) are in good agreement with the numerical solutions reported in Lecampion and Detournay (2007).
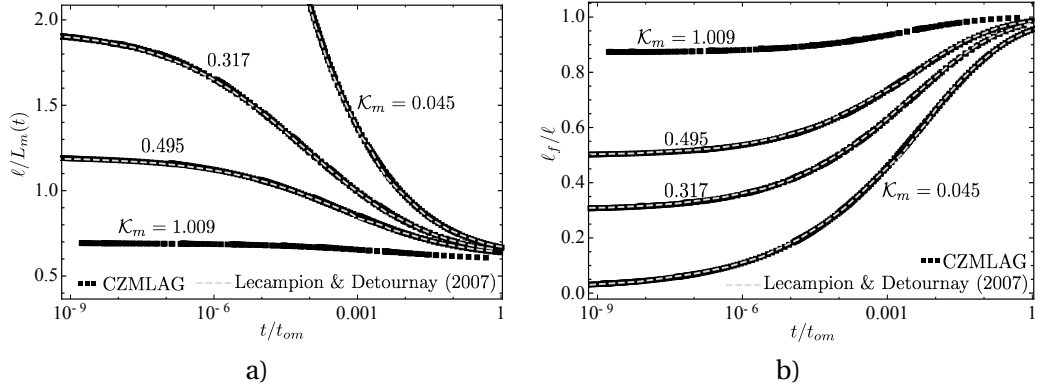
Figure 4.18 – Time evolution of a) the half fracture length and b) fluid fraction in viscosity scaling for different dimensionless toughness $\mathcal{K}_m$.

4.9 Supporting materials: Energy balance

Following Lecampion and Detournay (2007), we write the energy balance of a propagating cohesive HF by combining the energy dissipation in the fluid and solid. The external power provided by injecting fluid at a flow rate Q_o, under the inlet pressure $p_f(x = 0, t)$, is balanced by the rate of work expended by the fluid on the walls of the fracture and by viscous dissipation. Hence,

$$Q_o p_f(x = 0, t) = 2\int_0^{\ell_f} p_f \frac{\partial w}{\partial t}\mathrm{d}x - 2\int_0^{\ell_f} q\frac{\partial p}{\partial x}\mathrm{d}x, \quad q = -\frac{w^3}{\mu' f}\frac{\partial p}{\partial x} \tag{4.52}$$

where the cavity pressure in the lag zone is neglected in the above expression. By differentiating the global continuity equation with time,

$$Q_o = 2\int_0^{\ell_f} \frac{\partial w}{\partial t}\mathrm{d}x + 2\dot{\ell}_f w(\ell_f) \tag{4.53}$$

After multiplying the above expression by σ_o and subtracting it from Eq. (4.52), we obtain an alternative form of the energy balance in the fluid,

$$Q_o p_{f0} = Q_o\sigma_o + 2\int_0^{\ell_f} p\frac{\partial w}{\partial t}\mathrm{d}x - 2\int_0^{\ell_f} q\frac{\partial p}{\partial x}\mathrm{d}x - 2\sigma_o\dot{\ell}_f w(\ell_f) \tag{4.54}$$

For a fracture propagating quasi-statically in limit equilibrium in the solid, the fracture energy release rate is then written as the decrease of the strain energy rate and the work rate of the external forces (Keating and Sinclair, 1996).

$$\int_0^{\ell_f} p\frac{\partial w}{\partial t}\mathrm{d}x - \int_0^{\ell_f} w\frac{\partial p}{\partial t}\mathrm{d}x - \int_{\ell_f}^{\ell} \sigma_o\frac{\partial w}{\partial t}\mathrm{d}x + \int_0^{\ell} \sigma_{coh}\frac{\partial w}{\partial t}\mathrm{d}x - \int_0^{\ell} w\frac{\partial \sigma_{coh}}{\partial t}\mathrm{d}x = 0 \tag{4.55}$$

Eqs. (4.54) and (4.55) can be combined to yield an energy balance for the whole system.

$$P_e = Q_o p_{f0} = \dot{W}_o + \dot{W}_e + \dot{W}_l + D_k + D_v \tag{4.56}$$

where

$$
\begin{aligned}
\dot{W}_o &= Q_o \sigma_o, \\
\dot{W}_e &= \int_0^{\ell_f} p \frac{\partial w}{\partial t} dx + \int_0^{\ell_f} w \frac{\partial p}{\partial t} dx - \sigma_o \int_{\ell_f}^{\ell} \frac{\partial w}{\partial t} dx, \\
\dot{W}_l &= 2\int_{\ell_f}^{\ell} \sigma_o \frac{\partial w}{\partial t} dx - 2\sigma_o \dot{\ell}_f w(\ell_f) = 2\sigma_o \frac{d}{dt}\int_{\ell_f}^{\ell} w dx, \\
D_k &= -\int_0^{\ell} w \frac{\partial \sigma_{coh}}{\partial t} dx + \int_0^{\ell} \sigma_{coh} \frac{\partial w}{\partial t} dx \\
D_v &= -2\int_0^{\ell_f} q \frac{\partial p}{\partial x} dx
\end{aligned}
\tag{4.57}
$$

Using the linear-softening cohesive traction-separation law, we rewrite D_k in the coordinates of a moving tip

$$D_k = \int_{\ell-\ell_{coh}}^{\ell} \sigma_c \frac{w}{w_c} \frac{\partial w}{\partial t} dx + \int_{\ell-\ell_{coh}}^{\ell} \sigma_c \left(1 - \frac{w}{w_c}\right) \frac{\partial w}{\partial t} dx = \sigma_c \int_{\ell-\ell_{coh}}^{\ell} \frac{\partial w}{\partial t} dx = \sigma_c \int_0^{\ell_{coh}} \frac{\partial w}{\partial t} d\hat{x} \tag{4.58}$$

where

$$\hat{x} = \ell - x, \quad \frac{\partial w}{\partial t} = \left.\frac{\partial w}{\partial t}\right|_{\hat{x}} - (-\dot{\ell})\frac{\partial w}{\partial \hat{x}} \tag{4.59}$$

The energy dissipation during the fracturing process D_k can be thus simplified as follows

$$D_k = \sigma_c \int_0^{\ell_{coh}} \left.\frac{\partial w}{\partial t}\right|_{\hat{x}} d\hat{x} + \sigma_c \dot{\ell}\int_0^{\ell_{coh}} \frac{\partial w}{\partial \hat{x}} d\hat{x} = \sigma_c \int_0^{\ell_{coh}} \left.\frac{\partial w}{\partial t}\right|_{\hat{x}} d\hat{x} + 2\dot{\ell}(\frac{1}{2}\sigma_c w(\hat{x} = \ell_{coh})) \tag{4.60}$$

4.10 Supporting materials: Complementary results for a smooth cohesive hydraulic fracture with $\mathcal{K}_m = 0.495$

We show the time evolution of the cohesive zone length, the ratio between the lag and cohesive zone sizes, the apparent fracture energy, and the ratio of the energies dissipated in fluid viscous flow and in the creation of new fracture surfaces in Fig. 4.19 as complimentary information of Fig. 7 in the main text.

4.11 Supporting materials: Tip asymptote comparison with solutions for a semi-infinite cohesive hydraulic fracture

When the cohesive fraction is very small in a smooth HF, the tip asymptote tends to converge to the semi-infinite cohesive hydraulic fracture solution as reported in Garagash (2019). We show this trend in Fig. 4.20 for $\sigma_o/\sigma_c = 0.1, 1$ with different values of the cohesive-to-lag fracture
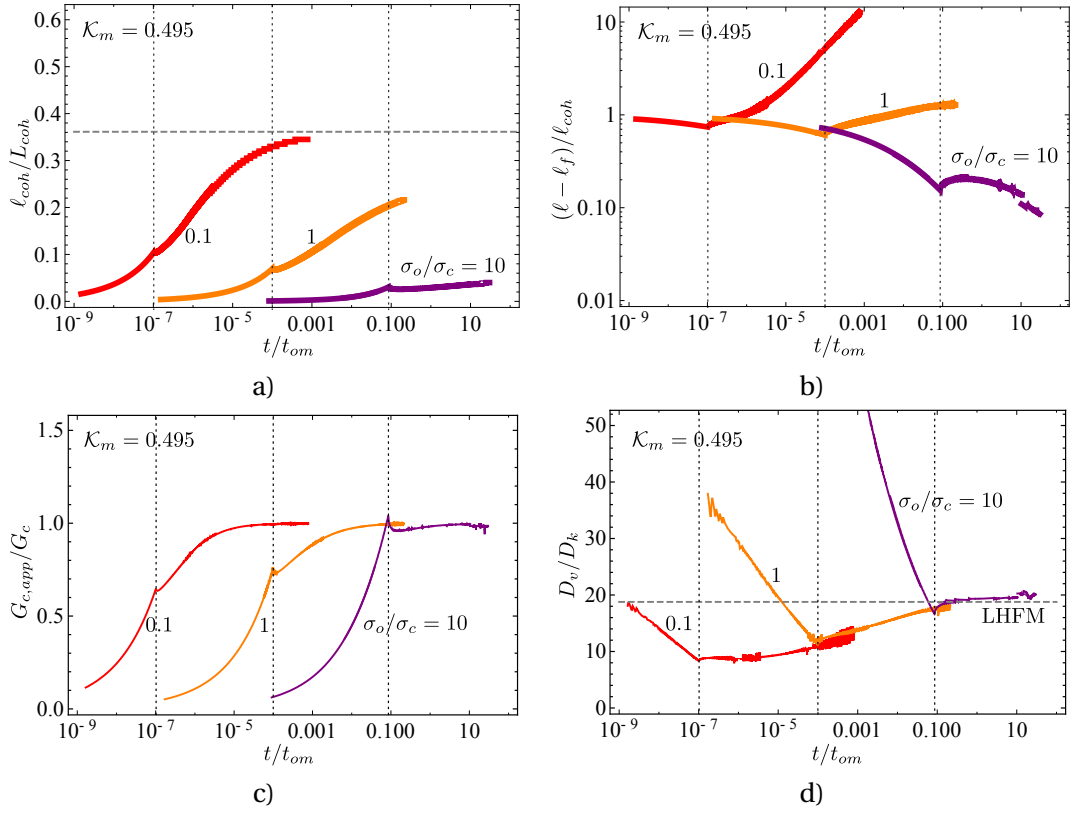
Figure 4.19 – $\mathcal{K}_m = 0.495$: evolution of a) the cohesive zone length ℓ_{coh}/L_{coh}, b) the ratio between the lag and cohesive zone sizes $(\ell - \ell_f)/\ell_{coh}$, c) the apparent fracture energy $G_{c,app}/G_c$, and d) the ratio of the energies dissipated in fluid viscous flow and in the creation of new fracture surfaces D_v/D_k with t/t_{om}. The red, orange and purple curves indicate the smooth cohesive hydraulic fracture with the confining stress $\sigma_o/\sigma_c = 0.1, 1, 10$ with the dotted vertical lines as their corresponding cohesive zone nucleation period. The dashed horizontal line in Figure a) represents the small-scale yielding asymptote ($\approx 0.115\pi$) of the cohesive zone length for the linear-softening cohesive model (Dempsey et al., 2010). The dashed horizontal line in Figure d) represents the LHFM limit with zero lag.
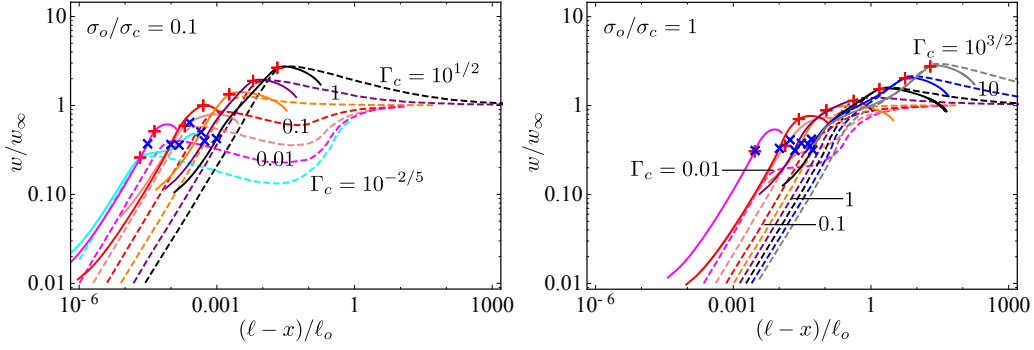
Figure 4.20 – The crack opening normalized by the far-field 'm'-asymptote for $\sigma_o/\sigma_c = 0.1, 1$ and various values of $\Gamma_c = G_c/G_o$ (see the definition in Eq. (4.61)) between $10^{-5/2}$ and $10^{3/2}$ in $10^{1/2}$ increments on the logarithm scale. The dashed curves are semi-infinite solutions in Garagash (2019). The solid curves are results of a smooth plane-strain cohesive hydraulic fracture whose corresponding cohesive fractions are shown in Table. 4.5. "+" indicates the boundary of the cohesive zone and "×" the fluid front location.

energy ratio Γ_c which is defined as

$$\Gamma_c = \frac{G_c}{G_o} = \frac{G_c}{w_o\sigma_o} = \frac{1}{2}\frac{w_c\sigma_c\sigma_o}{E'\mu'V} \tag{4.61}$$

$$w_o = \frac{\sigma_o}{E'}\ell_o, \quad \ell_o = \frac{\mu'V}{E'}\left(\frac{E'}{\sigma_o}\right)^3 \tag{4.62}$$

where V represents the fracture front velocity and ℓ_o the lag length scale (Garagash, 2019). The fracture opening in Fig. 4.20 is normalized by the far field 'm' asymptote:

$$w_\infty = 2^{1/3}3^{5/6}\left(\frac{\mu'V}{E'}\right)^{1/3}(\ell-x)^{2/3} \tag{4.63}$$

The tip asympotote of a finte fracture shows an offset from the semi-infinite solution (Fig. 4.20). This offset results from the finite size of the fracture dimension and a relatively important fraction of the cohesive zone (see Table. 4.5).

$\Gamma_c = G_c/G_o$	$10^{-5/2}$	0.01	$10^{-3/2}$	0.1	$10^{-1/2}$	1	$10^{1/2}$	10	$10^{3/2}$
Color in Fig. 4.20	Cyan	Magenta	Pink	Red	Orange	Purple	Black	Blue	Gray
ℓ_{coh}/ℓ ($\sigma_o/\sigma_c = 0.1$) (%)	5.0	33.7	6.90	44.0	5.57	11.5	11.4		
ℓ_{coh}/ℓ ($\sigma_o/\sigma_c = 1$) (%)		26.2	4.9	22.9	3.50	39.2	3.50	11.1	10.9

Table 4.5 – Cohesive fractions of finite fractures in Fig. 4.20.

Experiments Part II

5 Time-lapse reconstruction of the fracture geometry using acoustic transmission and diffraction

4D acoustic imaging via an array of 32 sources / 32 receivers is used to monitor hydraulic fracture propagating in a 250 mm cubic specimen under a true-triaxial state of stress. This chapter presents a method based on the arrivals of diffracted waves to reconstruct the fracture geometry (and fluid front when distinct from the fracture front). Using Bayesian model selection, we rank different possible fracture geometries (radial, elliptical, tilted or not) and estimate model error. The imaging is repeated every 4 seconds and provide a quantitative measurement of the growth of these low velocity fractures. We test the proposed method on two experiments performed in two different rocks (marble and gabbro) under experimental conditions characteristic respectively of the fluid lag-viscosity (marble) and toughness (gabbro) dominated hydraulic fracture propagation regimes. In both experiments, about 150 to 200 source-receiver combinations exhibit clear diffracted wave arrivals. The results of the inversion indicate a radial geometry evolving slightly into an ellipse towards the end of the experiment when the fractures feel the specimen boundaries. The estimated modelling error with all models is of the order of the wave arrival picking error. Posterior estimates indicate an uncertainty of the order of a millimeter on the fracture front location for a given acquisition sequence. The reconstructed fracture evolution from diffracted waves is shown to be consistent with the analysis of 90° incident angle transmitted waves across the growing fracture.

This chapter is a modified version of the following scientific article:

Liu, D., Lecampion, B., Blum, T. (2020), Time-lapse reconstruction of the fracture front from diffracted waves arrivals in laboratory hydraulic fracture experiments, *Geophysical Journal International*, 223, 180–196.

Authors contributions

B. Lecampion and T. Blum have designed the loading frame and the active acoustic measurement system. D. Liu has designed the hydraulic fracture injection under the guidance of B. Lecampion. D. Liu has performed the laboratory experiments under the guidance of T. Blum.

B. Lecampion, T. Blum, and D. Liu have set up the methodology of the analysis. D. Liu has written the numerical code to pick the diffracted arrivals. Based on these picked arrivals, D. Liu and B. Lecampion have written the numerical code to reconstruct the fracture geometry. D. Liu has analyzed the experimental results under the guidance of B. Lecampion. D. Liu and B. Lecampion have written the manuscript.

5.1   Introduction

Hydraulic fractures (HF) are a class of tensile fractures that propagate in a material as a result of fluid pressurization (Detournay, 2016). They are encountered in a number of industrial applications such as oil and gas production, geothermal energy and block caving mining. HFs also propagate naturally in the form of magmatic dikes (Rivalta et al., 2015), or at glaciers bed due to the sudden release of surface melt water lakes (Tsai and Rice, 2010). Investigation of the growth of such fluid-driven fractures under controlled conditions at the laboratory scale plays an important role in order to validate theoretical predictions.

Since the early work of Hubbert and Willis (1957), the measurement of the hydraulic fracture geometry has evolved from simple postmortem observations after the experiment to the use of continuous monitoring techniques during fracture growth. These developments have been slow and in most cases only post mortem observations are reported although sometimes via high resolution X-ray CT (Liu et al., 2016). A photometry method based on the intensity drop of a back-light source as it passes through a dyed fracturing fluid has been successfully used to monitor hydraulic fractures in transparent materials (Bunger, 2006). Such an optical technique has allowed to measure the evolution of both the fracture extent and the full field of fracture opening. Combined with particle image velocimetry, it also allows to measure the fluid velocity field in the growing fracture (O'Keeffe et al., 2018). These experimental techniques have provided invaluable data sets and insights into hydraulic fracture growth in transparent materials, such as PMMA, glass and hydrogel. They have notably helped in validating important theoretical predictions of hydraulic fracture mechanics (Bunger and Detournay, 2008; Wu et al., 2008; Bunger et al., 2013; Xing et al., 2017). However, by definition, these optical methods can not be used in non-transparent materials. In rocks, acoustic emission (AE) monitoring is the main technique used to track the evolution of rupture (Lockner and Byerlee (1977); Zoback et al. (1977); Ishida (2001); Stanchits et al. (2014, 2015); Goodfellow et al. (2015); Stoeckhert et al. (2015) to cite a few). AE events, however, do not provide a direct measurement of fracture geometry as they are mostly associated with micro-slips around the growing fracture (Rodriguez et al., 2016). The observations of self-potential (Moore and Glaser, 2007; Haas et al., 2013) during HF experiments correlate with pressure evolution and appear to highlight fluid flow patterns but do not provide an accurate measurement of the growing fracture. Advanced imaging techniques such as Neutron imaging have been recently attempted (Roshankhah et al., 2018) as well as 2D digital image correlation (DIC) (Jeffrey et al., 2015; Zhao et al., 2020). Neutron imaging necessitates the use of relatively small specimen (to achieve sufficient resolution) while the application of 2D DIC imposes the use of intricate

specimen geometry and boundary conditions not suited to hydraulic fracturing.

We focus here on active acoustic imaging, a method akin to a 4D seismic survey at the laboratory scale in the ultrasonic range. Earlier studies (Medlin et al., 1984; De Pater et al., 1996; Glaser and Hand, 1998; van Dam, 1999; Groenenboom and van Dam, 2000) have shown its capability to obtain quantitative information during laboratory hydraulic fracture experiments. The wave-field interacts in different ways with the growing fracture. It can be diffracted by the fracture tip (as well as the fluid front if a lag is present near the fracture tip) but also reflected by and transmitted through the fluid-filled fracture. The evolution of transmitted waves has notably allowed to identify a dry region near the fracture tip (fluid lag) (Medlin et al., 1984; De Pater et al., 1996). Records of the arrival times of waves diffracted by the fracture have enabled to estimate the evolving fracture tip position under the hypothesis of a horizontal radial fracture centered on the injection point (Groenenboom and van Dam, 2000; Groenenboom and Falk, 2000). Opening of the fracture results in attenuation and delay of transmitted waves. It thus allows to evaluate the fluid layer thickness by matching the spectrum of the transmitted signals with the transmission coefficient of a three layers model (Groenenboom and Fokkema, 1998). These two techniques (diffraction and transmission) have been shown to provide results in agreement with optical methods (Kovalyshen, 2014).

In this chapter, we improve the imaging of a growing hydraulic fracture by using an unprecedented amount of piezoelectric source/receiver pairs and relaxing the assumption of a centered horizontal radial fracture. We test the method on two experiments performed in quasi-brittle rocks (marble and gabbro) which may exhibit different fracture growth behavior compared to PMMA, plaster or cement-based materials used in the previous studies cited above. We first present our experimental set-up, the rocks and experimental conditions used. After illustrating the type of diffracted waves measured in these experiments, we develop an inverse problem for the fracture / fluid front reconstruction. This inversion is then performed repeatedly in time for each acquisition sequence. We use different shapes (ellipse, circle with or without tilt) to parameterize the fracture front geometry and use Bayesian model selection to rank these different models. We finally compare the results obtained from the inversion of diffracted waves with transmitted waves data.

5.2 Experimental methods

5.2.1 Experimental set-up and specimen preparation

Hydraulic fracture growth experiments are carried out in 250 mm cubic rock samples under a true triaxial compressive state of stress as illustrated in Fig. 5.1. The confinement is applied by symmetric pairs of flat jacks in the three axis of a poly-axial reacting frame. Compressive stresses up to 20 MPa can be applied prior to injection. The fracturing fluid is injected in a central wellbore by a syringe pump (ISCO D160) at a constant flow rate (in the range 0.001 mL/min to 107 mL/min) with a maximum injection pressure of 51 MPa. An interface
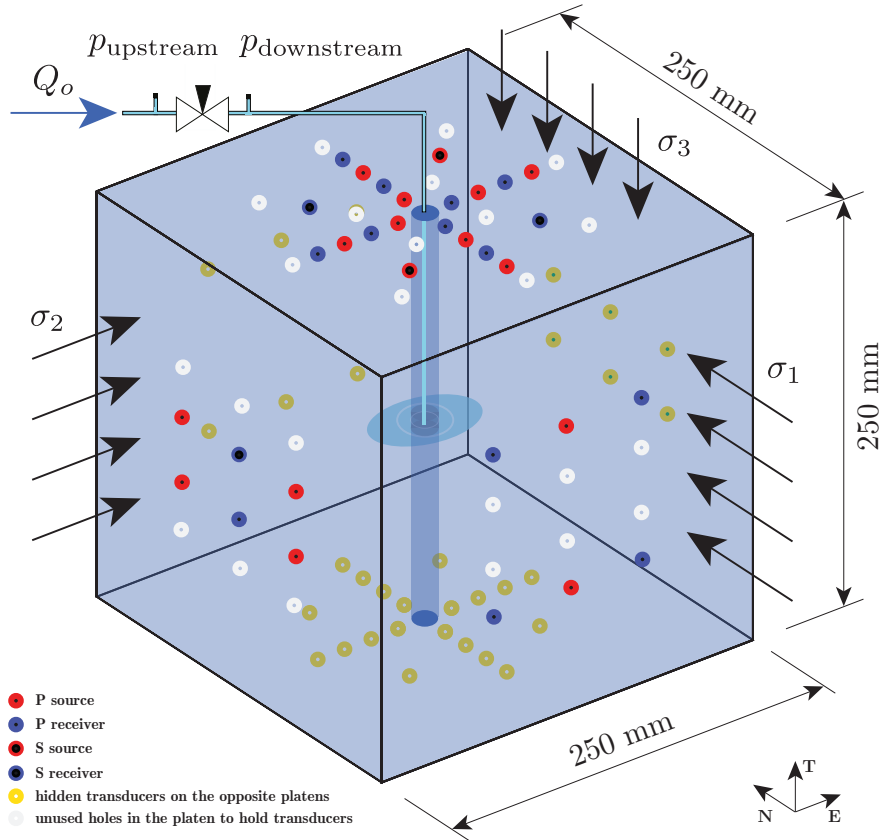
Figure 5.1 – Schematic illustration of the rock sample showing the transducers disposition for the GABB-001 experiment. Additional holes are available in the platens allowing the use of various transducer dispositions. Two facing platens share the same transducers disposition and source / receivers transducers are alternately located on opposite platens for robustness.

vessel in the injection line allows to inject a wide range of fluid type with viscosity ranging from 1 mPa.s to 1000 Pa.s. Due to the compliance of the injection system (i.e. volume of fluid in the injection line), upon fracture initiation the flow rate entering the fracture does not equal the pump injection rate Q_o during a transient phase (Lhomme, 2005; Lecampion et al., 2017). A needle valve is thus placed in the injection line close to the well-head in order to control the release of fluid compressed during the pressurization phase. Using volume conservation within the injection system (pump to fracture inlet), it is possible to estimate the flow rate $Q_{in}(t)$ entering the fracture by taking the derivatives of the fluid pressure measurements (see Section 5.7.1 for details).

The rock sample is first rectified as a cube of 250 mm × 250 mm × 250 mm dimensions. We polish the specimen surfaces to minimize friction and to ensure a good contact between the piezo-electric transducers and the rock. A wellbore of 16 mm diameter is drilled through the block and a horizontal axisymmetric notch (with a diameter of 21 mm ± 1 mm) is created in the middle of the sample via a specifically designed rotating cutting tool. The resulting notch

Table 5.1 – Material properties (V_p and V_s are measured directly on the cubic rocks during the pressurization stage prior to any fracture growth).

Rock	V_p (m/s)	V_s (m/s)	ρ ($\times 10^3$kg/m^3)	Grain size (mm)
Carrara marble	6249.8 ± 54.0	3229.9 ± 176.2	2.69	0.1-0.2
Zimbabwe gabbro	6679.0 ± 113.2	3668.5 ± 41.3	3.00	1-3

Table 5.2 – Sample configuration and experimental parameters for Zimbabwe gabbro and Carrara marble.

Rock sample	Block size (mm)	σ_3 (MPa)	$\sigma_1 = \sigma_2$ (MPa)	Location of the notch from the sample bottom x_3 (mm)
GABB-001	$250 \times 250 \times 251$	0.5	10.5	128.5
MARB-005	$257 \times 256 \times 256$	10	20	131
	Fracturing fluid	Viscosity μ (Pa.s)	Injection rate Q_o (mL/min)	System compliance U (mL/GPa)
GABB-001	Glycerol	0.6	0.2	217.3
MARB-005	Silicone oil	100	0.2	282.5

is axisymmetric and its plane perpendicular to the well axis. A completion tool connected to a injection tubing is epoxied in the wellbore and allows to inject fluid only at the notch level.

Active acoustic monitoring is integrated within the poly-axial cell. 64 piezoelectric transducers are included in the loading platens: 32 transducers act as sources and 32 as receivers. This array of transducers consists of 10 shear-wave transducers and 54 longitudinal-wave ones. We use a source function generator connected to a high-power amplifier to send a Ricker excitation signal with a given central frequency that can be set between 300 and 750 kHz depending on the material type. The source signal is routed to one of the 32 source transducers via a multiplexer. The 32 receiver transducers are connected to a high-speed acquisition board in order to record the signal simultaneously on all receivers with a sampling frequency of 50 MHz. As the switch between sources is limited by the multiplexer, the excitation of a given source is repeated 50 times and the data stacked to improve signal to noise. Spanning of the 32 sources defines an acquisition sequence and takes about 2.5 seconds in total. In addition to acoustic data, we record fluid injection pressure (upstream and downstream the needle valve), volume and pressure of each flat-jack pairs at 1 Hz. All the measurements are synchronized via a dedicated LabView application.

5.2.2 Laboratory hydraulic fracturing experiments

We discuss in this chapter two experiments performed respectively in Zimbabwe gabbro and Carrara marble. Zimbabwe gabbro (plagioclase, mica, biotite and amphibole, quartz) has a larger grain size than Carrara marble (calcite, mica) as illustrated in Fig. 5.2, which usually implies a larger fracture process zone (Ouchterlony, 1982). Both rocks have isotropic acoustic properties (see in Table. 5.1). We impose a bi-axial state of stress on the block setting

Table 5.3 – Characteristic time-scales for a radial hydraulic fracture: viscosity-toughness transition t_{mk}, fluid lag disappearance time scale t_{om}. We estimate these time-scales using the averaged entering flow rate into the fracture $< Q_o >$ during the fracture duration t_{prop} and the following material properties: a) for Zimbabwe gabbro, $E = 68.4$ GPa (Technologies, 2005), $v = 0.3$ (assumed), $K_{Ic} = 3.03$ MPa.m$^{1/2}$ (Meredith and Atkinson, 1985); b) for Carrara marble, $E = 65$ GPa, $v = 0.25$ (Gulli et al., 2015), $K_{Ic} = 1.38$ MPa.m$^{1/2}$ (Ouchterlony, 1990).

Rock	$< Q_o >$ (mL/min)	Propagation duration t_{prop} (s)	t_{mk} (s)	t_{om} (s)
GABB-001	0.074	≈ 410	4.0×10^{-4}	3.3×10^5
MARB-005	0.046	≈ 582	5.0×10^4	5.8×10^3

$\sigma_1 = \sigma_2$, while the minimum stress $\sigma_3 < \sigma_1 = \sigma_2$ is set parallel to the wellbore in order to favour a planar fracture initiating from the axisymmetric notch, in other words, promoting a transverse fracture to the wellbore (as shown in Fig. 5.2). Glycerol (gabbro) or silicone oil (marble) is used as fracturing fluids. The fluid is injected at a constant rate. All experimental parameters are listed in Table 5.2. The active acoustic monitoring is conducted with a central frequency of 750 kHz for the source excitation. This results in a wavelength of around 9 mm for compressional waves in both rocks whose grain size is at most 3 mm in gabbro and 0.2 mm in marble. In both experiments, acoustic acquisition is performed with a larger period during the pressurization phase and then switched to every 4 seconds during fracture propagation as shown in Fig. 5.3 and Fig. 5.4.

Injection Design

The propagation of a fluid-driven fracture is a multiscale physical process. For a radial hydraulic fracture propagating in a tight material, it is now well established that initially at early time due to the injection of a viscous fluid, a fluid-less cavity (fluid lag) forms at the fracture tip (see Detournay (2016) and references therein). The fluid front then catches up with the fracture front over a characteristic time-scale

$$t_{om} = E'^2 \mu' / \sigma_3^3 \tag{5.1}$$

where $E' = \frac{E}{1-v^2}$ is the plane-strain elastic modulus related to the Young's modulus and Poisson's ratio, $\mu' = 12\mu$ with μ the fluid viscosity and σ_3 is the minimum applied stress (normal to the fracture plane). In addition, as the perimeter of the radial fracture grows, the energy spent in creating new fracture surfaces increases. The propagation switches from a regime dominated by fluid viscosity to a regime dominated by fracture toughness. This evolution is captured by a dimensionless toughness $\mathcal{K} = (t/t_{mk})^{1/9}$, where t_{mk} is the transition time-scale from the viscosity to toughness dominated regimes of growth:

$$t_{mk} = \frac{E'^{13/2} Q_o^{3/2} \mu'^{5/2}}{K'^9}, \quad K' = \sqrt{\frac{32}{\pi}} K_{Ic}, \tag{5.2}$$
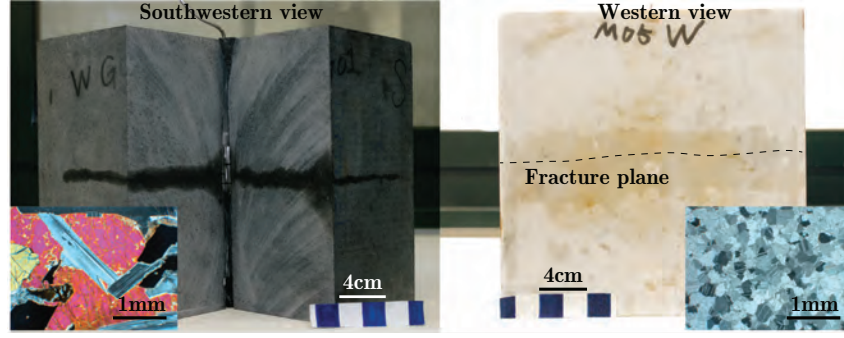
Figure 5.2 – Thin section of Zimbabwe gabbro and Carrara marble and the postmortem photos of the cut blocks after GABB-001 and MARB-005 experiments. The wet region around the fracture in the gabbro block does not necessarily indicate a large leak-off during the injection. The visible inhibition occurred mostly after the experiment as the block was cut and photographed 25 days after the experiment.

where K_{Ic} is the mode I fracture toughness. More precisely, the fracture grows in the viscosity dominated regime as long as $\mathcal{K} \lesssim 1$ and strictly in the toughness dominated regime for $\mathcal{K} \gtrsim 3.5$ (Savitski and Detournay, 2002). Moreover, the fluid lag vanishes at all time in the toughness dominated regime (Lecampion and Detournay, 2007). In other words, if $t_{mk} \ll t_{om}$, no fluid lag is observed.

Experimentally, for a given rock, one can adjust the injection rate Q_o, fluid type (viscosity μ) and the minimum stress perpendicular to the fracture plane σ_3 to explore a given propagation regime. We refer to Bunger et al. (2005b) for the proper scaling and experimental design of laboratory hydraulic fracture experiments. The two experiments reported herein are characteristic examples of two very different hydraulic fracture propagation regimes (toughness and lag-viscosity dominated). Table 5.3 lists the corresponding time-scales estimated using values of the rock properties from the literature and the averaged injection rate. In both experiments, the compliance of the injection system is rather important. As a result, the flow rate entering the fracture Q_{in} is not constant and equal to the pump rate. It can however be estimated from the injection pressure and injection system compliance (see Section 5.7.1 for details). The GABB-001 experiment is toughness dominated as the propagation time is much larger than the viscosity - toughness transition time-scale and no fluid lag is expected during the fracture propagation ($t_{mk} < t_{om}$). On the other hand, the MARB-005 experiment is such that the propagation occurs in the so-called lag / viscosity dominated regimes (Lecampion et al., 2017): the propagation duration is smaller than both t_{om} and $t_{mk} > t_{om}$.

Toughness-dominated experiment GABB-001

The gabbro experiment (GABB-001) is a so-called toughness dominated experiment. For such type of experiments, the fluid pressure downstream of the valve responds almost instantly to fracture growth and the fracture propagation might be over in a few seconds due to the
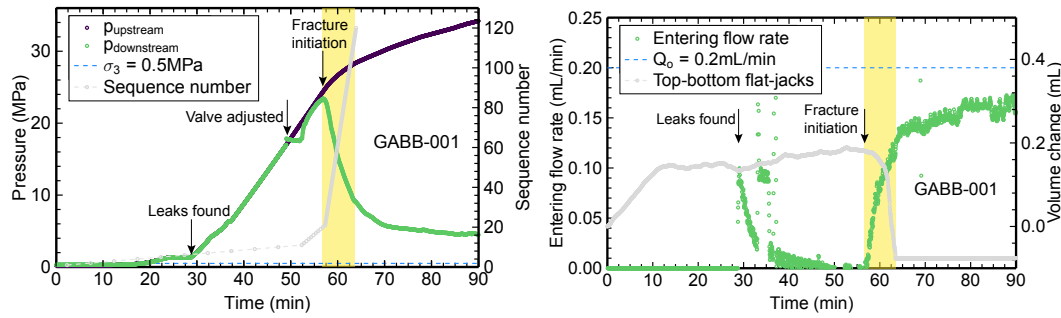
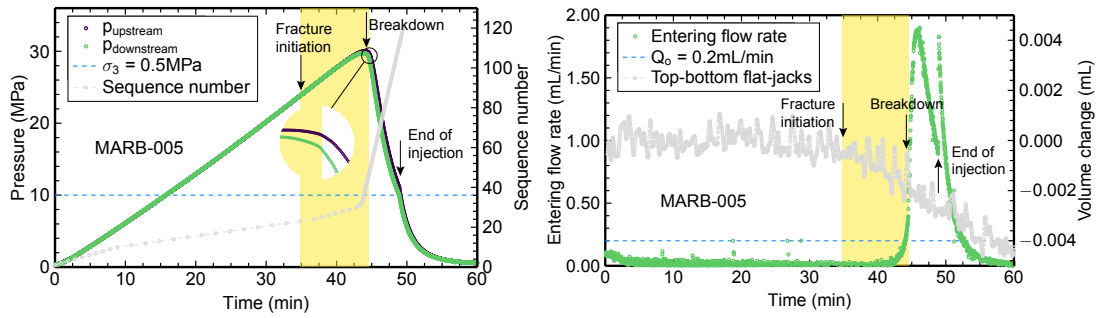Figure 5.3 – GABB-001 experiment: evolution of the upstream and downstream pressure, and the mapping relation between the number of acquisition sequence and experimental time (left); and evolution of the entering flow rate of the fluid into the fracture, and the volume change of the top-bottom flat-jacks (right). The yellow coloured time interval indicates the propagation of the fracture through the block (from the notch to the end of the block).

sudden release of the compressed fluid following the fracture initiation (see Lecampion et al. (2017) for discussion). It is therefore necessary to constrain the fluid flow with the needle valve to obtain a steady and sufficiently long fracture growth. In this experiment, the needle valve is open at the start of the pressurization. We then partly close the needle valve after we observe a linear increase of the pressure with a rate of Q_o/U (pending the fix of an initial leak in the injection line) as can be seen in Fig. 5.3. To do so, we first completely close the needle valve for several minutes during which the upstream pressure continues to increase. We then slightly reopen the valve position to ensure that it sufficiently damps the entering flux. We then keep it in that position for the remainder of the experiment. As shown in Fig. 5.3, in that experiment, the fracture initiates shortly after the adjustment. The needle valve does prevent a complete sudden release of the fluid pressurized in the line. More fluid enters into the upstream injection line from the pump rather than flows downstream of the needle valve: the upstream pressure keeps rising whereas the downstream one drops due to the fluid flow into the newly created fracture. The fracture initiation time is confirmed by the response of the flat-jacks volume parallel to the fracture plane - as well as the acoustic data as later presented. When the fracture front reaches the edges of the block, there are no more constraints on its deformation and a sudden response of the flat-jacks is observed as well as a kink in the downstream injection pressure (see Fig. 5.3).

Lag-viscosity experiment MARB-005

The marble experiment (MARB-005) is characterised by a large fluid lag and strong viscous drop. A restriction tube with a diameter of 1 mm was placed in the injection line instead of the needle valve. Silicone oil was used as a fracturing fluid. Due to the large viscous effect, it takes time for the fluid to enter the fracture. The fracture initiation can be estimated from the response of the top-bottom flat-jacks and the appearance of acoustic diffraction. It is however indistinguishable from the pressure record - inline with previous observations (Zhao et al.,

Figure 5.4 – MARB-005: evolution of the upstream and downstream pressure, and the mapping relation between the number of acquisition sequence and experimental time (left); and evolution of the entering flow rate of the fluid into the fracture, and the volume change of the top-bottom flat-jacks (right). The volume change of the top-bottom flat-jacks in MARB-005 is much smaller than for the GABB-001 experiment. This is most likely due to the presence of air bubbles inside the flat-jacks. The yellow coloured time interval indicates the propagation of the fracture through the block (from the notch to the end of the block).

1996; Lecampion et al., 2017). As can be seen from Fig. 5.4, the entering flow rate remains limited after fracture initiation. A large fluid lag develops behind the fracture front (as can be seen from the acoustic data on Fig. 5.5). The pressure in the injection line keeps increasing until the fracture front almost reaches the edges of the block. The fluid front continues to grow afterwards but the elastic deformation (and thus the hydro-mechanical coupling) is now different. This results in an increase of the entering flow rate which correlates with a small kink in the downstream pressure. We thus use this point to approximate the time at which the fracture reaches the end of the block. It is worth noting that the maximum pressure (often misleadingly denoted as the breakdown pressure) occurs just before that time.

5.3 Examples of acoustic diffraction data

As observed in previous laboratory experiments (Groenenboom and Falk, 2000; De Pater et al., 2001), the initial notch, fracture front, and fluid front (Groenenboom and van Dam, 2000) may all serve as a source of diffraction. Each receiver may record its corresponding compressional or shear component of both the compressional wave (P-wave) and shear wave (S-wave) depending on the arriving incident angle. Following Groenenboom and Falk (2000), we categorise different acoustic events. We denote the diffraction along the fracture or fluid front with a 'd' and the interactions (reflection or diffraction) at the notch with an 'n'. We recall here some travel paths of diffracted waves observed in the two experiments presented here:

- direct diffraction of the body wave at the fracture or fluid front with or without mode conversion: for example compressional waves diffracted by the fracture front without mode conversion (PdP), or shear waves diffracted by the fracture front with mode conversion (SdP).
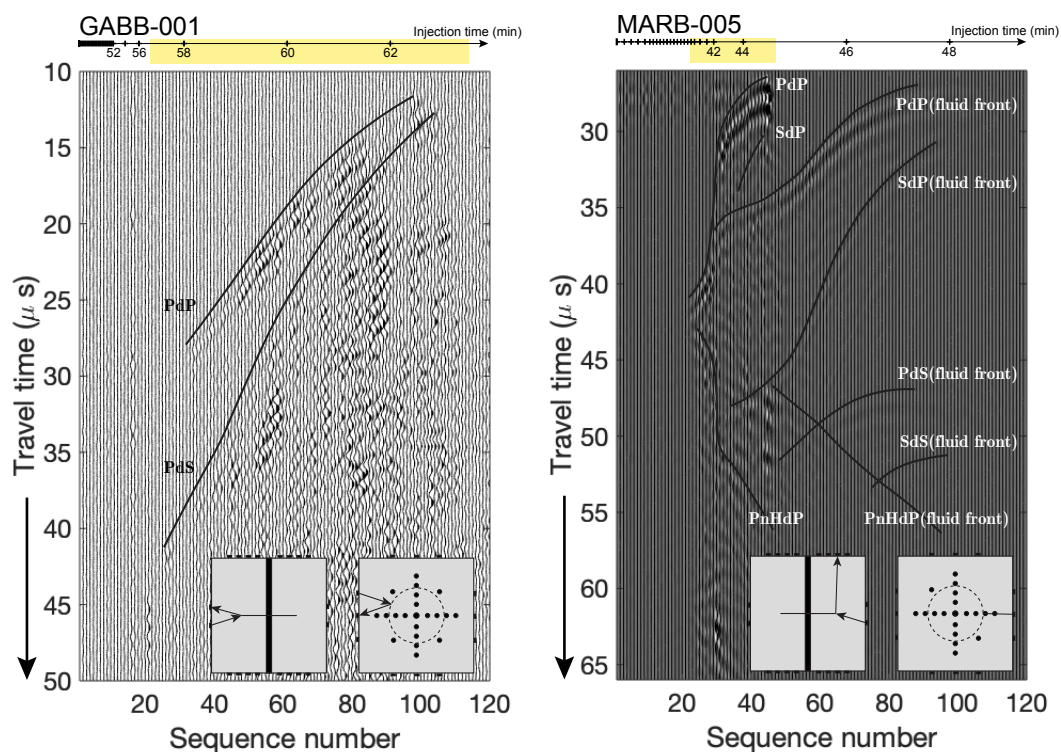
Figure 5.5 – Illustration of different diffracted waves pattern in GABB-001 and MARB-005 experiments. For MARB-005, a gray-scaled image of the data is shown combined with a wiggle plot. The yellow coloured time interval represents approximately the propagation of the fracture (from the notch to the end of the block).

- diffraction of the head wave (P wave guided by the fracture interface, denoted as H (Savic, 1995)) at the fracture tip with or without mode conversion. For example, PnHdP represents a P wave that is guided along the fracture interface after interacting with the notch. It is then diffracted at the fracture tip without mode conversion (see Fig. 5.5).

Previous studies (Groenenboom and Falk, 2000; De Pater et al., 2001) have observed more events related to reflections of the wavefield at the borehole tube and generalized Rayleigh waves propagating along the fracture. Such diffraction events arrive much later than the direct diffraction of body waves. Their signal to noise is often not sufficient to allow a proper picking of these later arrivals. We thus focus mainly on the diffracted body waves (PdP, PdS and SdP here). As shown in Fig. 5.5, we are only able to observe PdP and PdS arrivals in GABB-001 for the chosen transducer pair, while for most transducer pairs only PdP arrivals can be clearly identified. In MARB-005, we are able to recognize more diffracted waves, notably by both the fracture and the fluid fronts but also by the notch (PnHdP). In particular, the fluid front acts as a strong diffractor.

There are multiple techniques to visualize the evolution of the diffracted waves, as shown in Fig. 5.5. Groenenboom (1998) and Savic (1995) have proposed to remove the direct incident wavefield by subtracting the signal recorded at a given time with the one recorded in the absence of the fracture at the beginning of the experiment. This is sufficient to properly see the first diffracted wave arrival PdP. However, we have found that for our experiments, subtracting the signal recorded at a given acquisition sequence with the one of the previous sequence provide a clearer image of the diffracted waves (notably the later ones). This is akin as a high pass filter along the experimental time axis (dimension of the sequence number) on the diffraction plots as in Fig. 5.5.

The reason why making the difference with the first sequence provides more blurry image is likely due to the evolution of the scattering background associated with the fracture roughness. The diffracted coda wave is much more noisy in the gabbro compared to the marble experiment, in line with the difference of rock grain size and posterior fracture roughness observed.

5.4 Reconstruction of the fracture and fluid fronts using Bayesian inversion

From the picking of the diffracted wave arrivals (for different source-receiver pairs), we invert for the geometry of the fracture or fluid front. We do so using different geometries for the diffraction front. We use a Bayesian framework to rank these different geometrical models. The inverse problem is performed for each acquisition sequence independently in order to finally obtain the time evolution of the fracture geometry.
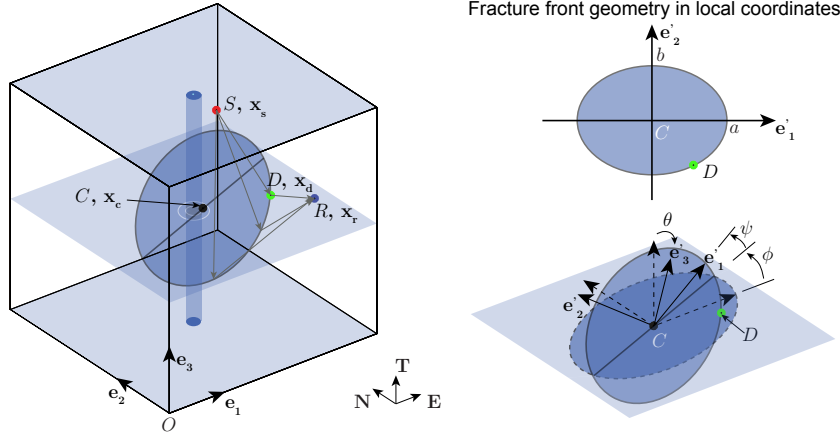
Figure 5.6 – Illustration of the fracture front geometry and its corresponding diffractor position for a given source-receiver pair. The diffractor position D (in green) characterises the shortest travelling time between the source S (in red) and the receiver R (in blue) among all positions along a given fracture front. The fracture geometry is assumed to be planar and is defined in a local coordinate system ($\mathbf{e'_i}$, $i = 1, 2, 3$) with its geometric center C as the origin. The geometric description in the global coordinate system ($\mathbf{e_i}$, $i = 1, 2, 3$) is obtained after coordinates transformation (rotation and translation).

5.4.1 Forward models

In the case of the direct diffraction of a body wave by the fracture front, the theoretical arrival t^d_{sr} of the diffracted wave for a chosen source-receiver pair is simply given by

$$t^d_{sr} = \frac{\|\mathbf{x_s} - \mathbf{x_d}\|}{V_{sd}} + \frac{\|\mathbf{x_d} - \mathbf{x_r}\|}{V_{dr}} \tag{5.3}$$

where V_{sd} and V_{dr} are respectively velocities of the incident wave and diffracted wave (P-wave or S-wave). $\mathbf{x_s}$, $\mathbf{x_r}$ represent the coordinates of the source and receiver transducers and $\mathbf{x_d}$ the coordinates of the diffractor, as illustrated in Fig. 5.6. For a given fracture front geometry, $\mathbf{x_d}$ is obtained as the point which gives the minimal diffracted wave arrival t_{sr} for a given source-receiver pair. We assume here that the diffraction front is planar. We parametrize it using a simple shape. We consider a possible offset of the fracture geometric center C with the injection point and denote $\mathbf{x_c} = (x_1, x_2, x_3)$ its coordinates. We also allow a possible tilt of the fracture plane captured by the three Euler angles: the dip θ, azimuth ϕ, and precession ψ (see Fig. 5.6).

We use an ellipse or a circle to describe the geometry of the diffraction front. In order to account for a possible tilt of the fracture, we invert the data with four different forward models having different number of parameters $\mathbf{m}$ as listed in Table 5.4. In the case of an elliptical diffraction front, 8 parameters describe its geometry: the semi-lengths of the ellipse a and b, $\mathbf{x_c} = (x_1, x_2, x_3)$ the position of the geometric center and three Euler angles ϕ, θ, ψ characterising the fracture plane orientation (see Fig. 5.6).
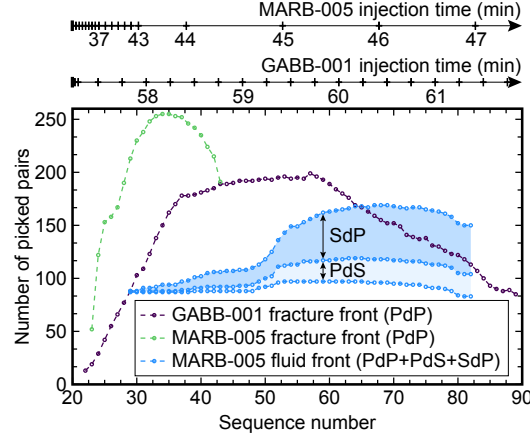
Figure 5.7 – The number of diffracted arrivals picked from different source-receiver pairs in GABB-001 and MARB-005 experiments. The corresponding acquisition time is indicated at the top of the figures with one tick every 15 seconds for GABB-001 and every minute for MARB-005.

For a given geometrical model of the fracture front, we relate the measured diffracted arrivals for the different source-receiver pairs with the forward predictions as

$$\mathbf{d} = \mathbf{G}(\mathbf{m}) + \epsilon \tag{5.4}$$

where $\mathbf{d}$ denotes the picked arrival time for the different source-receiver pairs, $G(\mathbf{m})$ the arrival time predicted by the forward model, and ϵ combines both measurement and modelling errors. For simplicity (Tarantola, 2005), we will assume that ϵ follows a Gaussian distribution with zero mean and variance of σ^2. We will notably invert for σ here thus providing a measure of the modelling error.

For a chosen source-receiver pair, we manually pick the arrival time of the diffracted waves for different sequences using plots similar as Fig. 5.5. A spline is first drawn along the diffracted arrival. The coordinates of the spline passing through the corresponding sequence numbers are then collected as picked arrival time. It is worth noting that the number of picked source-receiver pairs may vary with time, as notably the diffracted arrivals are less visible for some pairs at early (close to initiation for small fractures) and late time (due to proximity of the fracture front with the edges of the block). The number of picked arrivals and their types of diffraction events for the different acquisition sequence is reported in Fig. 5.7.

5.4.2 Inverse problem

We seek to estimate both the model parameters $\mathbf{m}$ as well as the measurement/model error σ (Lecampion and Gunning, 2007). The likelihood of the data being correctly predicted by the model assumes a multivariate normal probability density function (PDF) for Eq. (5.5) with a

Table 5.4 – Model description and model parameters. N_p is the number of the parameters. $A = \ln a$, $B = \ln b$, $R = \ln r$ are adjusted fracture size parameters accounting for the values of original parameters, e.g. a, b, r, greater than zero. $\mathbf{x_c} = (x_1, x_2, x_3)$ characterises the offset of the geometric center of the diffraction front with respect to the origin of the global coordinate system.

Model	Model description	N_p	Model parameters $\mathbf{m}$
$\mathcal{M}_1$	Elliptical shape	8	$[A, B, x_1, x_2, x_3, \psi, \theta, \phi]$
$\mathcal{M}_2$	Circular shape ($a = b = r$, $\psi = 0$)	6	$[R, x_1, x_2, x_3, \theta, \phi]$
$\mathcal{M}_3$	Horizontal elliptical shape ($\theta = \phi = 0$)	6	$[A, B, x_1, x_2, x_3, \psi]$
$\mathcal{M}_4$	Horizontal circular shape ($\psi = \theta = \phi = 0$)	4	$[R, x_1, x_2, x_3]$

Table 5.5 – Table of priors used for different models. Prior standard deviations are shown in the parentheses.

Experiment	A, B, R	x_1, x_2 (m)	x_3 (m)	ψ (rad)	θ (rad)	ϕ (rad)
GABB-001	ln(0.05) (-ln(0.125))	0.125 (0.02)	0.1285 (0.006)	0 ($\pi/4$)	0 ($\pi/60$)	0 ($\pi/2$)
MARB-005	ln(0.05) (-ln(0.125))	0.125 (0.02)	0.131 (0.013)	0 ($\pi/4$)	0 ($\pi/40$)	0 ($\pi/2$)

standard deviation σ:

$$p(\mathbf{d}|\mathbf{m}, \sigma) = \frac{1}{(2\pi\sigma^2)^{N_d/2}} \exp\left(-\frac{1}{2\sigma^2} (\mathbf{d} - \mathbf{G}(\mathbf{m}))^T (\mathbf{d} - \mathbf{G}(\mathbf{m}))\right) \qquad (5.5)$$

where N_d is the number of measurements. The standard deviation σ encapsulates both measurement and modelling errors and is determined here during the inversion. We refer to it later as the estimated 'noise' level. It has to be ultimately compared with the typical accuracy of the picking of the diffracted waves arrival (denoted as σ_d) to quantify the modelling error. We assume independent the prior PDFs on the model parameters $\mathbf{m}$ and noise variance σ: $p(\mathbf{m}, \sigma) = p(\mathbf{m})p(\sigma)$. The noise level can only be positive (Jeffrey's parameter). We thus invert of $\beta = \ln\sigma$, $\beta \in (-\infty, \infty)$ and assume a uniform prior PDF for β, $p(\beta) = 1$ ($p(\sigma) = 1/\sigma$ - Jeffrey's prior (Tarantola, 2005)). We model the prior knowledge on the model parameters as a multivariate Gaussian PDF:

$$p(\mathbf{m}) = \frac{1}{(2\pi)^{N_p/2} |\mathbf{C}_p|^{1/2}} \exp\left(-\frac{1}{2} \left(\mathbf{m} - \mathbf{m}_p\right)^T \mathbf{C}_p^{-1} \left(\mathbf{m} - \mathbf{m}_p\right)\right) \qquad (5.6)$$

$\mathbf{m}_p$ are prior means for the N_p model parameters (see Table. 5.4) where we use $A = \ln a$, $B = \ln b$, $R = \ln r$ as the fracture dimensions (a, b, r) must be strictly positive. We assume that the different model parameters are a-priori un-correlated ($\mathbf{C}_p$ is diagonal). As shown in Table. 5.5, the same priors standard deviations are taken for all the models and are chosen to be rather uninformative. The vertical position of the fracture center x_3 and the tilting angle of the fracture plane θ are however more constrained than the other parameters according to post mortem analysis of the fracture plane location inside the block.

Using Bayes theorem and considering the probability of the data being observed as a nor-

malizing constant, introducing $\mathbf{z} = (\mathbf{m}, \beta)$ we write the normalized posterior PDF as $\Pi(\mathbf{z}|\mathbf{d}) = p(\mathbf{d}|\mathbf{z})p(\mathbf{m})p(\beta)$. Several techniques can be used to quantify such a posterior PDF - e.g. from global Markov-Chain Monte Carlo (MCMC) sampling, to local quasi-Newton searches. Our aim here is to seek the most probable solution (PDF mode) and estimate the posterior uncertainties around this solution. This is equivalent to finding the minimum of $-\ln \Pi(\mathbf{z}|\mathbf{d})$. The posterior uncertainties can be grasped either via direct Monte Carlo sampling or in a cheaper way by approximating the posterior PDF as a multivariate Gaussian near its mode:

$$\Pi(\mathbf{m}, \sigma_m|\mathbf{d}) = \Pi(\mathbf{z}|\mathbf{d}) \approx \Pi(\tilde{\mathbf{z}}|\mathbf{d})\exp(-\frac{1}{2}(\mathbf{z}-\tilde{\mathbf{z}})^T\tilde{\mathbf{C}}^{-1}(\mathbf{z}-\tilde{\mathbf{z}})) \tag{5.7}$$

where $\tilde{\mathbf{z}}$ represents the most probable model parameters and modelling noise and $\tilde{\mathbf{C}}$ the posterior covariance matrix at $\tilde{\mathbf{z}}$.

We have applied different algorithms to estimate $\tilde{\mathbf{z}}$ here. For robustness, although a simple local quasi-Newton scheme is sufficient for most cases, we present results obtained using a global minimization algorithm (direct differential evolution (Storn and Price, 1997)). The posterior covariance matrix is estimated from the Hessian of $-\ln \Pi(\mathbf{z}|\mathbf{d})$ at $\tilde{\mathbf{z}}$. We have notably compared the posterior mode and uncertainties with the results obtained from MCMC sampling of the posterior PDF $\Pi(\mathbf{m}, \sigma_m|\mathbf{d})$. The results obtained are similar (see supporting information for a detailed comparison).

5.4.3 Bayes factor

The data are inverted with the different geometrical models listed in Table 5.4. The selection of the most suitable model is drawn not only from the quality of fit, but must also account for model complexity. We use Bayes factor to rank between two possible models assuming equi-probable models a-priori. The Bayes factor between model i and j is defined as the ratio of the marginal probability of the data for the given model (Raftery, 1995):

$$B_{ij} = \frac{p(\mathbf{d}|\mathcal{M}_\mathbf{i})}{p(\mathbf{d}|\mathcal{M}_\mathbf{j})} \tag{5.8}$$

where the marginal probability of the data $p(\mathbf{d}|\mathcal{M})$ is obtained by integrating the posterior PDF for the given model over the complete model parameters space:

$$p(\mathbf{d}|\mathcal{M}) = \int_{\mathbf{m}_k} \int_{\sigma_k} \Pi(\mathbf{d}|\mathbf{m}_k, \sigma_k)\mathrm{d}\mathbf{m}_k\mathrm{d}\sigma_k \tag{5.9}$$

To obtain such a probability by cheaper means than Monte Carlo sampling, we approximate the posterior PDF around the most probable value as a multivariate Gaussian (see Eq.(5.7)). We thus estimate the marginal probability of the model (5.9) as

$$p(\mathbf{d}|\mathcal{M}) \approx \Pi(\tilde{\mathbf{z}}|\mathbf{d})(2\pi)^{(N_p+1)/2}|\tilde{\mathbf{C}}|^{1/2} \tag{5.10}$$
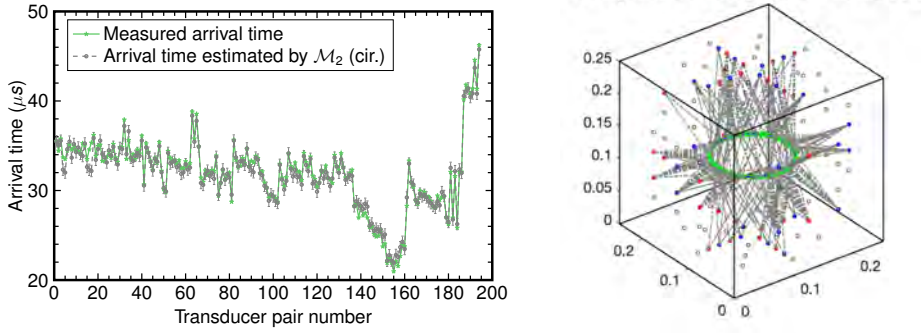
Figure 5.8 – Comparison of the measured arrival and predicted arrival time for model $\mathcal{M}_2$ - sequence 50 in GABB-001 experiment and illustration of diffractors (in green) along the fracture front with its corresponding travel path (in gray) for acoustic diffraction. The red and blue points represent respectively the sources and receivers.

As noted in Raftery (1995), for a Bayes factor $B_{ij} > 10$, the data clearly favours the model $\mathcal{M}_i$ over the model $\mathcal{M}_j$ (respectively $\mathcal{M}_j$ over $\mathcal{M}_i$ for $B_{ij} < 0.1$). For a Bayes factor between 0.2 and 5, the models are equivalent.

5.5 Results and discussions

The number of source-receiver pairs with picked diffracted arrivals vary between acquisition sequences, type of diffracted waves (fracture tip PdP, fluid front PdP and PdS) and experiments. Except for early sequences, the data pair is always larger than 100 (see Fig. 5.7). For one chosen model and a given sequence, we perform the inversion using all the picked diffracted arrivals. Fig. 5.8 displays an example of the model predictions and data (left panel) as well as the corresponding fracture front and diffracted waves ray path for that sequence (right panel). We repeat the inversion procedure for each sequence and obtain the evolution of the fracture, fluid front together with their posterior covariances. We do this for all four forward geometric models in Table 5.4 and rank them using the estimated Bayes factors. We also compare the noise level σ estimated with the picking accuracy of the diffracted wave arrivals σ_d. A large difference between σ and σ_d (about one order of magnitude) indicates that the chosen model is clearly not capable of properly reproducing the data.

5.5.1 Toughness dominated experiment GABB-001

The GABB-001 experiment presents a steady fracture growth throughout the block as illustrated in Fig. 5.9. This is in line with the steady increasing entering flux shown in Fig. 5.3 as previously discussed. No fluid lag was observed from the acoustic diffraction data during the fracture growth. Larger posterior uncertainties and estimated model noises (Fig. 5.10) are found for early sequences due to the limited number of picked arrivals pairs (see Fig. 5.7).

All four geometrical models provide a good fit to the data with an estimated noise level of the
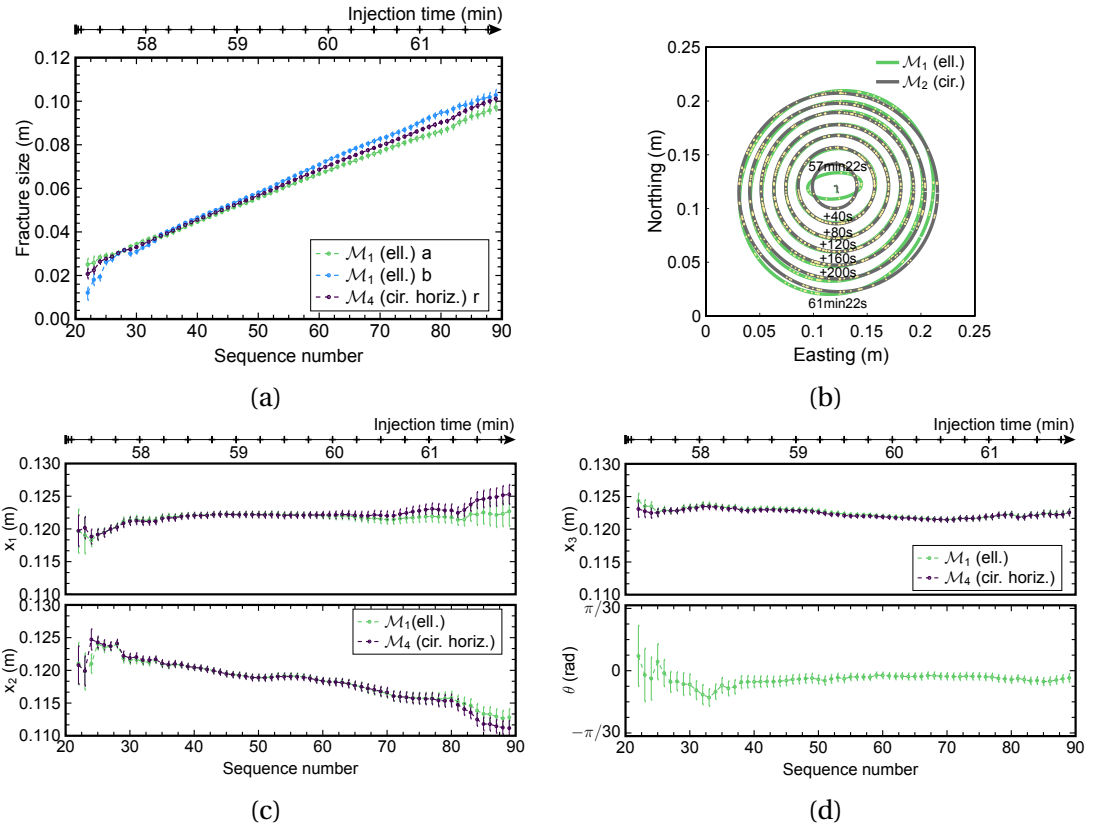
Figure 5.9 – GABB-001 experiment: evolution of the fracture size (a), offset of the fracture center (c) and tilt of the fracture plane (d). The figure (b) displays the footprint of the fracture from a top view (from sequence 22 to sequence 82) shown every 10 sequences. The yellow dots in (b) indicate the diffractors at the fracture front for the different source receiver pairs picked.
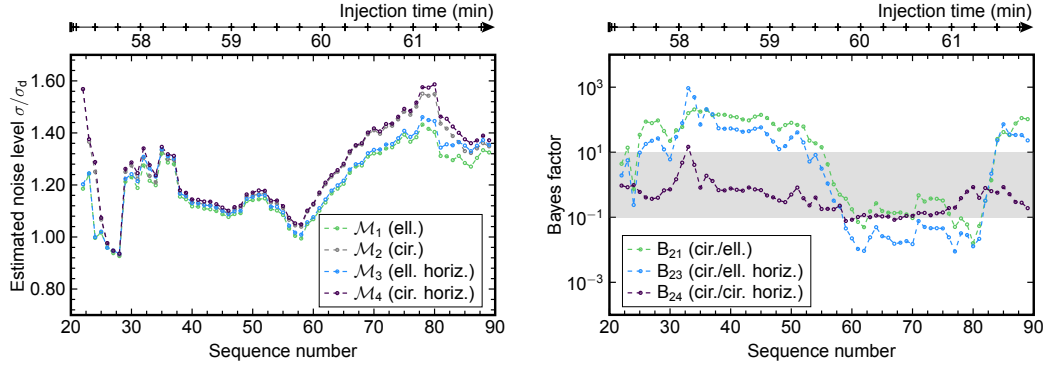
Figure 5.10 – GABB-001 experiment: evolution of estimated noise level (left, the estimated picking error $\sigma_d = 0.5$ μs in GABB-001) and Bayes factor (right). The gray region characterises $0.1 < B_{ij} < 10$, where $\mathscr{M}_i$ and $\mathscr{M}_j$ can not be decisively ranked.

same order of magnitude as the estimated manual picking accuracy $\sigma_d = 0.5$ μs as shown in Fig. 5.10. From the Bayes factor, the fracture shape appears to be better described by a radial geometry than an elliptical one, particularly during the first half stage of the propagation as $B_{21}, B_{23} > 10$ (see Fig. 5.10). The strong posterior correlation between the two semi-lengths for the elliptical model $\mathscr{M}_1$ (Fig. 5.11) and an aspect ratio around 1 (Fig. 5.14) confirms the preference for the circular geometry. The latter stage of the fracture propagation presents a slightly larger estimated noise level (Fig. 5.10) even though the number of picked arrival remains large (see Fig. 5.7). This hints that the chosen models start to become inadequate at later times. This is most likely due to the non-uniformity of the stress field near the bock edges which results in a deviation of the fracture geometry from a circular / elliptical shape. Over that period, a drop of B_{21}, B_{23} in Fig. 5.10 can be observed. The inversion then slightly favours the elliptical fracture models although their estimated noise level increase similarly than the radial models (Fig. 5.10).

The fracture plane remains approximately horizontal during the whole fracture growth with a dip fluctuating around zero. This horizontal geometry is further confirmed by the Bayesian analysis. Given that B_{24} remains in the range $0.1 - 10$ most of the time, the model ($\mathscr{M}_2$) allowing for a possible tilt of the fracture plane is nearly equivalent to the strictly horizontal one ($\mathscr{M}_4$) for the same radial fracture geometry. The fracture center deviates little in the vertical direction through the entire propagation (Fig. 5.9). As a result, strong posterior correlations among the different Euler angles as well as with the fracture center coordinates are observed for the elliptical model (Fig. 5.11).

5.5.2 Lag-viscosity dominated experiment MARB-005

Fig. 5.12 shows a fast growth of the fracture front followed by a gradual evolution of the fluid front. Due to the strong viscous effect, we observe a continuous increase of the fluid pressure even after fracture initiation. The entering flow rate remains very small up to around 8 minutes
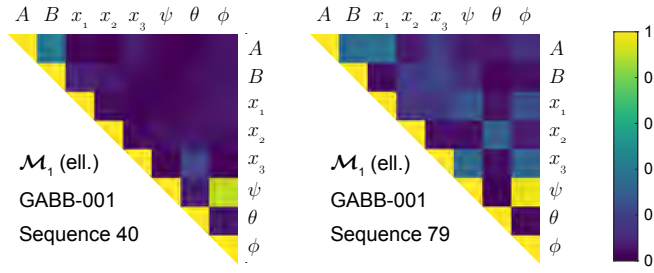
Figure 5.11 – GABB-001 experiment: posterior correlation (absolute value) between $\mathcal{M}_1$ (ellipse) model parameters corresponding respectively to the early time and the mid-to-late stage of fracture growth.
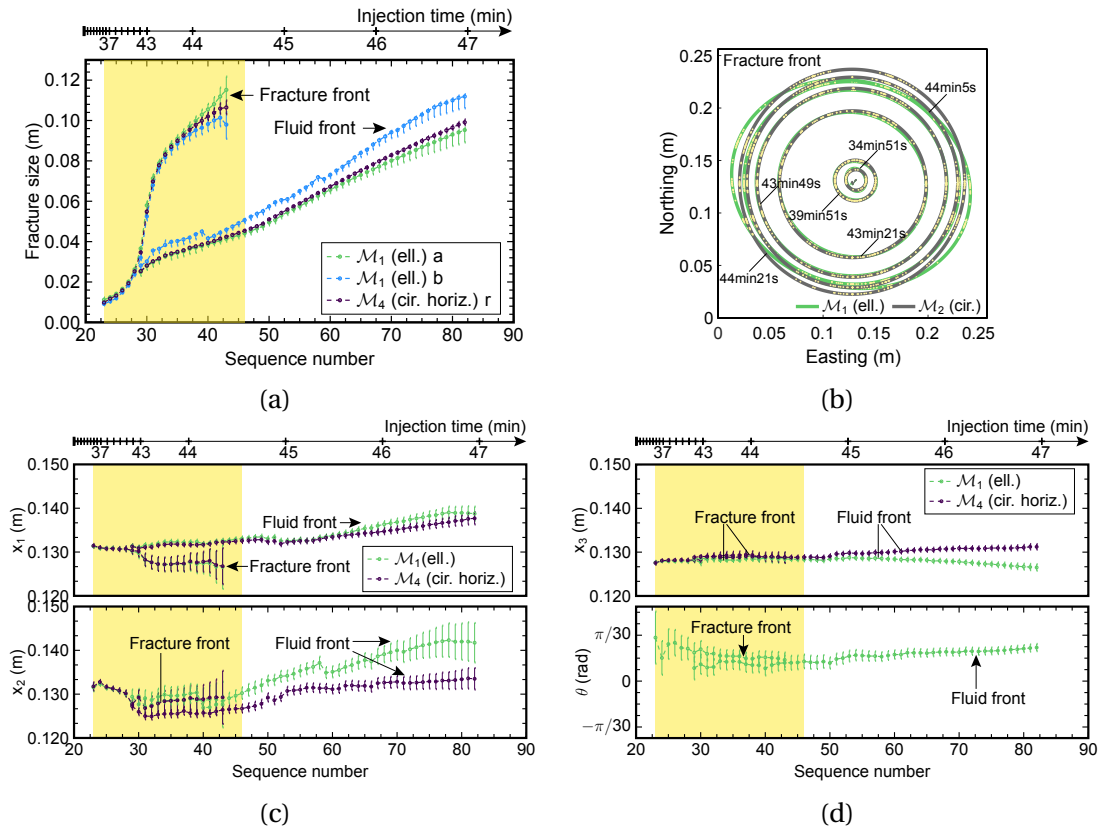
Figure 5.12 – MARB-005 experiment: evolution of fracture size (a), fracture center offset (c) and the tilt of the fracture plane (d). The yellow coloured time interval represents the propagation of the fracture through the specimen. The figure (b) displays the footprint of the fracture front and the fracture center from the top view (from sequence 23 to sequence 43, shown every 4 sequences). The yellow dots in (b) indicate the diffraction points at the fracture front for the different source receiver pairs picked. The corresponding footprint of the fluid front is reported in Fig. 1 of the supporting information.
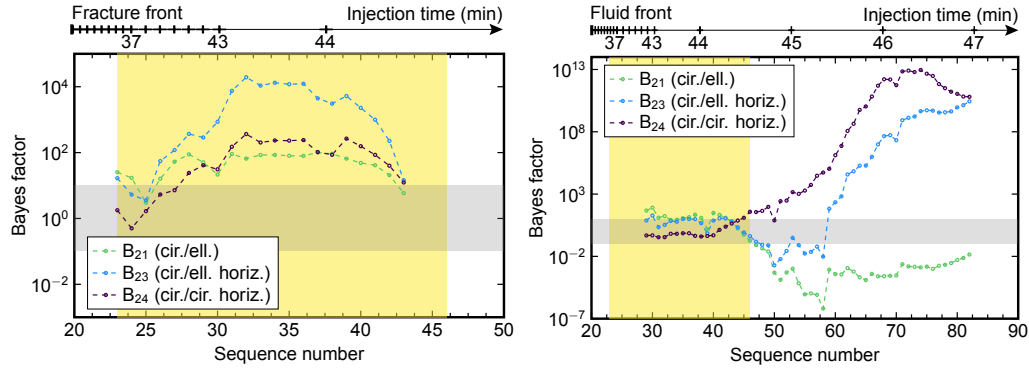
Figure 5.13 – MARB-005 experiment: evolution of Bayes factor for the fracture front (left) and the fluid front (right). The yellow coloured time interval represents approximately the propagation of the fracture from initiation to the edges of the block. The gray region characterises $0.1 < B_{ij} < 10$, where $\mathcal{M}_i$ and $\mathcal{M}_j$ are considered equivalent in fracture geometry description.
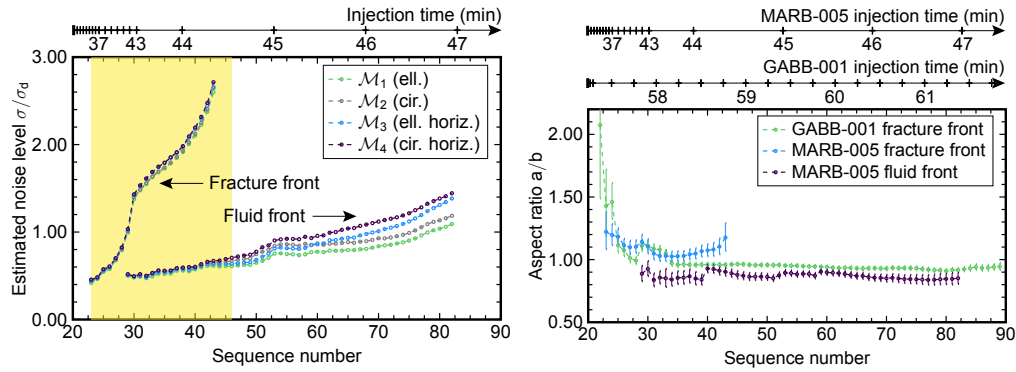
Figure 5.14 – Evolution of the modelling noise in MARB-005 (left, the estimated picking error $\sigma_d = 1 \ \mu$s in MARB-005). The yellow coloured time interval represents approximately the propagation of the fracture from initiation to the edges of the block. Evolution of aspect ratio (right) in GABB-001 and MARB-005 experiments by assuming an elliptical fracture geometry ($\mathcal{M}_1$).

after initiation (Fig. 5.4). It then increases significantly when the fracture reaches the edge of the block.

During most of fracture growth, the fracture front geometry is better described by the circular model $\mathcal{M}_2$ as $B_{21}, B_{23}, B_{24} > 10$ (see Fig. 5.13). The radial geometry is favoured for the fluid front shortly after fracture initiation. The tilted models and particularly the elliptical tilted model (for the fluid front) become more probable after 44 to 45 minutes of injection which corresponds to the time when the fracture front reaches the end of the block (see Fig. 5.13).

The fracture plane does not remain horizontal during the fracture growth as illustrated in Fig. 5.12. This is in line with the evolution of the Bayes factors with $B_{23}, B_{24} > 10$ for most sequences (Fig. 5.13). The tilt of the fracture plane has been confirmed by postmortem observations with an averaged tilt of around $\pi/50$ (3.6°). The fluid front however evolves differently from the fracture front, characterised by a different size and center (Fig. 5.12). At early time, no decisive discrimination can be made between the tilted plane models and horizontal ones. After 44 to 45 minutes of injection when the fracture front reaches the edge, the fluid flows much more freely between the fractured surfaces and the fluid front geometry tends to favour the tilted models given the increase of B_{23} and B_{24}.

The quality of the fit to data is acceptable. The estimated modelling noise is of the same order of magnitude as the picking error $\sigma_d = 1$ μs in Fig. 5.14. The fluid front presents a lower noise level even though less picked arrivals were used in the inversion (Fig. 5.7). This explains a better fit of the predicted arrivals to the picked ones for the fluid front. In the latter half of the fluid front propagation, we observe an important difference between models and their noise level $\mathcal{M}_1 < \mathcal{M}_2 < \mathcal{M}_3 < \mathcal{M}_4$. This is consistent with the estimation of Bayes factors which indicates also a preference for $\mathcal{M}_1$ over $\mathcal{M}_2$, $\mathcal{M}_3$, $\mathcal{M}_4$ (Fig. 5.13) during the same period.

5.5.3 Comparison with acoustic transmission data

We now compare our estimation of the fracture (and fluid for MARB-005) front position using transmitted waves. Transmitted waves exhibit an increase in arrival time and attenuation when passing through a fracture. The attenuation of transmitted waves appears when the fracture front crosses the line between facing source receiver transducers located on opposite platens. It can thus be compared with the estimation from diffracted waves.

We evaluate a transmitted "energy" by computing the signal strength $E_i^{1/2}$ of a given wave arrival (P or S) for the acquisition sequence i as

$$E_i^{1/2} = \sqrt{\sum_{j=j_{min}}^{j_{max}} u_i^2(t_j)} \tag{5.11}$$

where $u_i(t)$ is a low-pass filtered (at 2MHz) waveform which is cropped by a tapered Hamming window centered on the interest arrival with a size of $(t_{j_{max}} - t_{j_{min}}) = 14\mu$s. We then

choose a reference signal obtained before fracture initiation and define the attenuation ratio $(E_i/E_{ref})^{1/2}$.

An alternative is to follow the procedure presented in Groenenboom and Fokkema (1998) to estimate the fracture width from transmitted waves. In the frequency domain, the transmitted compressional signal $\hat{u}_{fracture}$ can be compared to the prediction obtained by the product of the transmission coefficient $T(\zeta, w)$ for a three layers model (rock-fluid-rock) and a reference signal $\hat{u}_{base}$ recorded before fracture initiation. The fluid layer thickness (fracture width) w is estimated by minimizing the misfit for frequencies around the central frequency of the source signal ($\zeta_{min} < \zeta < \zeta_{max}$). In addition to frequency, the transmission coefficient $T(\zeta, w)$ depends on both solid and fluid acoustic impedances and the thickness of the fluid layer (the fracture width). The expression of $T(\zeta, w)$ is recalled in the supporting information. This method has been shown to compare well with optical measurements for the case of waves arriving at a 90 degree incident angle to the fracture (Kovalyshen, 2014). We apply it to the toughness-dominated GABB-001 experiment for which the fracture is flat (thus ensuring a 90 degree incident angle for some source receiver-pairs) and do not exhibit any fluid lag (we take $\rho_f = 1260$kg/m^3 and $V_{p,f} = 1960$m/s for the properties of glycerol). We set the lower and upper frequency bounds to $\zeta_{min} = 500$ kHz and $\zeta_{max} = 1100$ kHz given the central frequency of 750 kHz of the source signal. We do not use such a method for the marble experiment (MARB-005) which exhibits a very large fluid lag.

Lag-viscosity dominated experiment MARB-005

As illustrated in Fig. 5.15, both compressional and shear waves significantly lose their amplitude in between the time when the fracture and fluid front passes through the corresponding ray path. Following the arrival of the fluid front, the compressional wave regains its amplitude but not the shear wave. Such a characteristic shear wave shadowing due to the lack of shear stiffness of the fluid is consistent with previous observations (Groenenboom and van Dam, 2000).

We use the time evolution of the transmitted energy ratio defined in Eq. (5.11) for all the pairs of compressional waves transducers in the opposite top and bottom platens (sub-parallel to the created fractures) and compare it with the fracture and fluid front previously reconstructed from diffracted waves (see Fig. 5.16). We use a threshold of 0.8 for $(E/E_{ref})^{1/2}$ to binarize the loss (for value below the threshold) of the transmitted wave.

As shown in Fig. 5.16, we first clearly see that the transmitted signal is lost when the reconstructed fracture front reaches the transducers location (black curve in the snapshot of Fig. 5.16). The signal is then regained upon the arrival of the fluid front (blue curve in the snapshot of Fig. 5.16), but eventually lost again due to the increase of the fracture width as the viscous fluid front penetrates more into the fracture. Overall, we observe in Fig. 5.16 a good agreement between the evolution of the signal strength ratio of the transmitted P waves and the evolution of the fracture and fluid fronts reconstructed from diffraction data.
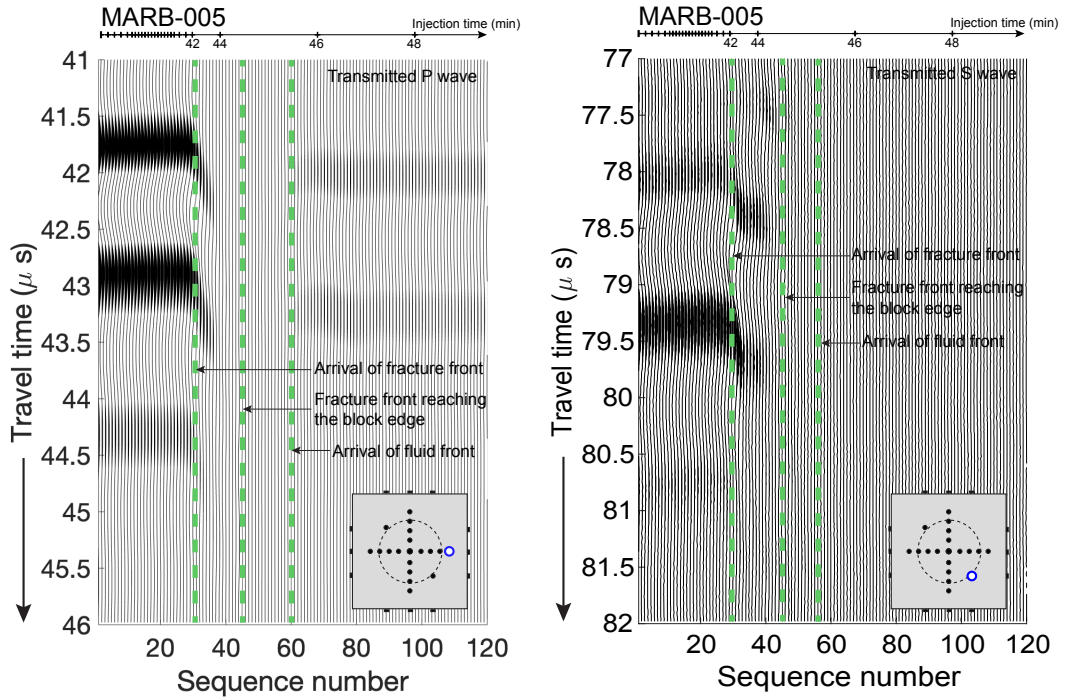
Figure 5.15 – Evolution of the recorded signal for opposite source-receiver pair during the MARB-005 experiment: attenuation of the compressional (left) and shear wave (right).
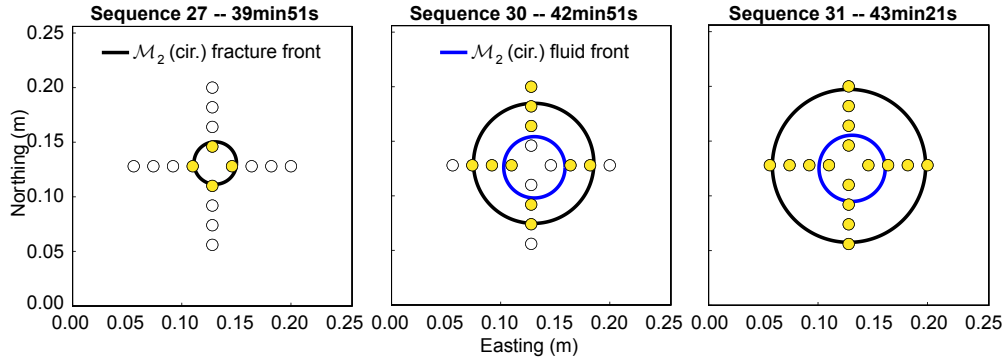
Figure 5.16 – MARB-005 experiment: top view of the extent of the hydraulic fracture from transmitted waves (from top-bottom platens). The P-wave transducers turn yellow if the attenuation ratio of the signal strength $(E/E_{ref})^{1/2}$ goes below 0.8. We take sequence 16 (before fracture initiation) as the reference sequence for the calculation of the attenuation ratio. The corresponding footprint of the fracture and fluid fronts obtained from the inversion of diffracted waves are displayed for comparisons.
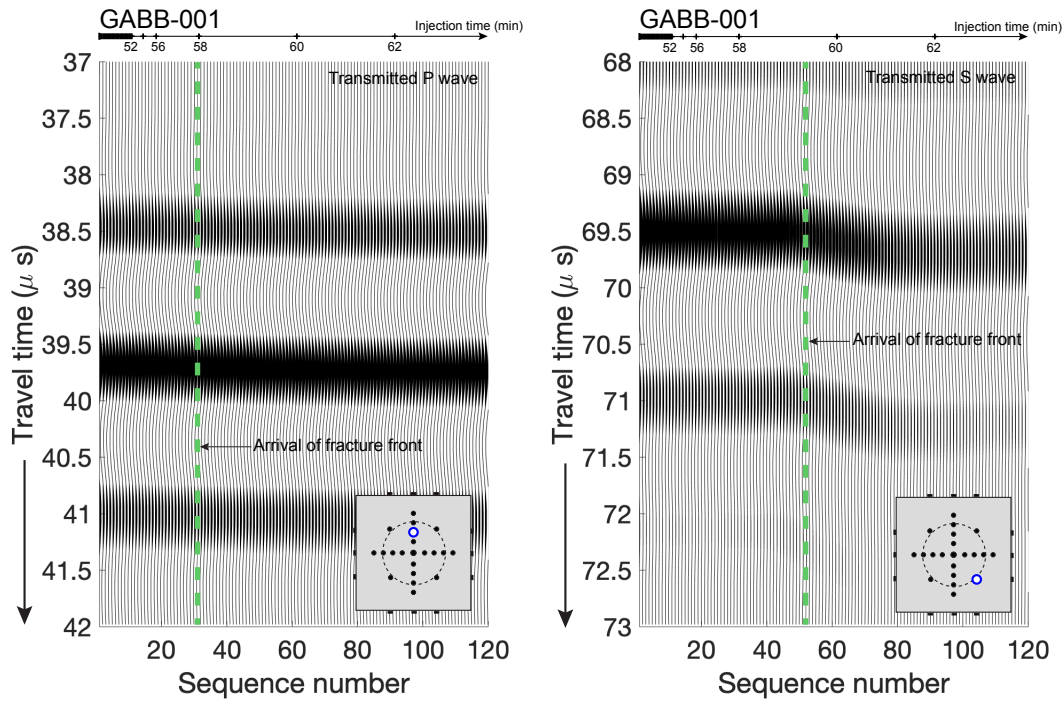
Figure 5.17 – GABB-001 experiment: gradual attenuation of the compressional wave (left) and shear wave (right).

Toughness-dominated experiment GABB-001

In the GABB-001 experiment, the fracture front coincides with the fluid front (no fluid lag). The transmitted shear waves present a gradual attenuation after the arrival of the fracture front as shown in Fig 5.17. Such a weak shear shadowing effect is probably due to the smaller width of the fracture as well as the possible existence of solid bridges between fractured surfaces. In order to separate apart the created fracture surfaces, we had to hammer a sub-sampled part of the specimen in gabbro. On the other hand, it is worth noting that the marble block was already completely separated after the experiment and exhibited smoother surfaces.

The compressional waves do not attenuate significantly during the fracture growth (Fig. 5.17) but sufficiently to allow the reconstruction of the fracture width using the three layers model described previously. The evolution of fracture extent grasped via the evolution of the fracture widths inverted for all the top bottom platens P transducers pairs is shown in Fig. 5.18. It agrees relatively well with the fracture front reconstructed from the diffracted waves although a damage zone ahead of the reconstructed fracture tip may indeed exist. In addition, the order of magnitude of the fracture widths is in line with the predictions of the toughness dominated solution for a radial hydraulic fracture (Savitski and Detournay, 2002). By using the averaged entering flow rate $< Q_o >$ for estimation and the properties listed in Table 5.3, the toughness dominated radial solution predicts respectively a maximum width (at the fracture center) of respectively 12 μm, 19 μm and 24 μm for the presented sequences.
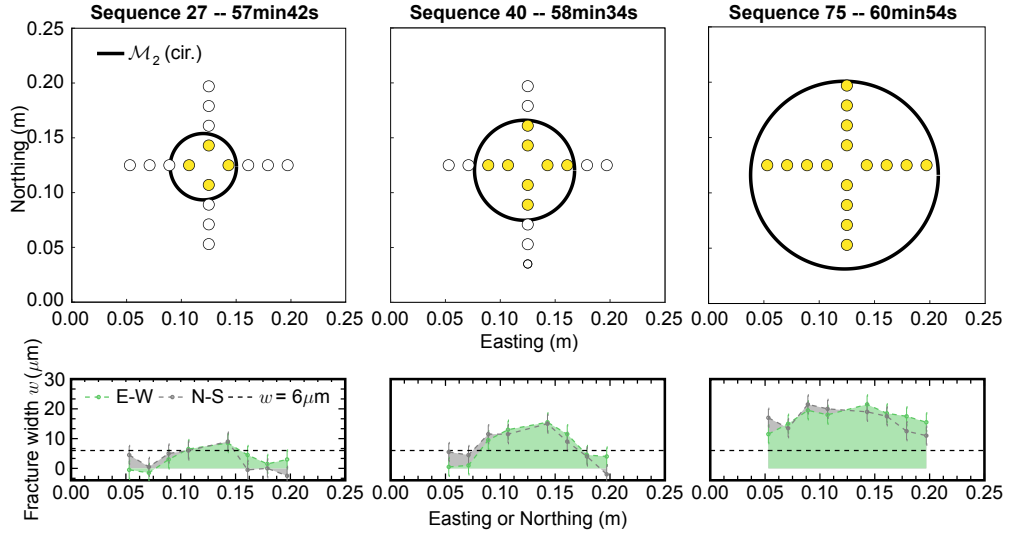
Figure 5.18 – GABB-001 experiment: top view of the extent of the hydraulic fracture. The P-wave transducers turn yellow if the fracture opening goes above 6 μm with an error of around 3 μm. This error on the fracture width estimation was obtained from the maximum width obtained when no fracture was present in the block (using acquisition sequences prior to fracture initiation).

The existence of a "tappered" width profile near the tip associated with the existence of the process zone is not extremely clear (due to the resolution of the fracture width estimation). Another line of evidence for the presence of a process zone relates to attenuation of transmitted waves propagating parallel to the fracture plane (above and below it). We choose side transmitted pairs with a good signal to noise ratio and evaluate their attenuation ratio using Eq. (5.11). Transducers on the north-southern sides of the block which are located approximately 5 cm away from the fracture plane present a difference of signal strength of around 5% after fracturing. The transducer pairs on the west-eastern sides which are 2 cm from the fracture plane, present a larger attenuation as shown in Fig. 5.19. It looks like a band of $\pm$ 2 cm above and below the fracture plane is influenced. Such an attenuation has two possible explanations. First, the waves interact with the presence of the fracture thus decreasing the received amplitude. Another possibility lies in the presence of micro-cracks surrounding the growing fracture which are known to strongly attenuate transmitted waves (Zhang and Gross, 1993; Zang et al., 2000). Further analysis is required in order to decipher between these two explanations.

5.6 Conclusions

We have improved the resolution of the monitoring of growing hydraulic fracture using diffraction data recorded by a large amount of piezoelectric source/receiver pairs. Using Bayesian inversion, we have developed a workflow to select the most probable fracture geometry from a finite number of simple models (circle, ellipse, horizontal or not). This model ranking allows
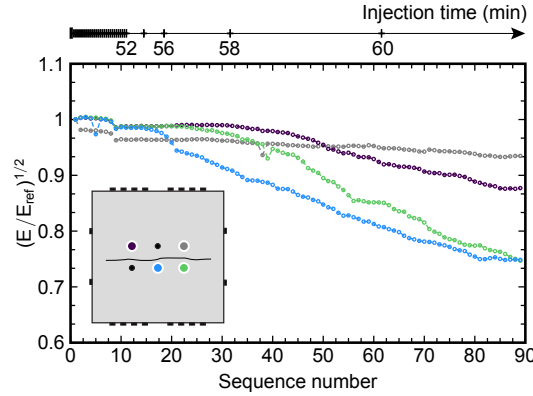
Figure 5.19 – GABB-001 experiment: attenuation of the compressional waves propagating parallel to the fracture surface with a location of around 2 cm away from the fracture.

to gain confidence in the important possible deviation of the fracture from the simplest radial shape. Moreover, the inversion of the modelling error σ (which combines model and measurement error) allows to quantify the ability of any chosen model to reproduce the data. The method has been successfully tested on two experiments representative of two very different HF propagating regimes (toughness and lag-viscous dominated). In both cases, the fractures were mostly radial although a deviation towards a more elliptical shape is visible when the fracture feels the edge of the specimen (where the applied stress field is likely less uniform). Although it is difficult to precisely gauge the accuracy of the reconstruction, the resulting posterior uncertainties of the fracture extent are around 1-2 mm for the gabbro experiment (GABB-001) and 2-4 mm for the marble experiment (MARB-005). The fronts reconstructed from diffracted waves agree well with the analysis of the attenuation of compressional waves traversing the propagating fractures. It is also important to recall that in our analysis, the data for one acquisition sequence is assumed to be acquired at the same time while an acquisition lasts about 2.5 seconds (spanning of all the sources). As a result, this imaging technique is appropriate only for low velocity fractures: the average fracture velocity is around 300 μm/s for GABB-001, and 1 mm/s for the (faster) MARB-005 experiment.

The method presented here can be improved in a number of ways. First, instead of using parametrized fracture shapes, a direct extension is to use a 3D spline curve to describe the fracture front (at the expense of more model parameters). Secondly, in order to better quantify the possible damage around the growing fracture, the hypothesis of a constant wave velocity in the sample during fracture growth should be at least partly relaxed (to account for the effect of possible micro-cracking around the fracture). It would be interesting to combine the analysis of diffracted waves with recent acoustic tomography inversion that reconstructs such velocity changes in the bulk using only direct wave arrivals but combining passive and active acoustic data (Brantut, 2018; Aben et al., 2019). Full waveform inversion (likely in the frequency domain) would ultimately allow to combine the information of diffracted, transmitted (and reflected) waves, but this requires proper sensor calibration and the use of computationally expensive models able to resolve the sharp discontinuities induced by the fluid-filled fracture.

A more immediate/simpler improvement will likely come from the combination of the active 4D acoustic method presented here with passive listening for AE events (with localization and moment tensor estimation, see for example Stanchits et al. (2015)). This will surely enhance our understanding of hydraulic fracture growth, in particular with respect to a better quantification of the fracture process zone in rocks. In particular, the interplay between the evolution of the fluid lag and the process zone appears to be strongly influencing the overall HF propagation according to recent theoretical predictions (Garagash, 2019).

Data availability

The raw and processed data of these two experiments as well as the inversion results will be made available via the Zenodo platform with the identifier https://doi.org/10.5281/zenodo.3901193.

5.7   Supporting information

5.7.1   Evolution of the entering flow rate into the fracture

The interface vessel introduces a non-negligible system compliance. As a result, the flow rate entering into the fracture Q_{in} does not equal the pump injection rate Q_o upon fracture initiation. One can estimate Q_{in} based on the fluid pressure measurement and the estimation of the system compliance, using the global mass balance of fluid in the injection line from the pump to the fracture inlet. We thus obtain

$$Q_{in}(t) = Q_o - c_f V_d \frac{\mathrm{d}p_{\text{downstream}}(t)}{\mathrm{d}t} - (U - c_f V_d)\frac{\mathrm{d}p_{\text{upstream}}(t)}{\mathrm{d}t} \tag{5.12}$$

where p_{upstream} and $p_{\text{downstream}}$ represent respectively the fluid pressure upstream and downstream as shown in Fig. 5.1, and c_f the fluid compressibility and V_d the fluid volume downstream (from needle valve to fracture notch). The system compliance U can be estimated from the averaged pressurization rate before fracture initiation.

$$U = Q_o / \left(\frac{\mathrm{d}p_{\text{upstream}}}{\mathrm{d}t}\right) \tag{5.13}$$

5.7.2   Estimation of the fracture opening using compressional transmission

We estimate the fracture opening based on the previous investigation on the compressional transmission through a thin fluid layer following previous studies (Groenenboom and Fokkema, 1998; Kovalyshen, 2014). The fluid layer thickness (fracture width) w is obtained by minimising an objective function $f(w)$ around the central frequency of the transmitted compressional signal $(\zeta_{min}, \zeta_{max})$ in the frequency domain.

$$f(w) = \sum_{\zeta_{min}<\zeta<\zeta_{max}} \left| \hat{u}_{fracture} - T(\zeta, w)\hat{u}_{base} \right| \tag{5.14}$$

where $\hat{u}_{base}$ and $\hat{u}_{fracture}$ are the Fourier transforms of the signals which pass through the medium before (u_{base}) and after the fracture crosses the line of sight between the source-receiver pairs. ($u_{fracture}$). In the simplest case of normal incidence, the transmission coefficient $T(\zeta, w)$ describing the change in the spectrum can be written as (see e.g. Brekhovskikh and Godin (1990) for details):

$$T(\zeta, w) = \frac{(1 - r_{ff}^2)\exp(i\alpha)}{1 - r_{ff}^2\exp(2i\alpha)}, \quad r_{ff} = \frac{z_r - 1}{z_r + 1}, \quad z_r = \frac{\rho_f V_{p,f}}{\rho V_p}, \quad \alpha = \frac{2\pi\zeta w}{V_{p,f}} \tag{5.15}$$

where ρ and ρ_f are densities of the solid and the fracturing fluid respectively, V_p and $V_{p,f}$ are compressional wave velocities propagating in the solid and in the fluid.
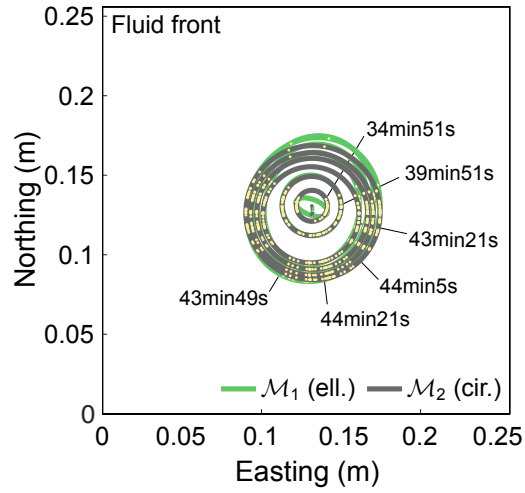
Figure 5.20 – MARB-005 experiment: footprint of the fluid front and and its geometric center from the top view (from sequence 23 to sequence 43, shown every 4 sequences). The yellow dots indicate the diffraction points at the fluid front for the different source receiver pairs picked.

5.7.3 Footprint of the fluid front in MARB-005

The footprint of the fluid front in the MARB-005 experiment is displayed in Fig. 5.20 - in complement of Fig. 12b of the main text.

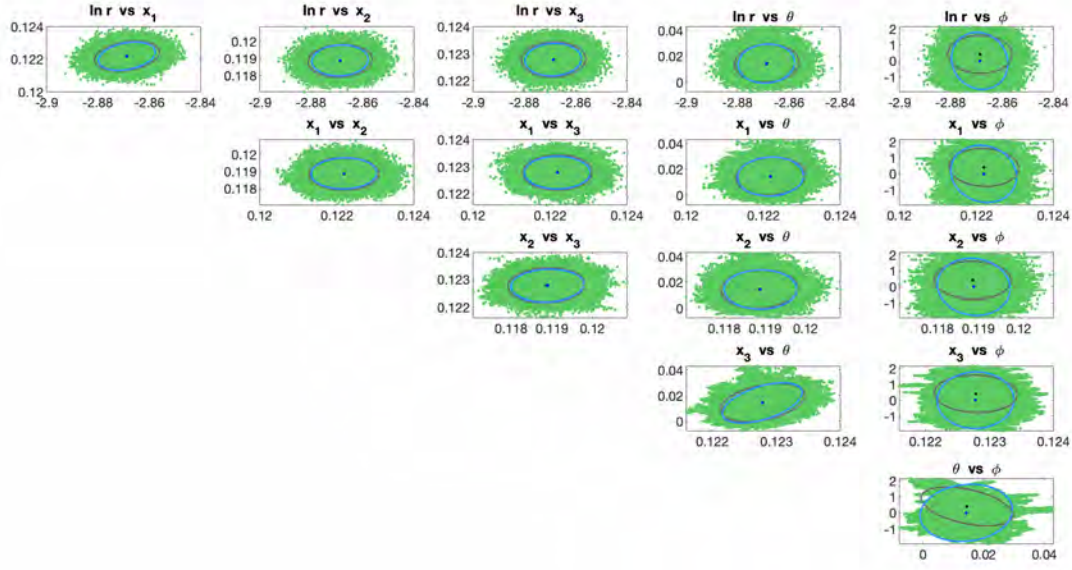Table 5.6 – GABB-001 experiment - acquisition sequence 50: comparison of posterior model parameters for the circular model allowing for a tilt ($\mathcal{M}_2$) and their uncertainties (standard deviation in parentheses). Comparisons between the results obtained via differential evolution maximising the posterior and a quadratic approximation at the most probable mode and the one from a Gaussian fit of a Markov-Chain Monte Carlo (MCMC) sampling (ran for a maximum step of 350000 after the burn-in period).

		Quadratic approximation at the most probable mode	MCMC Gaussian fit
$\ln r$	(ln m)	-2.869 (0.0055)	-2.869 (0.0062)
x_1	(m)	0.1222 ($4.27\,10^{-4}$)	0.1222 ($4.42\,10^{-4}$)
x_2	(m)	0.1189 ($4.49\,10^{-4}$)	0.1189 ($4.67\,10^{-4}$)
x_3	(m)	0.1228 ($3.01\,10^{-4}$)	0.1228 ($3.15\,10^{-4}$)
θ	(rad.)	0.0143 (0.008)	0.0146 (0.007)
ϕ	(rad.)	0.0041 (0.892)	-0.0450 (0.792)
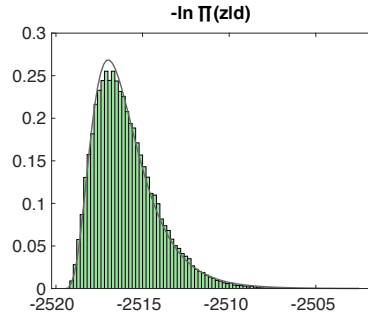
Figure 5.21 – GABB-001 experiment - acquisition sequence 50: normalized histogram of the posterior PDF (CDF integrates to unity), more precisely we display minus log-posterior ($-\ln\Pi(\mathbf{z}|\mathbf{d})$) for the circular model allowing for a tilt ($\mathcal{M}_2$). The samples have been obtained from a Markov-Chain Monte Carlo (MCMC) algorithm with 350000 steps after the burn-in period. The grey curve indicates the log-Gaussian fit of the log-posterior. This demonstrates that the posterior is well approximated by a normal PDF.

5.7.4 Posterior PDF via MCMC - GABB-001 - acquisition sequence 50 - model $\mathcal{M}_2$

We provide here a representative example for a given acquisition sequence of inversion results obtained via an optimisation method (minimisation of $-\ln\Pi(\mathbf{z}|\mathbf{d})$ via differential evolution) and a Markov-Chain Monte Carlo sampling. Fig. 5.21 displays minus log of the posterior - confirming the normal shape of the PDF. Table 5.6 displays the obtained model parameters and estimate variance by the two methods. Fig. 5.22 and Fig. 5.23 displays respectively the posterior PDF of the different model parameters and their cross-correlation obtained by the two methods. The results obtained are similar - and confirm that the posterior PDF can be well approximated by a normal PDF.
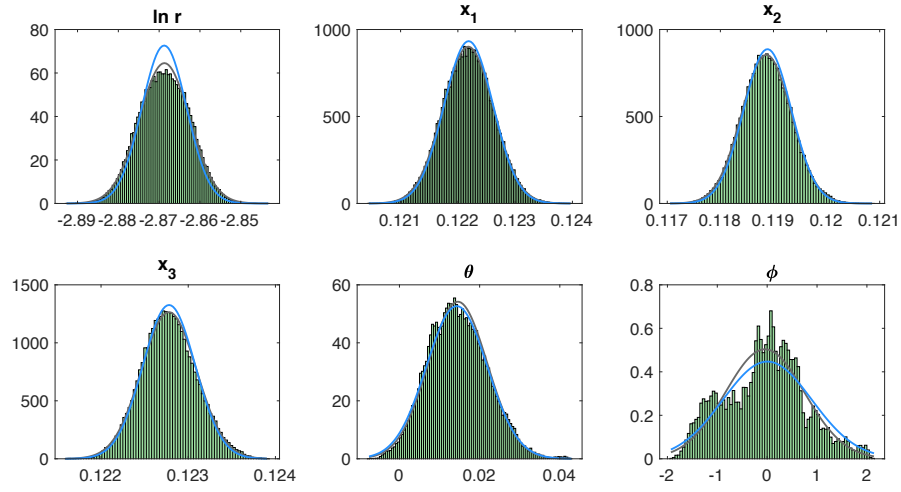
Figure 5.22 – GABB-001 experiment - acquisition sequence 50: normalized histogram of the posterior PDF of the model parameters for the circular model allowing for a tilt ($\mathcal{M}_2$) obtained from a Markov Chain Monte Carlo (MCMC) ran for 350000 steps after the burn-in period. The grey curve indicates the Gaussian fit of the MCMC sampling of the model parameter distribution. The blue curve represents the quadratic Gaussian approximation near the PDF mode obtained from the differential evolution algorithm. We refer to Table 5.6 for units of the different parameters.

Figure 5.23 – GABB-001 experiment - acquisition sequence 50: posterior correlation between model parameters for the circular model allowing for a tilt ($\mathcal{M}_2$) obtained from the MCMC chain ran for 350000 steps after the burn-in period. The grey ellipses indicate the confidence region obtained from the MCMC chain and the blue ellipses the ones obtained from the quadratic approximation of the most probably mode reached by a differential evolution algorithm. We refer to Table 5.6 for units of the different parameters.

6 HF growth in quasi brittle rocks under different confining stresses

A process zone exists around the tip of hydraulic fractures (HF) propagating in quasi-brittle materials. Such a process zone removes the stress singularity otherwise present in linear hydraulic fracture mechanics (LHFM), and is probably related to the toughening mechanism in rocks. To better understand its impact on the HF growth, we perform HF injections in rocks (marble and gabbro) exhibiting an order of difference in grain sizes and as a result possibly different sizes of the process zone. Controlled HF experiments are performed on $250 \times 250 \times 250$ millimeters rock samples under different level of confining stresses. The spatial-temporal fracture geometry is reconstructed via acoustic diffraction with a spatial resolution of a few millimeters. The transmitted acoustic energy attenuates prior to the arrival of the measured fracture tip from diffracted waves. This indicates the existence of a process zone ahead of the fracture front. Post-mortem observations show that solid bridging and crack branching characterize the process zone. During the fracture growth, the process zone size first grows with the fracture extent and then starts to feel the sample boundaries. This is associated with a first increase and then a drop of the apparent toughness during these HF laboratory experiments. The size of the process zone seems to be comparable to the fracture extent, which indicates a non-negligible size effect for laboratory HF experiments in rocks.

The results reported here will provide the basis of a future publication.

Authors contributions

D. Liu and B. Lecampion have formulated the problem. D. Liu has designed the hydraulic fracture injections under the guidance of B. Lecampion. D. Liu has performed the experiments and analyzed the results. B. Lecampion has participated in the roughness analysis of the fractured surfaces. D. Liu has written the current version of the manuscript.

Plain Language Summary

Well completion for oil and gas, geothermal energy as well as CO2 storage sometimes require hydraulic stimulation to achieve economical fluid flow rates (for both injector and producer wells). Predicting the growth of fluid-driven fractures in geological systems is essential for the sustainable and efficient engineering of those reservoirs. The quasi-brittle nature of rocks complexifies the coupling between fluid flow and fracture growth – especially in the fracture process zone. We are interested in the evolution of this non-linear zone during the growth of a hydraulic fracture in rocks with different grain sizes and under different stress conditions. We show that in both marble and gabbro, the attenuation of the transmitted wave implies the presence of a process zone ahead of the diffracted fracture front. Moreover, we show that the fracture resistance first increases and then decreases beyond a fracture radius, when the growth of the process zone is probably limited by sample dimensions. This implies possibly very different results at different scales for laboratory hydraulic fracturing experiments in quasi-brittle materials.

6.1 Introduction

Hydraulic fracturing (HF) is a technique often used in the oil and gas industry to enhance the production of tight reservoirs (Economides et al., 1989). It involves the process of the injection of fluid into rocks to propagate the fracture to increase the permeability. Linear elastic fracture mechanics (LEFM) combined with lubrication theory (linear hydraulic fracture mechanics - LHFM for short) have successfully predicted such hydraulic fracture growth for a simple planar geometry in model materials such as PMMA and glass (Bunger and Detournay, 2008; Wu et al., 2008; Lecampion et al., 2017; Xing et al., 2016). However, deviations from LHFM predictions have been reported at laboratory (Thallak et al., 1993; Van Dam and de Pater, 1999; Makhnenko et al., 2010) and field scales (Shlyapobersky, 1985; Shlyapobersky et al., 1988). An educated guess for the source of these deviations is the quasi-brittle nature of rocks: instead of a stress singularity predicted by LEFM, the fracture tip in rocks is characterized by a process zone where micro-cracking or large deformations can not be neglected. Moreover, the fracture roughness makes the fluid flow in small apertures deviate from the lubrication theory. Previous theoretical investigations (Papanastasiou, 1999; Garagash, 2019; Liu and Lecampion, 2021) point out a strong influence of the minmum confining stress perpendicular to the fracture plane. For the same material, a larger confining stress possibly results in more viscous dissipation inside rough apertures. Its influence is even stronger when the nonlinear zone is comparable with the fracture dimension (Liu and Lecampion, 2021). It is therefore interesting to know the size of this process zone in real rocks and how the fracture growth differs from each other under different confining stresses.

Laboratory HF experiments in rocks date back to 1950s (Hubbert and Willis, 1957) where proper measurements of fracture extent and width distribution are absent and only borehole pressure and the postmortem fracture geometry are reported. Active acoustic monitoring

has enabled the time-lapse reconstruction of the fracture geometry in rocks (Medlin et al., 1984; Groenenboom and Fokkema, 1998; Groenenboom, 1998; Liu et al., 2020) and passive acoustic monitoring provides a description of seismic events inside rocks and an indirect measurement of the fracture extent (Lockner and Byerlee (1977); Stoeckhert et al. (2015) to cite a few). However, very few in-depth analysis have been reported regarding the growth of process zone during hydraulic fracturing of rocks.

Ultrasonic waves act as an important approach to detect the process zone in rocks. Previous studies give a rough estimation of the process zone size around the fracture using active acoustic waves by recording the start of the attenuation of transmitted waves (Labuz et al., 1987), or detecting the arrivals of reflected waves from cracks (Glaser and Hand, 1998). The same can also be done via passive acoustic emissions by showing a map of seismic events in the process zone (Zietlow and Labuz, 1998; Zang et al., 2000; Stanchits et al., 2014). These two approaches are sometimes combined with a visualization of the fracture path which is often achieved by fluorescent / digital image correlation methods (Naoi et al., 2018; Lin et al., 2019). This application on HFs in rocks is very limited due to the lack of accurate description for the fracture geometry.

For HFs propagating in rocks, post-mortem observations have already confirmed the presence of a process zone characterized by crack bridging (see Lhomme (2005); Chen et al. (2015) for example). More efforts such as the measurement of the crack resistance (Hashida et al., 1993) and the HF tip bluntness (van Dam, 1999) have also been made to describe the growth of the process zone. van Dam (1999); Van Dam and de Pater (1999) pioneered the quantitative investigation on the process zone growth in HFs by performing HF injections in cement, plaster and diatomite. They calculate the plastic zone size based on the estimated stress field around the tip and points out a strong correlation between the estimated plastic zone size and fracture roughness. Interestingly, similar relations between the process zone size and roughness have also been reported in dry fracture mechanics (Morel et al., 2002; Nasseri et al., 2010; Barak et al., 2019): the off-plane height variation may present different roughness exponents above and below a "process zone" length scale (Mourot et al., 2005; Bonamy et al., 2006; Ponson et al., 2007; Morel et al., 2008). Moreover, a cut-off length scale representing the process zone size has been extracted from the spatial correlations of the slopes of a rough fracture surface (Vernède et al., 2015). Quantitative analysis of the fracture roughness have only been recently conducted for HF fracture surfaces (Movassagh et al., 2020).

In this chapter, we aim to understand the HF growth in rocks with different levels of solid non-linearity (grain sizes) under different confining stresses. We vary the confining stress, injection rate and the fluid type (viscosity) to make the fracture growth either dominated by the fluid lag and viscosity or fracture toughness. By reconstructing the fracture geometry using active acoustic monitoring with a better accuracy (Liu et al., 2020), we try to understand the process zone growth using the evolution of the transmitted energy and the fracture apparent toughness. We also report the roughness profiles created hydraulically by these fractures.

6.2 Materials and methods

We select two rocks with very low permeability: Zimbabwe gabbro and Carrara marble. They present an order of magnitude's difference in grain sizes, and as a result possibly different process zone sizes (see Table. 6.1). We present their mode-I fracture toughness values respectively obtained from the tampered double cantilever beam (TDCB) test (Vasudevan et al., 2021) and the semi-circular bend (SCB) test (Kuruppu et al., 2014) in Table. 6.2. The TDCB method assumes a horizontal fracture path while the real fracture path oscillates a lot. This oscillating fracture path leads to more energy dissipation than a horizontal one for the same fracture length. This is probably the reason why TDCB method gives larger fracture toughness values than the SCB method. Another possible explanation of the difference between these two methods is the effect of T-stress (the second term of William's series (Williams, 1997)), which is known as the representative of the crack tip constraint level (Gupta et al., 2015; Aliha et al., 2017).

We carry out HF injections in a 250 mm cubic rock sample using glycerol or silicone oil as the injection fluid (see Table. 6.3). The confinement can be applied up to 20 MPa by symmetric pairs of flat-jacks in the three axis of a poly-axial reacting frame as illustrated in Fig. 6.1. A wellbore of 16 mm diameter is drilled vertically through the block and a horizontal axisymmetric notch (with a diameter of 21 ± 1 mm is created in the center of the sample to facilitate the fracture initiation. A completion tool connected to a injection tubing is expoxied in the wellbore and allows to inject fluid only at the notch level. Prior to the injection, we apply a true triaxial stress state on the block through symmetric pairs of flat-jacks (respectively connected with three GDS pumps) in the three axis of a poly-axial reacting frame up to 20 MPa. The fluid is then injected through an interface vessel by a syringe pump (ISCO DC 160) with a maximum pressure of 51 MPa at a constant flow rate (in the range of 0.001 mL/min to 107 mL/min). We put a needle valve in the injection line to avoid the sudden release of pressurized fluid following the fracture initiation (Lhomme et al., 2005).

An active acoustic imaging system is integrated in the loading frame to monitor the fracture geometry as shown in Fig. 6.2. We have 64 piezoelectric transducers with 32 as sources and 32 as receivers respectively. This array of transducers consists 10 shear wave transducers and 54 longitudinal wave ones. We use a source function generator connected to a high-power amplifier to send a Ricker excitation signal at a central frequency of 750 kHz. The source signal is routed to one of the source transducers via a multiplexer such that the signals received by the 32 receivers are recorded with a sampling frequency of 50 MHz. The switch between sources is limited by the multiplexer such that it takes around 2.5 seconds to span all 32 sources. In this chapter, we take 0.25 Hz as the maximum frequency of the active acquisition. In addition to acoustic data, we record the fluid pressure upstream and downstream the valve, volume of pressure of each flat-jack pairs or displacement of the tip surface near the wellbore at 1 Hz. We synchronize different measurements via a dedicated LabView application.
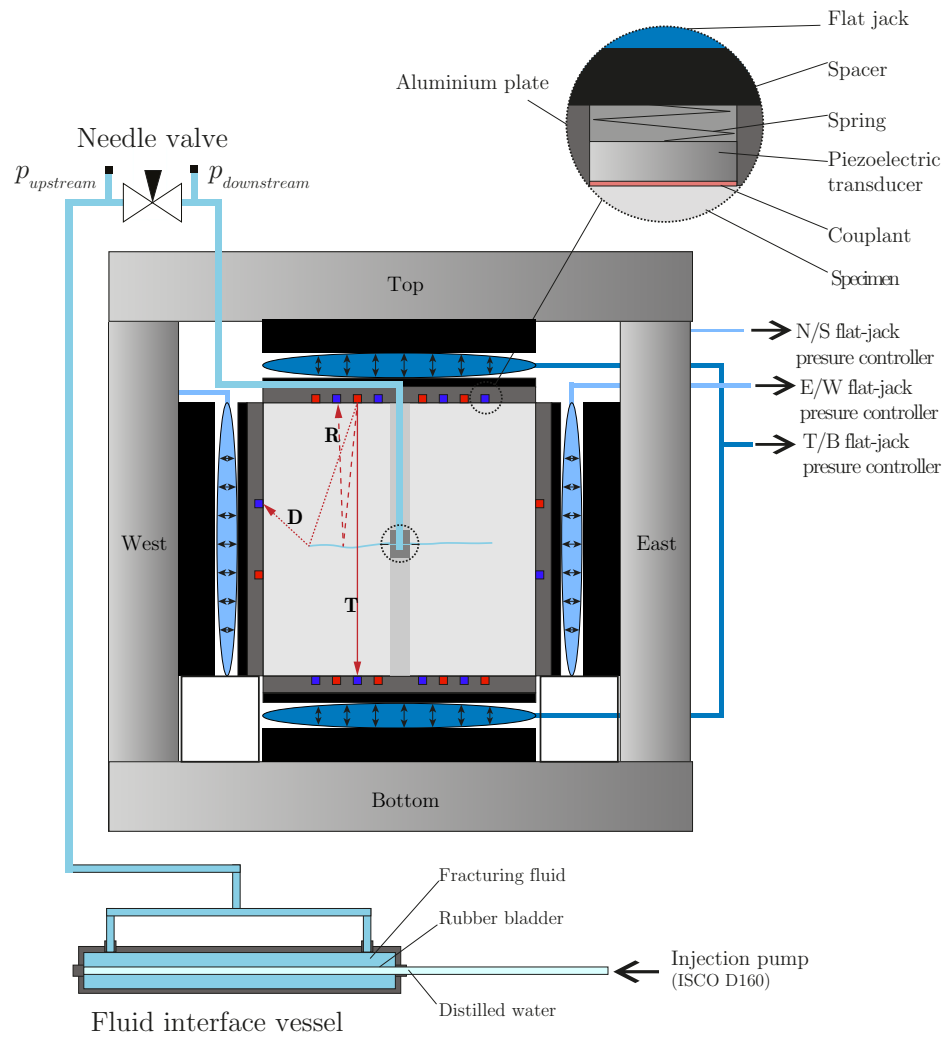
Figure 6.1 – Schematic illustration of the experimental setup.

Table 6.1 – Rock properties. Porosity represents the connected volume porosity measured using the gas pycnometer. Elastic properties are measured from static tri-axial tests.

Rock	E (GPa)	ν	ρ ($\times 10^3$kg/m^3)	Grain size (mm)	Porosity (%)
Carrara marble	60.6	0.30	2.69	0.1-0.2	0.60
Zimbabwei gabbro	99.7	0.29	3.00	1-3	0.32

Table 6.2 – Mode-I fracture toughness K_{Ic} measured using the semi-circular bend (SCB) test and tampered double cantilever beam (TDCB) test (see more details of these two methods in A.2).

Rock	SCB (MPa·m$^{1/2}$)	TDCB (MPa·m$^{1/2}$)	K_{Ic} in literature (MPa·m$^{1/2}$)
Carrara marble	1.55±0.11	1.97±0.08	1.38 (Ouchterlony, 1990)
Zimbabwei gabbro	2.79±0.11	4.05±0.09	3.03 (Meredith and Atkinson, 1985)

Table 6.3 – Viscosity of fracturing fluid.

Fluid	Glycerol	Silicone oil A	Silicone oil B
μ (Pa.s)	0.6	100	1000
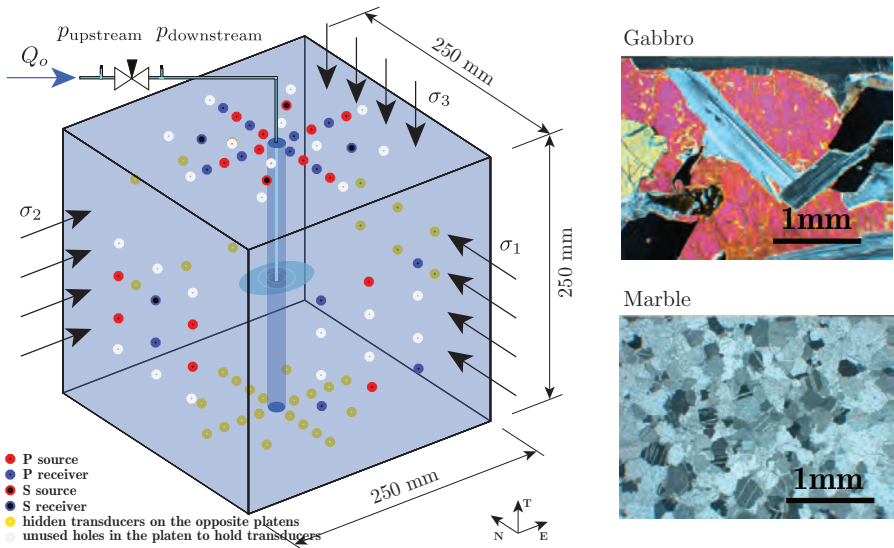
Figure 6.2 – Schematic illustration of the rock sample showing the transducers' disposition (left) and thin sections of Zimbabwe gabbro and Carrara marble (right). Additional holes are available in the platens allowing the use of various transducer dispositions. Two facing platens share the same transducers disposition and source/receivers transducers are alternatively located on opposite platens for robustness. This figure is adapted from Liu et al. (2020).
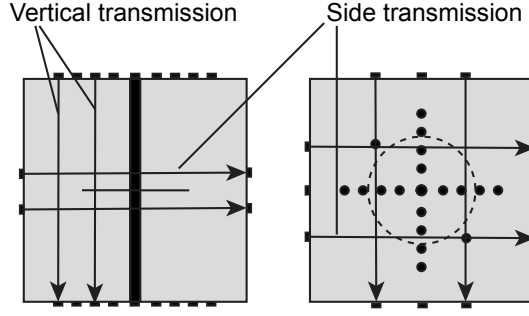
Figure 6.3 – Illustration of the vertical and side transmission.

6.2.1   Reconstruction of the fracture geometry

We reconstruct the fracture extent based on the time-arrival of the waves diffracted by the fracture front. As the fracture extent grows, the propagation time of the diffracted wave for a given pair of source and receiver also evolves. The time of these diffracted arrivals corresponds to the shortest ray path connecting the fracture front and source-receiver pairs. We then locate the diffracted positions along the fracture front knowing locations of source-receiver pairs and wave velocities propagating inside the block (see Table. 6.4). Assuming an elliptical or circular shape of the fracture, with or without tilts, we solve the inverse problem with four geometrical models and rank them using Bayes factors (see more details in Liu et al. (2020)).

6.2.2   Vertical transmission analysis

We refer the vertical transmission analysis as the analysis for acoustic transmitted waves obtained from the vertical facing source-receiver pairs, as shown in Fig 6.3. We refer those obtained from the horizontal facing source-receiver pairs as the side transmission.

Transmitted energy Transmitted waves attenuate when passing through a process zone characterized by micro-cracks and through the fluid-filled fracture. We estimate the size of the process zone around the fracture tip by combining such transmission attenuation and the fracture front geometry obtained from acoustic diffraction.

Following Liu et al. (2020), we compute the signal strength $E_i^{1/2}$ of a given transmitted wave arrival (P or S) for the acquisition sequence i as

$$E_i^{1/2} = \sqrt{\sum_{j=j_{min}}^{j_{max}} u_i^2(t_j)} \tag{6.1}$$

where $u_i(t)$ is a low-pass filtered (at 2MHz) waveform which is cropped by a tapered Hamming window centered on the interest arrival with a size of $(t_{j_{max}} - t_{j_{min}}) = 14 \, \mu$s. We then choose a reference signal obtained before fracture initiation and define the attenuation ratio as

$(E_i/E_{ref})^{1/2}$.

Fracture opening We estimate the fracture width based on compressional waves transmitted across the fracture plane between two facing transducers (Groenenboom and Fokkema, 1998). We set an interest region around the transmitted arrival and look at its frequency domain after Fourier transform. The transmitted signal $\hat{u}_{\text{fracture}}$ can be expressed as the product of a transmission coefficient $T(\zeta, w)$ and a reference signal $\hat{u}_{\text{base}}$ recorded before the fracture initiation. We then estimate the fluid layer thickness (fracture width) w by minimizing the misfit for frequencies around the central frequency of the source signal ($\zeta_{min} < \zeta < \zeta_{max}$).

$$f(w) = \sum_{\zeta_{min}<\zeta<\zeta_{max}} |\hat{u}_{\text{fracture}} - T(\zeta, w)\hat{u}_{\text{base}}| \qquad (6.2)$$

We set ζ_{min} = 500 kHz and ζ_{max} = 1100 kHz given the central frequency of 750 kHz of the source signal. We assume the simplest case of normal incidence (a three-layer-model) and write the transmission coefficient $T(\zeta, w)$ (see e.g. Brekhovskikh and Godin (1990) for details).

$$T(\zeta,w) = \frac{(1 - r_{ff}^2)\exp(i\alpha)}{1 - r_{ff}^2\exp(2i\alpha)}, \quad r_{ff} = \frac{z_r - 1}{z_r + 1}, \quad z_r = \frac{\rho_f V_{p,f}}{\rho V_p}, \quad \alpha = \frac{2\pi\zeta w}{V_{p,f}} \qquad (6.3)$$

where ρ and ρ_f are densities of the solid and the fracturing fluid respectively, V_p and $V_{p,f}$ are compressional wave velocities propagating in the solid and in the fluid (we take $\rho_f = 1260 kg/m^3$ and $V_{p,f} = 1960 m/s$ for the properties of glycerol). This width estimation is only valid for the fluid channel which do not exhibit any fluid lag. It has been shown to consist well with optical measurements for fractures fully filled by injection fluids (Kovalyshen, 2014). In the following, we estimate the fracture width assuming that the fracture is full of fluid.

The appearance of a fracture opening ahead of the fracture front indicates the presence of a process zone. The width estimation utilizes both the amplitude and phase information of transmitted signals, which possibly act as a more accurate approach to compare process zone sizes between different experiments.

6.2.3 Visualization of hydraulic fractures

We cut the samples after HF the experiments and observe the fracture path by eye as shown in C.3. We then choose a small part of the fractured sample and scan it using X-ray micro tomograph after putting it into the contrast agent liquid.

6.2.4 Roughness measurement of the hydraulically fractured surfaces

We map the fractured surface using a laser scanning surface profiler (VR-3200, Keyence Corporation, Japan). We measure the fracture roughness twice with different resolutions for the same sample. We first focus on a larger area of around 90×90 mm^2 with a spatial resolution
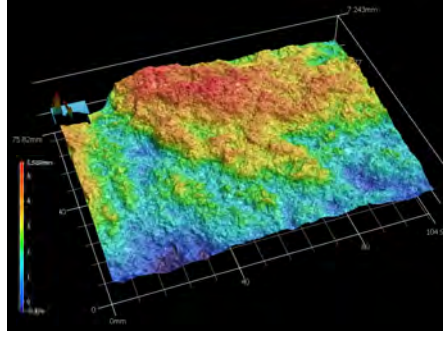
Figure 6.4 – Illustration of the measured fracture roughness surfaces of GABB-003 and its grooving pattern from the wellbore. The location of the measured area is shown in Fig. 6.24.

of 47.006μm for measurement, as shown in Fig. 6.4. We then focus on a smaller area of around 25×25 mm^2 close to the wellbore, and measure the roughness using a higher resolution of 14.777μm.

It is worthy to notice that the samples are not automatically separated after the experiments especially for gabbro experiments. We need to separate the fractured surfaces by applying a load on the whole sample parallel to the fracture plane or tapping half of the fractured sample with a hammer in the direction parallel to the fracture plane.

Following Van Dam and de Pater (1999), we use the root mean square roughness (RMS, a measure for the deviation of the roughness profile from a detrended profile) to characterize the roughness amplitude, and we use an average slope ϕ_s to characterize the tortuosity.

$$\text{RMS} = \left(\frac{1}{n} \sum_{i=1}^{n} (y_{\text{profile},i} - y_{\text{centerline},i})^2 \right)^{1/2} \tag{6.4}$$

$$\phi_s = \frac{1}{n-1} \sum_{i=2}^{n} \arctan\left(\left| \frac{y_{\text{profile},i} - y_{\text{profile},i-1}}{x_{\text{profile},i} - x_{\text{profile},i-1}} \right| \right) \tag{6.5}$$

where n is the number of points measured and $y_{\text{profile},i}$ and $x_{\text{profile},i}$ the height of the measured profile and the position along the measuring interval at measuring point i. Before calculating ϕ_s, the measured profile is tilted until a least-square linear fit through the profile has zero slope.

The fracture surface roughness exhibits robust universal fractal statistical properties (Mandelbrot et al., 1984; Bonamy and Bouchaud, 2011). In this chapter, we also look into the fractal properties of these hydraulic fracture surfaces. We are interested in the scaling of the off-plane height variation $\delta h = h(x + \delta x) - h(x)$ with the observation scale δx. The variance of this distribution shows a scaling law for a fractal surface

$$< \delta h^2 > \sim \delta x^{2\zeta} \tag{6.6}$$
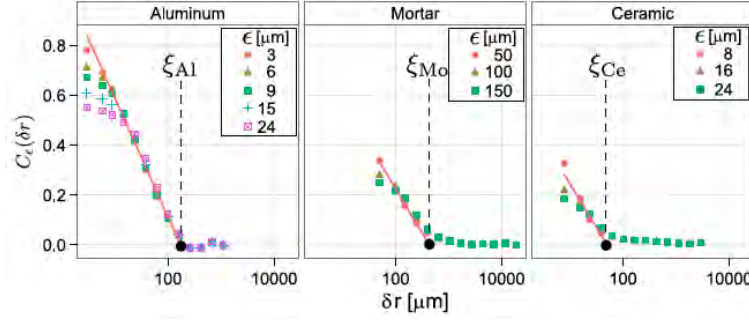
Figure 6.5 – Spatial correlations of ω_ϵ for the three materials considered (taken from Vernède et al. (2015)). The correlations are represented for ω_ϵ computed at different scales ϵ. The cutoff length ξ is represented for each case.

where ζ is the so-called roughness exponent. It is related to the fractal dimension $d_F = 2 - \zeta$ and the Fourier transform of $< \delta h^2 >$, denoted as the power spectrum $S(f)$.

$$S(f) \sim f^{-2\zeta - 1} \tag{6.7}$$

Following Vernède et al. (2015), we elicit different fracture mechanisms in two regimes. We introduce $\omega_\epsilon(x)$ to measure the intensity of the local height variations of the fracture surface on a scale ϵ:

$$\omega_\epsilon(x) = \frac{1}{2}\log(< \delta h(x, \delta x)^2 >_{|\delta_x| = \epsilon}) - \Omega_\epsilon \tag{6.8}$$

where Ω_ϵ is chosen such that the average of $\omega_\epsilon(x) = 0$. We further calculate the spatial correlations of ω_ϵ and average it over all directions.

$$C_\epsilon(\delta r) = < \omega_\epsilon(x)\omega_\epsilon(x + \delta x) >_{x, |\delta x| = \delta r} \tag{6.9}$$

These correlations are zero within statistical noise at large δr but present a logarithmical decay with the distance at small δr: $C_\epsilon(\delta r) \sim -\log(\delta r / \xi)$ (Vernède et al., 2015). ξ is the cut-off length scale at which C_ϵ extrapolates to zero. ξ characterizes the process zone size (Fig. 6.5).

These roughness analysis are often performed on linearly detrended roughness profiles and sometimes on profiles after removing the waviness (Movassagh et al., 2020). In this chapter, we deal with the roughness profiles after a linear detrending of the surface.

6.3 Experimental configurations

We perform HF injections in different propagating regimes by varying the rock and fluid type, the confining stresses, and the injection rate. As shown in Table. 6.5, we impose a bi-axial state of stress on the blocks $\sigma_1 = \sigma_2$. We set the minimum stress σ_3 parallel to the wellbore to favor a planar horizontal fracture. We keep the same deviatoric stress $\sigma_1 - \sigma_3 = 10$ MPa for all experiments except GABB-004 where $\sigma_1 - \sigma_3 = 8$ MPa.

Table 6.4 – Sample dimensions and wave velocities for different experiments. V_p and V_s are measured directly with the cubic rock samples during the pressurization stage prior to fracture growth. The mean and standard deviation values are calculated based on the vertical and horizontal ray paths for the first 10 acquisitions before the fracture initiation (16 vertical ray paths for the calculation of V_p and 5 horizontal ray paths (in the north-south and east-west directions) for that of V_s). The block size is indicated in the form of dimensions in north-south (N-S) × east-west (E-W) × top-bottom (T-B) directions. The notch position represents the vertical distance between the notch and the bottom surface of the rock. The fracture initiates from the notch for all experiments except for GABB-006, in which the fracture initiates 9.5 mm below the notch position as shown in C.3.

Rock	V_p (m/s)	V_s (m/s)	Block size (mm)	Notch position (mm)
MARB-005	6249.8 ± 54.0	3229.9 ± 176.2	257 × 256 × 256	131
MARB-007	6220.3 ± 45.4	3305.8 ± 36.9	258 × 258 × 256	127.5
MARB-008	6278.6 ± 24.1	3326.9 ± 34.8	250 × 250 × 251	126
MARB-009	6230.1 ± 20.0	3279.6 ± 12.0	250 × 251 × 252	126.5
MARB-010	6358.6 ± 24.8	3360.5 ± 14.3	252 × 250 × 251	124.9
GABB-001	6679.0 ± 113.2	3668.5 ± 41.3	250 × 250 × 251	128.5
GABB-002	6835.3 ± 18.5	3754.7 ± 23.2	255 × 255 × 255	125.5
GABB-003	6791.3 ± 14.2	3722.7 ± 43.2	250 × 249 × 250	125
GABB-004	5698.1 ± 69.1	3412.9 ± 54.2	250 × 251 × 245	123
GABB-005	6743.8 ± 149.5	3678.0 ± 122.8	250 × 250 × 251	126
GABB-006	6734.5 ± 168.4	3668.9 ± 196.5	250 × 250 × 249	124

We tune the number of turns of the needle valve in the injection line to dump the release of the pressurized fluid after fracture initiation. This acts the key to control the flux in the case of an important system compliance. The flux entering the fracture differs from the ISCO pump injection rate Q_o and needs to be estimated based on the the fluid pressure upstream and downstream the valve (see more details in C.1). As a result, the real fracture propagating regime might deviate from the designed one and needs to be re-evaluated after the experiments.

6.3.1 Estimation of the propagation regime

We estimate the dominant propagation regime based on the LHFM theory (see for example Detournay (2016)) even though these materials likely exhibit a quasi-brittle fracture behavior. The rocks are homogeneous and isotropic and present very low permeability. The fracture growth can be approximated as a radial HF propagating in an impermeable medium due to the notch, well completion and stresses applied. For such a radial HF, the fracture growth at the early time exhibits an important fluid lag between the fluid and fracture front (O-regime). The fluid front then slowly coalesces with the fracture front over a characteristic time scale t_{om}.

$$t_{om} = \frac{E'^2 \mu'}{\sigma_3^3} \qquad (6.10)$$

Table 6.5 – Sample configuration and experimental parameters for HF injections in gabbro and marble. The system compliance U is calculated from the time evolution of the pressure and the injection rate Q_o (see more details in C.1).

Rock sample	Fracturing fluid	σ_3 (MPa)	$\sigma_1 = \sigma_2$ (MPa)	Injection rate Q_o (mL/min)	System compliance U (mL/GPa)
MARB-005	Silicone oil A	10	20	0.2	282.5
MARB-007	Silicone oil B	0	10	0.02	319.5
MARB-008	Glycerol	0	10	0.03	210.7
MARB-009	Glycerol	0	10	0.05	217.9
MARB-010	Glycerol	8	18	0.03	181.3
GABB-001	Glycerol	0.5	10.5	0.2	217.3
GABB-002	Silicone oil A	0	10	0.05	255.1
GABB-003	Glycerol	10	20	0.08	301.0
GABB-004	Glycerol	15	22	0.07	237.6
GABB-005	Glycerol	5	15	0.04	222.2
GABB-006	Glycerol	10	20	0.04	225.9

where $E' = E/(1 - v^2)$ is the plane-strain elastic modulus related to the Young's modulus and Poisson's ratio, $\mu' = 12\mu$ the effective viscosity. As the fracture continues to grow, the increase of the perimeter of the fracture front results in more energy dissipated in the creation of fracture surfaces. The fracture growth starts to transition from a fluid viscosity dominated regime (M-regime) to a fracture toughness dominated regime (K-regime) over a time scale t_{mk}.

$$t_{mk} = \frac{\mu'^{5/2} Q_o^{3/2} E'^{13/2}}{K'^9}, \quad K' = \sqrt{\frac{32}{\pi}} K_{Ic} \tag{6.11}$$

where K_{Ic} is the mode I fracture toughness.

Most radial HF growth in laboratory spans part of the transition trajectory. Their propagating regime depends on the relation between the propagation time t and these two time scales. When there is no fluid lag ($t \gg t_{om}$), the transition state is captured by a single dimensionless toughness $\mathcal{K}_m$.

$$\mathcal{K}_m = (t/t_{mk})^{1/9} \tag{6.12}$$

The fracture grows in the viscosity dominated as long as $\mathcal{K}_m \leq 1$ and strictly in the toughness dominated regime when $\mathcal{K}_m \geq 3.5$ (Savitski and Detournay, 2002). Moreover, the fluid lag vanishes at all time in the toughness-dominated regime (Bunger, 2005). In other words, when $t \leq t_{om}$, no fluid lag is observed if $\mathcal{K}_m > 3.5$.

In this chapter, we calculate these two characteristic time scales and identify corresponding regimes depending on the relation between t_{om}, t_{mk} and propagation duration t_{prop}, as shown in Table. 6.6. Here, we estimate t_{prop} based on the fracture initiation time t_{ini} and

Table 6.6 – Characteristic timescales for a radial hydraulic fracture: viscosity–toughness transition t_{mk}, and fluid lag disappearance timescale t_{om}. For experiments where the applied minimum confining stress equals zero, we put weight on the top platen in some cases to ensure the good contact between acoustic sensors and the top surface of the rock. We calculate t_{om} using the estimated σ_3 from the self weight of the block and the added weight on the top platen. We estimate t_{mk} using the averaged entering flow rate into the fracture $< Qo >$ during the fracture duration t_{prop}, the elastic properties in Table. 6.1 and the fracture toughness measured by the SCB method (Table. 6.2).

Rock sample	$< Q_o >$ (mL/min)	Propagation duration t_{prop} (s)	t_{mk} (s)	t_{om} (s)	Estimated propagation regime
MARB-005	0.046	≈ 582	1.3×10^4	5.3×10^3	lag-viscosity
MARB-007	≈ 0.005	≈ 2711	1.5×10^5	2.5×10^{14}	lag-viscosity
MARB-008	1.713	≈ 25	8.5	1.5×10^{11}	lag-viscosity
MARB-009	0.731	≈ 92	2.3	4.9×10^{10}	lag-viscosity
MARB-010	0.015	≈ 534	7.0×10^{-3}	62.4	lag-toughness
GABB-001	0.074	≈ 410	9.4×10^{-3}	3.3×10^5	toughness
GABB-002	5.6×10^{-4}	≈ 8199	2.2	5.5×10^{13}	lag-viscosity
GABB-003	0.445	≈ 158	1.4×10^{-1}	85.3	toughness
GABB-004	2.434	≈ 40	1.8	25.3	lag-viscosity
GABB-005	0.0253	≈ 780	1.9×10^{-3}	682.5	toughness
GABB-006	0.2769	≈ 183	6.8×10^{-2}	85.3	toughness

approximate Q_o by the averaged injection rate during the propagation $< Q_o >$.

$$< Q_o >= \int_{t_{ini}}^{t} Q_{in}(t)\mathrm{d}t \tag{6.13}$$

where the method of determining Q_{in} and t_{ini} is shown in details in C.1.

As shown in Table. 6.6, we have $\sigma_3 \le 15\,\text{MPa}$ due to the maximum pressure limits of GDS pumps (pumps connected to flat-jacks controlling the applied confining stresses). We therefore have $t_{om} \gg t_{mk}$ for all HF experiments in Table. 6.6. When $t_{prop} \le t_{mk}$, a fluid lag always appears and the fracture growth is in the transition between lag and viscosity dominated regime. Otherwise $t_{prop} \gg t_{mk}$, the fluid lag disappears at very early time and the fracture toughness tends to dominate the HF propagation. However, in GABB-002, $t_{mk} \ll t_{prop} \ll t_{om}$ implies that fracture toughness dominates the HF growth. However, this estimation does not consist with the observations in GABB-002: the injection fluid stays around the wellbore acting as a point load. We observe a very important lag during the propagation, and the HF growth in GABB-002 is actually dominated by the fluid lag.

We classify the experiments of Table. 6.6 into three groups depending on their propagation regime, confining stresses, and material.

- GABB-001, GABB-003, GABB-005, and GABB-006 are toughness dominated experiments

in gabbro with no fluid lag observed. The deviatoric stress remains the same for all experiments $\sigma_1 - \sigma_3 = \sigma_2 - \sigma_3 = 10$ MPa yet the minimum confining stress σ_3 differs significantly with GABB-003=GABB-006>GABB-005>GABB-001.

- MARB-009 and MARB-010 experiments are performed in marble with the same deviatoric stress but different injection flux and confining stresses. In both experiments, a fluid lag appears at the early stage of the fracture propagation and then disappears before the fracture front reaching the sample edge.

- MARB-005, MARB-007 and GABB-002 are lag dominated experiments with the same deviatoric stress but different rocks/ fluids. An important fluid lag is detected throughout the fracture propagation in all experiments. We discuss these experiments in the Appendix. B.

In Table. 6.4, the GABB-004 block presents acoustic properties significantly different from the other gabbro blocks. The MARB-008 experiment shows a very fast fracture propagation such that very limited measurements are obtained during the growth. We therefore do not analyze these two experiments in the following.

6.3.2 Post-mortem observations

Solid bridging and crack branching are observed both in marble and gabbro using X-ray micro tomograph, as shown in Fig. 6.6. The crack branching deviates more from the main fracture path in gabbro (around $10^3 \mu$m) than in marble (around $10^2 \mu$m). The solid bridges are much easier to break in marble than in gabbro, with the former automatically detached in some cases. The fracture path in gabbro does not present a clear preference for intra-grain or inter-grain fracturing.

6.4 Toughness dominated experiments in gabbro under different confining stresses

In this section, we analyze the HF growth in GABB-001, GABB-003, GABB-005 and GABB-006 by combining different measurements, such as the fracture extent, fracture opening, vertical acoustic transmission, apparent toughness and fracture roughness.

6.4.1 Evolution of the fluid pressure and fracture radius

We show the time evolution of the fluid pressure, inlet flux and fracture radius in Figs. 6.7, 6.8, 6.9, and 6.10. During the pressurization stage, we first adopt a larger injection rate to detect possible leaks in the injection line, we then switch to the designed injection rate before the fluid pressure reaching the minimum confining stress σ_3. The valve is either adjusted during the pressurization stage (in GABB-001, GABB-005 and GABB-006) or prior to the fluid injection

Figure 6.6 – Micro-CT images of fracture paths in GABB-001 (a) and b)), GABB-002 (c) and d)) and MARB-008 (e) and f)). The fractures propagate upwards in these figures.

(GABB-003). The pressure increases linearly with time during the pressurization when there is no leaks and the position of the needle valve remains unchanged. When the fracture growth initiates from the notch, we observe an instant increase of volume in the top-bottom GDS pumps and a drop of the downstream pressure. The upstream pressure may either increase with time if the needle valve is over-constrained (GABB-001 and GABB-005) or decrease with time when the valve is widely opened (GABB-003). As the fracture front reaches the end of the block, the downstream pressure drops significantly and a kink is visible on the fluid pressure record as shown in Figs. 6.7, 6.8, and 6.10. It is worth recalling that no fluid lag is observed in these HF experiments.

Interestingly, we observe different maximum net pressures (peak of the downstream pressure) and initiation pressures in these experiments. Such a difference is possibly related to the different fracture toughness between samples and the notch sharpness (note that the fracture in GABB-006 does not initiate from the notch). The variation of the valve restriction, different injection rates will also play a role.

6.4.2 Evolution of the acoustic transmission across the fracture plane

Transmitted energy In the GABB-001 experiment, an attenuation of at most 10% is reported for all P-wave transducers on the top and bottom platens. The appearance of P-wave atten-
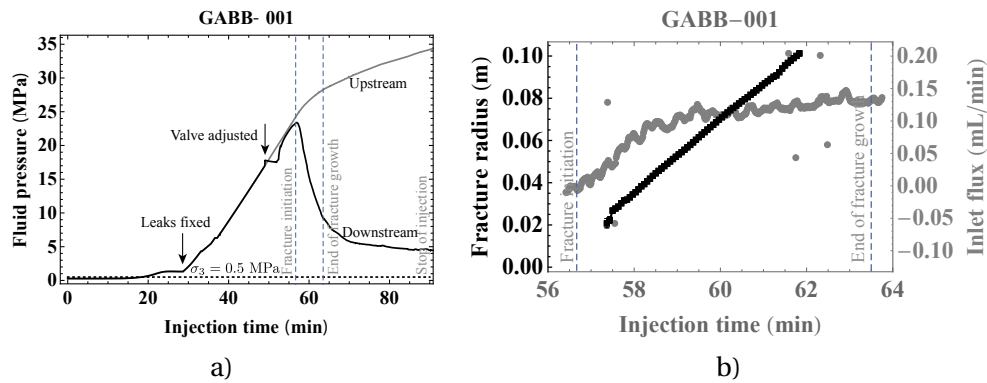
Figure 6.7 – GABB-001: time evolution of a) the injection pressure, b) the fracture radius and estimated flux entering into the fracture. The vertical lines indicate respectively the fracture initiation and fracture reaching the edge of the block, with both determined from the sudden change of the difference between the upstream and downstream pressure.
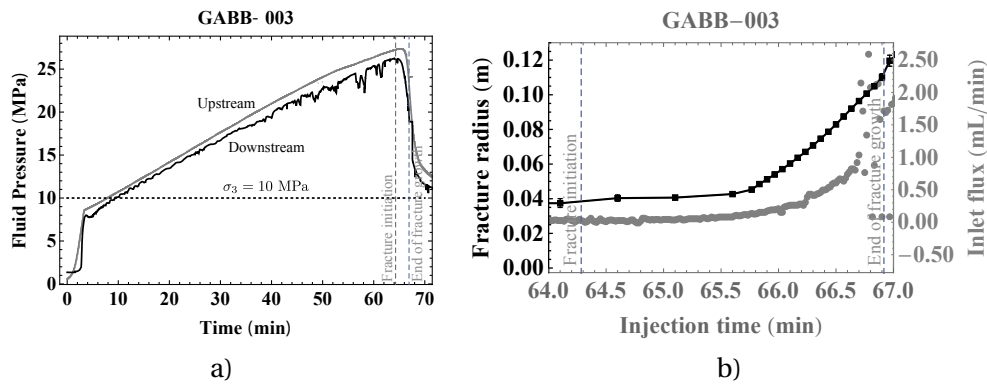
Figure 6.8 – GABB-003: time evolution of a) the injection pressure, b) the fracture radius and estimated flux entering into the fracture. The vertical lines indicate respectively the fracture initiation and fracture reaching the edge of the block, both determined by the volume change of the top-bottom flat jacks. The oscillations in the downstream pressure are caused by the silicone oil stuck in the restricting valve, as a result, oscillating the valve randomly during the pressurization stage.
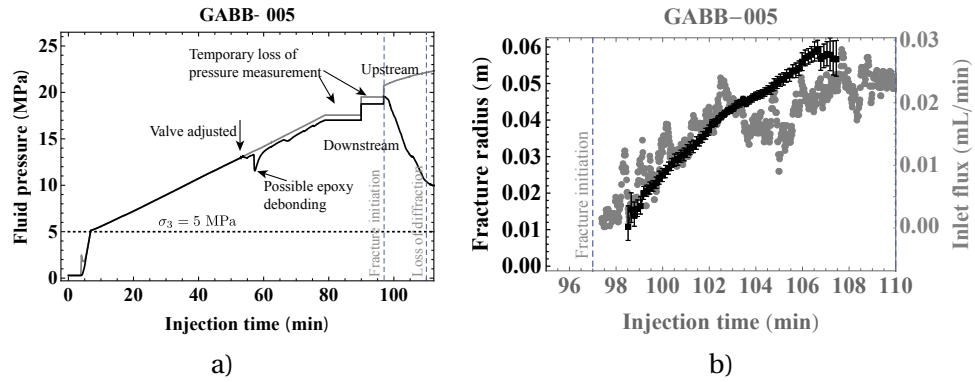
Figure 6.9 – GABB-005: time evolution of a) the injection pressure, b) the fracture radius and estimated flux entering into the fracture. The vertical lines indicate respectively the fracture initiation (determined by the volume change of the top-bottom flat-jacks/GDS pumps) and the disappearance of the detectable diffraction front due to the bad visibility. The dotted line indicates the minimum confining stress. The pressure drop during the pressurization stage is probably related to the debonding of the epoxy going downward. The pressure plateau prior to the downstream pressure drop is related to a temporary loss of the connection of the pressure gauges with the measurement system. This happens slightly prior to the fracture initiation.
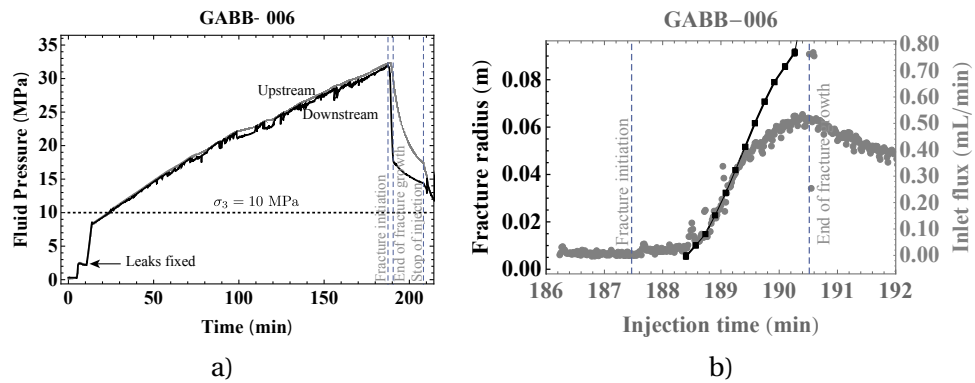
Figure 6.10 – GABB-006: time evolution of a) the injection pressure, b) the fracture radius and estimated flux entering into the fracture. The vertical lines indicate respectively the fracture initiation, fracture reaching the edge of the block, and the end of the injection, with the former two determined by the change of the difference between the upstream and downstream pressure. The oscillations in the downstream pressure are caused by small leaks in the injection line close to the restricting valve.
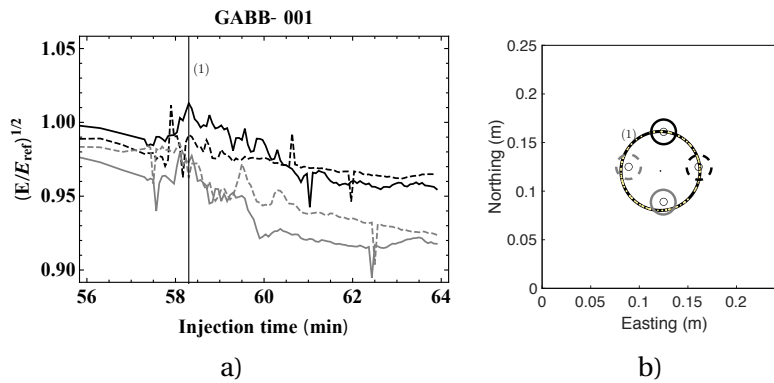
Figure 6.11 – GABB-001: time evolution of a) the transmitted compressional wave energy and b) the fracture geometry at the start of transmission attenuation. Locations of the transducers in figure a) are indicated by circles in figure b) using the same line style. The fracture extent associated with the numbered vertical lines in figure a), is also shown in figure b) using the same number.

uation corresponds well to the arrival of the fracture front (Fig. 6.11). However, the S-wave attenuation occurs (even at the time of the fracture initiation) prior to the fracture front arrival (Fig. 6.12).

This attenuation of transmitted energy (either in shear or compressional waves) ahead of the fracture front is observed in all four toughness dominated experiments (see more details in C.2). It implies the existence of a process zone ahead the fracture tip. This attenuation ahead of the fracture front is more visible for transducers away from the wellbore. In Figs. 6.12, C.2, C.5, C.8, we plot the fracture front geometry at the time where the attenuation of the transmitted energy becomes visible. The distances between the transmitted wave transducer pair and the the fracture front provides an estimation of the process zone size. We show these estimated process zone sizes for four experiments in Table. 6.7. Interestingly, the process zone size is always comparable to the fracture extent and the process zone size does not necessarily increase with the fracture radius.

This transmission attenuation provides a very coarse estimation of the process zone size. The ray paths are limited to a small number of source-receiver pairs. The criterion to determine the moment of the attenuation can be not clearly defined for different experiments since the transmitted energy depends a lot on materials, confining stresses and the state of the contact between the transducers and the specimen (see C.4 for more details).

Fracture opening Fracture width estimation is based on the assumption of smooth parallel fracture surfaces. Fracture roughness and solid bridging may influence a lot the estimation when the roughness scale is comparable to estimated width. Moreover, the drying of the couplant between the transducer and the rock surface during the pressurization stage may also result in attenuation of transmitted waves and a slight overestimation of the fracture
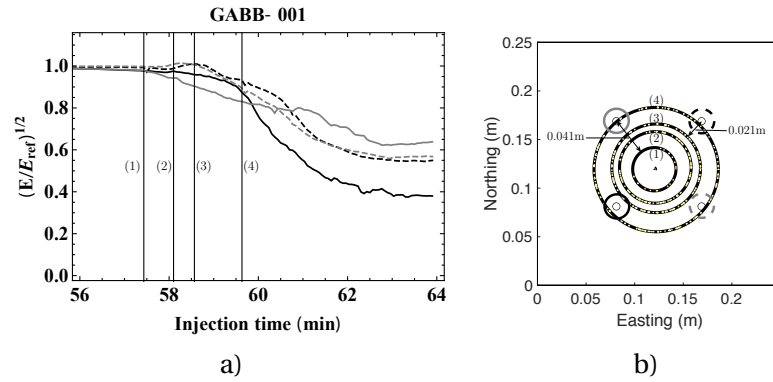
Figure 6.12 – GABB-001: time evolution of a) the signal strength of transmitted shear waves and b) the fracture geometry at different times of the fracture growth. Locations of the transducers in figure a) are indicated by circles in figure b) using the same line style. The fracture extent associated with the numbered vertical lines in figure a), is also shown in figure b) using the same number.

Rock sample	σ_3 (MPa)	Transducer type	Fracture radius (m)	Estimated process zone size (m)
GABB-001	0.5	b)	0.022 ± 0.0016	0.041
GABB-001	0.5	b)	0.046 ± 0.0028	0.021
GABB-003	10	a)	0.041 ± 0.0011	0.036-0.038
GABB-003	10	b)	0.043 ± 0.0012	0.013
GABB-003	10	b)	0.048 ± 0.001	0.022
GABB-005	5	b)	≈ 0.011	≈ 0.054
GABB-005	5	a)	0.024 ± 0.0023	0.042-0.069
GABB-006	10	b)	0.010 ± 0.0017	0.047
GABB-006	10	b)	0.032 ± 0.0012	0.031
GABB-006	10	a)	0.032 ± 0.0012	0.034-0.049

Table 6.7 – Estimated process zone size based on the attenuation of the vertical transmitted waves. The transducers used to identify the process zone are classified into two types: a) P-wave transducers located farthest away from the wellbore and b) S-wave transducers.
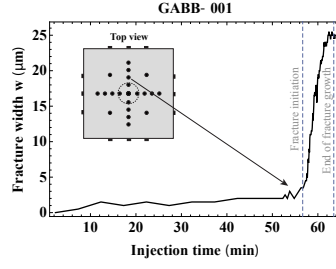
Figure 6.13 – GABB-001: time evolution of the fracture width. We have a maximum fracture width around 3 μm prior to fracture initiation.
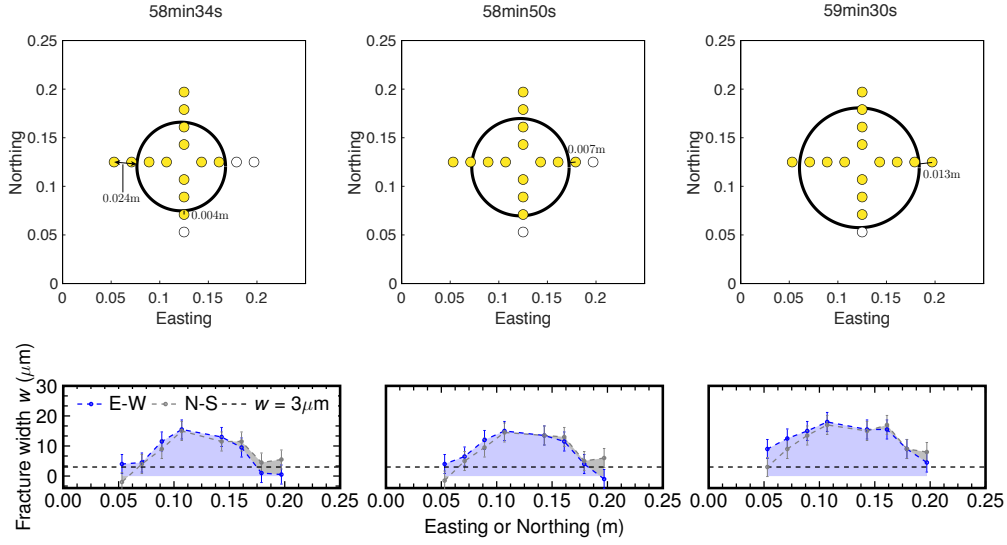
Figure 6.14 – GABB-001: top view of the extent of the hydraulic fracture. The P-wave transducers turn yellow if the fracture opening goes above 3 μm. 3 μm is the maximum estimated width prior to fracture initiation which is taken as the error of width estimation.

width. We estimate the error induced by the drying couplant or other acoustic noises using the maximum fracture openings obtained from transmitted waves prior to the fracture initiation. This error is around 2-3 μm for gabbro HF experiments (see Fig. 6.13 for example).

We observe in all four experiments the appearance of the fracture opening prior to the fracture front arrival, as shown in Fig. 6.14 for example (We show similar plots for GABB-003, GABB-005 and GABB-006 in C.2). This is against the observation of the transmitted energy evolution in GABB-001(Fig. 6.11), where no attenuation is observed prior to the fracture front arrival. This implies that opening calculation tends to be more sensitive to the process zone and that a process zone leads to both attenuation of the transmitted amplitude and a phase shift. If we set the width estimation error ($w = 3$ μm) as an indicator of the process zone's presence: when the fracture opening at the location of one transducer goes beyond the width estimation error, a process zone is considered to form at this location. The estimated process zone sizes obtained using this method (Fig. 6.14, Figs. C.3, C.6, C.9) are smaller than those obtained

using the evolution of transmitted energy (Table. 6.7). This estimation of the process zone size of course depends a lot on the accuracy of the width estimation and the threshold width used.

6.4.3 Estimation of the stress intensity factor using the estimated fracture radius and measured fluid pressure

The evolution of the apparent fracture toughness is probably associated with that of the process zone. We approximate the apparent toughness using the opening-mode (mode I) stress intensity factor (K_I) under the assumption of stable fracture propagation ($K_I = K_{Ic}$). We estimate the stress intensity factor (Tada et al., 1973) using the analytic solution for the opening of a uniformly pressurized circular crack ('Sneddon's solution'):

$$K_{Ic} \approx K_I = \frac{2}{\sqrt{\pi}}(p_{f,0} - \sigma_3)\sqrt{R} \qquad (6.14)$$

where $p_{f,0}$ is the downstream fluid pressure at the inlet and R the fracture radius. This method applies only when the pressure distribution is uniform inside the fracture. This corresponds to the fracture growth dominated by fracture toughness, which requires $\mathcal{K}_m > 3.5$ for a radial HF (Savitski and Detournay, 2002). This requirement is harsh yet can be relaxed since a borehole / notch removes the pressure singularity at the inlet. For example, with a borehole of 4.2 mm in radius and a notch of 6 mm in radius, the actual minimum value of $\mathcal{K}_m$ for the application of this method can be relaxed to $\mathcal{K}_m \geq 2.95$ (Bunger, 2006). We investigate this requirement more in details by calculating the dimensionless toughness $\mathcal{K}_m$ of the CSIRO Block-4 test (the wellbore radius of this test is 8.35 mm and the notch radius 9.8 mm), which has been already been properly reproduced with a constant toughness linear elastic solver (Lecampion et al., 2017). We evaluate the dimensionless toughness $\mathcal{K}_m$ using the instant inlet flux Q_{in}. As shown in Fig. 6.16, the instant stress intensity factor overestimates the fracture toughness after the fracture initiation due to the large pressure gradient inside the fracture associated with an important system compliance. It drops back approximately to the constant fracture toughness by the time $\mathcal{K}_m \geq 2.5$. For all experiments presented in this chapter, the wellbore radius is around 8 mm and the notch radius is around 10.5 mm, which is either similar to or larger than that in the CSIRO test. This larger ratio between the wellbore and fracture radius (larger values of ρ in Fig. 6.15) should result in a even smaller difference between the inlet pressure and the pressure elsewhere compared with the CSIRO test. We therefore conclude that this method which assumes uniform pressure is valid only for dimensionless toughness $\mathcal{K}_m \geq 2.5$.

This method also requires a good measurement of the minimum confining stress σ_3. However, this applied confining stress is probably not uniform on the fracture plane. It is often smaller than the designed value due to the holes of platens and the imperfections of block dimensions and flat-jacks. Friction may occur between the rock sample and the platens. As pointed out by Moukhtari (2020), for a cubic block (with the same dimensions as our case) under a hydrostatic loading condition with $\sigma_1 = \sigma_2 = \sigma_3 = 20$ MPa, a radial area of around 60 mm is characterized with a stress attenuation of around 15% ($\sigma_3 \approx 17$ MPa). Moreover, Moukhtari (2020) reports
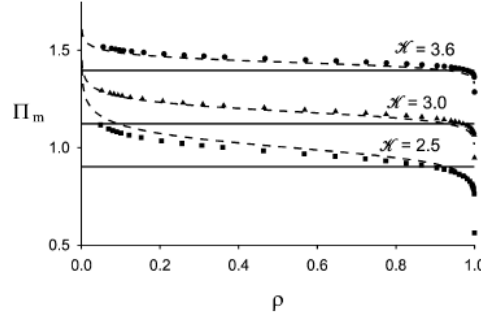
Figure 6.15 – Dimensionless pressure $\Pi_m = (p_f - \sigma_3)/(E'^{2/3}\mu'^{1/3}/t^{1/3})$ distribution inside the fracture ($0 \le \rho = x/R \le 1$) for different dimensionless toughness $\mathcal{K}_m$ in a radial HF (taken from Savitski and Detournay (2002)).

that the shear stress is around 0.2 MPa on the horizontal plane in the middle of the block. In this chapter, we assume that σ_3 is uniformly applied on the fracture plane and that there is no friction. However, such an assumption may lead to the underestimation of the mode I stress intensity factor.

We plot the evolution of the apparent toughness and its associated dimensionless toughness (estimated using Q_{in} and the SCB toughness value or the median apparent toughness value) in Fig. 6.16. We find that $\mathcal{K}_m \ge 2.5$ for GABB-001 and GABB-005, and that $\mathcal{K}_m > 2.5$ for GABB-003 (if we estimate $\mathcal{K}_m$ using the median apparent toughness) and GABB-006 most time of the fracture propagation. This fulfills the conditions to approximate the apparent toughness using the stress intensity factor obtained from Eq. (6.14). As illustrated in Fig. 6.16, the apparent toughness differs a lot between experiments and seems to depend on the stress state and material heterogeneity between blocks. However, it presents a similar evolution in all experiments: the apparent toughness first increases with the fracture radius and then decreases as the fracture front approaches the edge of the sample. This evolution is possibly associated with a growing process zone with the fracture propagation with its size limited by the sample dimensions when feeling the edge of the sample. Moreover, we find that the apparent toughness at the first half of the stage evolves with the fracture radius by approximately following a power law $K_I \sim R^\alpha$ (Liu and Lecampion, 2019). As shown in Fig. 6.17, $\alpha = 0.2 \sim 0.45 \le 0.5$ which indicates the same range as that pointed out by Liu and Lecampion (2019). We summarize the maximum and median value of the stress intensity factor in Table. 6.9.

We plot in Fig. 6.18 the fracture front geometry at the moment which corresponds to the peak value of the stress intensity factor. The shortest distance between the sample edge and the fracture front can be considered as the maximum process zone size. This maximum process zone size of 6.7 cm for GABB-001, 2.6 cm for GABB-003, 6.6 cm for GABB-005, and 5.1 cm for GABB-006, as shown in Table. 6.8. It seems that the estimated process zone size decreases as we increase the minimum confining stress.

We summarize the process zone sizes estimated using different approaches in Fig. 6.19. The

Experiment	σ_3 (MPa)	Fracture radius (m)	Estimated process zone size (m)
GABB-001	0.5	0.051 ± 0.0003	0.067
GABB-003	10	0.092 ± 0.0009	0.026
GABB-005	5	0.037 ± 0.0014	0.066
GABB-006	10	0.032 ± 0.0007	0.051

Table 6.8 – Estimated process zone size corresponding to the peak value of the apparent toughness (K_{Ic} from p and R).

Experiment	Minimum confining stress σ_3 (MPa)	Maximum value of K_{Ic} * (MPa·m$^{1/2}$)	Median value of K_{Ic} * (MPa·m$^{1/2}$)	K_{Ic} from tip asymptotes (MPa·m$^{1/2}$)
GABB-001	0.5	4.63	4.41	2.78 ± 0.48
GABB-003	10	4.04	3.74	3.87 ± 1.03
GABB-005	5	2.36	2.14	2.95 ± 0.48
GABB-006	10	3.61	2.97	2.78 ± 0.94

Table 6.9 – Estimation of the fracture toughness K_{Ic} based on the stress intensity method (K_{Ic} obtained from p and R, indicated with a superscript $*$) and the fracture opening tip asymptotes method (K_{Ic} obtained from $w(\hat{x})$). We recall here that the fracture toughness measured in dry fracture mechanics is $K_{Ic} = 2.79 \pm 0.11$ MPa·m$^{1/2}$ using the SCB method and $K_{Ic} = 2.79 \pm 0.09$ MPa·m$^{1/2}$ using the TDCB method, as reported in Table. 6.2.

process zone sizes depend a lot on the adopted estimation approach, but in all cases they can not be neglected compared to the fracture radius.

6.4.4   Estimation of the fracture toughness via width and near-tip asymptotics

For a radial HF propagating in a linear elastic solid, the fracture width presents a k-asymptote near the fracture tip (Rice, 1968) characterized by the fracture toughness,

$$w \sim \left(\frac{32}{\pi}\right)^{1/2} \frac{K_I}{E'} \hat{x}^{1/2}, \quad \frac{\hat{x}}{R} \ll 1 \tag{6.15}$$

and an m-asymptote away from the fracture tip characterized by the fluid viscosity $w \sim 2^{1/3} 3^{5/6} \left(\mu' V / E'\right)^{1/3} \hat{x}^{2/3}$. $\hat{x}$ is the distance away from the crack tip, $V = \dot{R}$ the fracture front velocity and R the fracture radius. The k-asymptote corresponds to the dissipation in creation of fracture surfaces and m-asymptote the fracture propagation dominated by the dissipation in the viscous fluid flow. A length scale $\ell_{mk} = K'^6 / (E'^4 \mu'^2 V^2)$ characterizes the transition from the near-tip k-asymptote to the far-tip m-asymptote. When $\ell_{mk}/R \gg 1$, this k-asymptote prevails the whole width profile, otherwise, this square-root relation only prevails within the length scale of ℓ_{mk} away from the fracture tip. For a radial HF propagating in a linear elastic medium, $\mathcal{K}_m \geq 1.89$ is necessary to estimate the fracture toughness using the k-asymptote (Bunger, 2006).

In quasi-brittle materials, the k-asymptote may still appear during the HF growth (Garagash,
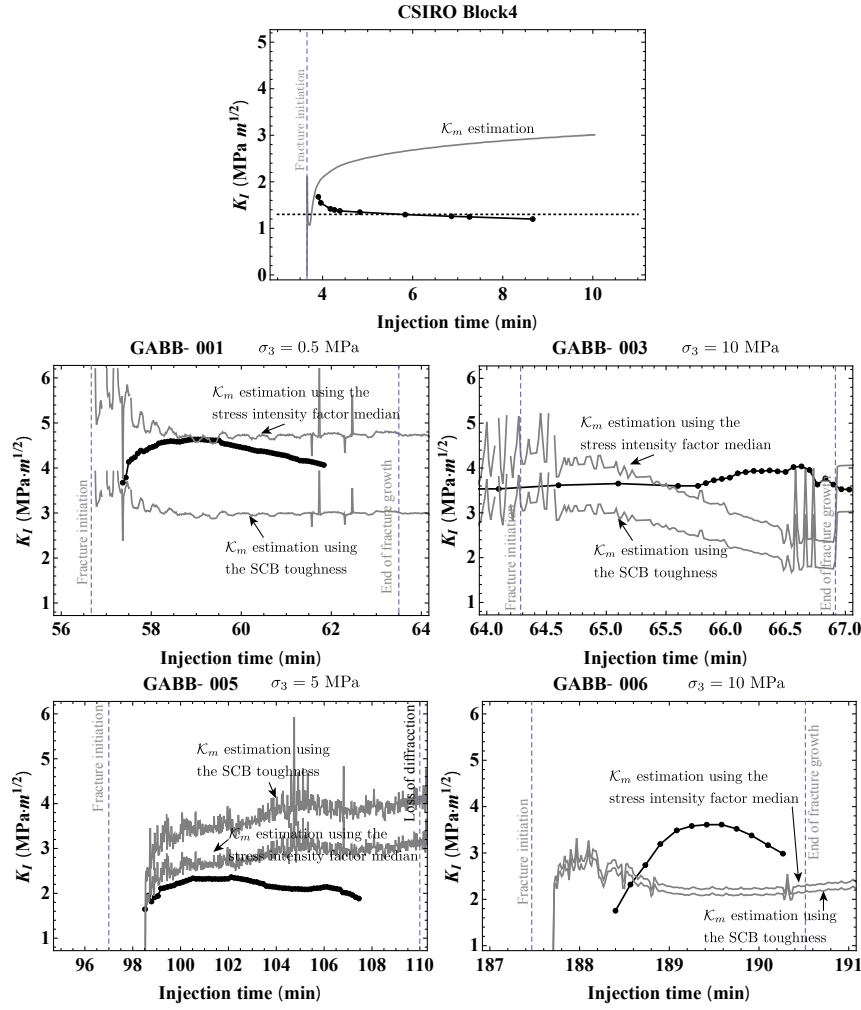
Figure 6.16 – Time evolution of the estimated stress intensity factor K_{Ic} (in black) and dimensionless toughness $\mathcal{K}_m$ (in gray). The dotted horizontal line in the figure of CSIRO Block4 test represents the fracture toughness fitted by the LHFM solver (Lecampion et al., 2017). $\mathcal{K}_m$ is evaluated using the instant inlet flux and the toughness measured using the SCB method (Table. 6.2) or the median value of the estimated stress intensity factor (Table. 6.9).
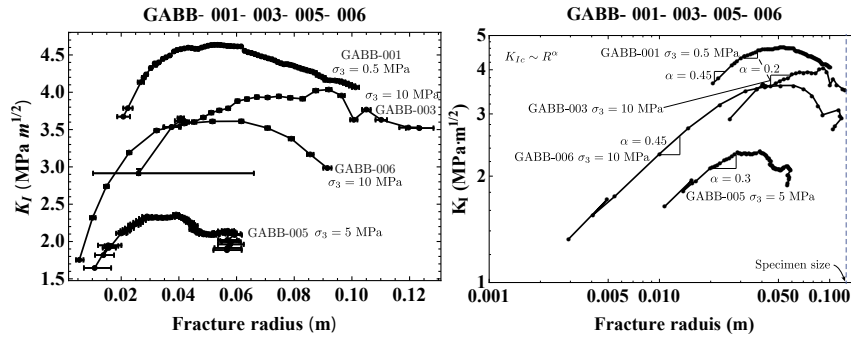
Figure 6.17 – Evolution of apparent fracture toughness with the fracture radius in GABB-001, GABB-003, GABB-005, and GABB-006.
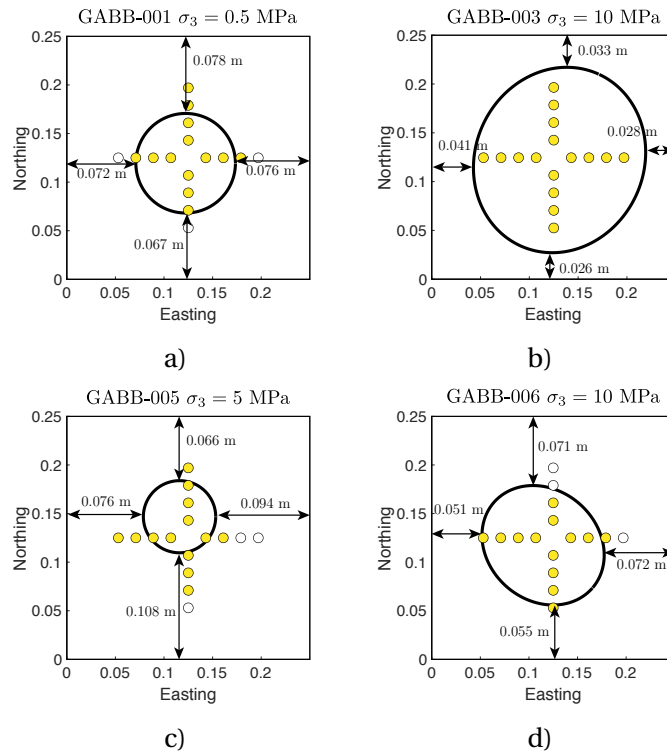
Figure 6.18 – Fracture radius before the decrease of the apparent toughness in a) GABB-001, b) GABB-003, c) GABB-005 and d) GABB-006.
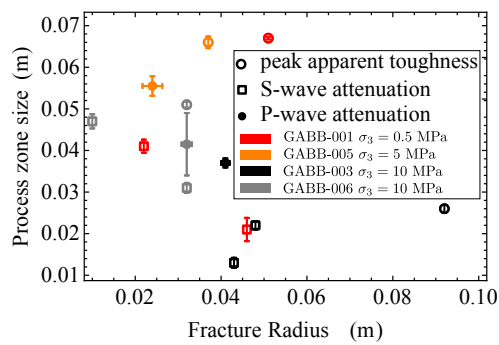
Figure 6.19 – Estimated process zone size in GABB-001, GABB-003, GABB-005 and GABB-006 experiments using different approaches.
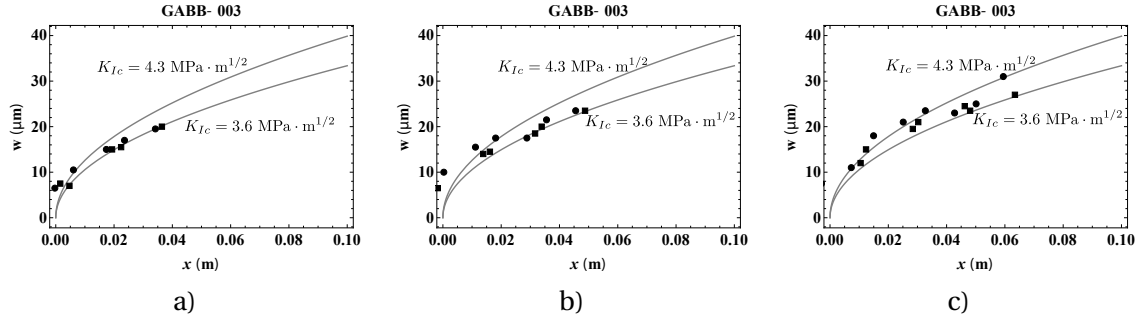
Figure 6.20 – GABB-003: fracture width profile corresponding to a fracture radius of a) 0.032 m, b) 0.071 m, and c) 0.113 m. The disks indicate the width obtained from the P-wave transducers in the east-west direction and the squares that from the P-wave transducers in the north-south direction. The solid curves indicate the k-asymptotes of the fracture opening plotted with different toughness values using $E' = 99.7/(1 - 0.29^2)$ GPa.

2019). For these four experiments, we only observe an obvious k-asymptote profile at different time in GABB-003, as shown in Fig. 6.20. We plot the width at the locations of all P-wave transducer pairs at all times in function of their distances to the fracture tips in Fig. 6.21. In some experiements (GABB-001 for example), when we are interested in the width at the location of one specific transducer pair i, we find that the width $w_i(t)$ at this location seems to evolve with time by approximately following a square-root relation of its distance from the tip $w_i(t) \sim (\hat{x}_i(t))^{1/2}$. For different transducer locations i, we plot the width profile using k-asymptote solutions $w_i(t) \sim K'(\hat{x}_i(t))^{1/2}/E'$ with different toughness values. These fracture toughness values doe not change significantly with time but seems to depend on transducers. Such an effect is more or less observed in all four experiments except in GABB-003.

We try to estimate the apparent toughness from the fracture width using Eq. (6.15). For all four experiments, $\ell_{mk}/R \geq 10^4$ during most time of the HF growth, which, according to LHFM, would lead to an accuracy of 3.5% of approximating the whole width profile with the k-asymptote (Bunger and Detournay, 2008). Moreover, the presence of a process zone (process zone) results in an overestimation of the fracture width. With a smaller fracture width near the tip and a larger width away from the tip, this overestimation due to the process zone leads to a more important relative error of the fracture width near the tip. We therefore estimate the fracture apparent toughness using the width away from the tip taking the results Fig. 6.22 with $\hat{x}/R > 0.25$. We obtain $K_I \approx 2.78 \pm 0.48, 3.87 \pm 1.03, 2.95 \pm 0.48$, and 2.78 ± 0.94) MPa·m$^{1/2}$ respectively for GABB-001, GABB-003, GABB-005 and GABB-006, as shown in Table. 6.7. The toughness values are equivalent to those obtained the stress intensity factor method for GABB-003, yet smaller for GABB-001 (by 63%) and GABB-006 (by 6%), larger for GABB-005 (by 38%). We summarize the apparent toughness values obtained using different approaches in Fig. 6.23.
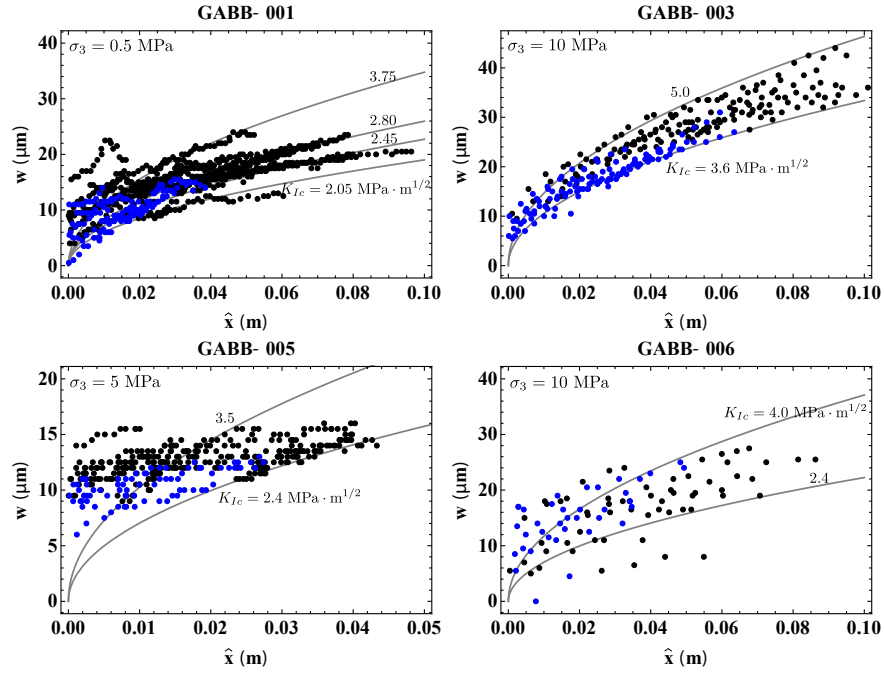
Figure 6.21 – Fracture opening w obtained from all the vertical 16 P-wave transducers as a function of their distance to the crack tip $\hat{x}$ at all time. The blue dots indicate the fracture opening data obtained before the stress intensity factor reaching its peak in Fig. 6.17. The gray curves indicate k-asymptotes of the fracture opening plotted with different toughness values using $E' = 99.7/(1 - 0.29^2)$ GPa.
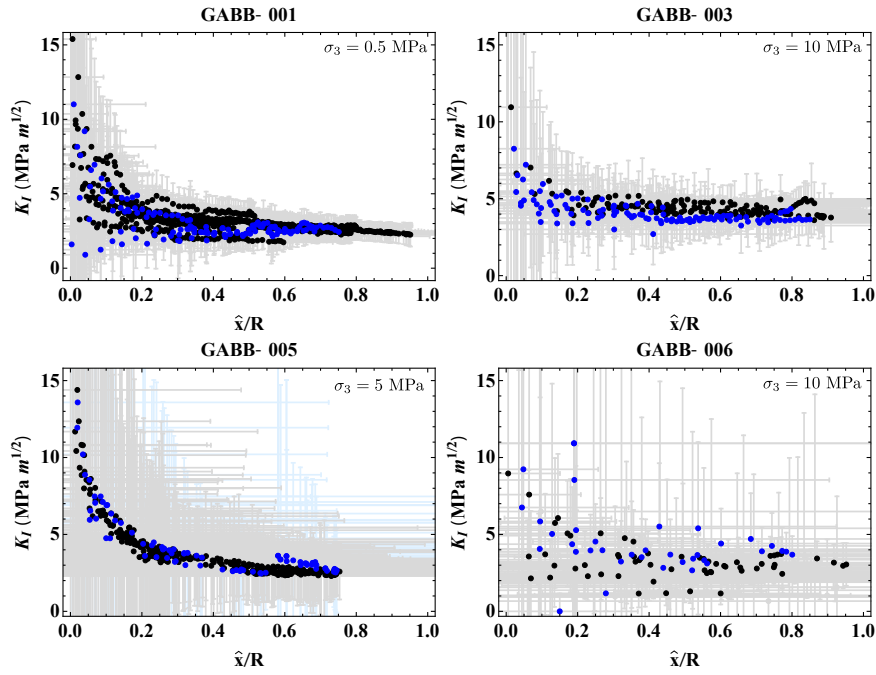
Figure 6.22 – Fracture toughness as a function of distance from the crack tip normalized by the mean fracture radius $\hat{x}/R$. The blue dots indicate the fracture opening data obtained before the stress intensity factor reaching its peak in Fig. 6.17.
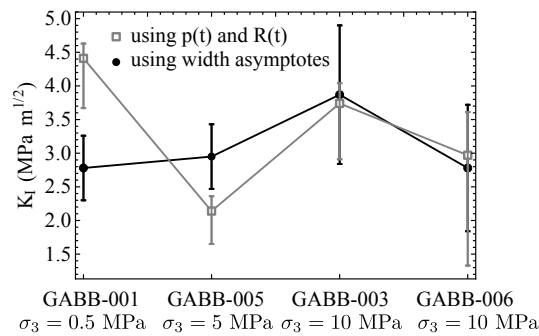
Figure 6.23 – Fracture apparent toughness obtained using different approaches.
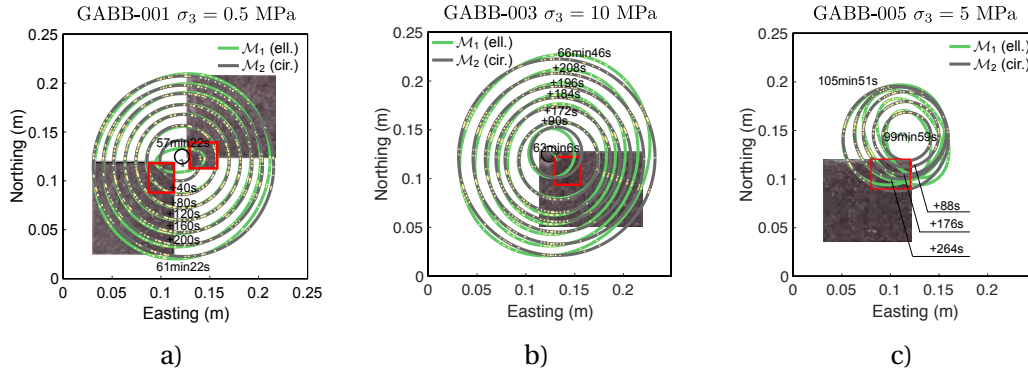
Figure 6.24 – Top view of a) GABB-001, b) GABB-003, and c) GABB-005 with fracture footprints. The larger scanned area corresponds to a resolution of 47.006μm indicated by the photo and the smaller interest area indicated by a red rectangle corresponds to a resolution of 14.777μm.

6.4.5 Hydraulic fracture surface roughness

The roughness results from the creation of fractures by the fluid injection as well as the splitting of the connected surfaces/solid-branching/solid-bridging after the injections. A rougher surface indicates a larger real fracture energy within the same nominal area, implying a larger apparent fracture toughness. In the following, we analyze the roughness of fractured surfaces in all experiments to characterize the apparent toughness during the HF growth and its associated process zone size.

Post-mortem observations A grooving pattern is observed on the surface of GABB-001 and GABB-003 (Fig. 6.4 for example), which has been reported in previous works (Van Dam and de Pater, 1999) for hydraulically fractured samples. However, such a pattern is not observable for GABB-005. In addition, a "mirror" zone at the origin of the crack and a "mist" zone away from the fracture center reported in (Van Dam and de Pater, 1999) are not observed in our experiments.

Statistical analysis of roughness profiles We show in Table. 6.10 the roughness analysis of different fractured areas for three experiments. The measurement region and the resolution shows a significant influence on the roughness: larger measurement region tends to lead to larger RMS, and smaller resolution tends to lead to smaller average slopes. If we are interested in roughness measured with a resolution of 14.771μm, we find that larger stresses σ_3 lead to rougher surfaces (larger ϕ_s and RMS). This dependency on the stress is consistent with observations of the near-wellbore roughness reported in Van Dam and de Pater (1999). However, no obvious correlation is found between the roughness (ϕ_s and RMS) and the apparent toughness.

We focus in the following on the calculation of roughness exponents of the hydraulic fracture

Experiment	σ_3 (MPa)	Position	Scanned area (mm^2)	RMS (μm)	$\phi_{s,x}$ (rad)	$\phi_{s,y}$ (rad)
GABB-001	0.5	SWB	94.996 × 83.153	656.4	0.256	0.239
GABB-001	0.5	NEB	84.375 × 90.486	753.1	0.248	0.240
GABB-003	10	SEB	94.622 × 83.153	773.7	0.261	0.238
GABB-005	5	SWB	90.486 × 84.375	933.9	0.266	0.244
GABB-001	0.5	SWB	26.14 × 29.745	446.0	0.337	0.317
GABB-001	0.5	NEB	26.509 × 28.445	502.4	0.345	0.328
GABB-003	10	SEB	26.509 × 28.445	585.6	0.370	0.338
GABB-005	5	SWB	30.750 × 23.288	631.8	0.352	0.331

Table 6.10 – Characterization of the fracture roughness. The larger scanned area corresponds to a resolution of 47.006μm and the smaller scanned area corresponds to a resolution of 14.777μm.

and its corresponding cut-off length scale ξ (process zone length scale). The roughness exponents ζ are obtained from the power spectrum $S(f) \sim f^{-2\zeta-1}$ (Fig. 6.26). The process zone length scales are obtained from the cut-off length of $C_\epsilon(\delta r)$ as shown in Fig. 6.25. We summarize these exponents and the process zone sizes in Table. 6.11 and Table. 6.12.

The roughness exponents and the associated cut-off length scales depend a lot on the scanned region and the spatial resolution. A larger scanned area with a lower spatial resolution often leads to a larger cut-off length scale (Fig. 6.25). It is interesting to notice that the obtained process zone length scale is even smaller than the grain size. It is thus likely that the cut-off length scale in our analysis actually characterizes the grain size. Moreover, the correlation C_ϵ does not always present a logarithm decay with δ_r, especially when ϵ is taken as the spatial resolution, as shown in Fig. 6.25.

The roughness exponent is reported to be $\zeta = 0.4 - 0.5$ for purely brittle failure and $\zeta = 0.75 - 0.85$ for materials that undergo damage during failure (Bonamy and Bouchaud, 2011). It has been conjectured that this difference results from the signature of the fracture mechanism above and below the size of the process zone (Bonamy et al., 2006). In our case, the roughness exponents present more the ductile characteristic $\zeta = 0.65 - 0.7$ for a larger scanned area measured with a lower spatial resolution (Table. 6.11). They present more the brittle characteristic with $\zeta = 0.45 - 0.55$ for a smaller scanned area measured with a higher spatial resolution (Table. 6.12).

We also perform the same analysis accounting for the radial propagation direction of the hydraulic fracture. We assume a fixed fracture center during the propagation and select it as the averaged fracture center coordinates at different sequences. The roughness profile radiating from the fracture center is then obtained through interpolation.

As shown in Table. 6.13, the roughness exponent here spans a large range from 0.45 to 0.8, reflecting both brittle and quasi-brittle/ductile characteristics. As shown in Table. 6.13, this
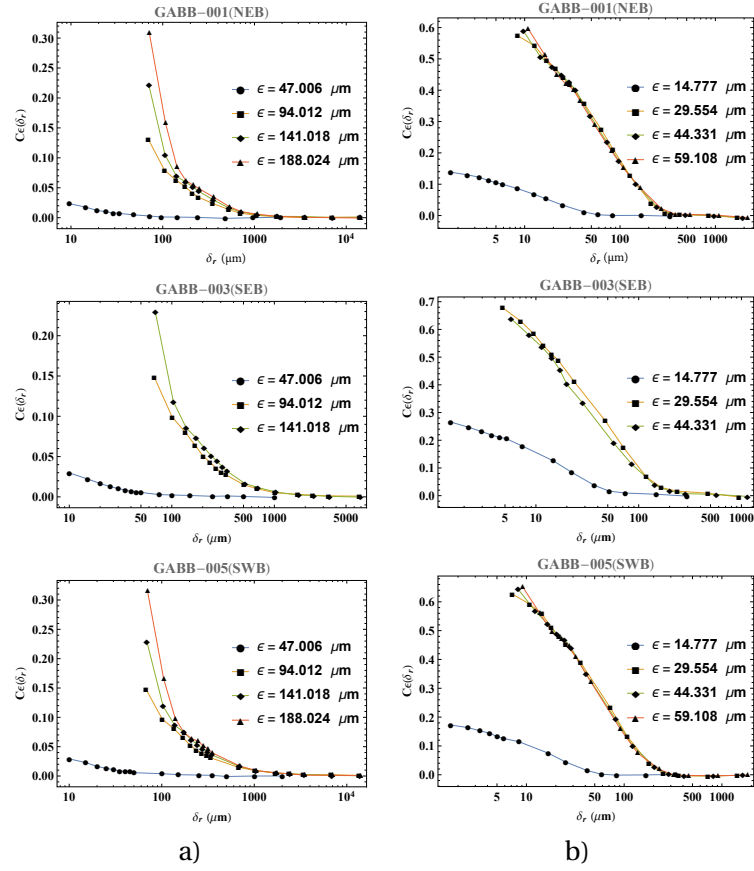
Figure 6.25 – Illustration of dependence of the cut-off length scale on measurement region and resolution. The results are obtained form the northeastern part of the bottom fractured surface in GABB-001 as shown in Fig. 6.24, with a spatial resolution of 47.006 μm in a) and 14.777 μm in b). NEB represents the northeastern part of the bottom fractured surface.

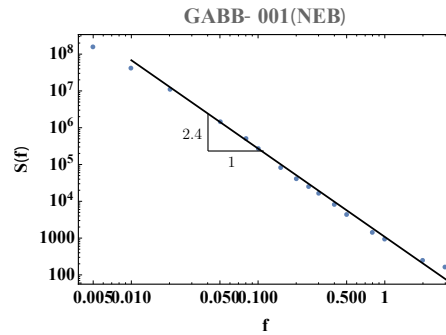Figure 6.26 – Illustration of the roughness exponent ζ obtained from the power spectrum $S(f)$ using the roughness profiles measured for the lower northeastern part of GABB-001. The spatial resolution of the roughness measurement is of 47.006μm.

Experiment	σ_3 (MPa)	Position	ξ (mm)	ζ
GABB-001	0.5	NEB	0.8-0.9	0.7
GABB-003	10	SEB	0.9-1.0	0.65
GABB-005	5	SWB	0.9-1.0	0.675

Table 6.11 – Fractal analysis of fractured surfaces without accounting for the radial propagation direction. The roughness profiles used in this table corresponds to a larger scanned area around 90×90mm^2 measured with a spatial resolution of 47.006μm. NEB represents the northeastern part of the lower fractured surface.

Experiment	σ_3 (MPa)	Position	ξ (mm)	ζ
GABB-001	0.5	NEB	0.30	0.5
GABB-003	10	SEB	0.20	0.45
GABB-005	5	SWB	0.25	0.55

Table 6.12 – Fractal analysis of fractured surfaces without accounting for the radial propagation direction. The roughness profiles used in this table corresponds to a smaller scanned area around 25×25mm^2 measured with a spatial resolution of 14.777 μm. NEB represents the northeastern part of the bottom fractured surface.

exponent and its associated cut-off length scale still depend a lot on the scanned region and the spatial resolution. The correlation C_ϵ may present a one or two-branch logarithm decay, implying the appearance of other length scales, as shown in Fig. 6.27.

The obtained results do not seem conclusive. The analysis depends a lot on the region and resolution of the roughness measurement. When accounting for the radial propagation direction the hydraulic fracture, the results further depend on the fracture front geometry, and the location of the averaged fracture center. Moreover, the process zone size is around $\xi \sim$ 1 mm if we focus on a smaller measurement region with a higher resolution for all toughness dominated experiments in gabbro. This is much smaller than that predicted by the previously mentioned methods. This possibly indicates that the roughness method we apply does not characterize the process zone size in our case but the grain size.

6.5   HF experiments in marble under O-M and O-K regimes

In this section, we are interested in the comparison between lag-viscosity (MARB-009) and lag-toughness (MARB-010) dominated experiments in marble. We show the evolution of the pressure, inlet flux and the fracture radius in Figs. 6.29 and 6.30. The fracture growth in MARB-009 is faster due to the insufficient control of the entering flux with the restriction valve too widely open. This results in a more important effect of the compressibility and the viscous fluid flow. In these two experiments, the diffracted arrival of the fluid front is visible in some source-receiver pairs shortly after the fracture initiation. The fluid front coalesces with that of the fracture font at later time of the propagation. However, the picked diffracted arrivals are not sufficient to correctly reconstruct the fluid front and we therefore do not report its time

Experiment	σ_3 (MPa)	Position	Scanned area (mm^2)	ξ (mm)	$\phi_{s,r}$ (rad)	ζ_s	ζ_h
GABB-001	0.5	NEB	94.996 × 83.153	0.9		0.6	0.8
GABB-001	0.5	SWB	26.14 × 29.745	1	0.274	0.6	0.45
GABB-001	0.5	NEB	26.14 × 29.745	2	0.337	0.5	0.55
GABB-003	10	SEB	94.622 × 83.153	10		0.7	0.6
GABB-003	10	SEB	26.509 × 28.445	0.8	0.371	0.45	0.45
GABB-005	5	SWB	90.486 × 84.375	1		0.8	0.6
GABB-005	5	SWB	30.750 × 23.288	0.9	0.328	0.5	0.55

Table 6.13 – Fractal analysis of fractured surfaces accounting for roughness profiles along the radial propagation direction. The larger scanned area corresponds to a resolution of 47.006 μm and the smaller scanned area corresponds to a resolution of 14.777 μm. ξ represents the cut-off length scale characterizing the process zone size. ζ_s and ζ_h represents respectively the roughness component obtained from the power spectrum (Eq. (6.7)) and from the height-height correlation function (Eq. (6.6)).
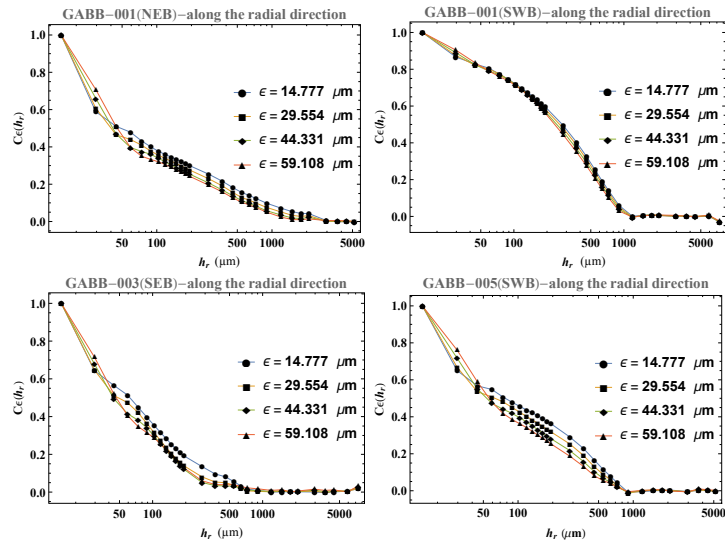
Figure 6.27 – Illustration of different patterns of the logarithm decay of $C_\epsilon(h_r)$ with the distance h_r (μm) along the radial direction. The results shown in this figure are based on the roughness measurement using a spatial resolution of 14.777 μm.
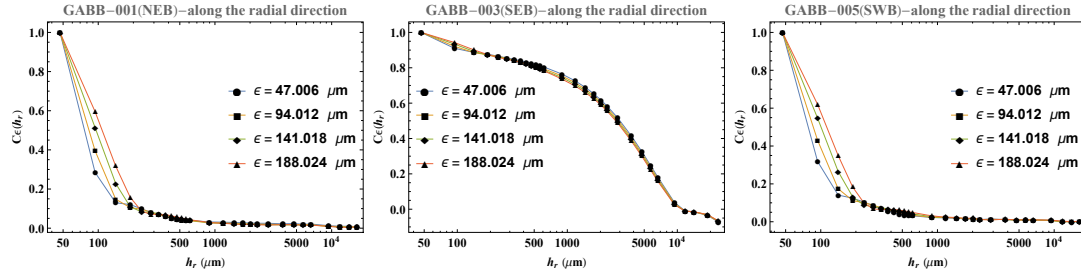
Figure 6.28 – Illustration of different patterns of the logarithm decay of $C_\epsilon(h_r)$ with the distance h_r (μm) along the radial direction. The results shown in this figure are based on the roughness measurement using a spatial resolution of 47.006 μm.
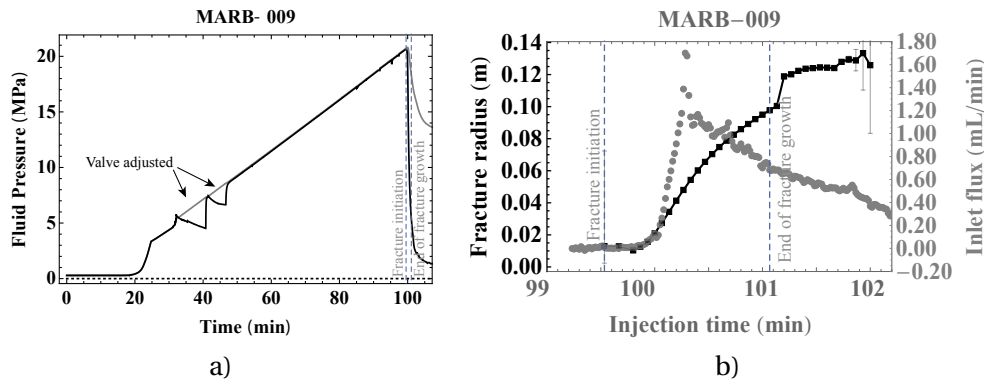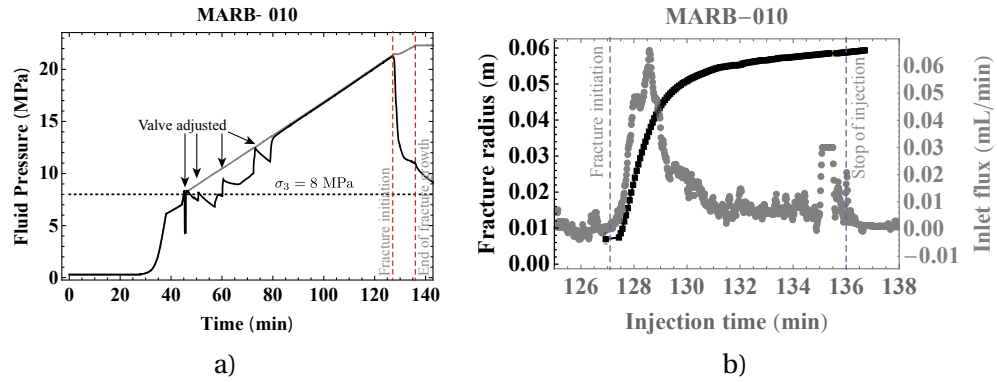

Figure 6.29 – MARB-009: time evolution of the a) injection pressure, b) fracture front and estimated inlet flux. The vertical lines indicate respectively the fracture initiation (determined by the change of near wellbore displacement) and fracture reaching the edge of the block (determined by the evolution of the downstream pressure). No stress is applied in the vertical direction.

evolution.

As shown in Figs. 6.31, 6.32, shear waves attenuate prior to the fracture front arrival both in MARB-009 and MARB-010 experiments. We show the corresponding predicted process zone in Table. 6.14. The process zone size is comparable to the fracture extent even though the grain size is very small (0.1-0.2 mm) in marble.

In addition, after the coalescence of the fluid front and fracture front in MARB-010, we observe the regain of the shear transmitted shear energy– a typical phenomenon when the fluid front passes the location of the transducer pair following the fluidless cavity. We observe twice the attenuation followed by the regain of transmitted P waves during the fracture growth in both experiments, note that the drop and regain of the signal strength appears only once in the lag dominated experiment MARB-005 (Fig. B.7). We do not have a good explanation for this yet.

There is a strong viscous effect during the HF propagation in MARB-009 and MARB-010. The pressure distribution is probably not uniform inside the fracture during most time of the

Figure 6.30 – MARB-010: time evolution of the a) injection pressure, b) fracture and fluid front and estimated inlet flux. The vertical lines indicate respectively the fracture initiation (determined by the change of the difference between the upstream and downstream pressure) and stop of the injection. The dotted line indicates the minimum confining stress.
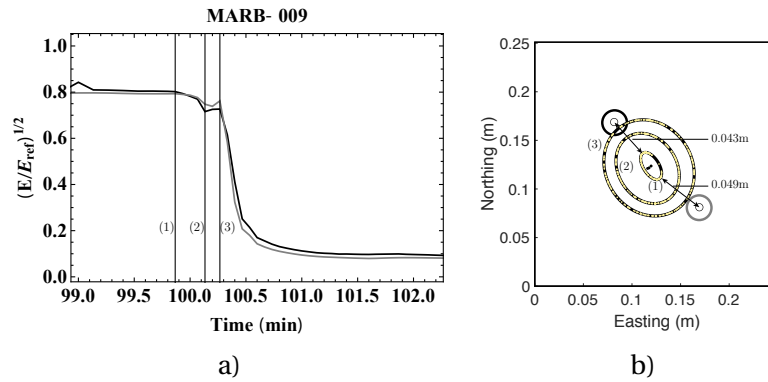
Figure 6.31 – MARB-009: time evolution of a) the signal strength of transmitted shear waves, and b) the fracture geometry at different times of the fracture growth. Locations of the transducers in figure a) are indicated by circles in figure b) using the same line style. The fracture extent associated with the numbered vertical lines in figure a), is also shown in figure b) using the same number.
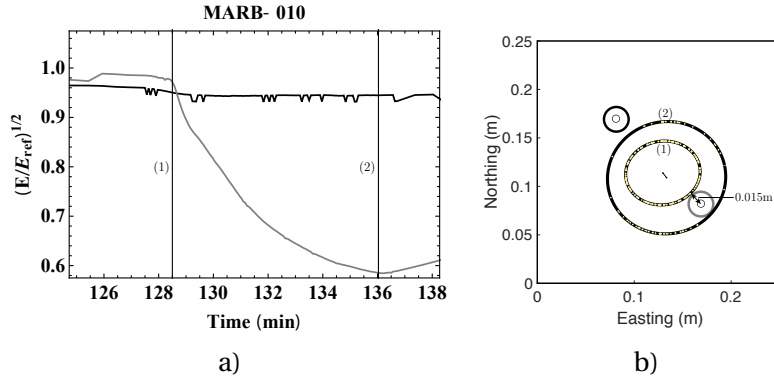
Figure 6.32 – MARB-010: time evolution of a) the signal strength of transmitted shear waves, and b) the fracture geometry at different times of the fracture growth. Locations of the transducers in figure a) are indicated by circles in figure b) using the same line style. The fracture extent associated with the numbered vertical lines in figure a), is also shown in figure b) using the same number.
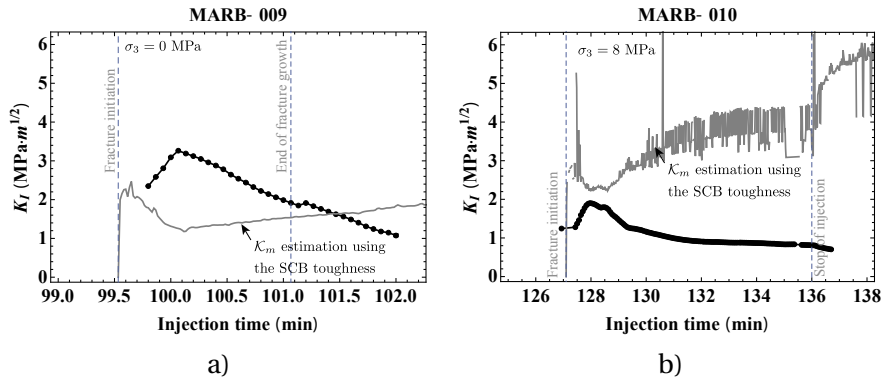
Figure 6.33 – Time evolution of the estimated stress intensity factor K_{Ic} (in black) and dimensionless toughness $\mathcal{K}_m$ (in gray) for a) MARB-009 and b) MARB-010. $\mathcal{K}_m$ is evaluated using the instant inlet flux and the toughness measured using the SCB method (Table. 6.2).

propagation. As a result, the stress intensity factor estimated using Eq. (6.14) overestimates the fracture apparent toughness. Moreover, as the fracture growth transitions from viscosity to toughness dominated regime, one would expect a drop of the stress intensity (Figs. 6.33, 6.34). It is therefore inappropriate to estimate the process zone size using the distance between the fracture geometry at the peak of the apparent toughness and the closest boundary of the sample, otherwise it may overestimate the process zone size (Fig. 6.35).

We measure part of the fractured surfaces as shown in Fig. 6.36. Compared with the gabbro samples, the fractured surfaces in marble are very easily separated and the fracture roughness is much smaller. In the MARB-010 experiment which has a larger minimum stress σ_3 than MARB-009, we observe larger oscillations of the heights (larger ϕ_s) but a smaller RMS (see Table. 6.15). As shown in Table. 6.16, marble presents a smaller cut-off length scale similar
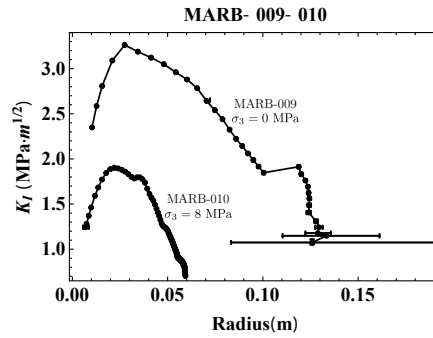
Figure 6.34 – Evolution of apparent fracture toughness with the fracture radius in MARB-009, and MARB-010.
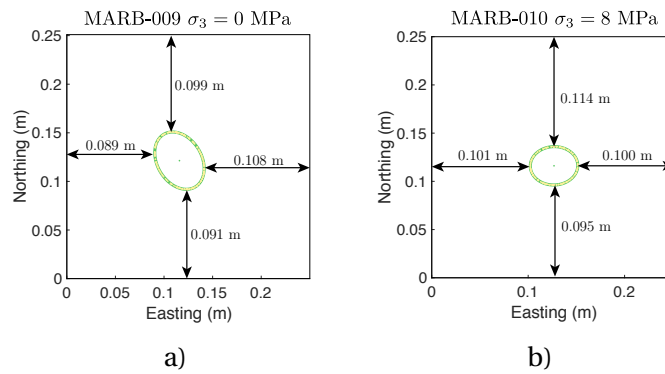
Figure 6.35 – Fracture front geometry before the decrease of the apparent toughness in a) MARB-009 and b) MARB-010.

Experiment	σ_3 (MPa)	Transducer type	Fracture radius (m)	Estimated process zone size (m)
MARB-009	0	S-wave	0.021 ± 0.0023	0.043-0.049
MARB-010	8	S-wave	0.035 ± 0.0024	0.015

Table 6.14 – Estimated process zone size based on the attenuation of the vertical transmitted waves. We use here the S-wave transducers to identify the process zone. The time-evolution of the P-wave transducers do not present a clear start time of the signal strength attenuation.
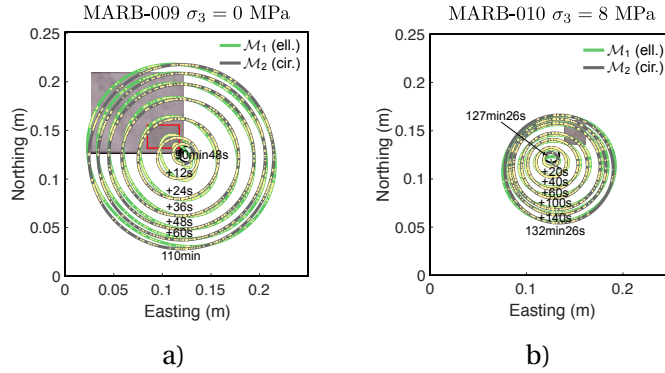
Figure 6.36 – Top view of a) MARB-009 and b) MARB-010 with fracture footprints. The larger scanned area corresponds to a resolution of 47.006μm and the smaller scanned area corresponds to a resolution of 14.777μm indicated by a red rectangle.

Experiment	σ_3 (MPa)	Position	Scanned area (mm^2)	RMS (μm)	$\phi_{s,x}$ (rad)	$\phi_{s,y}$ (rad)
MARB-009	0	NWB	94.622×83.153	334.1	0.189	0.179
MARB-009	0	NWB	32.967×23.835	237.3	0.314	0.277
MARB-010	8	NEB	22.667×25.15	123.9	0.341	0.278

Table 6.15 – Fracture roughness, the larger scanned area corresponds to a spatial resolution of 47.006μm and the smaller scanned area corresponds to a spatial resolution of 14.777μm as indicated in Fig. 6.36.

to its grain size. It is likely that the roughness analysis here measures the grain size rather than the process zone size. Moreover, the cut-off length scale of marble is smaller that that of gabbro, which is consistent with their relation of the grain size.

6.6   Conclusions

We have investigated the growth of hydraulic fractures in marble and gabbro in different propagation regimes and under different stress states. We find that solid bridging and crack branching exist in both rocks, with the crack band of gabbro wider than that of marble. The transmission attenuation and the appearance of the fracture width prior to the fracture front arrival, indicate the presence of a process zone ahead of the fracture tip.

Experiment	σ_3 (MPa)	Position	ξ (mm)	ζ
MARB-009	0	NEB	0.15	0.5
MARB-010	8	NEB	0.15	0.55

Table 6.16 – Fractal analysis of fractured surfaces without accounting for the radial propagation direction. The roughness profiles used in this table corresponds to a smaller scanned area around 25×25mm^2 measured with a spatial resolution of 14.777 μm.

For toughness-dominated experiments in gabbro, the apparent toughness, which is associated with the process zone size, develops as the fracture grows and is finally limited by sample dimensions. The peak value of this apparent toughness during the HF growth corresponds to a process zone size of several centimeters. This results in a large ratio between the process zone size and the fracture radius, however the fracture width still follows the k-asymptote as predicted in LHFM. The apparent toughness estimated from this k-asymptote consists more or less well with that obtained from the stress intensity factor calculation. However, the estimated apparent toughness differs a lot between four experiments. No obvious correlation is found between the apparent toughness and the confining stress. The difference in apparent toughness results more from the difference of material properties between blocks, and probably the stress states.

Fracture roughness depends a lot on the material type (grain size), the loading condition inside the fracture and the applied confining stresses. A larger grain size or less uniform distribution of the fluid pressure, as in the case of a lag-dominated experiment in gabbro, often results in rougher fractured surfaces. However, the effect of the confining stress does not remains very clear and calls for further investigation. The method of process zone size estimation using roughness (Vernède et al., 2015) seems to give a length scale of the grain size in our case. The fracture path does not present an obvious preference for intra-grain failure or inter-grain failure. A more quantitative study on solid bridges between fractured surfaces is necessary.

We have investigated the process zone growth in different HF experiments by combining acoustic measurement, X-ray micro tomograph, stress intensity factor, and fracture roughness. However, all these approaches present limited precision. A better description of the process zone evolution requires a more accurate description of the fracture and fluid front. Geometrical models such as closed splines can be adopted to reconstruct the fracture geometry. A better estimation for the fracture width is also required especially when the fracture surfaces are rough and not parallel and when there is a fluid lag. Passive acoustic monitoring is encouraged to apply together with the active measurement in order to give a more direct image of the process zone.

Acknowledgments

Conclusions Part III

7 Conclusions and perspectives

Summary

This thesis investigates the growth of hydraulic fractures (HF) in quasi-brittle rocks using a combination of theoretical, numerical, and experimental approaches. We aim to understand the possible toughening mechanism due to the solid non-linearity and its impact on HF growth. We also perform HF injections in quasi-brittle rocks at the laboratory scale, hoping to decipher the evolution of the non-linear zone (process zone) during the HF propagation.

For the theoretical and numerical investigation, we discuss the growth of a plane-strain / radial HF in a homogeneous, isotropic, and impermeable medium. We assume that the fracture is driven by a Newtonian fluid under a constant injection rate. We first aim to investigate quantitatively the toughening effect associated with the solid non-linearity during HF growth. In Chapter 3, we propose a macroscopic model assuming an increase of apparent toughness with fracture length. Such a model approximates macroscopically the reported increase of energy spent in some lab and field scales observations. We perform simulations under the framework of LHFM for sufficiently deep fractures (such that the fluid lag can be neglected). We find that this apparent toughness leads to shorter fracture lengths, larger fracture openings, net pressures, and emplacement ratios compared with LHFM solutions. When the apparent toughness reaches a stable state and no longer increases with fracture length, the solution slowly transitions back to the constant toughness solution. The fracture growth solution can be approximated by the self-similar constant toughness solution using the instantaneous toughness. From a computational perspective, we have developed an efficient numerical solver with spectral accuracy. It elegantly combines Gauss-Chebyshev quadrature and barycentric Lagrange interpolation techniques to solve the growth of a finite planar HF in simple geometries (plane-strain and axisymmetry).

We then explore a possible toughening mechanism in Chapter 4. We investigate the growth of a plane-strain HF by relaxing some of the underlying assumptions of LHFM. We adopt a cohesive zone model to simulate the process zone effect and account for fracture roughness' impact on fluid flow inside the created fracture. We show that the cohesive HF growth consists of

three stages: a nucleation stage of the cohesive zone, an intermediate stage, and a small-scale-yielding stage. The fracture growth first deviates from LHFM solutions during the first two stages and then slowly converges to LHFM solutions at late times. This evolution results from a decreasing fraction of the cohesive zone compared to the fracture length and an interplay between the fluid front and cohesive zone. We show that the fracture growth depends on a dimensionless toughness and a time scale characterizing the fluid lag disappearance similar to LHFM. It further depends on the ratio of in-situ stress and peak material cohesive stress: larger in-situ-to-cohesive stress ratios result in larger deviations from LHFM solutions during the first two stages. This deviation is mostly limited to the nucleation stage for a smooth cohesive zone. However, it can be much more significant for a rough cohesive zone, even when the cohesive zone takes a small fraction of the fracture length. In a rough cohesive HF, we report an increase of the fracture resistance with shorter fracture lengths, larger fracture openings, and net pressures. We show that this toughening effect results from the viscous energy dissipated inside the rough cohesive zone. Similar conclusions can be drawn for a radial HF using the scaling analysis and numerical scheme presented in this chapter after slight adaptions.

On the experimental front, we first develop a method in Chapter 5 using diffracted acoustic waves to reconstruct the fracture geometry in nontransparent rocks. We perform a Bayesian analysis to select different possible geometrical models and estimate their errors of prediction. It provides the basis to locate the position of the process zone with respect to the fracture front.

We report in Chapter 6 a series of HF experiments in rocks exhibiting different grain sizes (different levels of solid non-linearity), most of which are in toughness-dominated regimes or lag-viscosity/toughness regimes. We show through CT images that a process zone exists around the diffracted fracture front. Attenuation of the transmitted waves perpendicular to the fracture plane also indicates a change of the material properties ahead of the reconstructed fracture front from diffracted waves. We estimate the apparent toughness associated with this process zone using the fluid pressure and fracture radius. The apparent toughness first increases and then drops with fracture radius during the fracture growth. Such an apparent toughness evolution implies that sample dimensions possibly limit the growth of the process zone. This refers to an important size-effect for laboratory HF tests in these rocks. In the end, we perform fractal analysis on the roughness of these HFs to extract length scales related to the process zone. However, the roughness is not necessarily created by HFs, and its statistical properties show a strong dependence on the measurement resolution.

The theoretical and experimental investigations performed in this thesis are closely related to each other. Chapter 3 provides the theoretical basis for the apparent toughness estimation in Chapter 6: fracture growth is influenced almost instantly by the change of the apparent toughness. It is thus possible to use the apparent toughness to describe the instant growth of the process zone. Moreover, Chapter 6 gives experimental evidence for the assumptions adopted in Chapter 4: a process zone characterized by crack branching and bridging effect exists ahead of the fracture front.

174

Future perspectives

We have explored different techniques to investigate the HF growth in quasi-brittle materials, some of which can be extended to solve other problems. In the following, we briefly discuss some possible directions for future work.

- Chapter 3 offers a very efficient method to solve problems related to the growth of a finite fracture. One can use it after slight adaptions to investigate the shut-in of a finite HF, the effect of shear-thinning/ power-law fluids on the growth of a finite HF, and the effect of sub-critical propagation conditions.

- Chapter 4 investigates the growth of a plane-strain cohesive hydraulic fracture via a simple linear-weakening cohesive zone model and a phenomenological correction to Poiseuille's law. A better description of the details of both the traction separation law and the effect of roughness on fluid flow is necessary and will likely modify quantitatively the hydraulic fracturing growth at the early and intermediate stages. An algorithm with an adaptive mesh refinement needs to be developed to ensure a sufficiently fine resolution of the process zone and fluid lag to further investigate fracture growth under large confining stresses at large times. To better understand the results of our numerical simulations and compare them with laboratory experiments, we can extend this work on the plane-strain hydraulic fracture to the case of a radial hydraulic fracture.

- We adopt a rough cohesive zone model to investigate the possible toughening mechanism during the hydraulic fracture growth. However, this cohesive zone model is over-simplified and reflects only two main characteristics of the hydraulic fracture growth in quasi-brittle materials: the zero-singularity of the tip stress field and the crack bridging effect. It would be interesting to account for the interaction between the main hydraulic fracture and the inelastic deformations or micro-cracks around the tip.

- The reconstruction of the hydraulic fracture geometry in Chapters 5 and 6 is based on a series of assumptions: a) we assume that the diffraction results from the fracture and fluid front. This assumption is intuitive and may not be valid in particular for quasi-brittle rocks due to the difficulty to locate the physical fracture tip with the presence of the process zone. Further investigation is necessary to find out the exact location of the diffraction source. b) We estimate the fracture width based on a three-layer model with parallel and smooth fracture surfaces with zero fluid lag. More accurate methods are necessary to estimate the fracture width for non-parallel rough fractures with a fluid lag. c) We assume that the acoustic wave propagates at a constant velocity in the rock samples. It is necessary to account for the influence of the material heterogeneity, the possible appearance of micro-cracks, and the possible fluid diffusion inside the rocks on the acoustic wave propagation.

- We reconstruct the fracture front using active diffracted waves and estimate the process zone size combining the diffraction front and transmitted waves. The location of trans-

ducers limits a lot the estimation accuracy of the process zone size. Passive acoustic monitoring is highly encouraged to perform in combination with active acoustic monitoring to directly demonstrate the locations of micro-cracks or micro-slips inside the process zone. Besides, a more quantitative study via CT images or other postmortem observations is necessary to investigate the microstructure around the fracture tip/process zone, such as the solid bridging, crack branching, and the location of the fracture path with respect to that of the grains.

A Material characterization

A.1 Mineralogy

The mineralogy composition and organic content of the gabbro and marble are determined through powder X-ray diffraction analysis (XRD). The intensity of the diffraction presented as the peak height and as the integrated intensity at peak angle is given in Fig. A.1. The concentration of different minerals is shown in Table. A.1.

A.2 Fracture toughness characterization in dry fracture mechanics

We test the mode I fracture toughness K_{Ic} using the ISRM-suggested semi-circular bend (SCB) method (Kuruppu et al., 2014). We show the specimen geometry and one of the test loading curve in Fig. A.2, and we calculate K_{Ic} using the observed peak load $P_{\max}$.

$$K_{Ic} = Y' \frac{P_{\max}\sqrt{\pi a}}{2RB} \tag{A.1}$$

$$
\begin{aligned}
Y' = -1.297 + 9.516(s/2R) - (0.47 + 16.457(s/2R))(a/R) \\
+ (1.071 + 34.401(s/2R))(a/R)^2
\end{aligned}
\tag{A.2}
$$

Rock type	Phyllosilicates	Quartz	Feldspath-K	Plagioclase-Na	Calcite	Residual
Gabbro	18.88	3.05	11.06	45.69	0	21.33
Marble	0.30	0.58	0	0	98.23	0.89

Table A.1 – Mineral concentration for gabbro and marble. The dosage of gabbro is indicative due to the lack of mineral component standard for gabbro in the laboratory. This can be seen from its very high value of the residual. The value of plagioclase (soilide solution) for gabbro is probably incorrect.
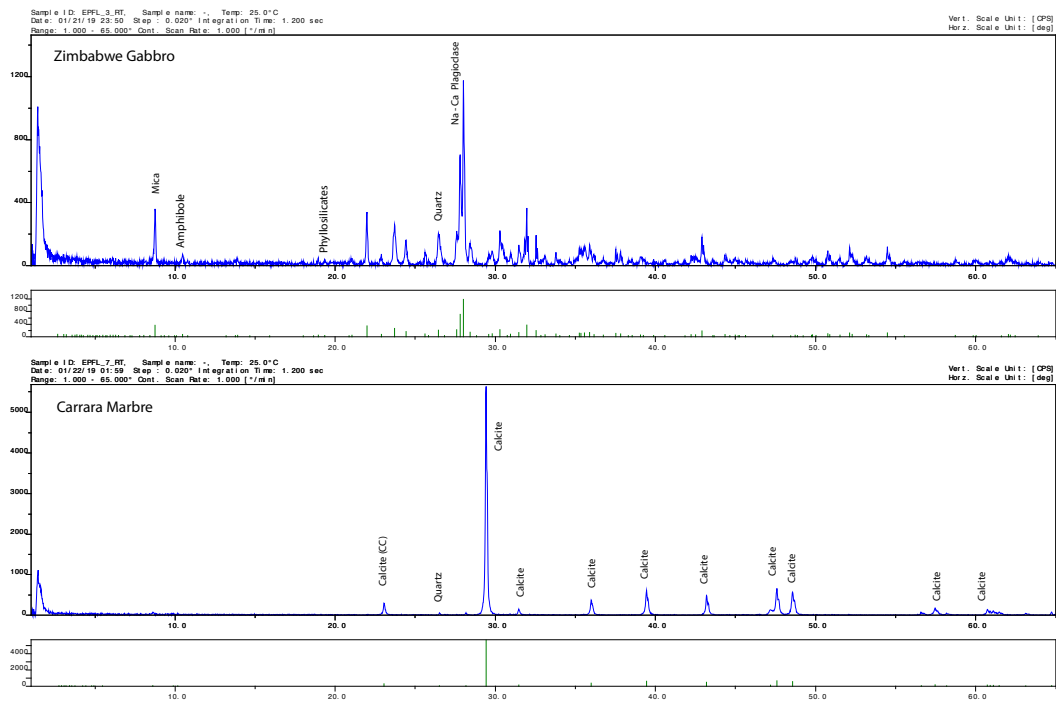
Figure A.1 – Mineralogical composition of gabbro and marble in intensity using X-ray diffraction analysis (XRD).
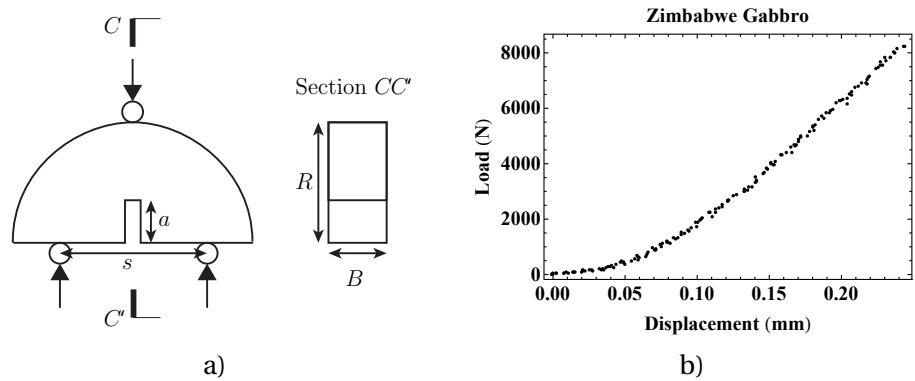
Figure A.2 – Illustration of a) the fracture toughness test specimen and b) the loading curve (the point load F vs the cracking tip opening δ) during the fracture toughness for gabbro.

Specimen test	Rock type	R (mm)	B (mm)	S (mm)	a (mm)	Number of tests
SCB_1	Gabbro	39.8	32.0	44	17.8	5
SCB_2	Gabbro	39.8	19.6	44	17.8	1
SCB_3	Marble	29.7	31.1	44	17.2	7

Table A.2 – Dimensions for SCB specimens adopted in Chapter 6.

a)

b)

Figure A.3 – Illustration of a) the fracture toughness test specimen and b) the loading curve during the fracture toughness for gabbro. $L = 10$ cm, $h_1 = 3$ cm, $h_2 = 4.5$ cm, $l_x = 1.28$ cm, $l_y = 1.4$ cm and $R = 0.25$ cm. The values of the initial notch/crack length c_{ini} and sample width b are shown in Table. A.3.

Specimen test	Rock type	c_{ini} (mm)	b (mm)	Number of tests
TDCB_1	Gabbro	27.5	10.0	3
TDCB_2	Marble	37.5	10.0	2

Table A.3 – Dimensions for TDCB specimens.

We also test the fracture toughness using the tampered double cantilever beam (TDCB) method (Vasudevan et al., 2021). We show the specimen geometry and the loading curve in Fig. A.3, where we apply the load using the displacement control, and we measure the fracture opening δ using an extensometer.

$$G_c = \frac{\text{area of OBB'}}{\Delta c \, b} \tag{A.3}$$

where Δc is the increment of the fracture length and b the sample width. Knowing the compliance λ at one point, for example point B, we have its corresponding crack length

$$c = \ln\left(Eb\frac{\lambda}{\lambda_o}\right)c_o, \quad \lambda_o = \beta\frac{c_o^2}{h_1 l_x} \tag{A.4}$$

where $c_o = 0.389L - 0.0229$ (in meters). However, this method is valid only for $1/3 < c/L < 2/3$, and it may overestimate the fracture toughness when the fracture path is not horizontal. In our case, the fracture paths in marble are more or less straight and horizontal while those in gabbro present more oscillations (Fig. A.4).

a)   b)
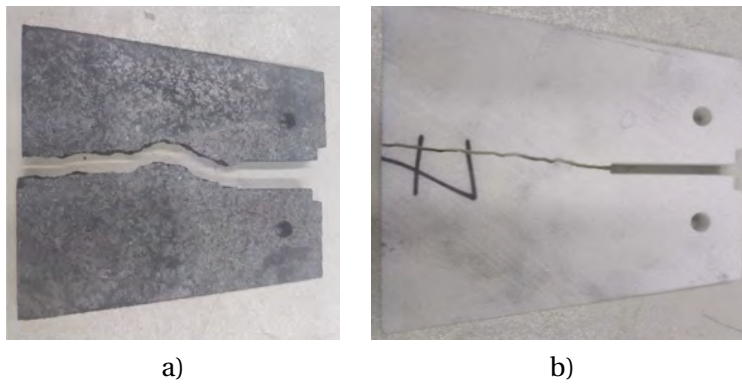
Figure A.4 – Illustration of the fracture path in a) gabbro and b) marble tests.

B Lag dominated experiments

GABB-002, MARB-005 and MARB-007 experiments ($t_{prop} \ll t_{om}$) are characterized with an important lag between the fracture and fluid front. We show in Figs. B.1, B.2 and B.3 the evolution of the pressure, inlet flux, fracture and fluid front. In these experiments, the downstream pressure may still increase after the fracture initiation due to the strong viscous effect in the fluid. The growth of the fluid front is characterized by the increase of inlet flux and can occur much later than the fracture initiation.

As shown in Fig. B.3, we observe a post-shut-in growth of the fracture and fluid front in MARB-007. This results from the redistribution of the fluid pressure inside the fracture after shut-in, which leads to a stress-intensity factor large enough to continuously drive the fracture propagation. In addition, post mortem observations of the fracture surface indicate a a reasonable assumption of a circle or an ellipse for the fluid front (Fig. B.10).

B.1   Evolution of the acoustic transmission across the fracture plane

These three experiments present a larger fracture opening and a fluid lag compared to the previous toughness-dominated experiments. The assumption of the fracture width estimation – a single fluid layer between two smooth surfaces– is no longer valid. We focus here on the evolution of the transmitted energy to understand the growth of the fracture front, fluid front and process zone.

As shown in Figs. B.5, B.6, B.7, B.8, B.9, transmission attenuation occurs before the fracture front arrival, same as in toughness dominated experiments. Such attenuation ahead of the fracture front is more obvious for transducers farther away from the wellbore and shear waves indicate a larger process zone than compressional waves (see Fig. B.5 and B.6).

In MARB-005, the signal strength of transmitted waves decreases upon the arrival of the fracture front and regains its amplitude following the arrival of the fluid front. It finally decreases with time as the fracture width increases and results in more loss in transmitted energy (Fig. B.7). Similar evolution is also observed in GABB-002 and MARB-007, however the
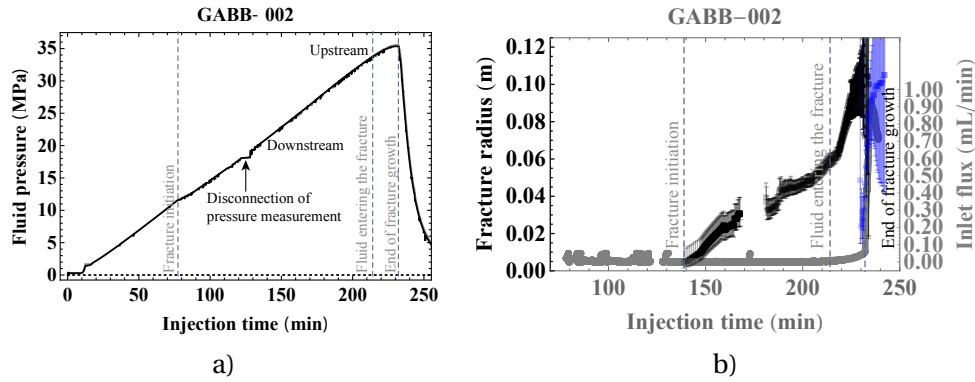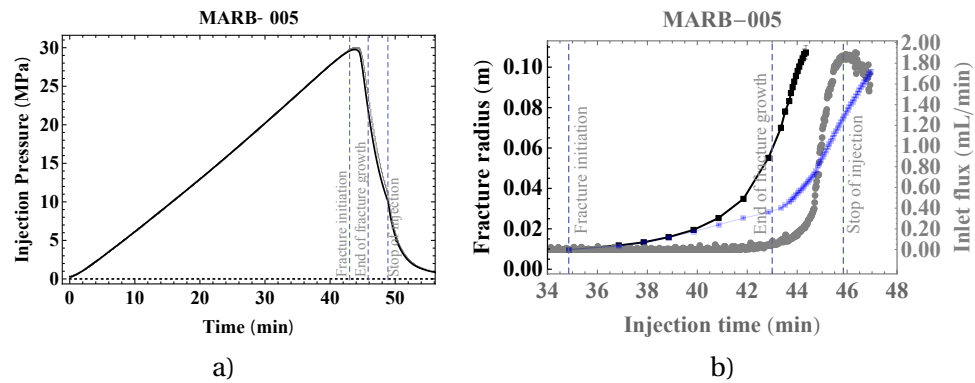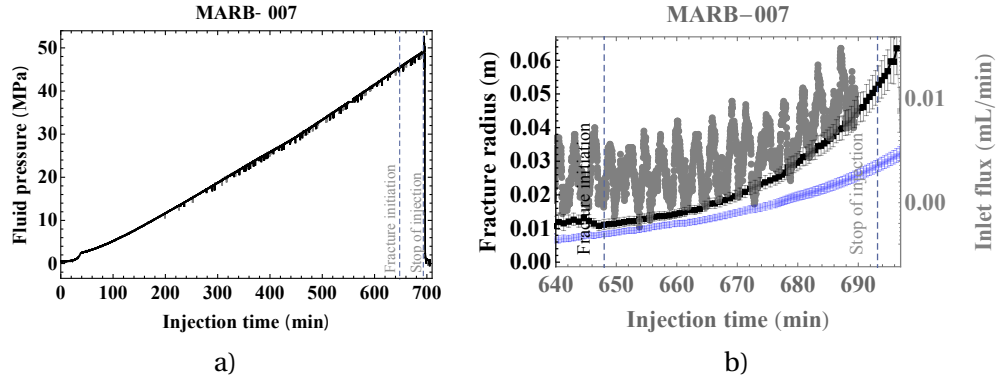
Figure B.1 – GABB-002: time evolution of the a) injection pressure, b) fracture (black) and fluid front (blue), and estimated inlet flux. The vertical lines indicate respectively the time of fracture initiation (determined by the start of the visible diffraction), start of fluid front growth (determined by the increase of the inlet flux), and fracture front reaching the edge of the block (determined by the very fast increase of the inlet flux). No stress is applied in the vertical direction.

Figure B.2 – MARB-005: time evolution of the a) injection pressure, b) fracture (black) and fluid front (blue), and estimated inlet flux. The vertical lines indicate respectively the time of fracture initiation (determined by the volume change of the top-bottom flat-jacks), fracture front reaching the edge of the block (determined by the downstream pressure evolution) and the stop of the injection. No stress is applied in the vertical direction.

Figure B.3 – MARB-007: time evolution of the a) injection pressure, b) fracture (black) and fluid front (blue), and estimated inlet flux. The vertical lines indicate respectively the time of fracture initiation (determined by the sudden vertical displacement near the wellbore on the top surface), and the stop of the injection. No stress is applied in the vertical direction.

regain of the transmitted energy occurs prior to the diffracted fluid front arrival (see Figs. B.8 and B.9 for example).

B.2 Visualization of hydraulically fractured surfaces

We adopt silicone oil as injection fluids for these three experiments. Since it is difficult to clean the silicone oil left on the fractured surface without destroying the roughness. We therefore do not report the real roughness profile but show some photos of the fractured surface. As shown in Fig. B.10, a grooving pattern is visible in MARB-007 but can not be clearly observed in GABB-002 and MARB-005. The roughness seems to depend both on the grain size of the material and loading conditions during the fracture growth. The fracture roughness in gabbro is much larger than that in marble from the eye observation. For the two experiments in the same material MARB-005 and MARB-007, MARB-007 presents a more important effect of the lag/viscous flow (t_{prop}/t_{om}). As a result, the fluid pressure distribution is less uniform in MARB-007 and this non-uniform loading condition contributes to a larger roughness in MARB-007.
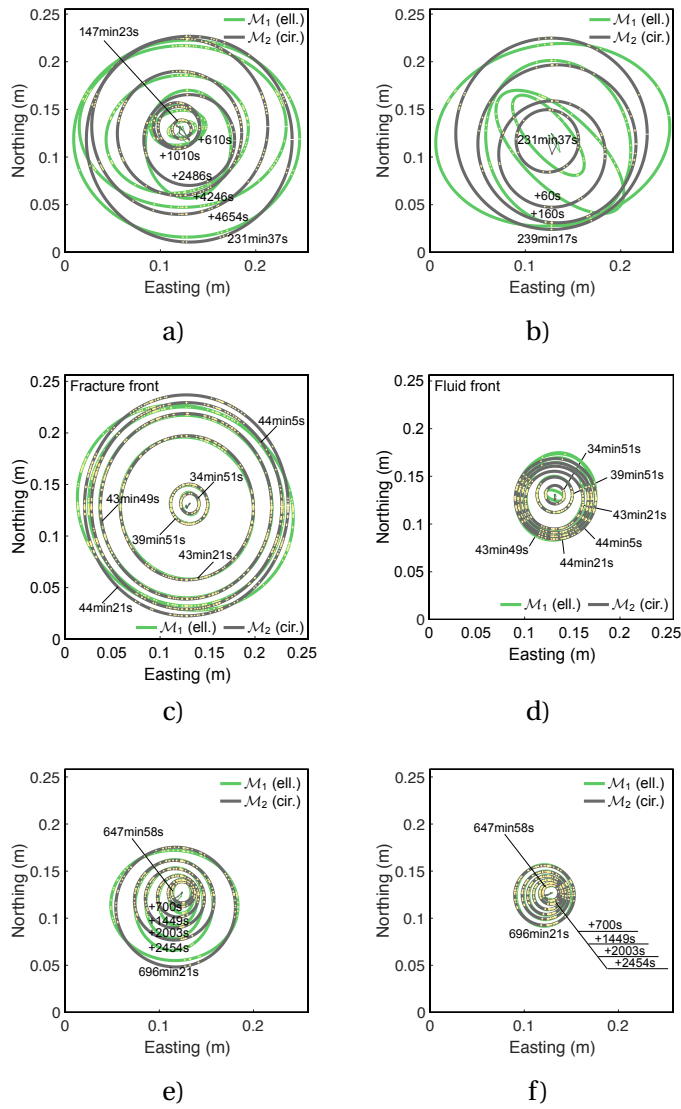
Figure B.4 – Lag-dominated experiments: top view of a) the fracture and b) fluid front in GABB-002, c) the fracture and d) fluid front in MARB-005, and e) the fracture and f) fluid front in MARB-007.
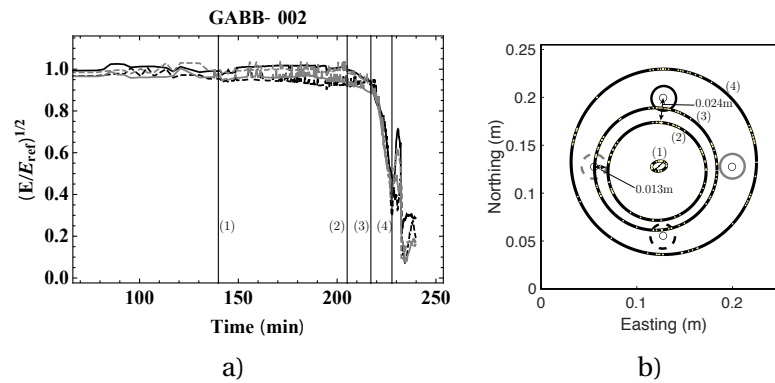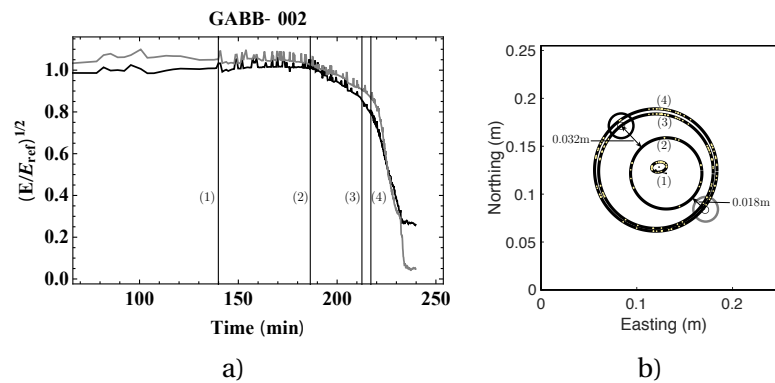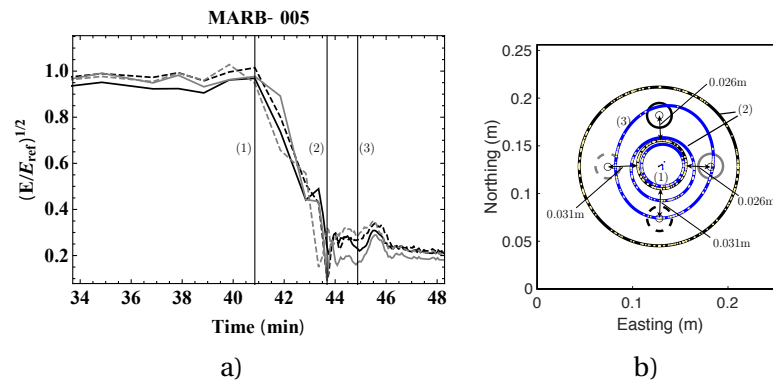
Figure B.5 – GABB-002: time evolution of a) the signal strength of transmitted compressional waves and b) the fracture geometry at different times of the fracture growth. Locations of the transducers in figure a) are indicated by circles in figure b) using the same line style. The fracture extent associated with the numbered vertical lines in figure a), is also shown in figure b) using the same number. The fluid front enters into the fracture nearly at the end of the fracture propagation and is therefore not shown here.

Figure B.6 – GABB-002: time evolution of a) the signal strength of transmitted shear waves, and b) the fracture geometry at different times of the fracture growth. Locations of the transducers in figure a) are indicated by circles in figure b) using the same line style. The fracture extent associated with the numbered vertical lines in figure a), is also shown in figure b) using the same number. The fluid front enters into the fracture nearly at the end of the fracture propagation and is therefore not shown here.

Figure B.7 – MARB-005: time evolution of the signal strength of transmitted compressional waves, and b) the fracture geometry at different times of the fracture growth. Locations of the transducers in figure a) are indicated by circles in figure b) using the same line style. The fracture (in black) and fluid (in blue) extent associated with the numbered vertical lines in figure a), is also shown in figure b) using the same number.
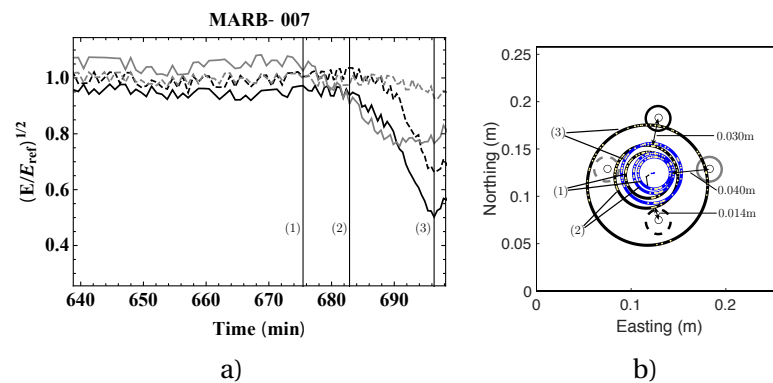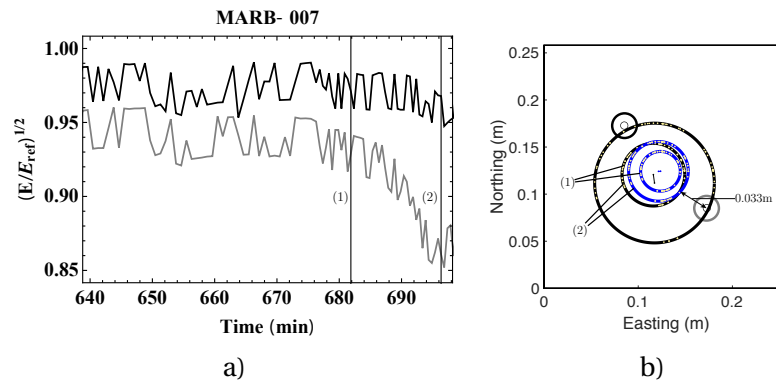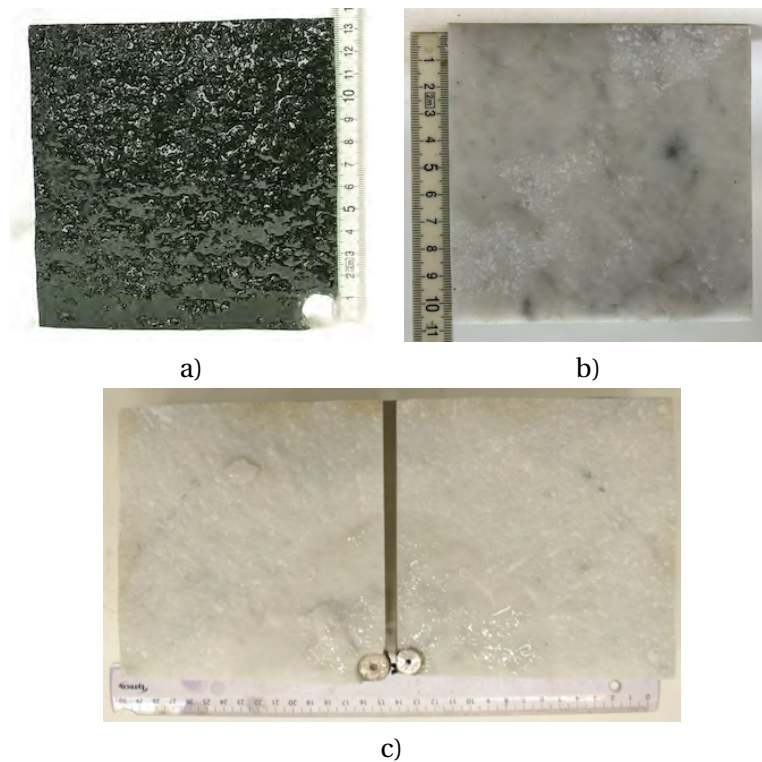

Figure B.8 – MARB-007: time evolution of the signal strength of transmitted compressional waves, and b) the fracture geometry at different times of the fracture growth. Locations of the transducers in figure a) are indicated by circles in figure b) using the same line style. The fracture (in black) and fluid (in blue) extent associated with the numbered vertical lines in figure a), is also shown in figure b) using the same number.

a) b)

Figure B.9 – MARB-007: time evolution of the signal strength of transmitted shear waves, and b) the fracture geometry at different times of the fracture growth. Locations of the transducers in figure a) are indicated by circles in figure b) using the same line style. The fracture (in black) and fluid (in blue) extent associated with the numbered vertical lines in figure a), is also shown in figure b) using the same number.

a) b)

c)

Figure B.10 – Fractured surface of a) the southwestern lower part of GABB-002, b) the southwestern lower part of MARB-005 and c) the southwestern part of MARB-007. Note that the MARB-007 is created by two injections with the second one performed under a much larger rate one day after the first injection reported in Fig. B.3.

C Complementary information on HF experiments

C.1 Estimation of the inlet flux and fracture initiation time

Estimation of the inlet flux The inlet flux Q_{in} differs from that of the ISCO pump Q_o due to the restriction value put in the injection line. We estimate Q_{in} using the global mass balance of fluid in the injection line from the pump to the fracture inlet.

$$Q_{in}(t) = Q_o - U_d \frac{\mathrm{d}p_{\mathrm{downstream}}(t)}{\mathrm{d}t} - (U - U_d) \frac{\mathrm{d}p_{\mathrm{upstream}}(t)}{\mathrm{d}t} \qquad (C.1)$$

where p_{upstream} and $p_{\mathrm{downstream}}$ represent respectively the fluid pressure upstream and downstream the valve as shown in Fig. 6.1, and U_d the downstream compliance representing the contribution from the valve to the inlet. We estimate this downstream compliance U_d either by the product of the fluid compressibility c_f and the volume downstream V_d ($U_d = c_f V_d$), or by the difference between the compliance of the system U and that of the upstream U_u ($U_d = U - U_u$).

$$U = Q_o / \left(\frac{\mathrm{d}p_{\mathrm{upstream}}}{\mathrm{d}t} \right) \qquad (C.2)$$

where U_u is estimated exactly the same way as U (Eq. (C.2)) but with the pressure measured while keeping the valve completely closed during the pressurization.

Determination of the time of fracture initiation We determine the time of fracture initiation t_{ini} using the following events.

- Decrease of the volume in the top-bottom pair of flat-jacks; or increase of the displacement of the top block surface near the wellbore measured by the linear variable differential transformer (LVDT) when there is no confining stress applied on the top platen.

- Increase of the inlet flux or change of the pressure difference between the upstream and downstream. This is only valid for toughness-dominated experiments, otherwise it
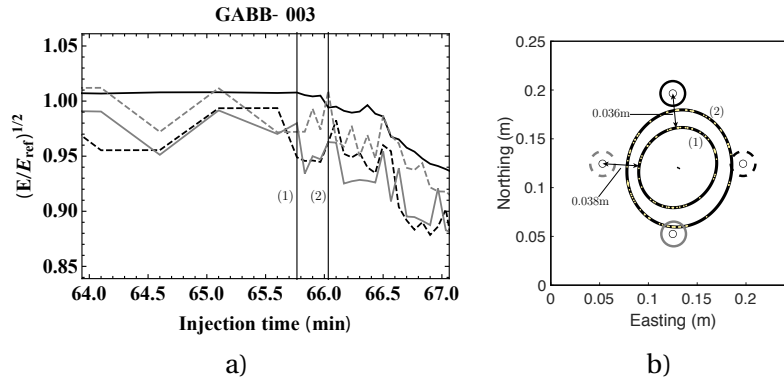
Figure C.1 – GABB-003: time evolution of a) the signal strength of transmitted compressional waves and b) the fracture geometry at different times of the fracture growth. Locations of the transducers in figure a) are indicated by circles in figure b) using the same line style. The fracture extent associated with the numbered vertical lines in figure a), is also shown in figure b) using the same number.

represents the moment of the fluid starting entering into the fracture.

- Deviation of the downstream pressure from the linear pressurization. This is valid for toughness-dominated experiments, otherwise the deviation might not occur or occurs with an important delay after the initiation time.

- Start of the visible diffraction by the growing fracture front. This depends a lot on the quality of the active acoustic measurement. It possibly leads to a delay in the estimation compared with the exact initiation time.

C.2 Supplementary information on vertical transmission for gabbro tests

GABB-003 P waves attenuation indicates a process zone of around 2-4 cm (Fig. C.1) while S wave attenuation corresponds well to the diffracted fracture front arrival with some oscillations/drops reported prior to the fracture front arrival (Fig. C.2).

GABB-005 Transmission attenuation occurs in all compressional and shear transducers shortly after the fracture initiation (Figs. C.4, C.5). This implies a process zone of around 7 cm. However, this attenuation is at most 5% for all compressional transducers, which is much less than that of GABB-001 and GABB-003 (Fig. C.4).

GABB-006 Attenuation is reported in both P and S wave transmission (Fig. C.7, C.8), indicating a process zone size of around 5 cm.
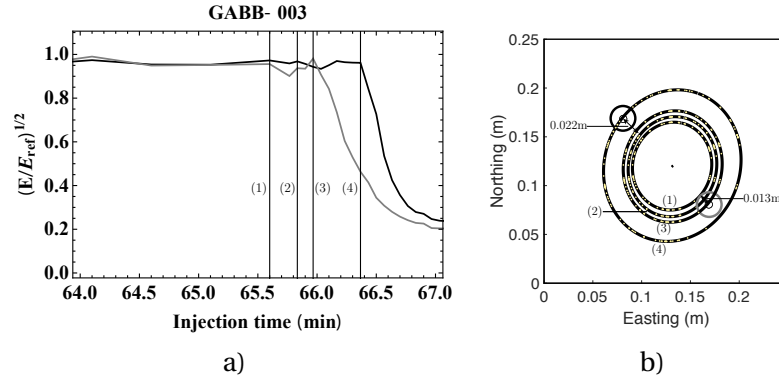
Figure C.2 – GABB-003: time evolution of a) the signal strength of transmitted shear waves and b) the fracture geometry at different times of the fracture growth. Locations of the transducers in figure a) are indicated by circles in figure b) using the same line style. The fracture extent associated with the numbered vertical lines in figure a), is also shown in figure b) using the same number.
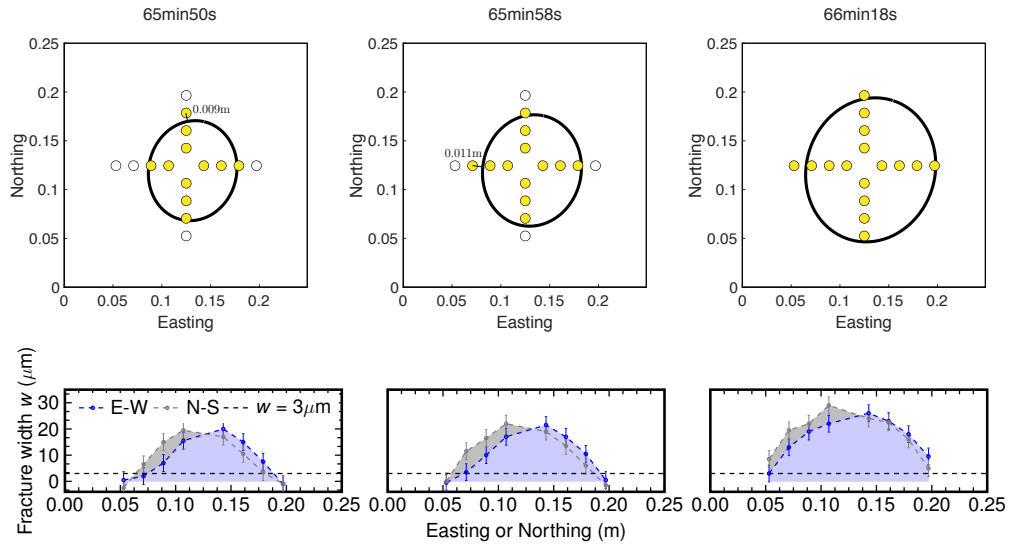

Figure C.3 – GABB-003: top view of the extent of the hydraulic fracture. The P-wave transducers turn yellow if the fracture opening goes above 3 μm. 3 μm is the maximum estimated width prior to fracture initiation which is taken as the error of width estimation.
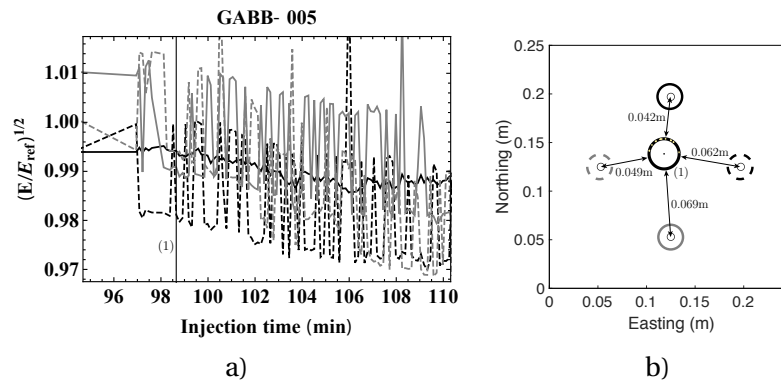
191

Figure C.4 – GABB-005: time evolution of a) the signal strength of transmitted compressional waves and b) the fracture geometry at different times of the fracture growth. Locations of the transducers in figure a) are indicated by circles in figure b) using the same line style. The fracture extent associated with the numbered vertical lines in figure a), is also shown in figure b) using the same number.
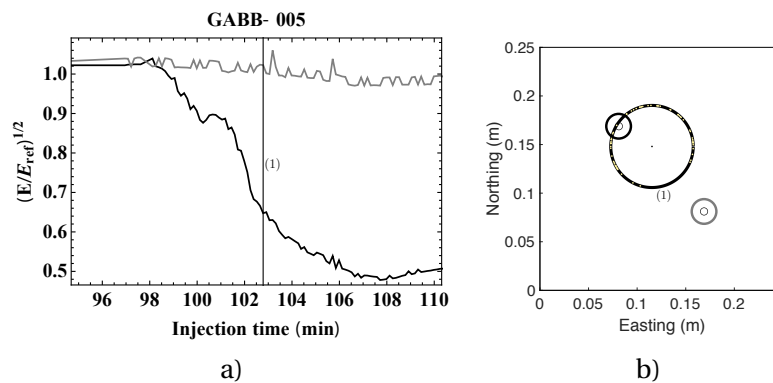

Figure C.5 – GABB-005: time evolution of a) the signal strength of transmitted shear waves and b) the fracture geometry at different times of the fracture growth. Locations of the transducers in figure a) are indicated by circles in figure b) using the same line style. The fracture extent associated with the numbered vertical lines in figure a), is also shown in figure b) using the same number.
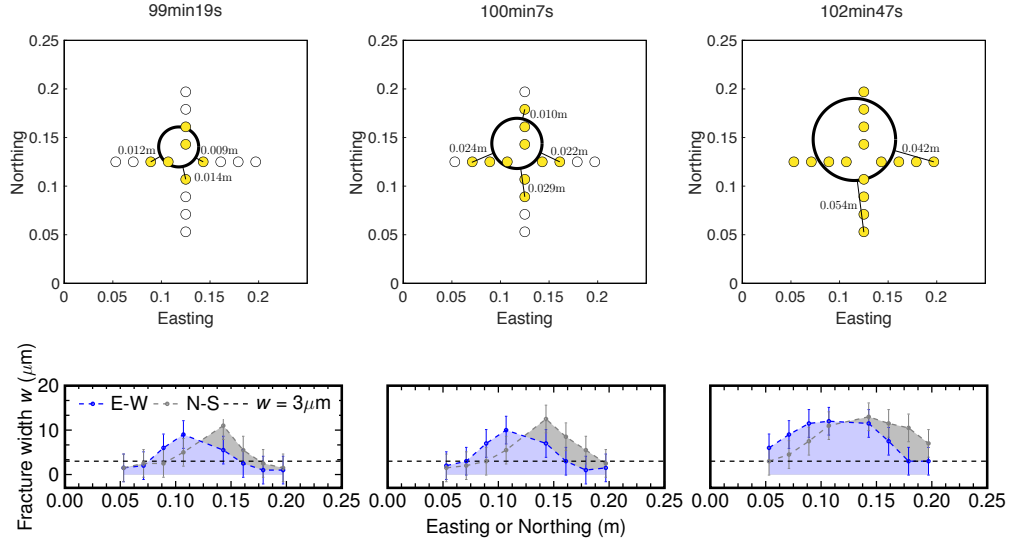
Figure C.6 – GABB-005: top view of the extent of the hydraulic fracture. The P-wave transducers turn yellow if the fracture opening goes above 3 μm. 3 μm is the maximum estimated width prior to fracture initiation which is taken as the error of width estimation.
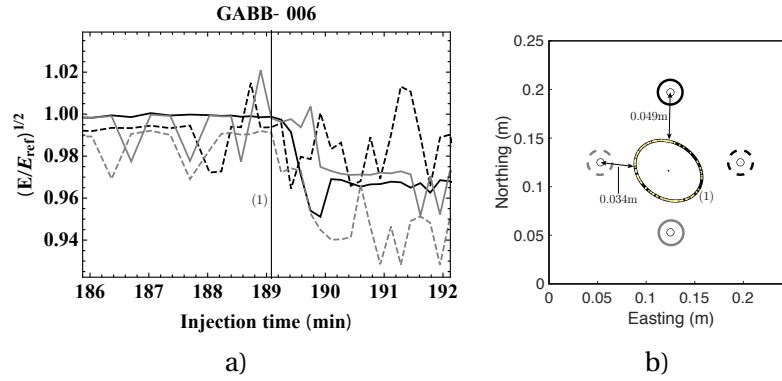

Figure C.7 – GABB-006: time evolution of a) the signal strength of transmitted compressional waves and b) the fracture geometry at different times of the fracture growth. Locations of the transducers in figure a) are indicated by circles in figure b) using the same line style. The fracture extent associated with the numbered vertical lines in figure a), is also shown in figure b) using the same number.
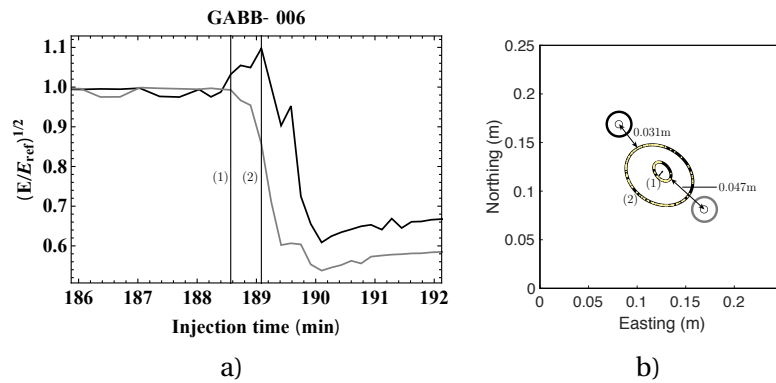
Figure C.8 – GABB-006: time evolution of a) the signal strength of transmitted shear waves and b) the fracture geometry at different times of the fracture growth. Locations of the transducers in figure a) are indicated by circles in figure b) using the same line style. The fracture extent associated with the numbered vertical lines in figure a), is also shown in figure b) using the same number.
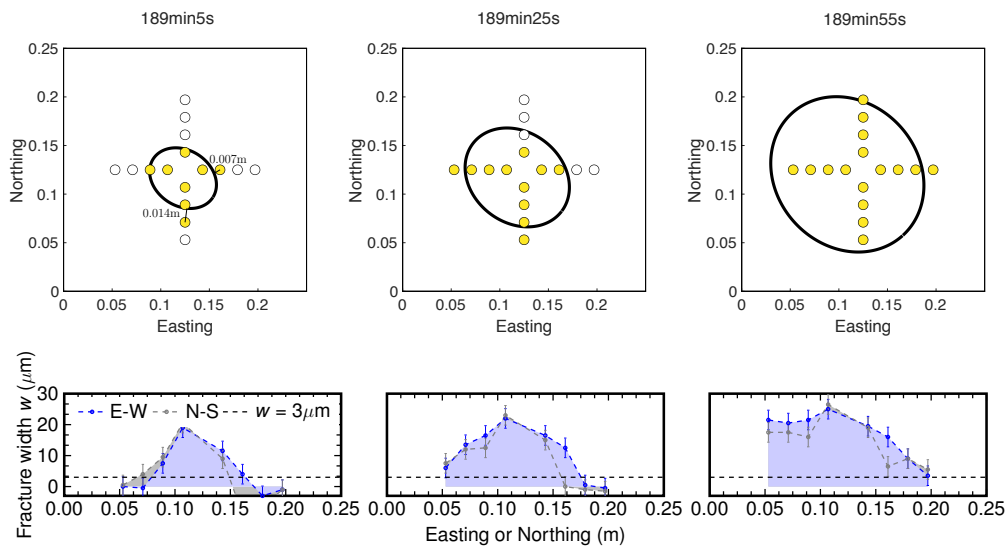

Figure C.9 – GABB-006: top view of the extent of the hydraulic fracture. The P-wave transducers turn yellow if the fracture opening goes above 3 μm. 3 μm is the maximum estimated width prior to fracture initiation which is taken as the error of width estimation.
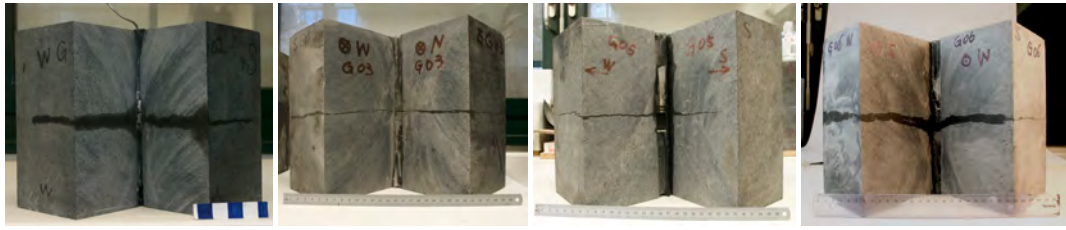
Figure C.10 – Toughness dominated experiments: GABB-001, GABB-003, GABB-005 and GABB-006. Note that the fracture in GABB-006 initiates at a position 9.5 mm below the notch. Two fractures initiate from the wellbore in GABB-006, which probably results from the complex injection history: we perform other injections with a much larger rate following the injection process shown in Fig. 6.10. This may lead to the creation of the second fracture.
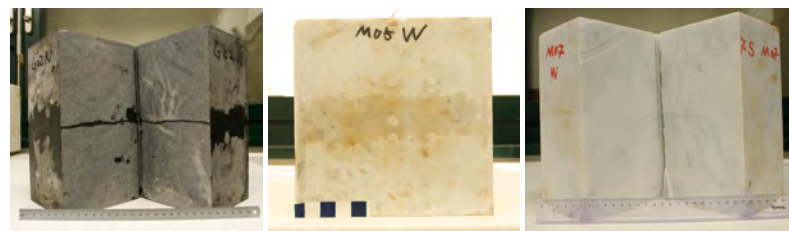

Figure C.11 – Lag dominated experiments: GABB-002, MARB-005 and MARB-007.

Fracture opening also indicates the presence of a process zone in all these three experiments, but the real process zone size depends a lot on the precision of the width estimation.

C.3 Visualization of the fracture geometry

We present here the post-mortem observation of the fracture plane after cutting the samples. We show the fracture path for toughness dominated experiments (GABB-001, GABB-003, GABB-005, GABB-006) in Fig. C.10, that for lag dominated experiments (GABB-002, MARB-005 and MARB-007) in Fig. C.11, and that for the transient experiments in marble (MARB-009 and MARB-010) in Fig. C.12. We show also the fracture path of GABB-004 and MARB-006 in Fig. C.13.

In addition, we present here the footprint of the fracture and fluid fronts for GABB-002, MARB-005 and MARB-007 in Fig. B.4, which are not illustrated in the main text.

C.4 Sensitivity of the transmission to the contact condition and stresses

The signal strength of transmitted waves depends on the stress field inside the rock and the contact condition between transducers and the rock surface. Moreover, it is difficult to completely separate the transmitted component from the diffracted component. In this
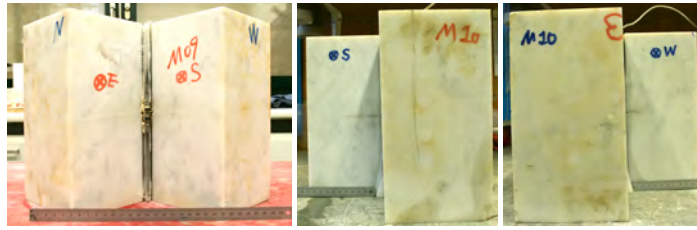
Figure C.12 – HF experiments in marble under different propagation regimes: MARB-009 and MARB-010.

Figure C.13 – Fracture path of GABB-004 and MARB-008. We stop the injection before the fracture front reaches the specimen edge in GABB-004 so that no fracture is observed on the side.
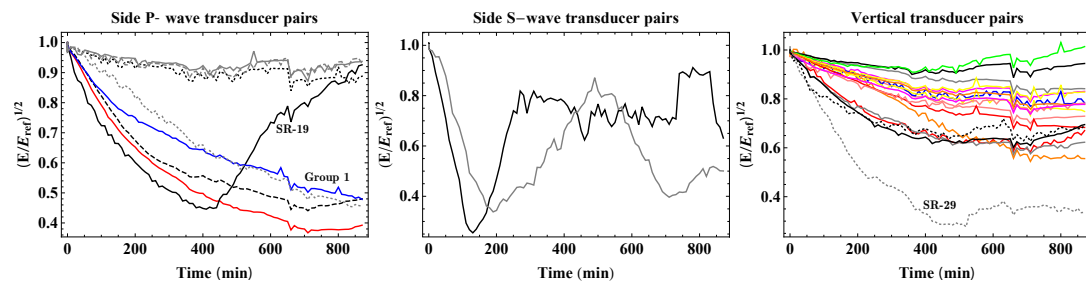
Figure C.14 – Effect of the drying couplant ($\sigma_1 = \sigma_2 = \sigma_3 = 5$ MPa) on the signal strength, taking the block of GABB-005 for example. The transducer disposition is shown in Fig. C.15.
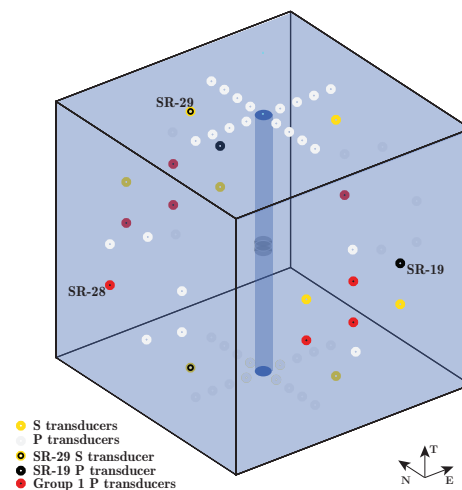
Figure C.15 – Transducer disposition of GABB-005.

Figure C.16 – Effect of the confining stress ($\sigma_1 = \sigma_2 = \sigma_3$) on the signal strength taking the block of GABB-005 for example. The transducer disposition is shown in Fig. C.15.
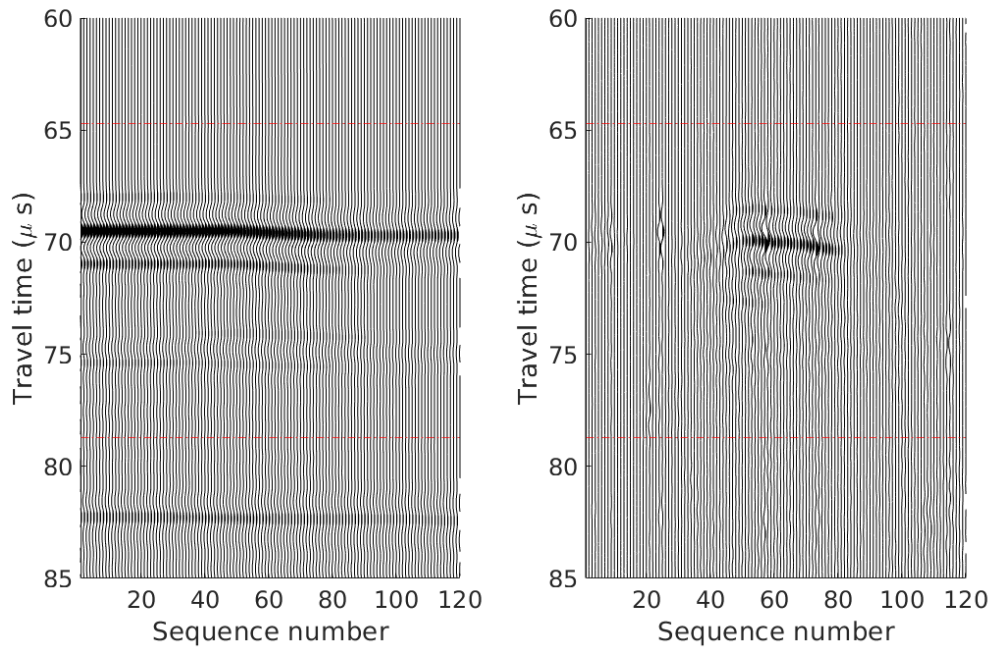
Figure C.17 – Illustration of the diffracted energy compared to the transmitted energy taking the example of a shear wave transducer pair in the vertical direction in GABB-001 (corresponding to the S-wave transducer pair on the top-bottom platens which is not indicated with any text in Fig. C.15).

section, we try to understand how these effects influence the transmitted energy.

As shown in Fig. C.17, the diffraction front first goes into the interest time window (we apply a tapered hamming filter on this time window with only 1/3 of the signal in the center of the window not attenuated, corresponding to a period of around 5 μs) and leaves again at a time much later than the start of the transmission attenuation. If this diffracted energy is important compared with the transmitted energy, one would expect a first increase and then a decrease of the transmitted energy. This is however not the case in GABB-001, implying that the energy of the diffracted arrival is smaller than that of the direct transmitted arrival.

We then apply a confining stress of 5 MPa on GABB-005 and run the acoustic measurement for more than 10 hours without the injection. As shown in Fig. C.14, the strength of most transmitted waves attenuates slowly due to the drying or absorption of the couplant. Side transducers present a more significant attenuation than vertical transducer pairs and the attenuation of shear waves is larger than that of compressional waves. In real experiments, this attenuation is most likely negligible or insignificant with the fracture propagation duration of several minutes, which is much shorter than the test time (> 10h) here. We also vary the confining stress applied on GABB-005 within a much shorter time assuming that the contact change due to the drying couplant is negligible. As shown in Fig. C.16, the signal strength of side transmitted waves presents a strong dependence on the confining stress: it evolves in a similar way as we change the confining stress ($\sigma_1 = \sigma_2 = \sigma_3$) from 5, to 10, 15 MPa and finally to 0.5 MPa. Moreover, for the side transmission, shear waves are more sensitive to the change of the confining stress than the compressional ones. This dependence on the confining stress is however not obvious for vertical transmitted energy.

In Chapter 6, we are interested in the analysis of vertical transmitted waves which do not seem to depend on the confining stress. However, we show some side transmission evolution in C.5 for the sake of curiosity.

C.5 Evolution of the acoustic transmission parallel to the fracture plane

In this section, we discuss the evolution of side transmitted energy (calculated using Eq. 5.11) in different experiments.

GABB-001 Attenuation occurs prior to the fracture initiation for side transducer pairs located 2 cm away from the fracture plane (denoted as close transducers), yet amplification occurs for transducer pairs located 5 cm away from the fracture plane (denoted as far transducers) (Fig. C.18).

Figure C.18 – GABB-001: time evolution of the signal strength of transmitted compressional waves on the E-W side. The vertical lines in the left figure correspond to the fracture radius reconstructed from the diffracted waves shown in the right figure.

GABB-003 Larger attenuation are observed in close transducers than those in GABB-001. Amplification are detected for far transducers (Fig. C.19).

GABB-005 Smaller attenuation are observed in close transducers than those in GABB-001 and GABB-003. Amplification are detected for far transducers.

GABB-006 Smaller attenuation are observed in close transducers than those in GABB-001 and GABB-003. No obvious changes are detected for far transducers.

MARB-009 Attenuation occurs both in close and far transducers during the fracture growth (Fig. C.21).

MARB-010 Attenuation occurs in far transducers while for close transducers amplification occurs during the fracture growth (Fig. C.22).

MARB-005, MARB-007 and GABB-002 There exists a ringing source on the side platens. It sends acoustic waves with a time shift compared with the other sources. This strongly affect the calculation of the side transmitted energy. We therefore do not go further on the side transmission analysis for these three experiments.

The evolution of transmitted energy results from the process zone around the fracture tip, the stress state of the block, the contact condition of transducers and the fracture-wave interactions. Further investigation is necessary to explain better the evolution of the side transmitted energy.
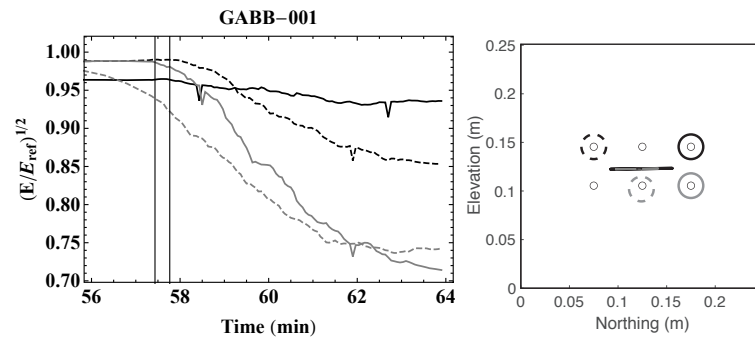
Figure C.19 – GABB-003: time evolution of the signal strength of transmitted compressional waves on the side. The vertical lines in the left figure correspond to the fracture radius reconstructed from the diffracted waves shown in the right figure.
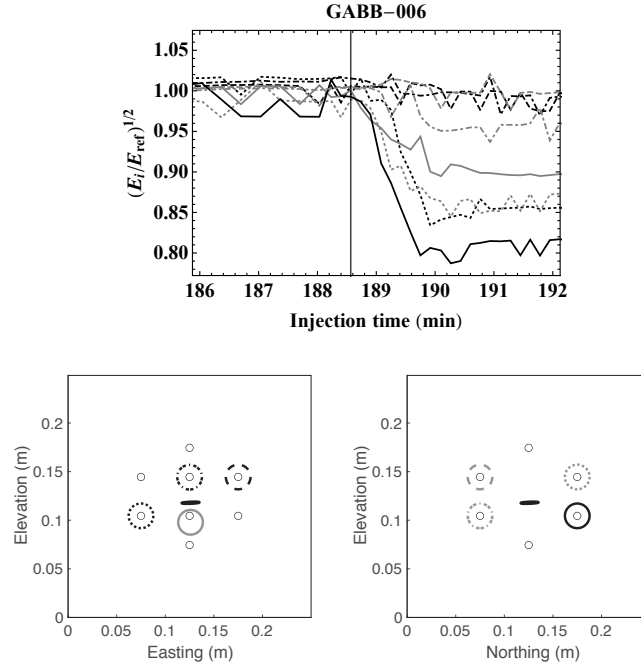
Figure C.20 – GABB-006: time evolution of the signal strength of transmitted compressional waves on the side. The vertical lines in the left figure correspond to the fracture radius reconstructed from the diffracted waves shown in the right figure.

Figure C.21 – MARB-009: time evolution of the signal strength of transmitted compressional waves on the side. The vertical lines in the left figure correspond to the fracture radius reconstructed from the diffracted waves shown in the right figure.
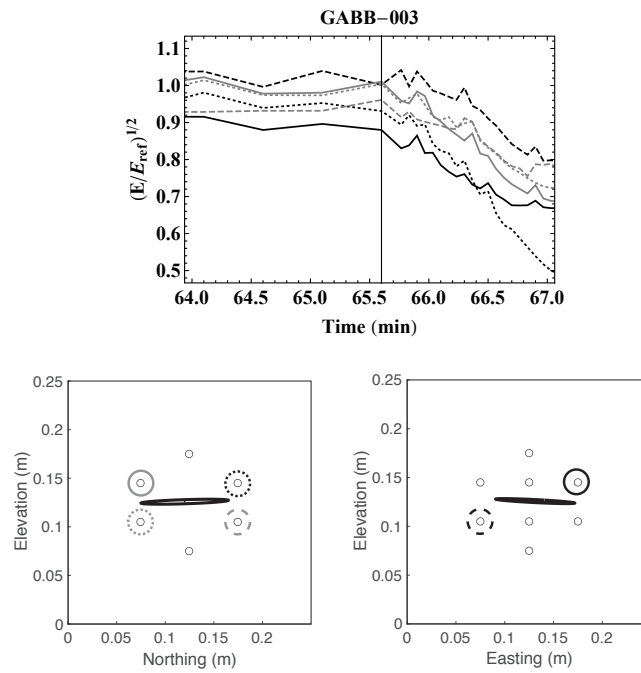

Figure C.22 – MARB-010: time evolution of the signal strength of transmitted compressional waves on the side. The vertical lines in the left figure correspond to the fracture radius reconstructed from the diffracted waves shown in the right figure.
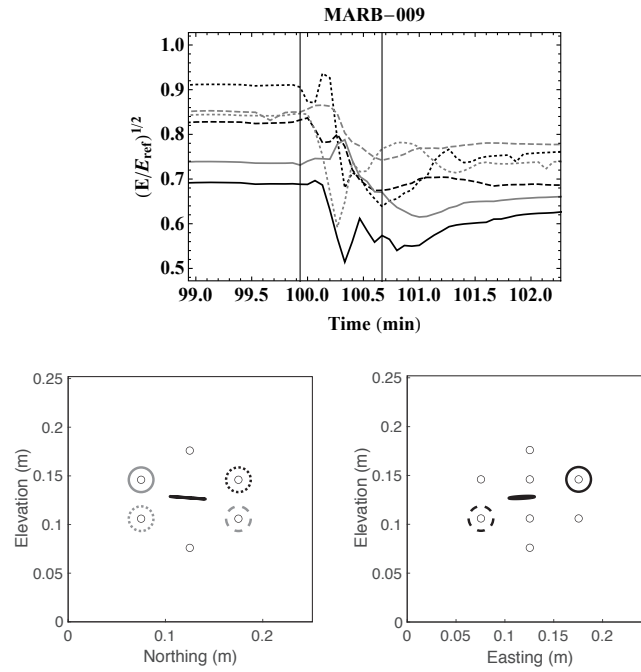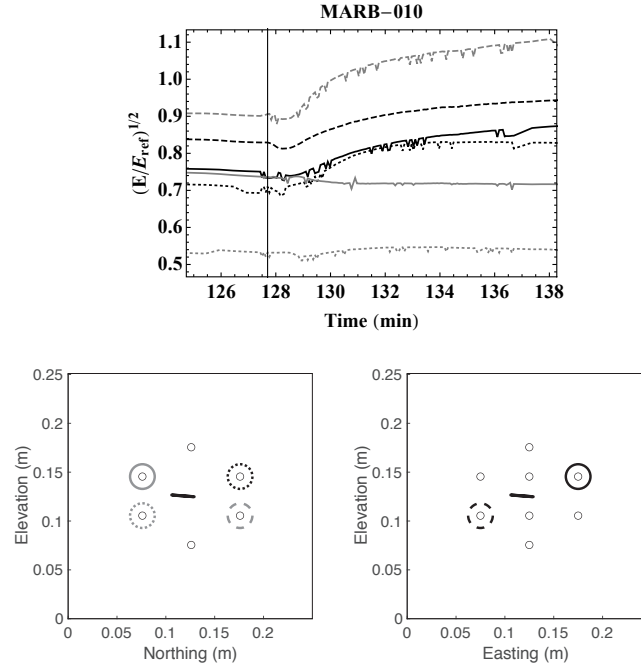
Bibliography

Abe, H., Keer, L., and Mura, T. (1976). Growth rate of a penny-shaped crack in hydraulic fracturing of rocks, 2. *Journal of Geophysical Research*, 81(35):6292–6298.

Aben, F. M., Brantut, N., Mitchell, T. M., and David, E. C. (2019). Rupture energetics in crustal rock from laboratory-scale seismic tomography. *Geophysical Research Letters*, 46(13):7337–7344.

Adachi, J. and Detournay, E. (2002). Self-similar solution of a plane-strain fracture driven by a power-law fluid. *International Journal for Numerical and Analytical Methods in Geomechanics*, 26(6):579–604.

Adachi, J. I. and Detournay, E. (2008). Plane strain propagation of a hydraulic fracture in a permeable rock. *Engineering Fracture Mechanics*, 75(16):4666–4694.

Aliha, M. R. M., Mahdavi, E., and Ayatollahi, M. R. (2017). The influence of specimen type on tensile fracture toughness of rock materials. *Pure and Applied Geophysics*, 174(3):1237–1253.

Anderson, T. L. (2017). *Fracture mechanics: fundamentals and applications.* CRC press.

Atkinson, B. K. (1984). Subcritical crack growth in geological materials. *Journal of Geophysical Research: Solid Earth*, 89(B6):4077–4114.

Atkinson, B. K. and Meredith, P. G. (1987). Experimental fracture nmechanics data for rocks and nminerals. *Fracture Mechanics of Rock*, page 477.

Barak, Y., Srivastava, A., and Osovski, S. (2019). Correlating fracture toughness and fracture surface roughness via correlation length scale. *International Journal of Fracture*, 219(1):19–30.

Barenblatt, G. I. (1959). The formation of equilibrium cracks during brittle fracture. general ideas and hypotheses. axially-symmetric cracks. *Journal of Applied Mathematics and Mechanics*, 23(3):622–636.

Batchelor, G. K. (2000). *An introduction to fluid dynamics.* Cambridge university press.

Bazant, Z. P. and Planas, J. (1997). *Fracture and size effect in concrete and other quasibrittle materials*, volume 16. CRC press.

Bibliography

Berrut, J.-P. and Trefethen, L. N. (2004). Barycentric lagrange interpolation. *Society for Industrial and Applied Mathematics.*

Bonamy, D. and Bouchaud, E. (2011). Failure of heterogeneous materials: A dynamic phase transition? *Physics Reports*, 498(1):1–44.

Bonamy, D., Ponson, L., Prades, S., Bouchaud, E., and Guillot, C. (2006). Scaling exponents for fracture surfaces in homogeneous glass and glassy ceramics. *Physical Review Letters*, 97(13):135504.

Brantut, N. (2018). Time-resolved tomography using acoustic emissions in the laboratory, and application to sandstone compaction. *Geophysical Journal International*, 213(3):2177–2192.

Brekhovskikh, L. M. and Godin, O. A. (1990). *Acoustics of layered media I: Plane and quasi-plane waves*, volume 5. Springer Science & Business Media.

Breysse, D. and Gérard, B. (1997). Transport of fluids in cracked media. *Rilem report*, pages 123–154.

Bueckner, H. (1970). A novel principle for the computation of stress intensity factors. *Zeitschrift fuer Angewandte Mathematik & Mechanik*, 50(9):529–546.

Bunger, A. (2006). A photometry method for measuring the opening of fluid-filled fractures. *Measurement Science and Technology*, 17(12):3237.

Bunger, A. and Cruden, A. (2011). Modeling the growth of laccoliths and large mafic sills: Role of magma body forces. *Journal of Geophysical Research: Solid Earth*, 116(B2).

Bunger, A. and Lecampion, B. (2017). Four critical issues for successful hydraulic fracturing applications. Number Chapter 16. CRC Press.

Bunger, A. P. (2005). *Near-surface hydraulic fracture*. PhD thesis, University of Minnesota.

Bunger, A. P. (2008). A rigorous tool for evaluating the importance of viscous dissipation in sill formation: it's in the tip. *Geological Society, London, Special Publications*, 304(1):71–81.

Bunger, A. P. and Detournay, E. (2007). Early-time solution for a radial hydraulic fracture. *Journal of Engineering Mechanics*, 133(5):534–540.

Bunger, A. P. and Detournay, E. (2008). Experimental validation of the tip asymptotics for a fluid-driven crack. *Journal of the Mechanics and Physics of Solids*, 56(11):3101–3115.

Bunger, A. P., Detournay, E., and Garagash, D. I. (2005a). Toughness-dominated hydraulic fracture with leak-off. *International Journal of Fracture*, 134(2):175–190.

Bunger, A. P., Gordeliy, E., and Detournay, E. (2013). Comparison between laboratory experiments and coupled simulations of saucer-shaped hydraulic fractures in homogeneous brittle-elastic solids. *Journal of the Mechanics and Physics of Solids*, 61(7):1636–1654.

Bunger, A. P., Jeffrey, R. G., and Detournay, E. (2005b). Application of scaling laws to laboratory-scale hydraulic fractures. In *Alaska Rocks 2005, The 40th US Symposium on Rock Mechanics (USRMS)*, pages ARMA/USRMS–05–818, Anchorage, Alaska.

Carrier, B. and Granet, S. (2012). Numerical modeling of hydraulic fracture problem in permeable medium using cohesive zone model. *Engineering Fracture Mechanics*, 79:312–328.

Chandler, M. R., Meredith, P. G., Brantut, N., and Crawford, B. R. (2016). Fracture toughness anisotropy in shale. *Journal of Geophysical Research: Solid Earth*, 121(3):1706–1729.

Chen, Y., Nagaya, Y., and Ishida, T. (2015). Observations of fractures induced by hydraulic fracturing in anisotropic granite. *Rock Mechanics and Rock Engineering*, 48(4):1455–1461.

Chen, Z. (2012). Finite element modelling of viscosity-dominated hydraulic fractures. *Journal of Petroleum Science and Engineering*, 88:136–144.

Chen, Z., Bunger, A., Zhang, X., and Jeffrey, R. G. (2009). Cohesive zone finite element-based modeling of hydraulic fractures. *Acta Mechanica Solida Sinica*, 22(5):443–452.

Chudnovsky, A., Fan, F., Shulkin, Y., Zhang, H., Dudley, J. W., and Wong, G. K. (2008). Hydraulic fracture simulation revisited. In *42nd US Rock Mechanics Symposium and 2nd US-Canada Rock Mechanics Symposium*. ARMA.

Cleary, M. and Wong, S. (1985). Numerical simulation of unsteady fluid flow and propagation of a circular hydraulic fracture. *International Journal for Numerical and Analytical Methods in Geomechanics*, 9(1):1–14.

Cowie, P. A. and Scholz, C. H. (1992). Physical explanation for the displacement-length relationship of faults using a post-yield fracture mechanics model. *Journal of Structural Geology*, 14(10):1133–1148.

De Pater, C., Desroches, J., Groenenboom, J., Weijers, L., et al. (1996). Physical and numerical modeling of hydraulic fracture closure. *SPE Production & Facilities*, 11(02):122–128.

De Pater, C., Groenenboom, J., van Dam, D., and Romijn, R. (2001). Active seismic monitoring of hydraulic fractures in laboratory experiments. *International Journal of Rock Mechanics and Mining Sciences*, 38(6):777–785.

Delaney, P. T. and Pollard, D. D. (1981). Deformation of host rocks and flow of magma during growth of minette dikes and breccia-bearing intrusions near ship rock, New Mexico. Technical report, USGPO,.

Delaney, P. T., Pollard, D. D., Ziony, J. I., and McKee, E. H. (1986). Field relations between dikes and joints: Emplacement processes and paleostress analysis. *Journal of Geophysical Research: Solid Earth*, 91(B5):4920–4938.

Bibliography

Dempsey, J., Adamson, R., and Mulmule, S. (1999). Scale effects on the in-situ tensile strength and fracture of ice. part II: First-year sea ice at resolute, nwt. *International Journal of Fracture*, 95(1-4):347.

Dempsey, J. P., Tan, L., and Wang, S. (2010). An isolated cohesive crack in tension. *Continuum Mechanics and Thermodynamics*, 22(6):617–634.

Desroches, J., Detournay, E., Lenoach, B., Papanastasiou, P., Pearson, J. R. A., Thiercelin, M., and Cheng, A. (1994). The crack tip region in hydraulic fracturing. *Proceedings of the Royal Society of London. Series A: Mathematical and Physical Sciences*, 447(1929):39–48.

Detournay, E. (2004). Propagation regimes of fluid-driven fractures in impermeable rocks. *International Journal of Geomechanics*, 4(1):35–45.

Detournay, E. (2016). Mechanics of hydraulic fractures. *Annual Review of Fluid Mechanics*, 48:311–339.

Detournay, E. and Peirce, A. P. (2014). On the moving boundary conditions for a hydraulic fracture. *International Journal of Engineering Science*, 84:147–155.

Dontsov, E. (2016). Tip region of a hydraulic fracture driven by a laminar-to-turbulent fluid flow. *Journal of Fluid Mechanics*, 797.

Dugdale, D. S. (1960). Yielding of steel sheets containing slits. *Journal of the Mechanics and Physics of Solids*, 8(2):100–104.

Economides, M. J., Nolte, K. G., et al. (1989). *Reservoir stimulation*, volume 2. Prentice Hall Englewood Cliffs, NJ.

Elliot, R. and Santiago, L. (2019). A decade in which fracking rocked the oil world. *Wall Street Journal.*

Engvik, A. K., Bertram, A., Kalthoff, J. F., Stöckhert, B., Austrheim, H., and Elvevold, S. (2005). Magma-driven hydraulic fracturing and infiltration of fluids into the damaged host rock, an example from Dronning Maud Land, Antarctica. *Journal of Structural Geology*, 27(5):839–854.

Erdogan, F., Gupta, G. D., and Cook, T. (1973). Numerical solution of singular integral equations. In *Methods of analysis and solutions of crack problems*, pages 368–425. Springer.

Falk, M. L., Needleman, A., and Rice, J. R. (2001). A critical evaluation of cohesive zone models of dynamic fractur. *Le Journal de Physique IV*, 11(PR5):Pr5–43.

Funatsu, T., Seto, M., Shimada, H., Matsui, K., and Kuruppu, M. (2004). Combined effects of increasing temperature and confining pressure on the fracture toughness of clay bearing rocks. *International Journal of Rock Mechanics and Mining Sciences*, 41(6):927–938.

Garagash, D. I. (2000). Hydraulic fracture propagation in elastic rock with large toughness. In *4th North American Rock Mechanics Symposium*. American Rock Mechanics Association.

Garagash, D. I. (2006a). Plane-strain propagation of a fluid-driven fracture during injection and shut-in: Asymptotics of large toughness. *Engineering Fracture Mechanics*, 73(4):456 – 481.

Garagash, D. I. (2006b). Propagation of a plane-strain hydraulic fracture with a fluid lag: Early-time solution. *International Journal of Solids and Structures*, 43(18–19):5811 – 5835.

Garagash, D. I. (2009). Scaling of physical processes in fluid-driven fracture: perspective from the tip. In *IUTAM symposium on scaling in solid mechanics*, pages 91–100. Springer.

Garagash, D. I. (2015a). How fracking can be tough. IMA Workshop Hydraulic Fracturing Modeling and Simulation to Reconstruction and Characterization, University of Minnesota.

Garagash, D. I. (2015b). Roughness-dominated hydraulic fracture propagation. In *2015 AGU Fall Meeting Abstracts*, San Francisco. AGU.

Garagash, D. I. (2019). Cohesive-zone effects in hydraulic fracture propagation. *Journal of the Mechanics and Physics of Solids*, 133:103727.

Garagash, D. I. and Detournay, E. (2000). The tip region of a fluid-driven fracture in an elastic medium. *ASME Journal of Applied Mechanics*, 67:183–192.

Garagash, D. I. and Detournay, E. (2005). Plane-strain propagation of a fluid-driven fracture: small toughness solution. *Journal of Applied Mechanics*, 72(6):916–928.

Garagash, D. I., Detournay, E., and Adachi, J. I. (2011). Multiscale tip asymptotics in hydraulic fracture with leak-off. *Journal of Fluid Mechanics*, 669:260.

Glaser, S. D. and Hand, M. K. (1998). Imaging of rock fractures with low-frequency ultrasonic reflection/diffraction. *Geotechnical Testing Journal*, 21(4):317–327.

Goodfellow, S., Nasseri, M., Maxwell, S., and Young, R. (2015). Hydraulic fracture energy budget: Insights from the laboratory. *Geophysical Research Letters*, 42(9):3179–3187.

Gordeliy, E., Abbas, S., and Peirce, A. (2019). Modeling nonplanar hydraulic fracture propagation using the XFEM: An implicit level-set algorithm and fracture tip asymptotics. *International Journal of Solids and Structures*, 159:135–155.

Gordeliy, E. and Detournay, E. (2011a). Displacement discontinuity method for modeling axisymmetric cracks in an elastic half-space. *International Journal of Solids and Structures*, 48(19):2614–2629.

Gordeliy, E. and Detournay, E. (2011b). A fixed grid algorithm for simulating the propagation of a shallow hydraulic fracture with a fluid lag. *International Journal for Numerical and Analytical Methods in Geomechanics*, 35(5):602–629.

Bibliography

Groenenboom, J. (1998). Acoustic monitoring of hydraulic fracture growth.

Groenenboom, J. and Falk, J. (2000). Scattering by hydraulic fractures: Finite-difference modeling and laboratory data. *Geophysics*, 65(2):612–622.

Groenenboom, J. and Fokkema, J. T. (1998). Monitoring the width of hydraulic fractures with acoustic waves. *Geophysics*, 63(1):139–148.

Groenenboom, J. and van Dam, D. B. (2000). Monitoring hydraulic fracture growth: Laboratory experiments. *Geophysics*, 65(2):603–611.

Gulli, D., Pellegri, M., Marchetti, D., et al. (2015). Mechanical behaviour of carrara marble rock mass related to geo-structural conditions and in-situ stress. In *ISRM Regional Symposium-8th South American Congress on Rock Mechanics*. International Society for Rock Mechanics and Rock Engineering.

Gulrajani, S. N., Nolte, K. G., and Romero, J. (1997). Evaluation of the M-Site B-Sand fracture experiments: The evolution of a pressure analysis methodology. In *SPE Annual Technical Conference and Exhibition*. SPE.

Gupta, M., Alderliesten, R., and Benedictus, R. (2015). A review of t-stress and its effects in fracture mechanics. *Engineering Fracture Mechanics*, 134:218–241.

Haas, A., Revil, A., Karaoulis, M., Frash, L., Hampton, J., Gutierrez, M., and Mooney, M. (2013). Electric potential source localization reveals a borehole leak during hydraulic fracturing. *Geophysics*, 78(2):D93–D113.

Hashida, T., Sato, K., and Takahashi, H. (1993). Significance of crack opening for determining the growth behavior monitor1 ng of hydrofractures. In *Eighteenth Workshop on Geothermal Reservoir Engineering*, pages 79–84, Stanford, California.

Hillerborg, A., Modéer, M., and Petersson, P.-E. (1976). Analysis of crack formation and crack growth in concrete by means of fracture mechanics and finite elements. *Cement and Concrete Research*, 6(6):773–781.

Hills, D., Kelly, P., Dai, D., and Korsunsky, A. (1996). *Solution of Crack Problems: The Distributed Dislocation Technique*. Journal of Applied Mechanics. Kluwer Academic Publishers.

Hills, D. A., Kelly, P., Dai, D., and Korsunsky, A. (2013). *Solution of crack problems: the distributed dislocation technique*, volume 44. Springer Science & Business Media.

Howard, G. C. and Fast, C. (1957). Optimum fluid characteristics for fracture extension. In *Drilling and production practice*. OnePetro.

Hu, J. and Garagash, D. (2010). Plane-strain propagation of a fluid-driven crack in a permeable rock with fracture toughness. *Journal of Engineering Mechanics*, 136(9):1152–1166.

Hubbert, M. K. and Willis, D. G. (1957). Mechanics of hydraulic fracturing. *Transactions of the AIME*, 210:153–168.

Ishida, T. (2001). Acoustic emission monitoring of hydraulic fracturing in laboratory and field. *Construction and Building Materials*, 15(5-6):283–295.

Jeffrey, R., Chen, Z., Mills, K., Pegg, S., et al. (2013). Monitoring and measuring hydraulic fracturing growth during preconditioning of a roof rock over a coal longwall panel. In *ISRM International Conference for Effective and Sustainable Hydraulic Fracturing*. International Society for Rock Mechanics and Rock Engineering.

Jeffrey, R., Kear, J., Kasperczyk, D., Zhang, X., Chuprakov, D., Prioul, R., Schouten, J., et al. (2015). A 2D experimental method with results for hydraulic fractures crossing discontinuities. In *49th US Rock Mechanics/Geomechanics Symposium*. American Rock Mechanics Association.

Jin, Y., Dong, J., Zhang, X., Li, X., and Wu, Y. (2017). Scale and size effects on fluid flow through self-affine rough fractures. *International Journal of Heat and Mass Transfer*, 105:443–451.

Jin, Z.-H. and Johnson, S. E. (2008). Magma-driven multiple dike propagation and fracture toughness of crustal rocks. *Journal of Geophysical Research: Solid Earth*, 113(B3).

Keating, R. and Sinclair, G. (1996). On the fundamental energy argument of elastic fracture mechanics. *International Journal of Fracture*, 74(1):43–61.

King, G. E. et al. (2012). Hydraulic fracturing 101: What every representative, environmentalist, regulator, reporter, investor, university researcher, neighbor and engineer should know about estimating frac risk and improving frac performance in unconventional gas and oil wells. In *SPE hydraulic fracturing technology conference*. Society of Petroleum Engineers.

Kovalyshen, Y. (2014). International journal of rock mechanics & mining sciences. *International Journal of Rock Mechanics and Mining Sciences*, 70:368–374.

Kuruppu, M., Obara, Y., Ayatollahi, M., Chong, K., and Funatsu, T. (2014). Isrm-suggested method for determining the mode i static fracture toughness using semi-circular bend specimen. *Rock Mechanics and Rock Engineering*, 47(1):267–274.

Labuz, J., Shah, S., and Dowding, C. (1987). The fracture process zone in granite: evidence and effect. In *International Journal of Rock Mechanics and Mining Sciences & Geomechanics Abstracts*, volume 24, pages 235–246. Elsevier.

Lecampion, B. (2012). Modeling size effects associated with tensile fracture initiation from a wellbore. *International Journal of Rock Mechanics and Mining Sciences*, 56:67–76.

Lecampion, B., Bunger, A., and Zhang, X. (2018). Numerical methods for hydraulic fracture propagation: a review of recent trends. *Journal of Natural Gas Science and Engineering*.

Bibliography

Lecampion, B., Desroches, J., Jeffrey, R. G., and Bunger, A. P. (2017). Experiments versus theory for the initiation and propagation of radial hydraulic fractures in low permeability materials. *Journal of Geophysical Research: Solid Earth*, 122.

Lecampion, B. and Detournay, E. (2007). An implicit algorithm for the propagation of a hydraulic fracture with a fluid lag. *Computer Methods in Applied Mechanics and Engineering*, 196(49-52):4863–4880.

Lecampion, B. and Gunning, J. (2007). Model selection in fracture mapping from elastostatic data. *International Journal of Solids and Structures*, 44(5):1391–1408.

Lecampion, B. and Zia, H. (2019). Slickwater hydraulic fracture propagation: near-tip and radial geometry solutions. *Journal of Fluid Mechanics*, 880:514–550.

Lenoach, B. (1995). The crack tip solution for hydraulic fracturing in a permeable solid. *Journal of the Mechanics and Physics of Solids*, 43(7):1025–1043.

Lhomme, T., Detournay, E., and Jeffrey, R. G. (2005). Effect of fluid compressibility and borehole on the initiation and propagation of a tranverse hydraulic fracture. *Strength, fracture and complexity*, 3(2-4):149–162.

Lhomme, T. P. Y. (2005). *Initiation of hydraulic fractures in natural sandstones*. TU Delft, Delft University of Technology.

Li, Y., Deng, J., Liu, W., and Feng, Y. (2017). Modeling hydraulic fracture propagation using cohesive zone model equipped with frictional contact capability. *Computers and Geotechnics*, 91:58–70.

Lin, Q., Wan, B., Wang, Y., Lu, Y., and Labuz, J. F. (2019). Unifying acoustic emission and digital imaging observations of quasi-brittle fracture. *Theoretical and Applied Fracture Mechanics*, 103:102301.

Lister, J. R. and Kerr, R. C. (1991). Fluid-mechanical models of crack propagation and their application to magma transport in dykes. *Journal of Geophysical Research: Solid Earth*, 96(B6):10049–10077.

Liu, D. and Lecampion, B. (2019). Propagation of a plane-strain hydraulic fracture accounting for the presence of a cohesive zone and a fluid lag. In *53rd US Rock Mechanics/Geomechanics Symposium*. ARMA.

Liu, D. and Lecampion, B. (2021). Propagation of a plane-strain hydraulic fracture accounting for a rough cohesive zone. *Journal of the Mechanics and Physics of Solids*, 149:104322.

Liu, D., Lecampion, B., and Blum, T. (2020). Time-lapse reconstruction of the fracture front from diffracted waves arrivals in laboratory hydraulic fracture experiments. *Geophysical Journal International*, 223(1):180–196.

Liu, D., Lecampion, B., et al. (2019a). Growth of a radial hydraulic fracture accounting for the viscous fluid flow in a rough cohesive zone. In *ARMA-CUPB Geothermal International Conference*. American Rock Mechanics Association.

Liu, D., Lecampion, B., and Garagash, D. I. (2019b). Propagation of a fluid-driven fracture with fracture length dependent apparent toughness. *Engineering Fracture Mechanics*, 220:106616.

Liu, P., Ju, Y., Ranjith, P. G., Zheng, Z., and Chen, J. (2016). Experimental investigation of the effects of heterogeneity and geostress difference on the 3D growth and distribution of hydrofracturing cracks in unconventional reservoir rocks. *Journal of Natural Gas Science and Engineering*, 35:541–554.

Lockner, D. and Byerlee, J. D. (1977). Hydrofracture in weber sandstone at high confining pressure and differential stress. *Journal of Geophysical Research*, 82(14):2018–2026.

Lomize, G. (1951). Water flow through jointed rock. *Gosenergoizdat, Moscow*, page 127.

López, J. M. and Schmittbuhl, J. (1998). Anomalous scaling of fracture surfaces. *Physical Review E*, 57(6):6405.

Madyarova, M. (2004). *Propagation of a penny-shaped hydraulic fracture in elastic rock*. PhD thesis, Master's thesis, University of Minnesota, Minneapolis.

Makhnenko, R., Bunger, A., and Detournay, E. (2010). Deviation from linear elastic fracture in near-surface hydraulic fracturing experiments with rock. In 44th *US Rock Mechanics Symposium and* 5th *US-Canada Rock Mechanics Symposium*. ARMA.

Mandelbrot, B. B., Passoja, D. E., and Paullay, A. J. (1984). Fractal character of fracture surfaces of metals. *Nature*, 308(5961):721–722.

Medlin, W., Masse, L., et al. (1984). Laboratory experiments in fracture propagation. *Society of Petroleum Engineers Journal*, 24(03):256–268.

Meredith, P. and Atkinson, B. (1985). Fracture toughness and subcritical crack growth during high-temperature tensile deformation of westerly granite and black gabbro. *Physics of the Earth and Planetary Interiors*, 39(1):33–51.

Moës, N. and Belytschko, T. (2002). Extended finite element method for cohesive crack growth. *Engineering Fracture Mechanics*, 69(7):813–833.

Mollaali, M. and Shen, Y. (2018). An elrod–adams-model-based method to account for the fluid lag in hydraulic fracturing in 2d and 3d. *International Journal of Fracture*, 211(1-2):183–202.

Moore, J. R. and Glaser, S. D. (2007). Self-potential observations during hydraulic fracturing. *Journal of Geophysical Research: Solid Earth*, 112(B2).

Bibliography

Morel, S., Bonamy, D., Ponson, L., and Bouchaud, E. (2008). Transient damage spreading and anomalous scaling in mortar crack surfaces. *Physical Review E*, 78(1):016112.

Morel, S., Bouchaud, E., Schmittbuhl, J., and Valentin, G. (2002). R-curve behavior and roughness development of fracture surfaces. *International Journal of Fracture*, 114(4):307–325.

Moukhtari, F.-E. (2020). *Propagation of fluid driven fractures in transversely isotropic material.* PhD thesis, EPFL.

Mourot, G., Morel, S., Bouchaud, E., and Valentin, G. (2005). Anomalous scaling of mortar fracture surfaces. *Physical Review E*, 71(1):016136.

Mourot, G., Morel, S., Bouchaud, E., and Valentin, G. (2006). Scaling properties of mortar fracture surfaces. *International Journal of Fracture*, 140(1-4):39–54.

Movassagh, A., Haghighi, M., Zhang, X., Kasperczyk, D., and Sayyafzadeh, M. (2020). A fractal approach for surface roughness analysis of laboratory hydraulic fracture. *Journal of Natural Gas Science and Engineering*, page 103703.

Murdoch, L. C. (2002). Mechanical analysis of idealized shallow hydraulic fracture. *Journal of Geotechnical and Geoenvironmental Engineering*, 128(6):488–495.

Naoi, M., Chen, Y., Nishihara, K., Yamamoto, K., Yano, S., Watanabe, S., Morishige, Y., Kawakata, H., Akai, T., Kurosawa, I., et al. (2018). Monitoring hydraulically-induced fractures in the laboratory using acoustic emissions and the fluorescent method. *International Journal of Rock Mechanics and Mining Sciences*, 104:53–63.

Nasseri, M., Grasselli, G., and Mohanty, B. (2010). Fracture toughness and fracture roughness in anisotropic granitic rocks. *Rock Mechanics and Rock Engineering*, 43(4):403–415.

Needleman, A. (2014). Some issues in cohesive surface modeling. *Procedia IUTAM*, 10:221–246.

O'Keeffe, N. J., Huppert, H. E., and Linden, P. F. (2018). Experimental exploration of fluid-driven cracks in brittle hydrogels. *Journal of Fluid Mechanics*, 844:435–458.

Olson, J. E. (2003). Sublinear scaling of fracture aperture versus length: An exception or the rule? *Journal of Geophysical Research: Solid Earth*, 108(B9).

Olson, J. E. and Schultz, R. A. (2011). Comment on "a note on the scaling relations for opening mode fractures in rock" by CH Scholz. *Journal of Structural Geology*, 33(10):1523–1524.

Ouchterlony, F. (1982). Review of fracture toughness testing of rock. *SM archives*, 7:131–211.

Ouchterlony, F. (1990). Fracture toughness testing of rock with core based specimens. *Engineering Fracture Mechanics*, 35(1-3):351–366.

Palmer, I. D. and Veatch Jr, R. W. (1990). Abnormally high fracturing pressures in step-rate tests. *SPE Production Engineering*, 5(03):315–323.

Papanastasiou, P. (1997). The influence of plasticity in hydraulic fracturing. *International Journal of Fracture*, 84(1):61–79.

Papanastasiou, P. (1999). The effective fracture toughness in hydraulic fracturing. *International Journal of Fracture*, 96(2):127–147.

Papanastasiou, P. and Atkinson, C. (2000). Representation of crack-tip plasticity in pressure sensitive geomaterials. *International Journal of Fracture*, 102(3):271–286.

Papanastasiou, P. and Atkinson, C. (2006). Representation of crack-tip plasticity in pressure sensitive geomaterials: Large scale yielding. *International Journal of Fracture*, 139(1):137–144.

Papanastasiou, P., Atkinson, C., et al. (2015). The brittleness index in hydraulic fracturing. In 49th *US Rock Mechanics /Geomechanics Symposium*. ARMA.

Papanastasiou, P., Papamichos, E., and Atkinson, C. (2016). On the risk of hydraulic fracturing in CO2 geological storage. *International Journal for Numerical and Analytical Methods in Geomechanics*, 40(10):1472–1484.

Papanastasiou, P. and Thiercelin, M. (1993). Influence of inelastic rock behaviour in hydraulic fracturing. In *International journal of rock mechanics and mining sciences & geomechanics abstracts*, volume 30, pages 1241–1247. Elsevier.

Park, K. and Paulino, G. H. (2011). Cohesive zone models: a critical review of traction-separation relationships across fracture surfaces. *Applied Mechanics Reviews*, 64(6).

Pollard, D. D. (1987). Theoretical displacements and stresses near fractures in rock: with applications to faults, joints, veins, dikes, and solution surfaces. *Fracture mechanics of rock*, pages 277–349.

Pollard, D. D. and Holzhausen, G. (1979). On the mechanical interaction between a fluid-filled fracture and the earth's surface. *Tectonophysics*, 53(1-2):27–57.

Ponson, L., Auradou, H., Pessel, M., Lazarus, V., and Hulin, J.-P. (2007). Failure mechanisms and surface roughness statistics of fractured fontainebleau sandstone. *Physical Review E*, 76(3):036108.

Raftery, A. E. (1995). Hypothesis testing and model. *Markov chain Monte Carlo in practice*, page 163.

Raven, K. and Gale, J. (1985). Water flow in a natural rock fracture as a function of stress and sample size. *International Journal of Rock Mechanics and Mining Sciences & Geomechanics*, 22(4):251–261.

Renshaw, C. E. (1995). On the relationship between mechanical and hydraulic apertures in rough-walled fractures. *Journal of Geophysical Research: Solid Earth*, 100(B12):24629–24636.

Bibliography

Rice, J. R. (1968). Mathematical analysis in the mechanics of fracture. *Fracture: an advanced treatise*, 2:191–311.

Rice, J. R. (1972). Some remarks on elastic crack-tip stress fields. *International Journal of Solids and Structures*, 8(6):751–758.

Rivalta, E. and Dahm, T. (2006). Acceleration of buoyancy-driven fractures and magmatic dikes beneath the free surface. *Geophysical Journal International*, 166(3):1424–1439.

Rivalta, E., Taisne, B., Bunger, A., and Katz, R. (2015). A review of mechanical models of dike propagation: Schools of thought, results and future directions. *Tectonophysics*, 638:1–42.

Rodriguez, I. V., Stanchits, S., and Burghardt, J. (2016). Insights on the robustness of event locations from analysis of acoustic emissions observed in a triaxial experiment. In *78th EAGE Conference and Exhibition 2016*.

Roper, S. and Lister, J. (2005). Buoyancy-driven crack propagation from an over-pressured source. *Journal of Fluid Mechanics*, 536:79–98.

Roper, S. and Lister, J. (2007). Buoyancy-driven crack propagation: the limit of large fracture toughness. *Journal of Fluid Mechanics*, 580:359–380.

Roshankhah, S., Marshall, J., Tengattini, A., Ando, E., Rubino, V., Rosakis, A., Viggiani, G., and Andrade, J. (2018). Neutron imaging: A new possibility for laboratory observation of hydraulic fractures in shale? *Geotechnique Letters*, 8(4):316–323.

Rubin, A. M. (1993). Tensile fracture of rock at high confining pressure: implications for dike propagation. *Journal of Geophysical Research: Solid Earth*, 98(B9):15919–15935.

Rubin, A. M. (1995). Propagation of magma-filled cracks. *Annual Review of Earth and Planetary Sciences*, 23(1):287–336.

Rybacki, E., Reinicke, A., Meier, T., Makasi, M., and Dresen, G. (2015). What controls the mechanical properties of shale rocks?–part I: Strength and Young's modulus. *Journal of Petroleum Science and Engineering*, 135:702–722.

Salimzadeh, S. and Khalili, N. (2015). A three-phase XFEM model for hydraulic fracturing with cohesive crack propagation. *Computers and Geotechnics*, 69:82–92.

Sarris, E. and Papanastasiou, P. (2011). Modeling of hydraulic fracturing in a poroelastic cohesive formation. *International Journal of Geomechanics*, 12(2):160–167.

Sarris, E. and Papanastasiou, P. (2013). Numerical modeling of fluid-driven fractures in cohesive poroelastoplastic continuum. *International Journal for Numerical and Analytical Methods in Geomechanics*, 37(12):1822–1846.

Savic, M. (1995). *Ultrasonic scattering from a hydraulic fracture: theory, computation and experiment*. TU Delft, Delft University of Technology.

Savitski, A. and Detournay, E. (2002). Propagation of a penny-shaped fluid-driven fracture in an impermeable rock: asymptotic solutions. *International Journal of Solids and Structures*, 39(26):6311–6337.

Scholz, C. H. (2010). A note on the scaling relations for opening mode fractures in rock. *Journal of Structural Geology*, 32(10):1485–1487.

Schrauf, T. and Evans, D. (1986). Laboratory studies of gas flow through a single natural fracture. *Water Resources Research*, 22(7):1038–1050.

Schultz, R. A., Mège, D., and Diot, H. (2008a). Emplacement conditions of igneous dikes in ethiopian traps. *Journal of Volcanology and Geothermal Research*, 178(4):683–692.

Schultz, R. A., Soliva, R., Fossen, H., Okubo, C. H., and Reeves, D. M. (2008b). Dependence of displacement–length scaling relations for fractures and deformation bands on the volumetric changes across them. *Journal of Structural Geology*, 30(11):1405–1411.

Shen, Y. (2014). A variational inequality formulation to incorporate the fluid lag in fluid-driven fracture propagation. *Computer Methods in Applied Mechanics and Engineering*, 272:17–33.

Shlyapobersky, J. (1985). Energy analysis of hydraulic fracturing. In *The 26th US Symposium on Rock Mechanics (USRMS)*, Rapid City, South Dakota. ARMA.

Shlyapobersky, J., Issa, M. A., Issa, M. A., Islam, M., Dudley, J. W., Shulkin, Y., and Chudnovsky, A. (1998). Scale effects on fracture growth resistance in poroelastic materials. In *SPE Annual Technical Conference and Exhibition*. SPE.

Shlyapobersky, J., Wong, G., and Walhaug, W. (1988). Overpressure calibrated design of hydraulic fracture stimulations. In *SPE Annual Technical Conference and Exhibition*. SPE.

Spence, D. and Sharp, P. (1985). Self-similar solutions for elastohydrodynamic cavity flow. *Proceedings of the Royal Society of London. A. Mathematical and Physical Sciences*, 400(1819):289–313.

Spence, D., Sharp, P., and Turcotte, D. (1987). Buoyancy-driven crack propagation: a mechanism for magma migration. *Journal of Fluid Mechanics*, 174:135–153.

Stanchits, S., Burghardt, J., and Surdi, A. (2015). Hydraulic fracturing of heterogeneous rock monitored by acoustic emission. *Rock Mechanics and Rock Engineering*, 48(6):2513–2527.

Stanchits, S., Surdi, A., Gathogo, P., Edelman, E., and Suarez-Rivera, R. (2014). Onset of hydraulic fracture initiation monitored by acoustic emission and volumetric deformation measurements. *Rock Mechanics and Rock Engineering*, 47(5):1521–1532.

Stoeckhert, F., Molenda, M., Brenne, S., and Alber, M. (2015). Fracture propagation in sandstone and slate–laboratory experiments, acoustic emissions and fracture mechanics. *Journal of Rock Mechanics and Geotechnical Engineering*, 7(3):237–249.

Bibliography

Storn, R. and Price, K. (1997). Differential evolution–a simple and efficient heuristic for global optimization over continuous spaces. *Journal of Global Optimization*, 11(4):341–359.

Szeri, A. Z. (2010). *Fluid Film Lubrication*. Cambridge University Press.

Tada, H., Paris, P. C., and Irwin, G. R. (1973). The stress analysis of cracks. *Del Research Corp, Hellertown PA*.

Talon, L., Auradou, H., and Hansen, A. (2010). Permeability of self-affine aperture fields. *Physical Review E*, 82(4):046108.

Tarantola, A. (2005). *Inverse Problem Theory and methods for model parameter estimation.* SIAM.

Technologies, T.-S. (2005). Zimbabwe black granite physical properties. Technical report, Tru-Stone technologies.

Thallak, S., Holder, J., and Gray, K. (1993). The pressure dependence of apparent hydrofracture toughness. In *The 34th US Symposium on Rock Mechanics (USRMS)*, Madison, Wisconsin. ARMA.

Tsai, V. and Rice, J. R. (2010). A model for turbulent hydraulic fracture and application to crack propagation at glacier beds. *Journal of Geophysical Research - Earth Surface*, 115(F3):F03007.

Turon, A., Dávila, C., Camanho, P., and Costa, J. (2007). An engineering solution for mesh size effects in the simulation of delamination using cohesive zone models. *Engineering Fracture Mechanics*, 74(10):1665 – 1682.

Van As, A. and Jeffrey, R. (2002). Hydraulic fracture growth in naturally fractured rock: mine through mapping and analysis.

Van Dam, D. and de Pater, C. (1999). Roughness of hydraulic fractures: The importance of in-situ stress and tip processes. In *SPE Annual Technical Conference and Exhibition*. SPE.

van Dam, D. B. (1999). *The influence of inelastic rock behaviour on hydraulic fracture geometry*. PhD thesis, TU Delft, Delft University of Technology.

Vasudevan, A., Grabois, T. M., Cordeiro, G. C., Morel, S., Ponson, L., et al. (2021). Adaptation of the tapered double cantilever beam test for the measurement of fracture energy and its variations with crack speed. *arXiv preprint arXiv:2101.04380*.

Vernède, S., Ponson, L., and Bouchaud, J.-P. (2015). Turbulent fracture surfaces: A footprint of damage percolation? *Physical Review Letters*, 114(21):215501.

Viesca, R. and Garagash, D. I. (2017). Numerical methods for coupled fracture problems. *Computational Methods in Applied Mechanics and Engineering*.

Wang, H. (2015). Numerical modeling of non-planar hydraulic fracture propagation in brittle and ductile rocks using xfem with cohesive zone method. *Journal of Petroleum Science and Engineering*, 135:127–140.

Weisinger, R., Costin, L., and Lutz, T. (1980). K_{Ic} and *J*-resistance-curve measurements on Nevada tuff. *Experiemntal Mechanics*, 20(2):68–72.

Williams, M. (1997). On the stress distribution at the base of a stationary crack.

Witherspoon, P. A., Wang, J. S., Iwai, K., and Gale, J. E. (1980). Validity of cubic law for fluid flow in a deformable rock fracture. *Water resources research*, 16(6):1016–1024.

Wolfram Research, Inc. (2016). *Mathematica*. Wolfram Research, Inc., Champaign, Illinois, version 11.0 edition.

Wu, R., Bunger, A., Jeffrey, R., Siebrits, E., et al. (2008). A comparison of numerical and experimental results of hydraulic fracture growth into a zone of lower confining stress. In *The 42nd US rock mechanics symposium (USRMS)*. American Rock Mechanics Association.

Xing, P., Bunger, A., Yoshioka, K., Adachi, J., El-Fayoumi, A., et al. (2016). Experimental study of hydraulic fracture containment in layered reservoirs. In *50th US Rock Mechanics/Geomechanics Symposium*. American Rock Mechanics Association.

Xing, P., Yoshioka, K., Adachi, J., El-Fayoumi, A., and Bunger, A. P. (2017). Laboratory measurement of tip and global behavior for zero-toughness hydraulic fractures with circular and blade-shaped (PKN) geometry. *Journal of the Mechanics and Physics of Solids*, 104:172–186.

Yao, Y., Liu, L., and Keer, L. M. (2015). Pore pressure cohesive zone modeling of hydraulic fracture in quasi-brittle rocks. *Mechanics of Materials*, 83:17–29.

Zang, A., Wagner, F. C., Stanchits, S., Janssen, C., and Dresen, G. (2000). Fracture process zone in granite. *Journal of Geophysical Research: Solid Earth*, 105(B10):23651–23661.

Zhang, C. and Gross, D. (1993). Wave attenuation and dispersion in randomly cracked solids— ii. penny-shaped cracks. *International Journal of Engineering Science*, 31(6):859–872.

Zhang, X., Jeffrey, R., and Detournay, E. (2005). Propagation of a hydraulic fracture parallel to a free surface. *International Journal for Numerical and Analytical Methods in Geomechanics*, 29(13):1317–1340.

Zhang, Z., Nemcik, J., Qiao, Q., and Geng, X. (2015). A model for water flow through rock fractures based on friction factor. *Rock Mechanics and Rock Engineering*, 48(2):559–571.

Zhao, C., Xing, J., Zhou, Y., Shi, Z., and Wang, G. (2020). Experimental investigation on hydraulic fracturing of granite specimens with double flaws based on DIC. *Engineering Geology*, page 105510.

Bibliography

Zhao, Z., Kim, H., and Haimson, B. (1996). Hydraulic fracturing initiation in granite. In 2nd *North American Rock Mechanics Symposium*, pages 1279–1284, Montreal, Quebec, Canada.

Zia, H. and Lecampion, B. (2017). Propagation of a height contained hydraulic fracture in turbulent flow regimes. *International Journal of Solids and Structures*, 110:265–278.

Zietlow, W. K. and Labuz, J. F. (1998). Measurement of the intrinsic process zone in rock using acoustic emission. *International Journal of Rock Mechanics and Mining Sciences*, 35(3):291–299.

Zimmerman, R. W. and Bodvarsson, G. S. (1996). Hydraulic conductivity of rock fractures. *Transport in Porous Media*, 23(1):1–30.

Zoback, M., Rummel, F., Jung, R., and Raleigh, C. (1977). Laboratory hydraulic fracturing experiments in intact and pre-fractured rock. In *International Journal of Rock Mechanics and Mining Sciences & Geomechanics Abstracts*, volume 14, pages 49–58. Elsevier.

Mr. Dong LIU
Ph.D. in Mechanics
Chinese citizen - 11. 1991 - Single

📍 1 Avenue du Mont d'Or, 1007 Lausanne, Switzerland

📞 +41 78 634 80 92   ✉ dongliu_epfl@163.com

EDUCATION

2016. 10 - Present	**École Polytechnique Fédérale de Lausanne, Lausanne, Switzerland** Geo-Energy Laboratory – Gaznat chair on Geo-Energy. Title of Ph.D. thesis: "Growth of hydraulic fractures in quasi-brittle materials".
2013. 09 - 2016. 09	**École Nationale des Ponts et Chaussées, Champs-sur-Marne, France** Diplôme d'ingénieur, double degree program with **Tongji University** in civil engineering. Master's degree in material science for sustainable construction.
2009. 09 - 2013. 07	**Tongji University, Shanghai, China** Bachelor's degree in civil engineering.
2010. 09 - 2012. 06	**Fudan University, Shanghai, China** Minor degree in finance.

PROFESSIONAL EXPERIENCE

2016. 10 - Present	Teaching assistant, **École Polytechnique Fédérale de Lausanne, Lausanne, Switzerland** Courses: Ouvrages Géotechniques. Supervisions of exercises sessions and students' projects.
2016. 03 - 2016. 08	Research Engineer (Internship), **EDF R&D, site des Renardières, Écuelle, France** Testing, validation and optimization of the EDF self-developed software Vi(CA)2T. Numerical investigation on the effect of the grain size distribution on the cement hydration.
2015. 07 - 2015. 08	Research Engineer (Internship), **Lafarge Holcim Centre de recherche, St Fallavier, France** Experimental study on the foliation of the cement surfaces due to the freezing-thawing cycles. Observation of the ice structure using microscopy.
2013. 03 - 2013. 07	Senior thesis, **Tongji University**, **Shanghai, China** Title: "Vulnerability analysis of a continuous girder bridge accounting for the material degradation and optimization of structural health monitoring sensor allocation".

SCIENTIFIC PUBLICATIONS

1. Liu, D. and Lecampion, B., 2020. Propagation of a plane-strain hydraulic fracture accounting for a rough cohesive zone. *Journal of the Mechanics and Physics of Solids*. (Manuscript submitted for publication). 10.1016/j.jmps.2021.104322

2. Liu, D., Lecampion, B. and Blum, T., 2020. Time-lapse reconstruction of the fracture front from diffracted waves arrivals in laboratory hydraulic fracture experiments. *Geophysical Journal International, 223.(1), 180-196.* 10.1093/gji/ggaa310

3. Liu, D., Lecampion, B. and Garagash, D.I., 2019. Propagation of a fluid-driven fracture with fracture length dependent apparent toughness. *Engineering Fracture Mechanics*, *220*, p.106616. 10.1016/j.engfracmech.2019.106616

4. Liu, D. and Lecampion, B., 2019, June. Propagation of a plane-strain hydraulic fracture accounting for the presence of a cohesive zone and a fluid lag. In *53rd US Rock Mechanics/Geomechanics Symposium,* ARMA-2019-0103.

5. Liu, D. and Lecampion, B., 2019, September. Growth of a Radial Hydraulic Fracture Accounting for the Viscous Fluid Flow in a Rough Cohesive Zone. In *ARMA-CUPB Geothermal International Conference*, ARMA-CUPB-19-4210.

LANGUAGES & SOFTWARE

English: Fluent, C1-C2 level.	**Chinese**: Native proficiency.
French: Fluent, B2-C1 level.	**German**: Beginner, A1-A2 level.

Software: Developing language: C/C++; Finite Element software: Ansys, Abaqus, Midas; Civil engineering software: AutoCAD, SolidWorks;	Version Control Systems: Git (Github, C4science) Prototyping programming: Python, Mathematica, Matlab; Other software: LaTeX, Microsoft Office, Adobe;

AWARDS

2014 – 2016	France Excellence Master Scholarship.
2009 – 2010	National Scholarship.
2010 – 2011	Tongji University Excellent Students.
2010 – 2011	Tongji University Outstanding Second-class Scholarship.
2011 – 2012	Tongji University Outstanding Second-class Scholarship.
2011 – 2012	Mao Yi-sheng Science and Technology Education Foundation Prize for Undergraduate Students.

SOCIAL SERVICES & SPORTS

Volunteer	WuZhiQiao (Bridge to China) Charitable Foundation, Sichuan, China
	Evaluation of a suspension bridge suffering from material degradation.
	Volunteer of the World Expo 2010 Shanghai.
Sports	Jogging, Hiking, Ski and Swimming.

REFERENCES

Prof. Brice Lecampion	Thesis supervisor, EPFL, Switzerland
	brice.lecampion@epfl.ch
	Tel: +41 (0) 21 693 27 07
Dr. Thomas Blum	Co-worker who has co-supervised my thesis at EPFL
	(now Research Engineer at L.E.S.S. SA), Switzerland
	thomas.blum@less-sa.com
	Tel: +41 (0) 21 552 08 77
Prof. Limin Sun	Master's thesis supervisor, Tongji University, China
	lmsun@tongji.edu.cn
	Tel: 65983116-2719